Xiao Hu

Multiscale Simulation of Metallic Copper and Copper Oxide
Atomic Layer Deposition from Cu Beta-diketonates

Xiao Hu

Multiscale Simulation of Metallic Copper and Copper OxideAtomic Layer Deposition from Cu Beta-diketonates

TECHNISCHE UNIVERSITÄT
CHEMNITZ

Universitätsverlag Chemnitz
2018

Impressum

Bibliografische Information der Deutschen Nationalbibliothek

Die Deutsche Nationalbibliothek verzeichnet diese Publikation in der Deutschen Nationalbibliografie; detaillierte bibliografische Angaben sind im Internet über http://dnb.d-nb.de abrufbar.

Multiscale Simulation of Metallic Copper and Copper Oxide Atomic Layer Deposition from Cu Beta-diketonates

Multiskalensimulation der Atomlagenabscheidung von metallischem Kupfer und Kupferoxid aus Cu Beta-Diketonate

Von der Fakultät für Elektrotechnik und Informationstechnik
der Technischen Universität Chemnitz

genehmigte

Dissertation

zur Erlangung des akademischen Grades

Doktoringenieur

(Dr.-Ing.)

vorgelegt

von	M.Sc. Xiao Hu
geboren am	19. Oktober 1985
in	Chongqing, China
eingereicht am	20. Dezember 2016
Gutachter	Prof. Dr. Stefan E. Schulz
	Prof. Dr. Johann W. Bartha
	Dr. Simon D. Elliott
Tag der Verleihung	02. November 2017

Bibliographic description

Multiscale Simulation of Metallic Copper and Copper Oxide Atomic Layer Deposition from Cu Beta-diketonates

Hu, Xiao – 197 Pages, 85 Figures, 23 Tables, 182 References

Technische Universität Chemnitz, Fakultät für Elektrotechnik und Informationstechnik

Dissertation (in English language), 2016

Abstract

Copper (Cu) interconnects have been widely used to replace aluminum in ultra-large-scale integration due to low resistivity and superior resistance to electromigration. Current processes for the fabrication of interconnects require thin Cu seed layers before the subsequent Cu filling by electrochemical deposition (ECD). It is crucial that these seed layers are coated conformally and smoothly in vias and trenches, ensuring that the ECD Cu films are free of voids. With the continuous scaling down of device dimensions, atomic layer deposition (ALD) has been considered as the most promising technology for making the Cu seed layers, because of its excellent conformality and precise thickness control.

This dissertation is dedicated to the multiscale simulation of Cu ALD using the Cu beta-diketonate precursors $(^nBu_3P)_2Cu(acac)$ and $Cu(acac)_2$. Different co-reactants (H, H_2, H_2O, O_3 and wet O_2) were investigated with respect to their application for the ALD of metallic Cu and Cu oxides. While Cu beta-diketonates have been widely applied in ALD, the mechanistic details of the surface reactions are still largely unknown.

Ab initio calculations were performed to obtain the input data for reactive molecular dynamics (RMD) simulations and thermodynamic modeling, which were realized at the molecular-scale and macroscale, respectively. In the gas-phase, the thermodynamic analysis predicts that the $(^nBu_3P)_2Cu(acac)$ precursor will dissociate into $(^nBu_3P)Cu(acac)$ and $^nBu_3P$ even at low temperatures (300–400 K). The further dissociation of $(^nBu_3P)Cu(acac)$ requires much higher temperatures (> 575 K), which prevents the undesired disproportionation reaction. On the other hand, the gas-phase decomposition of the $Cu(acac)_2$ precursor is unfavorable during ALD.

The adsorption and decomposition of Cu precursors were studied on the Ta(110), Cu(110), Ru(001), $Cu_2O(111)$, $SiO_2(001)$, and TaN(111) substrates. A simplified precursor model $(Me_3P)Cu(acac)$ was applied to save computational costs. The metallic substrates Ta, Cu, and Ru, exhibit a much higher reactivity towards Cu precursors as compared to the metal oxide (Cu_2O and SiO_2) and the metal nitride (TaN) substrates. It is evident that electrons are transferred from the metallic surface to the adsorbate, leading to the reduction of the Cu center atom.

RMD simulations were performed to understand the surface reactions between the Cu precursor and different co-reactants. Water reacts with adsorbed Cu(acac) through a ligand-exchange reaction, producing gaseous H(acac) and surface OH species. In the presence of O_2, the released H(acac) molecules can be further oxidized into CO_x and H_2O, which is under kinetic control. Molecular hydrogen is found to be nonreactive towards $Cu(acac)_2$; whereas atomic H can efficiently remove the surface acac-ligands, with C_xH_y and H_xO as the reaction products. A combustion-like reaction with the by-products CO_x and H_xO_y is observed in the reaction between $Cu(acac)_2$ and O_3. By comparison with the reaction rate and the carbon removal ratio under different conditions, it can be concluded that the reactivity of co-reactants towards $Cu(acac)_2$ follows the order $H > O_3 > H_2O > H_2$.

Keywords

Atomic Layer Deposition (ALD), Surface chemistry, Cu beta-diketonates, Stability and reactivity, Cu seed layer, Interconnects, Multiscale simulation, *Ab initio* calculations, Reactive molecular dynamics (RMD), Thermodynamic modeling, Force field development.

Referat

Kupferleitbahnen werden in höchstintegrierten Schaltkreisen aufgrund des niedrigen spezifischen Widerstands und der sehr guten Beständigkeit gegen Elektromigration verwenden. Aktuelle Verfahren zur Leitbahnherstellung erfordern dünne Cu Keimschichten vor der anschließenden Cu Füllung durch die elektrochemische Abscheidung (ECD). Dabei ist es entscheidend, dass diese Keimschichten konform und glatt in den Vias und Gräben abgeschieden werden können, so dass die ECD Cu-Filme frei von Hohlräumen sind. Mit der weiteren Skalierung wird die Atomlagenabscheidung (ALD) mit ihrer hohen Konformalität und der ausgezeichneten Dickensteuerung als die vielversprechendste Technik zur Herstellung der Cu Keimschichten betrachtet.

Die vorliegende Dissertation ist der Multiskalensimulation der ALD von metallischem Kupfer und Kupferoxiden aus Cu-beta-Diketonat Präkursoren ($^{n}Bu_3P)_2Cu(acac)$ und $Cu(acac)_2$ gewidmet. Verschiedene Koreaktanden H, H_2, H_2O, O_3 und feuchtes O_2 werden hinsichtlich ihrer Anwendung für die ALD von metallischem Kupfer oder Kupferoxid untersucht. Die Mechanismen der Oberflächenreaktionen dieser Präkursoren sind noch weitgehend unbekannt, obwohl die Cu Beta-Diketonate in der ALD bereits breite Verwendung finden.

Ab-initio-Rechnungen wurden durchgeführt, um die Eingangsdaten für die reaktive Moleklardynamiksimulation und die thermodynamische Modellierung zu erhalten, die sowohl auf molekularer wie auch auf makroskopischer Ebene durchgeführt wurden. Mit der thermodynamischen Analyse wird gezeigt, dass ($^{n}Bu_3P)_2Cu(acac)$ in der Gasphase auch bei tiefen Temperaturen (300–400 K) in ($^{n}Bu_3P)Cu(acac)$ und $^{n}Bu_3P$ dissoziiert. Die weitere Dissoziation des ($^{n}Bu_3P)Cu(acac)$-Komplexes erfordert höhere Temperaturen (>575 K), so dass die unerwünschte Disproportionierungsreaktion bei der ALD verhindert wird. Weiterhin wird gezeigt, dass im ALD Prozess keine Gasphasenzersetzung des $Cu(acac)_2$-Präkursors stattfindet.

Die Adsorption und die Oberflächenzersetzung der Kupferpräkursoren wurden auf Ta(110), Cu(110), Ru(001), Cu_2O(111), SiO_2(001), und TaN(111) Substraten untersucht. Dabei wird mit $(Me_3P)Cu(acac)$ ein vereinfachtes Modell des Kupferpräkursors verwendet, um den Rechenaufwand zu begrenzen. Die metallischen Substrate (Ta, Cu und Ru) sind für den Kupferpräkursor reaktiver im Vergleich zu Metalloxid- (Cu_2O und SiO_2) und Metallnitridsubstraten (TaN). Bei der Zersetzung werden Elektronen von den Metalloberflächen auf das Adsorbat übertragen, was zur Reduktion des Kupferatoms des Präkursor führt.

Simulationen mit reaktiver Molekulardynamik wurden durchgeführt, um die Oberflächenreaktionen zwischen dem Kupferpräkursor und verschiedenen Koreaktanden zu untersuchen. Wasser reagiert mit dem adsorbierten Cu(acac) durch eine Ligandenaustauschreaktion wobei gasförmiges H(acac) und Oberflächen-OH-Gruppen entstehen. Bei Anwesenheit von O_2, kann H(acac) weiter in CO_x und H_2O oxidiert werden, was unter kinetischer Kontrolle stattfindet. Molekularer Wasserstoff ist nicht reaktiv gegenüber dem Cu(acac)$_2$, während atomarer Wasserstoff die acac-Liganden auf der Oberfläche effizient entfernen kann, wobei C_xH_y und H_xO als Reaktionsprodukte entstehen. Verbrennungsreaktionen mit CO_x und H_xO_y als Nebenprodukte werden in der Reaktion zwischen Cu(acac)$_2$ und O_3 beobachtet. Beim Vergleich der Reaktionsgeschwindigkeiten und der Abtragsrate für Kohlenstoff unter verschiedenen Bedingungen ergibt sich, dass die Reaktivität der Koreaktanden der Reihenfolge $H > O_3 > H_2O > H_2$ folgt.

Stichworte

Table of Contents

Inhaltsverzeichnis

List of acronyms and symbols

Abbreviations

AIMD	*Ab initio* molecular dynamics
ALD	Atomic Layer Deposition
ANOVA	Analysis of Variance
BEOL	Back-End of Line
CI	Climbing Image
CMD	Classical Molecular Dynamics
CMP	Chemical Mechanical Polishing
CVD	Chemical Vapor Deposition
DFT	Density Functional Theory
DOF	Degrees of Freedom
DRAM	Dynamic Random Access Memory
ECD	Electrochemical Deposition
EFF	Empirical Force Field
EOS	Equations of States
EOT	Equivalent Oxide Thickness
FEOL	Front-End of Line
FeRAM	Ferroelectric random access memory
GEM	Gibbs Energy Minimization
GGA	Generalized Gradient Approximations
GPC	Growth Per Cycle
GRG	Generalized Reduced Gradient
HF	Hartree–Fock
HK	Hohenberg and Kohn
HOMO	Highest Occupied Molecular Orbital
IC	Integrated Circuit
KMC	Kinetic Monte Carlo

KS	Kohn and Sham
LDA	Local-Density Approximation
LSDA	Local-Spin-Density Approximation
LUMO	Lowest Unoccupied Molecular Orbital
MEP	Minimum Energy Path
MIM	Metal–Insulator–Metal
ML	Molecular Layering
MOSFET	Metal-oxide Field Effect Transistor
MPU	Microprocessor Unit
NEB	Nudged Elastic Band
OA	Orthogonal Array
PBE	Perdew–Burke–Ernzerhof
PCRAM	Phase-Change Random Access Memory
PEALD	Plasma-Enhanced Atomic Layer Deposition
PVD	Physical Vapor Deposition
PW	Perdew–Wang
QE	Quantum Espresso
RFF	Reactive Force Field
RMD	Reactive Molecular Dynamics
S/N	Signal-to-Noise
SPS	Single Parameter Search
TST	Transition State Theory
ULSI	Ultra-Large-Scale-Integration
vdW	van der Waals
XPS	X-ray Photoelectron Spectroscopy
ZPE	Zero Point Energy

List of symbols

A	Pre-exponential factor
a_{ij}	Number of atoms of jth element present in each species i
A_j	Total number of atoms of jth element in the system
BO	Bond order

C	Coupling capacitance
C_p	Thermal capacity
d	Distance
E_a	Activation energy
E_{ads}	Adsorption energy
E_{bond}	Bond energy
E_{conj}	Conjugation energy
$E_{Coulomb}$	Coulomb interaction energy
$E_{internal}$	Internal energy
E_{know}	Known energy functional
$E_{lateral}$	Lateral interactions
$E[n(\boldsymbol{r})]$	Energy functional
E_{NL}	Nonlocal energy functional
E_{over}	Overcoordination energy
E_{pen}	Penalty energy
E_{system}	System energy
E_{tors}	Torsion angle energy
E_{under}	Undercoordination energy
E_{val}	Valence angle energy
$E_{vdWaals}$	van der Waals interaction energy
E_{XC}	Exchange-correlation functional
$\mathcal{E}_{XC}$	Exchange-correlation energy per electron
F	Force
$f(\alpha)$	Reaction kinetics model
G	Gibbs free energy
$g(\alpha)$	The integrated form of the reaction model
G_{total}	Total Gibbs free energy
H	Enthalpy
$\hat{H}$	Hamilton operator
$\hat{H}_{elec}$	Electronic Hamilton operator
H_r	Enthalpy due to rotational motion
I	Moment of inertia
K	Vibrational mode
k_-	Rate constant of reverse reaction
k_+	Rate constant of forward reaction
k_B	Boltzmann constant
K_{eq}	Equilibrium constant
k_s	Spring constant
L	Lagrange function

m	Mass
MS_{error}	Mean squares of the error
MS_x	Mean squares for each factor
M_{Xi}	The mean S/N ratio
N	Number
$n(\boldsymbol{r})$	Density of electrons
N_C	Number of components
N_E	Number of external factors
N_P	Number of phases
$\emptyset(\boldsymbol{r}, \boldsymbol{r}')$	Kernel function
P_i	Partial pressure of species i
$Q_{abs.}$	Mulliken charge of the adsorbate
q_e	Electronic partition function
q_{IS}	Partition functions of the initial state
Q_o	Equilibrium angle
q_r	Rotational partition function
q_t	Translational partition function
q_{TS}	Partition functions of the transition state
q_v	Vibrational partition function
R	Resistance; gas constant; replica
r_{ij}	Interatomic distance
S	Entropy
S_r	Entropy due to rotational motion
SS	Sum of squares
T	Temperature
t	Reaction time
$\hat{T}_e$	Kinetic energy operator of electron
$T_e[n(\boldsymbol{r})]$	Electron kinetic energy
$\hat{U}_{ee}$	Potential energy operator between electrons
$U_{ee}[n(\boldsymbol{r})]$	Electron-electron interaction energy
V	Volume
Val	Number of bonding electron
$V_{Ne}[n(\boldsymbol{r})]$	Potential energy between the electron and nuclei
$\hat{V}_{Ne}$	Potential energy operator between electron and nuclei
$V_S(\boldsymbol{r})$	Effective potential
V_{XC}	Exchange-correlation potential
$X_{i,ReaxFF}$	ReaxFF value

$X_{i,\text{Ref}}$	Reference value
α	Extent of conversion
β	Scaling factor
Δ	Overcoordination
ε	Energy level; Kohn-Sham orbital energy
θ	Coverage
Θ_r	Characteristic rotational temperature
$\Theta_{v,K}$	Characteristic temperature for vibration K
$\phi_i(\boldsymbol{r})$	Kohn-Sham orbital
k	Dielectric constant
λ	Lagrange's multiplier
μ_i	Chemical potential of species i
τ	Interconnect delay
$\hat{\boldsymbol{\tau}}_i$	Normalized local tangent at replica i
Ψ	Wave function
ω	Degeneracy of the energy level

Abbreviations of chemicals and functional groups

acac	Acetylacetonate
amd	Amidinate
Bu	Butyl
dmamb	1-dimethylamino-2-methyl-2-butanolate
dmap	Dimethyl-2-propoxide
Et	Ethyl
hfac	Hexafluoroacetylacetonate
hmds	Hexamethyldisilazide
iPr	Isopropyl
Me	Methyl
mmp	1-methoxy-2-methyl-2-propoxide
NHC	N-heterocyclic carbene
pyrim	Pyrrolylaldiminate
TDMAH	Tetrakis(dimethylamido)hafnium
TEMAH	Tetrakis(ethylmethylamido)hafnium
thd	Tetramethylheptanedionate

TMA   Trimethylaluminum

tmvs   Trimethylvenylsilyl

$ZnEt_2$ Diethylzinc

Chapter 1 Introduction

In 1965, Gordon Moore noted in his groundbreaking paper [1] that "*The complexity for minimum component costs has increased at a rate of roughly a factor of two per year. Certainly over the short term this rate can be expected to continue if not to increase*". This exponential increase in the number of components per integrated circuit (IC) is known as "Moore's law". Later, this law was modified, stating that the number of transistors per IC doubles every two years and then every 18 months. Over the past decades, Moore's Law was found to be accurate and has been used to guide research and development in the semiconductor industry. To keep up with Moore's law, the feature size of metal-oxide field effect transistors (MOSFETs) is continuously scaled down, resulting in improvements in both device density and performance. However, the pace of advancement has recently slowed due to technical and physical limitations.

Fig. 1.1 illustrates a schematic view of a microprocessor unit (MPU) in cross-section [2]. The fabrication processes can be divided into two phases. Transistors are formed in the so-called Front-End of Line (FEOL) processes, while metal wirings are built in the Back-End of Line (BEOL) level. In the FEOL, the transistor performance improves with the scaling of channel length, channel width, and gate dielectric thickness. Each new technology node represents a ~0.7 times reduction in feature size [3]. Intel's latest generation of microprocessor (Core M) contains 1.3 billion transistors on an 82 mm^2 die size, which is manufactured using the 14 nm technology [3]. Nevertheless, the further scaling is becoming increasingly difficult due to several severe challenges, such as short channel effects, current leakage, and mobility degradation.

In the BEOL, shrinking of the cross-sectional dimensions of the interconnect lines degrades the signal propagation speed, compromising the benefits provided by transistor scaling. As shown in Fig. 1.2, the interconnect delay (also referred as RC delay) has become a dominant factor, rather than the transistor delay, in determining the chip performance [4]. Consequently, the importance of interconnects will greatly increase at each new technology node as scaling down continues. The interconnect delay (τ) can be estimated as follows

$$\tau = RC \tag{1.1}$$
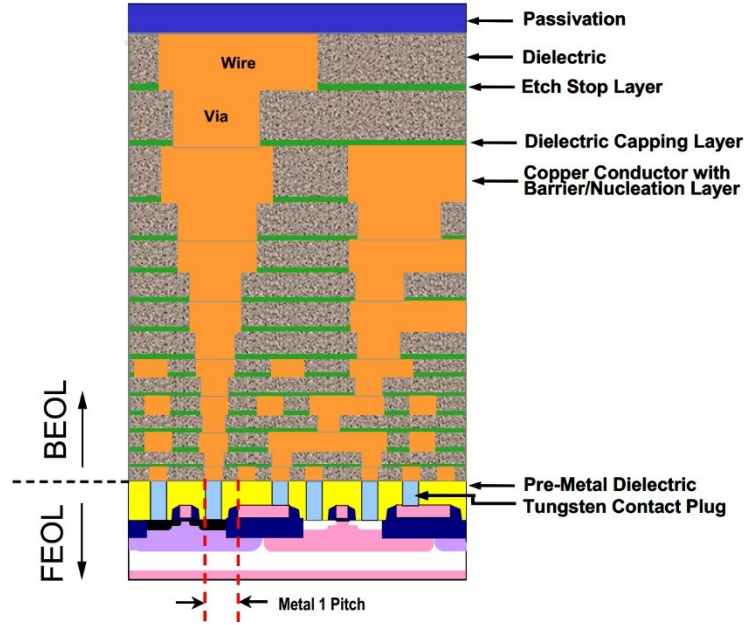
Fig. 1.1 Schematic view of a typical MPU device in cross-section (source of image: ITRS 2013 interconnect) [2].
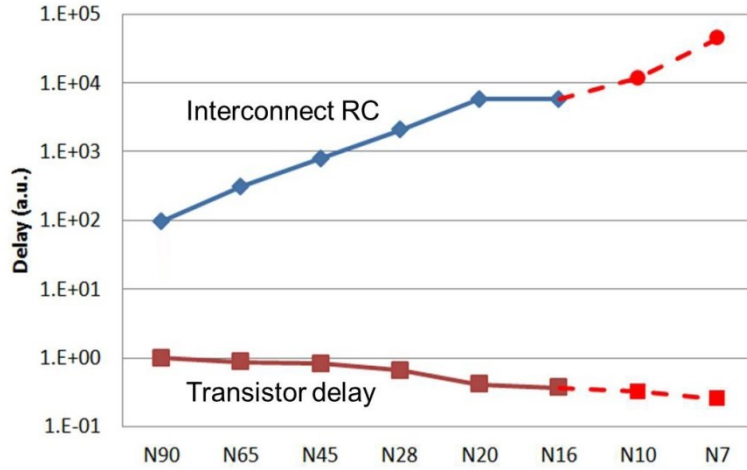
Fig. 1.2 Effect of scaling down of device dimension on the signal delay in interconnect and transistor. Reproduced from Ref. [4] with permission from IEEE, copyright 2013.

where R and C represent an interconnect's total resistance and coupling capacitance, respectively. To reduce the interconnect delay, low resistivity metal wiring and low-k intermetal dielectrics are required. Fig. 1.3 shows state-of-the-art copper interconnects together with air-gaps and ultralow-k dielectrics, fabricated within Intel's 14 nm technology [5].

The use of carbon doped oxide (SiCOH) low-k dielectrics ($k \approx 3$) started at the 90 nm technology node [6]. With C-doping, the dielectric constant of SiO_2 ($k \approx 4$) can be significantly reduced, due to decreased bulk density and electronic polarizability. Porous SiCOH low-k dielectrics ($k \approx 2.4$) were used at the 45 nm technology node to reduce further the interconnect capacitance and cross-talk noise [7]. At the 14 nm node [5], advanced air-gap
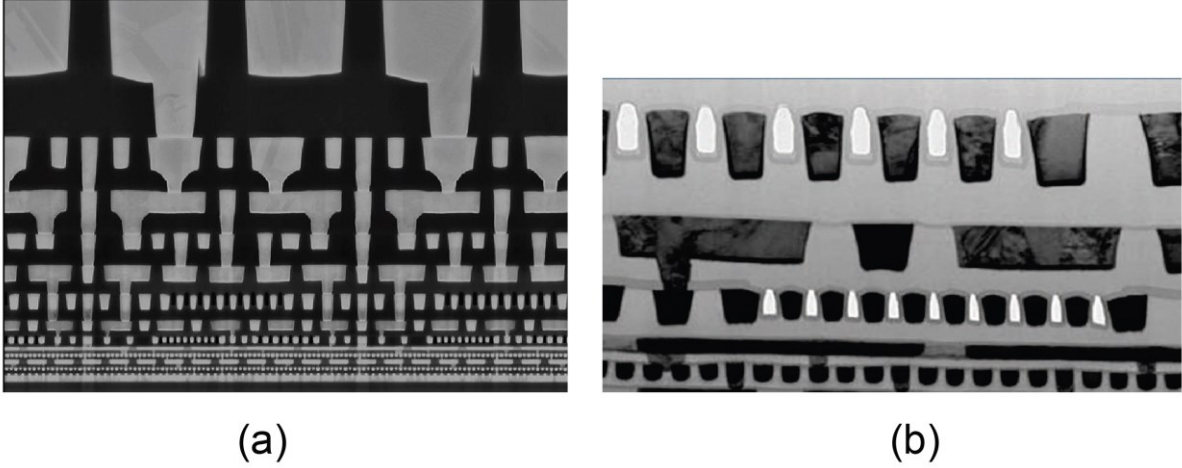
Fig. 1.3 Cross-section of an Intel Cu interconnects system. (a) The 12 metal layers of the interconnect stack. (b) Air gaps at metal layers 4 and 6. Reproduced from Ref. [5] with permission from IEEE, copyright 2015.

dielectrics (ideally $k \approx 1$) were first introduced (see Fig. 1.3 b), providing improved capacitance at performance-critical metal layers.

Copper interconnects have been widely used to replace aluminum in ultra-large-scale-integration (ULSI) metallization due to their low resistivity and superior resistance to electromigration. The bulk Cu has a resistivity of only 1.67 μΩ.cm, providing a nearly 40% reduction in resistivity over Al (2.67 μΩ.cm). Furthermore, Cu has twice the thermal conductivity of Al and is by a factor of 10–100 less susceptible to electromigration damage than Al [8]. While Cu interconnects offer promising performances, it also introduces several fabrication and integration challenges. For example, Cu cannot be patterned using the conventional approaches like reactive ion etching. It is also more difficult to fill trenches and vias without voids.

The Cu damascene process, first introduced by IBM in 1997, has emerged as a standard solution for chip interconnects [9]. The key steps of this process are schematically shown in Fig. 1.4. First, the damascene structures are patterned and etched into the dielectrics. Second, a diffusion barrier such as Ta/TaN layers is deposited on the patterned dielectrics, in order to prevent the migration of Cu into the dielectrics and to provide a good adhesion for Cu. Next, a conductive Cu thin film is grown on the diffusion barrier as a seed layer. Then, the pattern is filled by Cu using electrochemical deposition (ECD). Finally, chemical mechanical polishing (CMP) is used to planarize the wafer surface. A via and a trench can be metallized and planarized simultaneously, referred as a dual Damascene process.
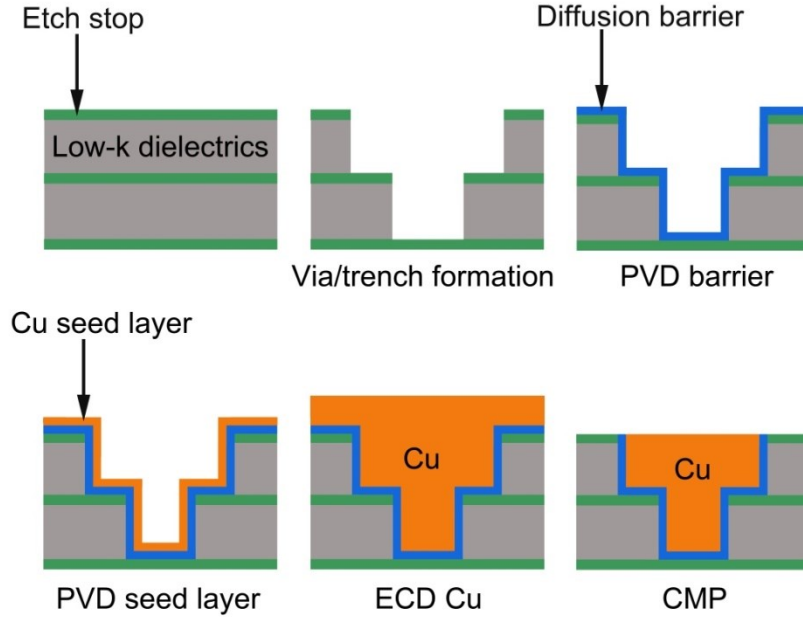
Fig. 1.4 Steps of the Cu dual damascene process.
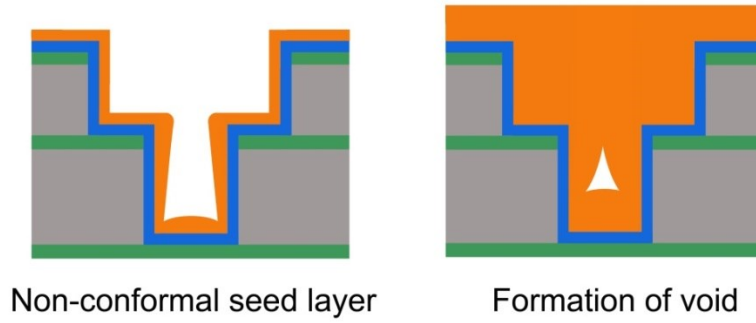
Fig. 1.5 Schematic of void formation in a high aspect ratio structure during the Cu ECD.

Conformality of the Cu seed layer is crucial for ECD, since a poor seed layer may lead to the formation of a void or seam, as shown in Fig. 1.5. Moreover, the seed layer is expected to be free of impurities for good adhesion with a substrate and efficient charge transfer during ECD. So far, physical vapor deposition (PVD) using ionized sputtering techniques in combination with high re-sputter ratio regimes, has been adopted as the desirable method for the barrier and Cu seed layer deposition [10]. However, with the ongoing scaling down of devices, PVD tends to fail due to its inherent nonconformal deposition characteristic. As projected by the ITRS [2], the metal 1 (M1) aspect ratio of MPUs is scheduled to reach 2 and the barrier thickness will be reduced to 1.3 nm by 2018. These requirements place several challenges on current film deposition techniques used in the device fabrication.

One promising alternative for making uniform and conformal Cu thin films is atomic layer deposition (ALD). ALD is a gas-phase thin film deposition technique based on sequential, self-terminating reactions between a surface and precursors [11, 12]. The self-limited growth nature of ALD allows thin film deposition with superior thickness control, step coverage, and reproducibility, even onto high aspect ratio structures. The precursor chemistry plays a key role in ALD. The candidate metal precursors must be volatile, thermally stable, and reactive. Moreover, a low-temperature process (ideally at $\leq 100\,°C$) is desirable for Cu ALD in order to avoid the agglomeration of Cu at elevated temperatures [13].

Recently, a number of Cu precursors have been studied for chemical vapor deposition (CVD) and ALD applications, such as beta-diketiminates [14, 15], beta-diketonates [16-20], amidinates [21, 22], aminoalkoxides [23], guanidinates [24, 25], and iminopyrrolidinates [26]. Among them, the Cu beta-diketonate family is promising because of its high stability and relatively low vapor pressures. The thermal Cu ALD process using Cu(acac)$_2$ (acac = acetylacetonate) and H$_2$ requires a deposition temperature of above $250\,°C$ and is thus undesirable [17]. The deposition temperature can be reduced below $100\,°C$ by utilizing the plasma enhanced ALD technology [27, 28]. However, this process leads to high roughness and reduced step coverage, which may not be applicable for high aspect ratio structures. On the other hand, an indirect ALD route to Cu films has been reported recently [19, 20]. This approach consists of two steps: 1) ALD of Cu$_2$O using (^{n}Bu$_3$P)$_2$Cu(acac) (Bu = butyl) and wet oxygen, and 2) reduction of Cu$_2$O into metallic Cu using formic acid as a reduction agent.

There have been a few studies regarding the surface chemistry of Cu(I) and Cu(II) beta-diketonates. In general, Cu(I) beta-diketonates are more reactive compared to Cu(II) beta-diketonates. However, the main limitation of Cu(I) beta-diketonates is that these precursors may easily undergo a disproportionation reaction, which defeats the self-limiting nature of ALD processes [19]. Previous *in situ* x-ray photoelectron spectroscopy (XPS) results suggest that the disproportionation of the (^{n}Bu$_3$P)$_2$Cu(acac) precursor, which produces metallic Cu and gaseous Cu(acac)$_2$, starts above $200\,°C$ on SiO$_2$ or above $125\,°C$ on Co [29, 30]. Hence, the upper-temperature limit for Cu ALD using this Cu(I) precursor lies below these temperatures. Another important issue regarding Cu beta-diketonates is the redox chemistry during ALD. In many cases, especially when metal ALD is desired, the metal center in a precursor is required to undergo a reduction step. It is generally assumed that such a step is accomplished during the second ALD half-cycle, which is associated with the introduction of a co-reactant [31]. However, recent studies [32] show that oxidation state changes in the metal can occur upon a precursor activated adsorption on the substrate, involving the partial loss and

transformations of ligands. Based on the XPS data, the initial loss of acac-ligands of Cu(acac)$_2$ precursor is found at 235 K on Cu(110) single-crystal surfaces [32]. The formation of metal–Cu(acac) complex is proposed. A noticeable oxidation state change of Cu has been seen between 250 K and 300 K. The adsorbed Cu(acac) species lose their remaining acac-ligands and Cu^{2+} is completely reduced to metallic Cu [32].

To develop and optimize an ALD process, it is important to elucidate the underlying microscopic details of film growth. Indeed, at the microscopic level, the surface chemistry involved in Cu ALD is quite complex and has not been well understood yet. For example, how does the Cu precursor adsorb and decompose on a substrate? How does the co-reactant react with adsorbed ligands to form volatile by-products? What is the rate-limiting step of Cu ALD? With the rapid improvement of computer power, *ab initio* calculations have become a powerful research tool for illuminating the chemical reactions at the atomic scale [33, 34]. However, due to the costs of treating the electronic degrees of freedom, *ab initio* calculations are restricted to model very small systems (a few hundred atoms) and short time scales (picoseconds). Therefore, the current work employs a multiscale approach to explore the surface chemistry of Cu ALD. Two related Cu (I) and (II) beta-diketonates, (^{n}Bu$_3$P)$_2$Cu(acac) and Cu(acac)$_2$, are used as Cu precursors. The input data for multiscale modeling is obtained by *ab initio* calculations, and thus the simulation methods at different scales are linked. The outline of this thesis is as follows:

The following Chapter 2 describes the fundamentals of the ALD technique and its important applications in microelectronics. ALD has been successfully applied in the FEOL for high-*k* dielectric fabrication, and it is a promising approach for the growth of ultrathin Cu seed layers at the 10 nm technology node and below. The commercial application of ALD in the BEOL is hindered by a lack of suitable precursors and a poor understanding of the ALD surface chemistry.

In Chapter 3, the simulation methodologies of ALD at different scales are introduced and discussed. Among them, *ab initio* calculations are widely used due to their high accuracy and parameter-free realization. However, there is a requirement for developing a multiscale simulation approach, since *ab initio* calculations are restricted to very short length and time scales. Reactive molecular dynamics (RMD) links the atomic-scale and the mesoscale, providing nearly the accuracy of *ab initio* calculations, but with much less computational costs. Because of the good transferability of reactive force fields, the application of RMD may be extended to the simulation of ALD. The equilibrium compositions of ALD surface

reactions can be predicted through thermodynamic modeling, which uses input data from *ab initio* calculations.

Chapter 4 presents the simulation results of Cu ALD from *ab initio* calculations and thermodynamic modeling. The stability of the $(^nBu_3P)_2Cu(acac)$ and $Cu(acac)_2$ precursors under different conditions is examined. In the gas-phase, $(^nBu_3P)_2Cu(acac)$ readily loses one of the $^nBu_3P$-ligands under typical ALD conditions, whereas the $Cu(acac)_2$ precursor is stable over wide temperature ranges. The metallic substrates Ta, Cu, and Ru, exhibit a high reactivity towards Cu precursors and easily lead to precursor decomposition upon charge transfer. The mechanisms of Cu oxide ALD on the Ta and Cu_2O substrates are discussed through thermodynamic modeling.

Chapter 5 is dedicated to the RMD simulations of ALD. The accuracy of ReaxFF potentials is assessed before simulations. The surface reactions between the Cu precursor and different co-reactants (H, H_2, O_3, H_2O and wet O_2), with respect to application for metallic Cu and Cu oxides ALD, are investigated systematically. The reactivity of these co-reactants towards $Cu(acac)_2$ follows the order H > O_3 > H_2O > H_2. Furthermore, the interplay between H_2O and O_2 in the ALD of Cu_2O has also been discussed.

Chapter 2 Fundamentals and applications of atomic layer deposition

Thin film deposition technologies are commonly used in microelectronics. The most relevant thin film technologies are summarized in Table 2.1. In general, these methods can be classified into the gas-phase deposition and liquid-phase deposition. The gas-phase deposition approaches are further classified into PVD and CVD. ALD is a variation of CVD based on the sequential and self-terminating reactions between a surface and precursors. As a consequence, when sufficient precursors are dosed, the growth rate in ALD is not flux-dependent, as is the case for other deposition techniques. Therefore, ALD is particularly suitable for the deposition of ultra-thin films, regardless of the substrate geometry.

2.1 Fundamentals of ALD

2.1.1 History of ALD

ALD has been invented independently twice; in the 1960s under the name "molecular layering" (ML) in the Soviet Union, and in the 1970s under the name "atomic layer epitaxy" (ALE) in Finland. Details of the ALD history have been summarized in recent essays [35, 36]. The principles of ML were first developed by Aleskovskii, Kolt'sov and colleagues at Leningrad Technological Institute [35]. These works were based on the theoretical "framework" hypothesis proposed by Aleskovskii in his doctoral dissertation in 1952. Research activities of ML at Leningrad Technological Institute covered a broad scope, from fundamental chemistry research to applied research with rubber fillers, selective sorbents,

Table 2.1 Overview of common thin film deposition methods used in microelectronics.

Gas-phase deposition		Liquid-phase deposition
Physical vapor deposition	Chemical deposition techniques	
Pulsed laser deposition	Chemical vapor deposition	Spin coating
Electron beam evaporation	Vapor phase epitaxy	Dip coating
Sputtering deposition	Atomic layer deposition	Electrochemical deposition
Ion plating		Chemical solution deposition
Molecular beam epitaxy		Electroless plating
		Sol-gel
		Spray deposition

heterogeneous catalysis, microelectronics and beyond [35]. The original pioneer of ALE was Suntola, who introduced the ALE technology for thin film electroluminescent display fabrication [37]. ALE as a method for compound thin films growth was granted United States patent in 1977 [37]. The first ALE works were aimed at the growth of ZnS by elemental Zn and S.

Since the mid-1980s, great efforts were made in ALE of III–V and II–VI compounds, but no real breakthrough was achieved, due to the complicated surface chemistry [38]. Since the mid-1990s, ALE has rapidly gained increasing interest, as a consequence of the shrinking device dimensions and increasing aspect ratios in integrated circuits [38]. Simultaneously, the main drawback of ALE, the low growth rate, became less important since the required film thicknesses often decreased to the order of nanometers. The transition from the term of "ALE" to "ALD" was due to the fact that thin films grown by sequential, self-limiting surface reactions are not always epitaxial to their underlying substrates [11]. Furthermore, amorphous films are most preferred for dielectric and diffusion barrier applications. Consequently, the use of "ALD" dominates among the practitioners in the field now.

2.1.2 Surface chemistry of Al_2O_3 ALD

The ALD process for the deposition of Al_2O_3 using trimethylaluminum (TMA) and water is usually treated as an ALD model system because the surface reactions are very efficient and self-limiting. As shown in Fig. 2.1, an ALD cycle consists of four steps:

(1) TMA precursors chemisorb on the Al_2O_3 surface and react with surface OH species to produce $CH_4(g)$ and $AlMe^*$ (Me = CH_3).

(2) A purge phase is employed to remove un-reacted precursor molecules as well as gaseous by-products.

(3) H_2O co-reactants are then supplied to clean up surface Me groups and to deposit reactive species OH^*.

(4) Another purging phase is introduced to evacuate excessive reactants and products.

By repeating these steps, the film growth is self-limiting, which leads to an excellent step coverage and a homogeneous deposition. Typical growth rates measured for Al_2O_3 ALD are 0.09–0.12 nm per cycle [39]. Based on the results of *in situ* Fourier transform infrared studies
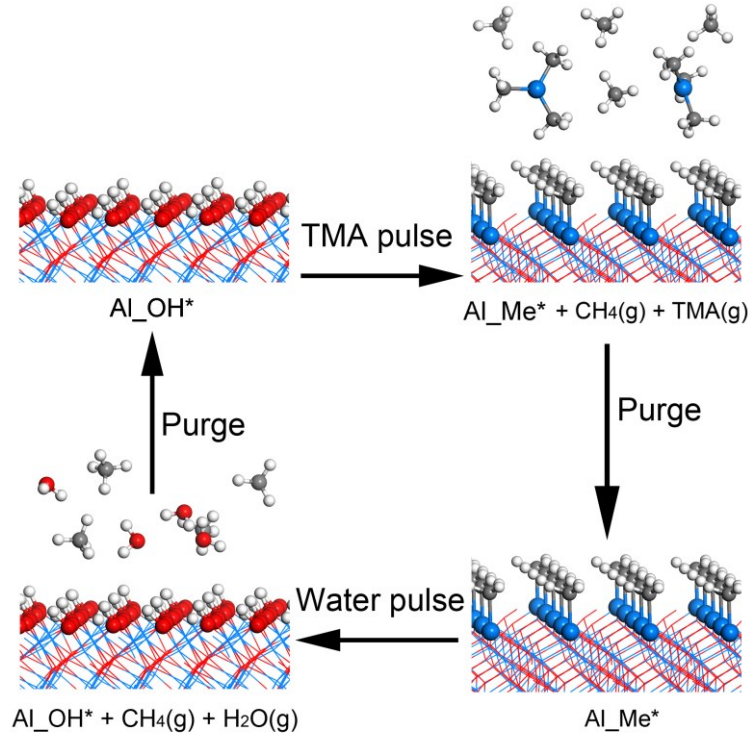
Fig. 2.1 Schematic illustration of the surface chemistry of Al$_2$O$_3$ ALD. (The red, white, grey, and blue spheres represent O, H, C, Al atoms, respectively)

and *ab initio* calculations [40, 41], the surface reactions of Al$_2$O$_3$ ALD can be described using a ligand-exchange mechanism

$$\text{TMA pulse:} \quad \text{AlMe}_3(g) + \text{Al\_OH}^* \rightarrow \text{Al\_O\_Al\_Me}_2^* + \text{CH}_4(g) \tag{2.1}$$

$$\text{Water pulse: Al\_Me}^* + \text{H}_2\text{O}(g) \rightarrow \text{Al\_OH}^* + \text{CH}_4(g) \tag{2.2}$$
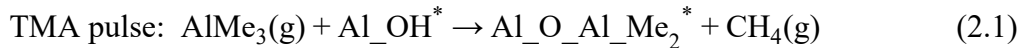
where the asterisks denote the adsorbed species on the surface. Both half-cycle reactions are found to proceed via the formation of Al–O Lewis acid-base adducts. The calculated reaction energies of Eqs. 2.1 and 2.2 using cluster models are −1.70 eV and −1.48 eV [40], respectively. This result indicates that Al$_2$O$_3$ ALD using TMA and water is a highly exothermic process.

2.1.3 Factors affecting the deposition rate of ALD

The distinctive features of ALD originate from self-terminating surface chemistry. The main factors identified for causing saturating adsorption are the steric hindrance of ligands and the limitation of surface reactive sites [12]. Steric hindrance is given when the adsorbed ligands shield the neighboring reactive sites, hindering the further adsorption of precursors. The surface then appears to be "full", although the reactive sites are not completely occupied.
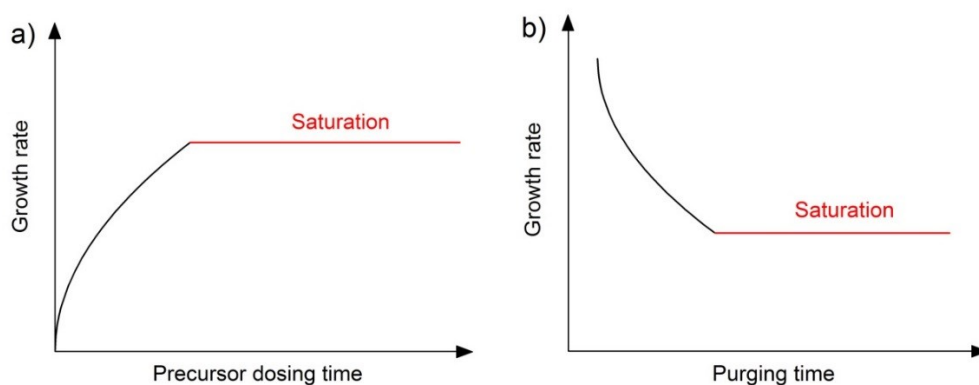
Fig. 2.2 Variation of the growth rate with the precursor dosing (a) and purging (b) time.
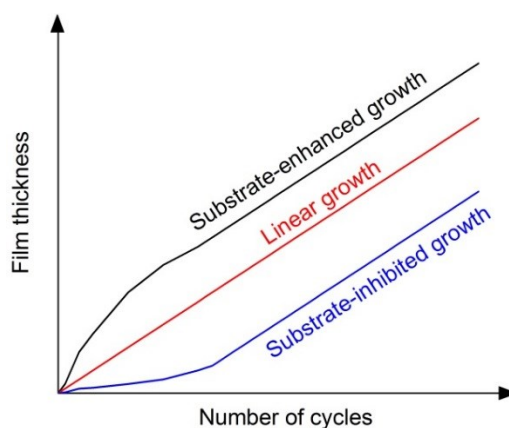
Fig. 2.3 Evolution of film thickness with the number of ALD cycles.

This case is more likely to occur when large metalorganic precursors are used. The number of reactive sites may also limit the ligand coverage since chemisorption cannot take place without an accessible reactive site. This case is only important when small-size precursors (e.g., $AlCl_3$) are used.

Fig. 2.2 shows the growth rate of ideal ALD versus precursor dosing and purging time. A sufficient length of precursor dosing is needed to achieve a constant growth rate in ALD (typically 5–10 s). Further increasing of the pulse length does not result in a higher growth rate since the surface reactions are self-terminating. On the other hand, an adequate purging time is needed to completely remove by-products and unreacted precursors, in order to prevent undesired gas-phase reactions within the next half-cycle.

The growth rate for ALD is typically described by growth per cycle (GPC), rather than by growth per unit time. In practice, GPC can be obtained by a linear fit to the evolution of thickness with the number of cycles. As depicted in Fig. 2.3, GPC is strongly dependent on substrate properties in the initial stage of ALD. Initial reactions of ALD occur on the original

substrate, while the following cycles proceed on the bilayer surface (i.e., original substrate precoated with ALD-grown films). Finally, surface reactions only appear on ALD-grown films, regardless of the original substrate used. If the structural and chemical properties of the original substrate are very close to those of ALD-grown films, the film thickness grows linearly with the number of deposition cycles. However, once the original substrate is notably different from the ALD-grown films, GPC varies with the number of deposition cycles [12]. In substrate-inhibited growth, the GPC in the initial stage of growth is lower than that in the steady regime. This case may be attributed to a poor nucleation on the substrate. In substrate-enhanced growth, GPC is higher in the initial growth steps than in the steady regime. This case may occur if the number of reactive sites on the original substrate is higher than that on the ALD-grown films.

The GPC in ALD generally varies with the temperature because both the number of reactive sites (e.g., OH^* groups) and the rate of surface reactions have a temperature-dependence. However, there exists a special temperature range, referred to as the "ALD window", in which GPC is independent of substrate temperatures (see Fig. 2.4). At lower deposition temperatures, there may be an increase in GPC due to the condensation of precursors, or a decrease due to the inadequate activation of surface reactions. At higher deposition temperatures, an increase in GPC can occur due to the decomposition of precursors (i.e., CVD behavior), whereas a decrease in GPC is due to the desorption of surface reactive species (e.g., OH^* groups). In most cases, the GPC in ALD is considerably less than a monolayer, as a result of the steric hindrance effect discussed above. For this reason, the term "**atomic layer** deposition" is somewhat misleading. For example, the GPC in the TMA/H_2O ALD process is 0.09–0.12 nm/cycle, which accounts for 30–40% of a monolayer [39].
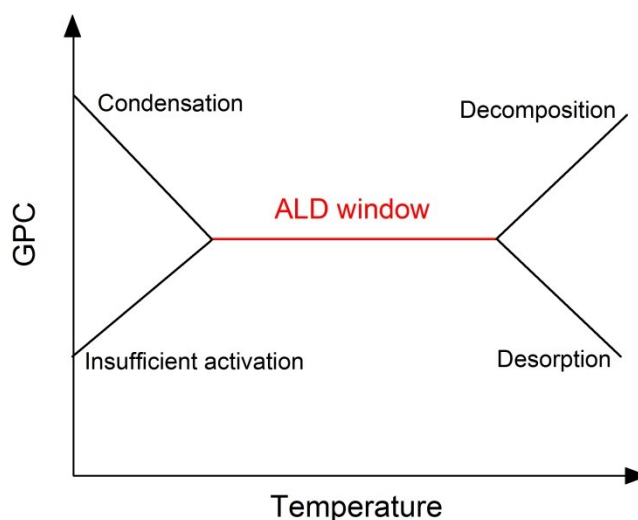
Fig. 2.4 Variation of GPC with the ALD processing temperature.

2.1.4 Plasma-enhanced ALD

Plasma-enhanced ALD (PEALD) is a modified ALD method where the reactivity of co-reactants is enhanced by the aid of plasma activation. There are no significant differences in process steps 1, 2 or 4 (see Section 2.1.2) between thermal ALD and PEALD, except that the plasma is activated in PEALD during the co-reactant exposure sequence (i.e., the 3rd step). As compared to conventional thermal ALD, PEALD offers several additional advantages in thin films fabrication. Using highly reactive radicals and ions generated by plasma, process temperatures can be significantly reduced. This is especially beneficial for Cu ALD, since Cu may agglomerate easily at elevated temperatures. Another merit of PEALD is its relatively high growth rate, because of a higher reactivity and enhanced initial nucleation [42]. However, to reach deep inside of highly structured surfaces, plasma species have to undergo several recombinations and collisions, which significantly reduce the local reactivity and the flux of plasma species [42]. As a consequence, PEALD may not be applicable for structures with high aspect ratios due to greater roughness and reduced step coverage. Furthermore, the plasma species may also directly react with the saturated reactive sites (e.g., OH*) to form stable molecules, destroying the self-limiting nature of ALD.

According to the location of plasma generation, PEALD devices can be divided into direct plasma, remote plasma, and radical enhanced systems, as shown in Fig. 2.5 [43]. In a direct plasma ALD system, plasma is generated inside the reactor chamber through the application of power between the showerhead and the substrate stage (Fig. 2.5a). In principle, this is a relatively simple approach that allows the reduced volume and complexity of a device. However, the deposited films may be damaged by high-energy plasma ions, which are generated very close to the substrate. In a remote plasma ALD reactor (Fig. 2.5b), plasma is activated in a remote location of the substrate stage, regardless of substrate conditions. Although the plasma radicals and ions are still in contact with the substrate, their impacting energies are well below the threshold value for causing damage [43]. Under particular conditions, the mild-energy species might even have a beneficial effect on ALD as they add energies to the surface reaction without heating the substrate. The contact between the substrate and plasma as well as the mild-energy ions distinguish remote plasma ALD from radical-enhanced ALD. In the latter (Fig. 2.5 c), plasma is generated at a location far away from the substrate, such that the electron and ion densities near the top of a substrate are decreased to zero.
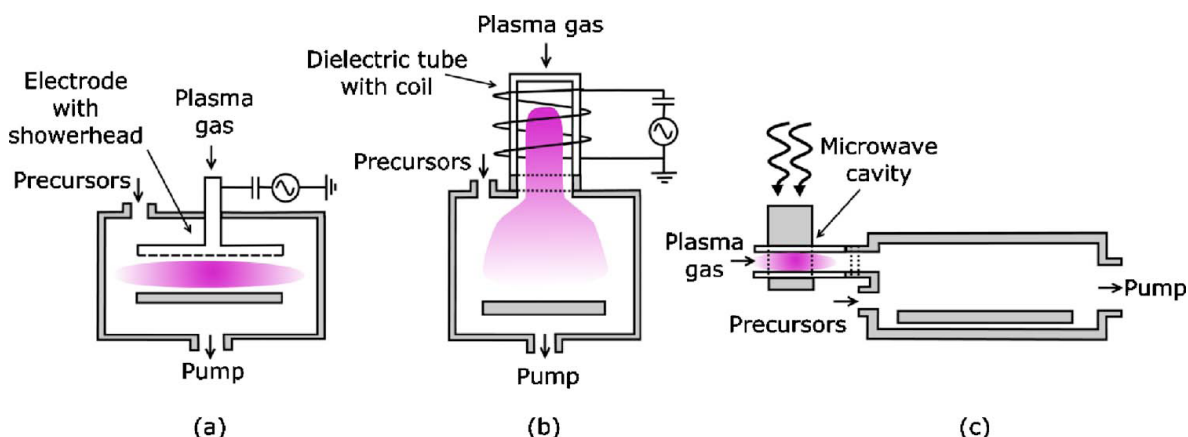
Fig. 2.5 Schematic drawings for (a) direct plasma, (b) remote plasma, and (c) radical-enhanced ALD systems. Reproduced from Ref. [43] with permission from AIP Publishing LLC, copyright 2007.

The PEALD of Al_2O_3 from TMA and O_2 plasma is used as a model system to compare the difference in reaction mechanisms between thermal ALD and PEALD. The first half-cycle (TMA pulse) reaction of PEALD is the same as that for the thermal ALD process (see Eq. 2.1). However, for the second half-cycle (O_2 plasma pulse) reaction, a combustion-like reaction with by-products of CO_2 and H_2O is observed in PEALD [44].

$$Al\_Me^* + 4O(g) \rightarrow Al\_OH^* + CO_2(g) + H_2O(g) \tag{2.3}$$
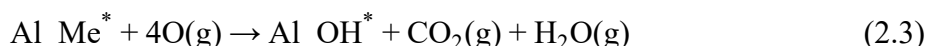
2.2 Applications of ALD

Currently, ALD is successfully applied in diverse fields, including microelectronics, nanofabrication, photovoltaics, catalysts, fuel cells, corrosion resistance, polymers, and so on [45–49]. This section mainly focuses on the discussion of its applications in the MOSFET fabrication, as shown in Fig. 2.6 [50]. In the FEOL, ALD has emerged as a key technique for the fabrication of high-k gate oxides and sidewall spacers. In the BEOL, ALD shows great potential for the deposition of metal nitride barriers, W nucleation layers, and Cu seed layers. Furthermore, ALD also plays an important role in the deposition of dielectrics for memory devices, such as dynamic random-access memory (DRAM), phase-change random access memory (PCRAM) and ferroelectric random access memory (FeRAM) [51].

2.2.1 ALD of high-k dielectrics

High-k dielectric materials are of great importance for application as capacitor dielectrics in DRAM and as gate oxides in MOSFET [51]. DRAM works as the main memory of every modern computer, because of its high density, high speed, and efficient memory function. Each DRAM cell consists of one transistor and one capacitor, which function as a switch and
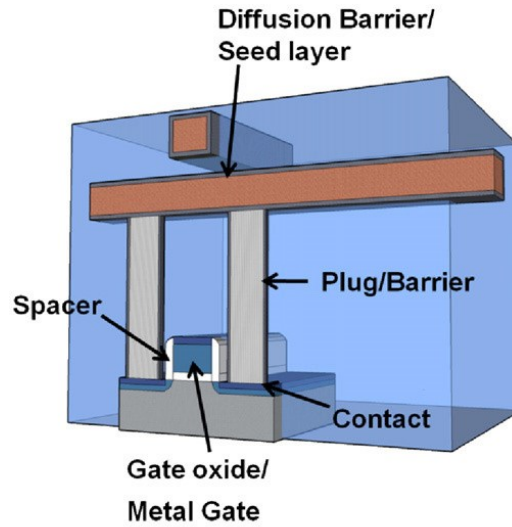
Fig. 2.6 Potential applications of ALD in the MOSFET fabrication. Reproduced from Ref. [50] with permission from Elsevier, copyright 2009.
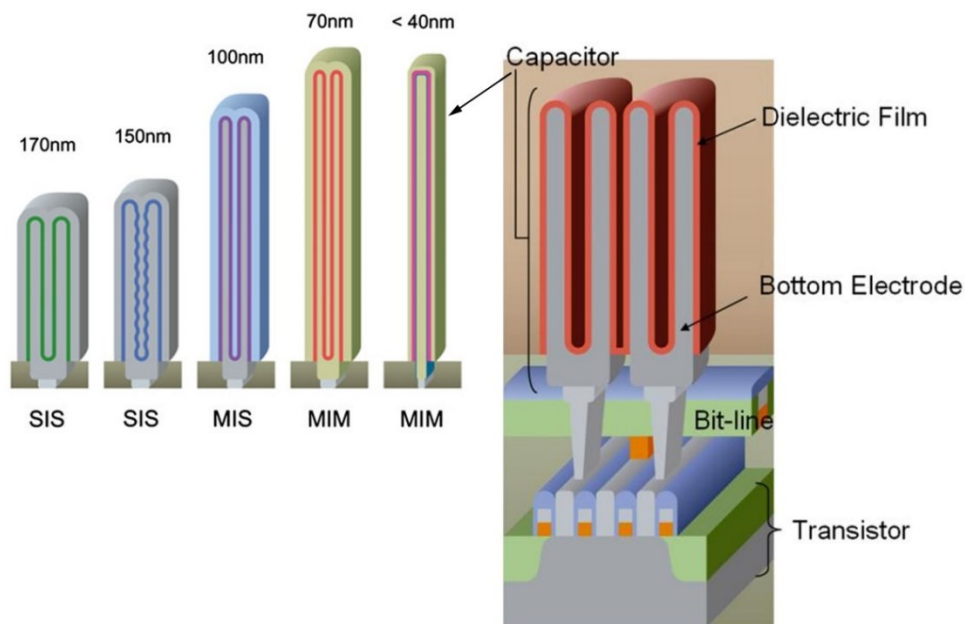
Fig. 2.7 Schematic diagram of DRAM cells with a MIM capacitor stack (SIS: semiconductor-insulator-semiconductor; MIS: metal-insulator-semiconductor). Reproduced from Ref. [53] with permission from John Wiley and Sons, copyright 2008.

storage cell, respectively (see Fig. 2.7) [52]. High-k dielectrics have been used in the production of metal–insulator–metal (MIM) capacitors for DRAM since the beginning of the last decade [52]. Currently, the dielectrics used in DRAMs are ZrO_2–Al_2O_3–ZrO_2 nano-laminates. Fig. 2.7 shows the evolution of the shape of DRAM capacitors according to the design rule shrinkage [53]. 3D stacked capacitor structures with a cylindrical shape have been developed, in order to maximize the active area of the device within a shrinking footprint.

26

ALD is the only method achieving the conformal growth of dielectric films on high aspect ratio electrodes. For future generation DRAMs, there is a need for extremely low equivalent oxide thickness (EOT) values (0.5 nm going down to 0.35 nm), while maintaining very low leakage currents ($\sim 10^{-8}$ A/cm^2 at 1 V) [51]. Potential long-term solutions are based on ultra-high-k dielectrics, such as perovskites [51].

In the MOSFET fabrication, SiO$_2$ traditionally served as the transistor gate insulator of choice, because of a feasible fabrication process and outstanding SiO$_2$/Si interface properties. However, continuous scaling down of the devices prompted the development of alternative gate dielectric materials and processes. In 2007, Intel announced the first mass production 45 nm MOSFETs containing an ALD Hf-based gate oxide together with a metal gate [54]. High-k/metal gate stacks substantially reduce the gate leakage currents, since physically thicker HfO$_2$ films can be used for the required EOT [54]. The suppression of gate leakage is crucial for realizing the continuous scaling down and improvement of the packing density of future MOSFET generations. In 2012, fully-depleted tri-gate MOSFETs were introduced at the 22 nm technology node [55]. As compared to a planar transistor, the tri-gate transistor largely reduces the short-channel effects, achieving an improved device performance and a low leakage current. Fig. 2.8 depicts the structures of planar and tri-gate transistors [56]. As shown in Fig. 2.8 b, the gate electrode of the tri-gate transistor wraps around three sides of a protruded fin, providing "fully depleted" operation. Tri-gate transistors can also have multiple fins, which are connected together to increase the total electrostatic control strength for higher performance. Thanks to the excellent conformality on 3D surface topologies and atomic-level controllability, ALD has become the predominant solution for fabricating ultrathin high-k gate oxides.

Fig. 2.9 shows the trend of band gaps as a function of the dielectric constant (k) observed for high-k dielectrics in general [57]. ALD Al$_2$O$_3$ thin films have been extensively studied as a gate dielectric in logic chips and as a capacitor dielectric in memory devices. Although Al$_2$O$_3$ has a relatively small dielectric constant (<10), it possesses a wide band-gap (8.8 eV), which is helpful to reduce tunneling leakage current. The available Al precursors include AlCl$_3$, Al(mmp)$_3$ (mmp = 1-methoxy-2-methyl-2-propoxide), Al(OEt)$_3$ (Et = ethyl), Al(OiPr)$_3$ (iPr = isopropyl), and TMA. Among them, TMA is most promising due to its high reactivity and self-limiting property, which provide highly uniform Al$_2$O$_3$ films on large wafers and a good step coverage over high-aspect-ratio structures. The details of the TMA/H$_2$O process have been discussed in Section 2.1.2.
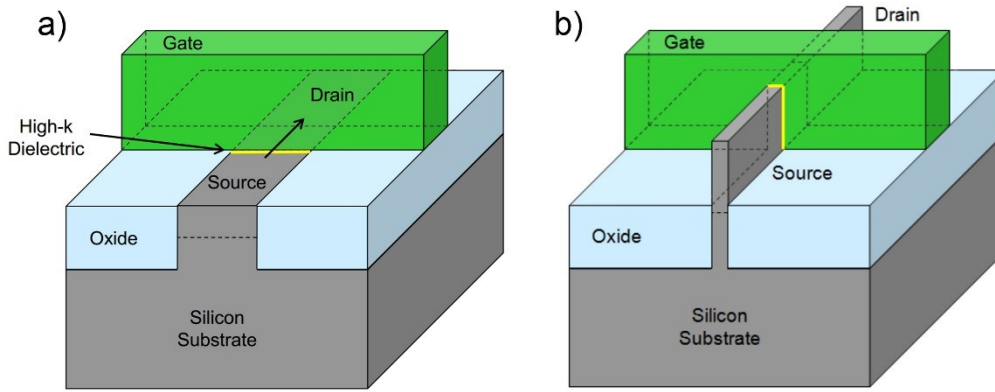
Fig. 2.8 Schematic view of planar (a) and tri-gate (b) transistors. Reproduced from Ref. [56] with permission from IEEE, copyright 2011.
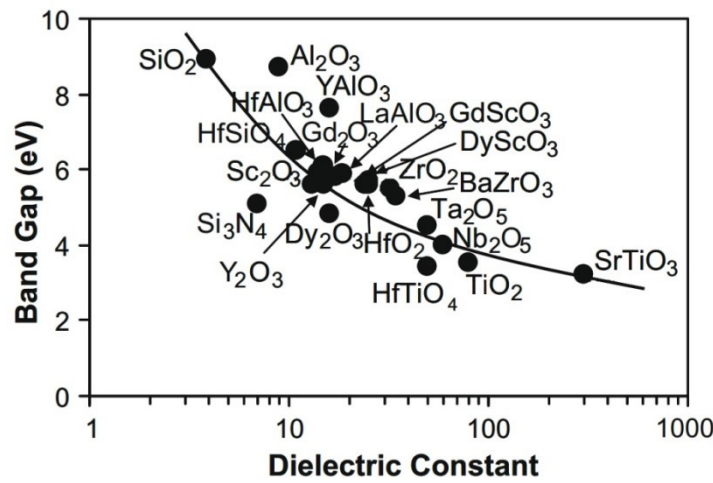
Fig. 2.9 Dielectric constant vs. band gap for several high-*k* dielectrics. Reproduced from Ref. [57] with permission from Elsevier, copyright 2009.

HfO_2 has replaced SiO_2 as the gate dielectric for high-performance MOSFETs, because of its high dielectric constant ($k = 16$–45), wide bandgap (5.5–5.8 eV), and sufficient thermal stability against the Si substrate. One of the most simple and thermally stable Hf precursors is $HfCl_4$ [58]. However, there are some drawbacks of the $HfCl_4$ based ALD process, for example, low reactivity on Si surfaces, low vapor pressure, and the presence of Cl impurities. Besides, the by-product HCl may cause undesired film etching and corrosion of reactor walls. Therefore, Hf metal–organic precursors, such as TEMAH [59] and TDMAH [60], have been introduced to obtain preferable growth behavior and film properties. The reactivity of these precursors is much higher than that of $HfCl_4$, due to a weaker Hf–N bond strength as compared to the Hf–Cl bond. As a consequence, ALD using Hf metal–organic precursors achieves higher growth rates, lower process temperatures, and less substrate-dependent growth. However, it is inevitable that C impurities are incorporated into HfO_2 films, deteriorating interface and bulk properties [61].

28

2.2.2 ALD of contacts and barriers

Metal contacts play an indispensable role in logic device performance, because of that a high contact resistance between source and drain and metal plugs would induce problems of high power consumption and long RC delay. Metal silicides, such as NiSi and CoSi$_2$, have been applied as contact materials because of their low resistivity, stability as well as good compatibility with Si [62]. The metal silicides can be fabricated by depositing metallic thin films on Si followed by annealing, or by directly depositing metal silicides without annealing [62]. So far, PVD is the generally employed approach for metal film deposition. However, with the continuous shrinkage of contact feature sizes, ALD is a good alternative to conventional PVD because of its excellent conformality and step-coverage. Recent progress in the ALD of first-row transition metals has been summarized in a review by Winter et al [63]. With the exception of Cu ALD, successful processes for the remaining metals (Ni to Ti) have not been established, mainly due to lack of suitably reactive and stable precursors [63]. The investigated Ni and Co precursors include M(C$_5$H$_5$)$_2$, M(iPrNCMeNiPr)$_2$, M(dmap)$_2$ (dmap = dimethylamino-2-propoxide), M(C$_5$H$_5$)(iPrNCMeNiPr), M(OCMe$_2$CH$_2$NMe$_2$)$_2$ (M = Ni or Co) and so on [63]. However, most of them are insufficiently reactive for common co-reactants (such as H$_2$). As a consequence, PEALD technology must be used, which may deteriorate the metal film properties and the step coverage of the deposition.

As scheduled by the ITRS roadmap [2], tungsten will continue to be used for local wiring and the contact level of the devices within MPUs, ASICs, Flash, and DRAM. The advantages of tungsten include high thermal stability, relatively low resistivity, low self-diffusivity and minimal electromigration. Typically, the W contacts are deposited by CVD using the WF$_6$ precursor, with H$_2$ as a reducing agent. In this process, barrier layers are required to hinder the undesired interactions between WF$_6$ and Si on dielectrics [64]. Because WF$_6$ easily reacts with Si to form gaseous SiF4, resulting in the formation of voids in contacts. In addition, this process also needs conformal and ultrathin nucleation layers, which are currently prepared through the reduction of WF$_6$ by SiH$_4$ [62]. With continued development, ALD can be used for fabricating the W nucleation layers on ultrahigh aspect ratio structures.

Metal nitrides, such as TaN and TiN, are widely used as barriers for Cu interconnect metallization as well as for W contact plugs, because of their high thermal stability and chemical inertness. The barrier materials for Cu interconnect are required to prevent Cu diffusion into the adjacent high-*k* dielectrics [65]. Besides, a liner material like Ta or Co is

applied to form a high-quality interface and to enhance the adhesion of Cu [65]. At present, Ta/TaN barriers fabricated by ionized PVD have been successfully implemented in mass production. However, the PVD barriers tend to narrow the upper part of the trench. This would lead to the reduced filling capability in the subsequent Cu ECD process. Therefore, ALD is expected to be the future predominant solution for the conformal growth of the ultrathin barriers. Furthermore, reduction of the barrier thickness is also beneficial for obtaining low resistive metal wiring [66]. The commonly used Ti and Ta precursors include $TiCl_4/TaCl_4$, $Ti(NMe_2)_4/Ta(NMe_2)_5$, $Ti(NEt_2)_4/Ta(NEt_2)_5$, $Ti(NEtMe)_4$, and so on [62]. A potential drawback for ALD barriers involves the penetration of precursors into the porous low-k dielectrics [2]. Further modification of the etched low-k sidewalls may be required to resolve this problem.

2.2.3 ALD of Cu seed layers

The ALD of Cu has recently attracted considerable attention due to its potential application as seed layers in interconnect metallization. Deposited Cu thin films need to meet the requirements of conformality and thickness uniformity, which are crucial for achieving a void-free filling by ECD. In addition, a low-temperature process (ideally at $\leq 100\,°C$) is desirable for Cu ALD in order to avoid the agglomeration of Cu at elevated temperatures [13]. The content of impurities (e.g., F, C, O) should be as low as possible, ensuring good adhesion and conductivity of the Cu films. Regarding the Cu precursor, it needs to be thermally stable below the temperature of ~200 °C and highly volatile above ~80 °C to allow a wide ALD temperature window. So far, none of the existing Cu ALD processes completely fulfills these requirements [63].

Table 2.2 Electrochemical potentials of different metal cations [67].

Metal cation	Potentials (V)
Al^{3+}	−1.66
Au^+	1.69
Au^{3+}	1.5
Co^{2+}	−0.28
Cr^{2+}	−0.91
Cu^+	**0.52**
Cu^{2+}	**0.34**
Fe^{2+}	−0.45
Fe^{3+}	−0.04
Mn^{2+}	−1.19
Ni^{2+}	−0.26
Pt^{2+}	1.18
Ti^{2+}	−1.63

The difficulty in reducing transition metal cations can be described by the electrochemical potentials listed in Table 2.2 [67]. As shown in Table 2.2, Cu^+ and Cu^{2+} can be easily reduced compared to many other non-noble metals, due to their positive standard reduction potentials. On the other hand, it is also difficult to obtain stable Cu precursors that only undergo self-limiting reaction in ALD conditions. The molecular structures of different Cu precursors discussed in this work are illustrated in Fig. 2.10.

According to the type of co-reactant used, the existing processes of Cu ALD can be divided into thermal ALD of Cu, indirect ALD of Cu, and PEALD of Cu, as shown in Tables 2.3–2.5. Both the thermal ALD of Cu and PEALD of Cu use reducing agents such as molecular H_2 or H_2 plasma as a co-reactant. The indirect approach of Cu ALD consists of two steps: 1) ALD of Cu oxide or Cu nitride using an oxidizing agent, and 2) reduction into metallic Cu using a reducing agent. The latter step (i.e., reduction) may also be integrated into the binary Cu oxide or Cu nitride ALD process.

Thermal ALD of Cu films

The initial works on thermal ALD of Cu focused on the CuCl precursor, with H_2 or Zn as the co-reactant [68]. However, very high process temperatures (360–410 °C) must be used, which leads to coarse-grained films or isolated Cu clusters. As a consequence, Cu metal organic precursors were introduced in subsequent researches because of their high volatility and reactivity. Martensson et al. [16] first reported the ALD of Cu using Cu(II) beta-diketonate [Cu(thd)$_2$] (thd = tetramethylheptanedionate) as precursor and H_2 as co-reactant. The process is self-limiting at temperatures between 190 °C and 260 °C. The overall chemical reaction proposed is shown below:

$$Cu(thd)_2(g) + H_2(g) \longrightarrow Cu^* + 2H(thd)(g) \tag{2.4}$$
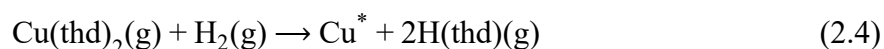
Similar metal (II) beta-diketonate precursors M(acac)$_2$ (M = Cu, Ni, Pt) were also employed along with H_2 as co-reactant for Cu, Ni, and Pt ALD at 250 °C [17]. It should be noticed that these processes occur at temperatures higher than 200 °C, which are infeasible to provide Cu films with low surface roughness. Furthermore, both Cu(thd)$_2$ and Cu(acac)$_2$ have high melting points of 198 °C and 284 °C, respectively [16, 17]. This makes the control of the sublimation rate inconvenient and non-reproducible since it strongly depends on the particle size, which changes during the sublimation process.
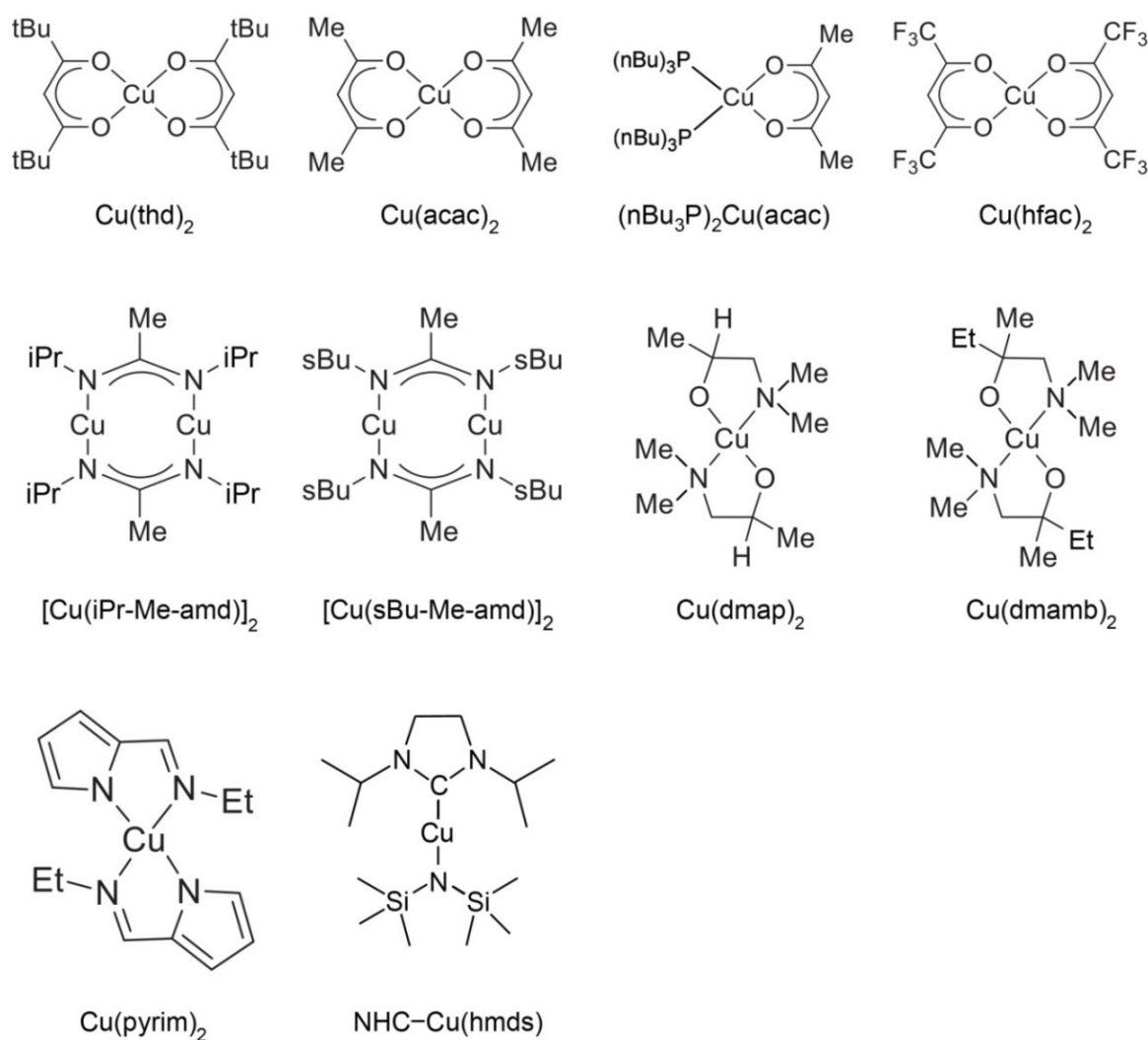
Fig. 2.10 Molecular structures of Cu precursors presented in Tables 2.3–2.5.

Table 2.3 Summary of the thermal Cu ALD processes.

Cu precursor	Reducing agent	Substrate T (°C)	Substrate	Year
CuCl	H$_2$/Zn	360–410	Ta	1997 [68]
Cu(thd)$_2$	H$_2$	190–260	Pt/Pd mixture	1998 [16]
Cu(acac)$_2$	H$_2$	250	Si, Ti, Al	2000 [17]
Cu(hfac)$_2$	CH$_2$O	300	Ta, TaN, TiN	2000 [69]
[Cu(iPr-Me-amd)]$_2$	H$_2$	280	SiO$_2$	2003 [21]
[Cu(sBu-Me-amd)]$_2$	H$_2$	150–190	SiO$_2$, Si$_3$N$_4$, Ru, Co	2006 [70]
Cu(dmap)$_2$	Et$_2$Zn	100–120	Si	2009 [15]
Cu(pyrim)$_2$	Et$_2$Zn	130–150	SiO$_2$, Ta, Ru	2010 [71]
Cu(hfac)$_2$	H$_2$	27–100	TiN	2010 [72]
NHC–Cu(hmds)	H$_2$	190–250	Pd	2014 [73]
(^{n}Bu$_3$P)$_2$Cu(acac)	H$_2$	125	Co	2016 [74]

Table 2.4 Summary of the indirect Cu ALD processes.

Cu precursor	Oxidizing agent	Reducing agent	Substrate T (°C)	Substrate	Year
[Cu(sBu-Me-amd)]$_2$	NH$_3$	H$_2$	160	Ru	2006 [75]
Cu(dmap)$_2$	Formic acid	N$_2$H$_4$	120	Si	2011 [13]
(^{n}Bu$_3$P)$_2$Cu(acac)	O$_2$/H$_2$O	Formic acid	100–130	Ru	2011 [20]
Cu(dmamb)$_2$	NH$_3$	H$_2$	120–140	Ru, SiO$_2$	2014 [76]
Cu(dmap)$_2$	Formic acid	BH$_3$(NHMe$_2$)	130–160	Pd, Pt	2015 [77]

Table 2.5 Summary of the Cu PEALD processes.

Cu precursor	Plasma type	Substrate T (°C)	Substrate	Year
Cu(thd)$_2$	Direct plasma	90–250	SiO$_2$, TaN, Au	2005 [78]
Cu(acac)$_2$	Direct plasma	85–135	TaN, Ru, SiO$_2$	2007 [28]
Cu(dmamb)$_2$	Unknown	100–180	Ta/SiO$_2$	2011 [79]
NHC–Cu(hmds)	Remote	225	Si	2013 [80]
[Cu(iPr-Me-amd)]$_2$	Remote	50–100	Si, SiO$_2$	2015 [81]

In 2005, a series of Cu(I) amidinate precursors were synthesized and applied for Cu ALD with H$_2$ as co-reactant [22]. These Cu compounds have very promising properties, which are well-suited for the thermal ALD of Cu [22]. Firstly, many of these amidinate complexes have low melting points (around 60–80 °C), providing very reproducible sources of vapor for ALD. Secondly, low deposition temperatures (around 180 °C) can be used due to a high reactivity of the Cu precursors, providing smooth film morphology by reducing the agglomeration. Thirdly, the amidinate precursors are fluorine-free, avoiding a major source of contamination that may cause adhesion problems. The Cu(I) amidinate precursors can also be used in indirect Cu ALD and Cu PEALD processes [75, 81].

Typically, molecular H$_2$ is used as the co-reactant for Cu ALD. However, H$_2$ is insufficiently reactive at low temperatures due to a large dissociation energy of the H–H bond (~4.5 eV). Transition metals such as Pd, Co, Ru, and Pt, can efficiently catalyze the dissociation of molecular H$_2$ into H adatoms, which enhances the reactivity of H$_2$ at low temperatures. However, it should be noticed that these metals (with a few exceptions like Ru and Co) are less useful for microelectronics applications. Hagen et al. [73] studied the ALD of Cu using an oxygen-free precursor (NHC)–Cu(hmds) (NHC = N-heterocyclic carbene, hmds = hexamethyldisilazide) with molecular H$_2$ on reactive substrates. The reactions are proposed to proceed as follows:

$$(NHC)-Cu(hmds)(g) \longrightarrow Cu(hmds)^* + NHC(g) \qquad (2.5)$$

$$H_2(g) \longrightarrow 2H^* \qquad (2.6)$$

$$Cu(hmds)^* + H^* \longrightarrow Cu^* + H(hmds)(g) \qquad (2.7)$$
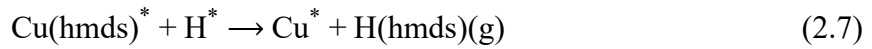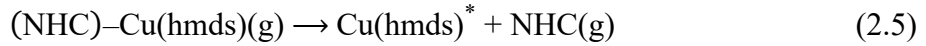
A significant substrate dependence of the growth process and the structure of the films has been reported [73]. On the Pd substrate, continuous Cu films could be obtained. An ALD window was observed between 190 °C and 250 °C [73]. However, when the growth was carried out on the Ru substrate an island growth mode has been observed [73]. Dhakal et al. [74] used the Co substrate to realize the thermal ALD of metallic Cu from (^{n}Bu$_3$P)$_2$Cu(acac) and H$_2$. (^{n}Bu$_3$P)$_2$Cu(acac) is a liquid and non-fluorinated precursor developed in Prof. Lang's group at Technische Universität Chemnitz [82]. The deposition process is substrate-enhanced with an initial GPC of 0.025 Å/cycle and a GPC of 0.008 Å/cycle after the initial nucleation [74]. No Cu film growth was obtained on the oxidized Co surface, indicating the catalytic role of Co metal towards molecular H$_2$ [74]. This approach is effective in obtaining ultrathin Cu films on Co substrates with a thickness below 1.5 nm, which is particularly suitable for Co/Cu multilayers in giant magnetoresistance and interconnect systems [74].

Another approach to realize a low-temperature Cu ALD is by introducing strong reducing agents, as demonstrated by Lee et al. [15]. High purity, low resistivity ALD Cu films were obtained by the self-limiting surface reactions between Cu(dmap)$_2$ and diethylzinc (ZnEt$_2$) at temperatures of 100–120 °C. The electrical resistivity of the 50 nm thick Cu thin films is about 2.78 µΩcm [15]. The reaction mechanisms of this ALD process can be described following [15]. First, a monolayer of Cu(dmap)$_2$ is adsorbed on a surface through dipole–dipole interactions between the precursor and the substrate. Next, the dosing of ZnEt$_2$ co-reactant removes the surface dmap-ligands by a ligand-exchange reaction (Eq. 2.8). The by-products Zn(dmap)$_2$ and C$_4$H$_{10}$ are desorbed from the substrate without surface decomposition. Finally, the formed metallic Cu provides active adsorption sites for the next monolayer of Cu(dmap)$_2$.

$$Cu(dmap)_2^* + Et_2Zn(g) \longrightarrow Cu^* + Zn(dmap)_2(g) + C_4H_{10}(g) \qquad (2.8)$$

ZnEt$_2$ was also used with the Cu(pyrim)$_2$ (pyrim = pyrimidine) precursor in a similar manner at deposition temperatures of 120–150 °C [71]. Smooth and conductive Cu films were deposited on SiO$_2$ as well as Ta substrates. However, there was a significant incorporation of impurities, with 8–15% Zn and a few oxygen contaminants in the Cu films [71].

Indirect ALD of Cu films

Compared to direct metal ALD, metal oxides and nitrides are typically more accessible by ALD. Waechtler el al. [20] reported the ALD of Ru-doped Cu_2O films using a Cu beta-diketonate precursor ($^nBu_3P)_2Cu(acac)$ with 1 mol% of $Ru(\eta^5-C_7H_{11})(\eta^5-C_5H_4SiMe_3)$ catalyst. A mixture of water vapor and oxygen (wet oxygen) was used as co-reactant, instead of using a strong oxidizing agent like O_3, to avoid the extensive oxidation of substrate materials [20]. An ALD window between 100 °C and 130 °C was identified, depending on the substrate used [20]. On TaN and SiO_2 substrates, smooth Cu_2O films and self-saturating film growth were obtained. On the Ru substrate, considerable intermixing of the as-deposited Cu_2O films with underlying Ru has been observed. The Ta substrate leads to the deposition of isolated clusters together with continuous films, as a result of the fast self-decomposition of the Cu precursor. The ALD-deposited Cu_2O can be reduced to metallic Cu using formic acid assisted by the Ru catalyst at low temperatures (110–120 °C) [20]. The presence of small amounts of Ru can catalyze the decomposition of formic acid into atomic H and CO [20] (Eqs. 2.9 and 2.10). Reduction of Cu_2O by atomic H and CO is favorable at room temperatures and above 180 °C, respectively (Eqs. 2.11 and 2.12).

$$HCOOH(g) \rightarrow CO_2(g) + 2H^* \tag{2.9}$$

$$HCOOH(g) \rightarrow CO^* + H_2O(g) \tag{2.10}$$

$$Cu_2O + 2H^* \rightarrow 2Cu + H_2O(g) \tag{2.11}$$

$$Cu_2O + CO^* \rightarrow 2Cu + CO_2(g) \tag{2.12}$$

Li et al. [75] demonstrated the ALD of Cu_3N from $[Cu(sBu-Me-amd)]_2$ and NH_3 at 160 °C, followed by the reduction of Cu_3N to Cu by H_2 at the same temperature. The resulting 3 nm thick Cu on 2 nm Ru films have a sheet resistance of less than 50$\Omega/\square$, a value low enough to serve as seed layers for the subsequent ECD process [75]. The Cu films are electrically continuous even as thin as 0.8 nm, as predicted by a grain-boundary-scattering model [75]. A similar process was also reported by Park et al. [76] using $Cu(dmamb)_2$ (dmamb = 1-dimethylamino-2-methyl-2-butanolate) as the Cu precursor. Indirect approaches via the reduction of ALD Cu_3N may avoid the oxidation of barrier metal below the Cu seed layer.

Knisley et al. [13] proposed a three-step Cu ALD process using $Cu(dmap)_2$, formic acid, and N_2H_4. The Cu formate intermediate, from reactions between $Cu(dmap)_2$ and formic acid, can be readily reduced to metallic Cu by N_2H_4 [13]. However, the $Cu(dmap)_2$ precursor is nonreactive towards N_2H_4 in a binary ALD process. The deposited Cu films are of high purity

and have low resistivities ranging from 9.6 μΩcm to 16.4 μΩcm [13]. A similar three-step Cu ALD process was recently reported by Kalutarage et al. [77] in the same group, but $BH_3(NHMe_2)$ was used as a reducing agent.

Plasma-enhanced ALD of Cu films

The main challenge in thermal Cu ALD is the low reactivity of co-reactants towards the Cu precursor at low temperatures. While the reactivity of co-reactants can be enhanced by introducing catalytic substrates, most of these materials are currently not applicable in microelectronics. Furthermore, thermal ALD is prone to impurities, which is caused by incomplete surface reactions between the Cu precursor and co-reactants. One common strategy for implementing low-temperature ALD is using the hydrogen plasma as a co-reactant. As listed in Table 2.5, the substrate temperatures of Cu PEALD processes can be reduced to below 100 °C, which is clearly infeasible for current thermal ALD technologies. Moreover, high-purity and low-resistivity Cu films can be obtained using PEALD, regardless of the substrate used. As mentioned in Section 2.1.3, one potential limitation of PEALD is its poor step coverage, which may be problematic for high aspect ratio structures.

Jezewski et al. [78] reported the PEALD of Cu using the $Cu(thd)_2$ precursor. The nonselective and self-limiting deposition was achieved on SiO_2, Au, and TaN_x substrates in a temperature range between 90 °C and 250 °C [78]. In contrast, thermal ALD via $Cu(thd)_2$ and H_2 is selective on noble metal substrates (i.e. Pd and Pt) [16]. No films were grown on hydroxyl- or oxygen- terminated substrates since the H_2 co-reactant cannot be activated on these substrates during thermal ALD [16]. Wu et al. [28] demonstrated the PEALD of Cu thin films from the $Cu(acac)_2$ precursor. Self-limiting growth of the continuous and high-purity ($\geq$ 95%) Cu films was achieved on TaN, Ru, and SiO_2 substrates between 85 °C and 135 °C [28]. The proposed reaction mechanisms are as follows

$$Cu(acac)_2(g) \longrightarrow Cu^* + 2acac^* \qquad (2.13)$$

$$acac^* + H(g) \longrightarrow H(acac)(g) \qquad (2.14)$$
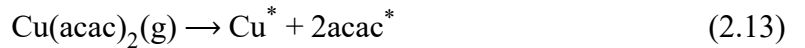
First, the $Cu(acac)_2$ precursor dissociates into Cu and acac-ligands on the surface, which block the surface sites until one monolayer of precursors is formed. During the hydrogen plasma pulse, atomic H reacts with the adsorbed acac-ligands, forming gaseous H(acac) by-product and leaving metallic Cu on the surface. The metallic Cu will then act as a new reactive site for the adsorption of additional Cu precursor, thus enabling the film growth of the PEALD process.

Recently, Guo et al. [81] developed a low-temperature PEALD process by employing the [Cu(iPr-Me-amd)]$_2$ precursor with hydrogen plasma. An ideal self-limiting ALD process with a GPC of 0.071 nm/cycle below 100°C was observed [81]. Benefitting from a low substrate temperature, the agglomeration of Cu films was largely suppressed. The Cu films deposited were pure, continuous, and highly conformal even on a high aspect ratio substrate [81].

Chapter 3 Theoretical background

3.1 Introduction

An understanding of chemical reaction mechanisms is important for the development and the optimization of ALD processes that are useful in industry applications. Recent advances in *in situ* characterization techniques, such as *in situ* XPS [29], quartz crystal microbalance [83], quadrupole mass spectroscopy [83], and ellipsometry [84], allow the observation of the evolution of chemical and physical properties during the film growth. Atomistic simulations might serve as an important complement to the *in situ* characterizations, providing additional information to aid in the interpretation of the ALD surface chemistry. For example, the adsorption structure and the binding energy of precursors on the substrate are rarely measured experimentally. Furthermore, intermediate or transition state species are very difficult to be detected, since they have a very short lifetime (e.g., a few picoseconds). Alternatively, the atomistic simulations through transition state search (TSS) or MD simulations provide a possibility to directly predict and observe such structures.

Table 3.1 Overview of theoretical studies of Cu ALD via atomic-scale simulation

Cu precursor	Co-reactant	Dynamics	Functional/code	Substrate model	Year/Ref.
CuCl	H_2	TSS	LDA/CASTEP	Periodic Cu(111)	1998-2000 [85,86,87]
Cu(hfac)(tmvs)	/	AIMD	LDA/SIESTA	Periodic TaN(001)	2005 [88]
Cu(II) beta-diketonates	/	/	B3LYP/Gaussian	/	2009 [89]
Cu(Bu-amd)	/	/	B3LYP/Gaussian	/	2010 [90]
Cu(Bu-amd)	Surface H	/	PBE/Dmol3	SiO_2(001) cluster	2010 [91]
Cu(acac)$_2$	Surface H	TSS	B3LYP/Gaussian	Si(100) cluster	2013 [92]
Cu(dmap)$_2$, Cu(acac)$_2$, Cu(PyrIm)$_2$	$ZnEt_2$/N_2H_4	/	PBE/TURBOMOLE	Cu(111) cluster	2012-2015 [93,94,95]
Cu(dmap)$_2$	/	/	PBE/VASP	Periodic Cu(111)	2015 [96]

One common strategy for treating simulations at the atomic-scale is the use of *ab initio* calculations, in particular, based on density functional theory (DFT) with a good balance between accuracy and cost. These methods accurately predict chemical and physical properties, without any empirical assumptions or adjustable parameters. Recently, DFT calculations have been widely used to elucidate the details of precursor adsorption, surface reactions, and by-products formation. Comprehensive reviews of the atomistic simulations of ALD can be found in Refs. [33, 34].

The references on the atomic-scale simulations of Cu ALD (all based on DFT) that are available to date are summarized in Table 3.1. Some works were focused on the stabilities of Cu precursors in the gas-phase or on the substrate. Thus, substrates or co-reactants were not considered. The first reported study is by Mårtensson et al. [85], who used DFT with periodic models to compute reaction energetics and activation energies involved in the CuCl/H_2 ALD process. The most probable surface reactions are either between adsorbed CuCl and adsorbed hydrogen, or between adsorbed CuCl and gaseous H_2 through the bridge formation pathways. Orimoto et al. [89] performed DFT calculations to estimate the stabilities of a series of Cu(II) beta-diketonate complexes. DFT was shown to be an efficient method for the computational screening of stable precursors. However, the Cu (I) beta-diketonates were not investigated in that work. Dey et al. [93] investigated the gas-phase mechanisms of Cu ALD by transmetalation from different Cu metalorganic precursors and $ZnEt_2$. This study was mainly based on thermodynamic considerations, which exclude unfavorable intermediates and products from highly endothermic steps. It was found that the accumulation of ZnEt-ligands would lead to zinc contamination by the formation of either Zn_2L_2 (L = ligand) or metallic zinc [93]. The ligand-exchange between Cu(II) and Zn(II) should proceed via a Cu(I) intermediate, otherwise the formation of a stable copper molecule is preferred rather than metallic copper [93]. Lin et al. [92] investigated the ligand-exchange and the dissociation of Cu(acac)$_2$ on the Si(100) surface. It was found that the undesired ligand-mediated adsorption on reactive sites competes with the desired ligand-exchange reaction both thermodynamically and kinetically. Most recent, Maimaiti et al. [96] calculated the adsorption energies of the Cu(dmap)$_2$ precursor on Cu surfaces using several van der Waals (vdW) functionals along with the pure PBE functional. vdW interactions were shown to play an important role in the adsorption geometries and energies of the precursor on Cu surfaces.

Perhaps due to the complexity of Cu ALD processes (except using the CuCl precursor), only very few works [88] so far were based on the concept of *ab initio* molecular dynamics

(AIMD) simulations. For example, Maimaiti et al. [96] used a periodic model containing ~180 atoms, to study the adsorption of Cu(dmap)$_2$ on Cu(111), which is the most fundamental and simple step of ALD. For simulation of the subsequent ALD steps, in which the adsorbed Cu precursors react with co-reactants or *vice versa*, models with more 200 atoms are required. While DFT balances accuracy and computational costs quite well, such large systems are still very burdensome for current computers. Using a simplified cluster model may reduce computational costs, but it neglects the effect of surface structural relaxation and electrostatic fields of the extended surface. Great caution must be taken when studying the surface phenomena based on cluster calculations. For these reasons, efficient multiscale approaches are necessarily needed to realize the atomistic simulation of Cu ALD, which will be discussed in the next section.

3.2 Multiscale simulation approaches of ALD

ALD processes are taking place on several length- and time-scales [33]. For example, precursors are pulsed into a meter-scale reactor, distributed around a millimeter-scale wafer, and react with surface species to deposit nanometer-thick thin films. On the other hand, film growth is obtained by a combination of fast (ps–ns) and slow (μs–s) surface reactions, while gases are pulsed and purged over second-long time-scales. The development and optimization of ALD processes require understanding how macroscopic conditions (e.g., flow rate, temperature, and pressure) affect the thin film growth on the microscopic level (e.g., growth rate, impurity concentration, reaction mechanism). However, most simulation methods are focused on specific length scale and timescale. For example, *ab initio* calculations [e.g., based on Hartree–Fock (HF) or DFT] are used for predicting the structural and electronic properties of precursors at atomic-scales; a ballistic model can be implemented for describing the topography evolution at feature scales; and continuum mechanics are applied for modeling the fluid dynamics at macroscales. These approaches provide useful insights into the underlying chemical and physical phenomena, but only at the level for which they apply. Therefore, there is a requirement for developing multiscale models that combine the selected scale approaches, as shown in Fig. 3.1. The physical and chemical properties are modeled on each level using the input data obtained from another level. The present study focuses on investigating the surface chemistry of Cu ALD, at atomic-scale and molecular-scale. The macroscopic properties of ALD such as growth rate and fluid dynamics, which can be studied using the finite element method (FEM) [97], will not be discussed in this thesis.
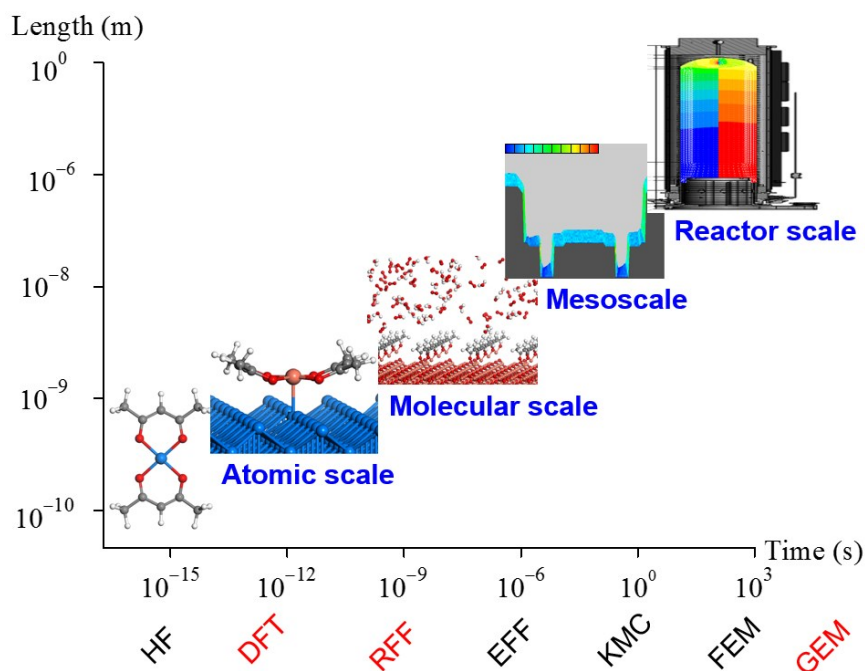
Fig. 3.1 Multiscale approach for ALD simulation. The DFT, RFF (reactive force field), and GEM (Gibbs energy minimization) methods are employed in this work.

Kinetic Monte Carlo (KMC) is a widely used approach to performing multiscale simulations of surface chemistry at the mesoscale (~10^{-6} m) [98]. It may be assumed as a coarse-grained modeling strategy that follows the time evolution of adsorbates on the surface lattice. The KMC model usually consists of a few thousand fixed adsorption sites with areas of the order of ~100 nm^2. The linking between the atomic-scale and the mesoscale in KMC simulations is the reaction rate. Kinetic data at the atomic-scale is typically obtained by *ab initio* calculations since the experimental data of surface reactions is often unavailable or not comprehensive. As compared to MD simulations, the continuous atomic trajectories are replaced by the discrete atomic jumps on adsorption sites. Therefore, KMC can reach simulation times in the order of second, while it preserves being a mesoscale model.

Recently, KMC approaches have been used in ALD simulations, extending *ab initio* calculations to predict the time evolution of thin film growth, by-products distribution, and stoichiometry of films. Dkhissi et al. [99, 100] studied the ALD of HfO_2 on the Si(100) surface, using $HfCl_4$ and H_2O as precursors. The proposed KMC models offer guidance in the optimization of the experimental deposition processes, regarding OH density on the substrate, optimal growth temperature, pulse durations, and finally growth kinetics. Shirazi et al. [101] presented a three-dimensional on-lattice KMC model to describe the ALD of HfO_2 from $Hf(NMe_2)_4$ and H_2O. This is the first KMC report which considers the steric demand of ligands and the cooperative effect on activation energies. The predicted film growth rates of

ALD agree with experiment to within 20%. Furthermore, ALD growth was observed to occur simultaneously in different layers, which may lead to an inhomogeneous growth process. These works demonstrate the power of KMC for the multiscale simulation of ALD. However, the development of a KMC model is difficult and time-consuming in terms of generating kinetic data and adjusting the lattice and preparing reaction lists [33]. Unfortunately, most of the KMC models have no transferability, since the surface reaction is strongly dependent on individual substrate properties. Furthermore, KMC models are built upon the "well-known" reaction mechanisms and kinetics of processes. Missing any important reaction pathway would lead to a poor simulation.

Another approach to realize multiscale modeling is classical molecular dynamics (CMD) simulations [102]. CMD solves Newton's equations of motion to determine the trajectories of atoms. The timestep in CMD must be smaller than the fastest vibrational frequency of the system to avoid discretization errors. A typical timestep for the CMD simulation is in the order of 1 fs. The potential energy between the individual atoms of the system is described using an empirical force field (EFF). Often, *ab initio* calculation results are used to fit the EFF parameters, linking the atomic-scale and molecular-scale simulations.

However, CMD approaches are rarely used in ALD simulations, perhaps due to the lack of adequate EFFs. Turner et al. [103] used a Buckingham potential to simulate the growth dynamics of amorphous Al_2O_3 films. The ALD surface reactions were not considered in MD simulations because of the nonreactive character of this potential. Instead, it was assumed that surface $AlMe_2$ species are fully hydroxylated during the H_2O pulse. Based on MD simulations, the growth rate of Al_2O_3 was predicted to be around 0.06 nm per cycle, which is very close to the experimental values (about 0.08 nm per cycle) [103]. Furthermore, densification that leads to an increased coordination number of Al has also been observed [103].

RMD is a special case of CMD, which employs a reactive force field (RFF) to describe bond forming and breaking as well as charge distribution with nearly the accuracy of *ab initio* molecular dynamics (AIMD) [104]. Therefore, RFF can be used to explore the reaction dynamics of relatively large systems (thousands of atoms), bridging the gap between DFT and EFF (Fig. 3.1). Another advantage of RFF is its good transferability. When an existing RFF is extended to a new system, most of the RFF parameters and the corresponding training sets can be safely retained. Compared with KMC approaches, assuming that the substrate has a long-range ordered structure, RMD simulations properly describe the evolution of amorphous

structures during the thin film growth. In summary, RMD is a promising approach for the multiscale simulation of ALD and thus it has been used in this work.

While the computational costs of RMD simulations are much lower than those of AIMD, the time-scale reached by RMD is in the order of ns (ps for AIMD). Therefore, some large-barrier reactions existing in ALD may still be unobservable since they occur on longer time scales. To complement RMD simulations, thermodynamic modeling based on the Gibbs energy minimization (GEM) method is performed to predict equilibrium compositions. At an equilibrium state, the concentrations of reactants and products will no longer change with time evolution. Previously, the GEM method has been successfully applied in CVD simulations [105], using the experimentally measured (macroscale) thermodynamic data. In this work, *ab initio* calculations are performed to obtain the thermodynamic data of ALD reactions, which links atomic-scale data and macroscale properties.

3.3 Density functional theory

One of the most important equations of the twentieth century is the Schrödinger Equation which describes the electronic structure of any system. The time-independent, non-relativistic form of the Schrödinger equation is

$$\hat{H}\Psi = E\Psi \tag{3.3.1}$$

Eq. 3.3.1 states that when the Hamilton operator $\hat{H}$ acts on a certain wave function Ψ, the result is proportional to the same wave function. By applying the Born-Oppenheimer approximation (neglecting the atomic core dynamics), the electronic Hamilton operator ($\hat{H}_{\text{elec}}$) is given by

$$\hat{H}_{\text{elec}} = \hat{T}_{\text{e}} + \hat{V}_{\text{Ne}} + \hat{U}_{\text{ee}} = -\frac{\hbar^2}{2m_i}\sum_{i=1}^{N}\nabla_i^2 + \sum_{i=1}^{N}V(\boldsymbol{r}_i) + \sum_{j>i}^{N}U(\boldsymbol{r}_i, \boldsymbol{r}_j) \tag{3.3.2}$$

where $\hat{T}_{\text{e}}$ is the kinetic energy operator of the electrons, $\hat{V}_{\text{Ne}}$ is the potential energy operator between electrons and nuclei, and $\hat{U}_{\text{ee}}$ is the potential energy operator between electrons. There are many sophisticated methods for solving the many-body Schrödinger equation based on the expansion of the wave function in Slater determinants. One simple approach is the HF method or post-HF methods (e.g., Møller–Plesset). However, the disadvantage of the post-HF approaches is the huge computational cost, which makes it difficult to apply them to larger and more complex systems. On the other hand, DFT provides an efficient and reliable way to

systematically map the many-body problem. The key variable in DFT is the electron density for a system with N electrons,

$$n(\boldsymbol{r}) = N \int d^3r_2 \cdots \int d^3r_N \Psi^*(\boldsymbol{r}, \boldsymbol{r}_2, \cdots, \boldsymbol{r}_N) \Psi(\boldsymbol{r}, \boldsymbol{r}_2, \cdots, \boldsymbol{r}_N) \tag{3.3.3}$$

The theoretical foundation of DFT is based on the two theorems proved by Hohenberg and Kohn (HK) [106], and based on the derivation of a set of equations by Kohn and Sham (KS) [107]. The first HK theorem states that the ground-state energy from Schrödinger's equation is uniquely determined by a functional of the electron density. This means that there exists a 1-to-1 correspondence between the ground-state wave function $\Psi_0(\boldsymbol{r}, \boldsymbol{r}_2, \cdots, \boldsymbol{r}_N)$ and the ground-state electron density $n_0(\boldsymbol{r})$. The proof of this theorem is based on reductio ad absurdum. The second HK theorem demonstrates the existence of a variational principle for the energy functional: the electron density that minimizes the energy functional is the exact electron density corresponding to the ground state solution of the Schrödinger equation. Based on the HK theorems, the energy functional $E[n(\boldsymbol{r})]$ can be expressed as

$$E[n(\boldsymbol{r})] = T_{\mathrm{e}}[n(\boldsymbol{r})] + V_{\mathrm{Ne}}[n(\boldsymbol{r})] + U_{\mathrm{ee}}[n(\boldsymbol{r})] \tag{3.3.4}$$

where $V_{\mathrm{Ne}}[n(\boldsymbol{r})]$ is the functional of the potential energy between the electron and nuclei, which depends on the system under study

$$V_{\mathrm{Ne}}[n(\boldsymbol{r})] = \int V(\boldsymbol{r}) n(\boldsymbol{r}) d^3r \tag{3.3.5}$$

$T_{\mathrm{e}}[n(\boldsymbol{r})]$ and $U_{\mathrm{ee}}[n(\boldsymbol{r})]$ are functionals that define the electron kinetic energy and the electron-electron interactions, respectively. However, the explicit form of the both functionals is still unknown. To solve this problem, Kohn and Sham [107] proposed a fictitious system consisting of non-interacting electrons, which move in a local effective potential $V_{\mathrm{S}}(\boldsymbol{r})$. The KS equations have the form

$$\left[-\frac{\hbar^2}{2m_i} \nabla^2 + V_{\mathrm{s}}(\boldsymbol{r}) \right] \phi_i(\boldsymbol{r}) = \epsilon_i \phi_i(\boldsymbol{r}) \tag{3.3.6}$$

where $\phi_i(\boldsymbol{r})$ are the KS orbitals that reproduce the electron density of the original interacting system, and ϵ_i are the corresponding orbital energies. The effective potential can be written in more detail as

$$V_{\mathrm{s}}(\boldsymbol{r}) = V(\boldsymbol{r}) + e^2 \int \frac{n(r\prime)}{|r-r\prime|} d^3\boldsymbol{r}' + V_{\mathrm{XC}}(\boldsymbol{r}) \tag{3.3.7}$$

where the second term is the Hartree potential that describes the Coulomb repulsion between the electrons. V_{XC} is the exchange-correlation term, which includes all the many-particle interactions

$$V_{XC}(\boldsymbol{r}) = \frac{\delta E_{XC}[n(r)]}{\delta n(r)} \tag{3.3.8}$$

Finally, the total energy of a system can be expressed as

$$E[n(\boldsymbol{r})] = -\frac{\hbar^2}{2m_i}\sum_{i=1}^{N}\int \phi_i^*(\boldsymbol{r})\nabla^2\phi_i(\boldsymbol{r})d^3r + \int V(\boldsymbol{r})n(\boldsymbol{r})d^3r$$

$$+ \frac{e^2}{2}\int\int\frac{n(r)n(r\prime)}{|r-\mathbf{r}\prime|}d^3rd^3r\prime + E_{XC}[n(\boldsymbol{r})] \tag{3.3.9}$$

Now, the complex many-body problem has been transformed into an effective single-particle problem, which is computationally much more feasible. However, the true form of the exchange correlation functional E_{XC} is simply not known. Finding good approximations for this functional is the main challenge of DFT. One of the most widely used approximations is the local-density approximation (LDA), which depends only on the electronic density at each point in space. For a spin-unpolarized system, the LDA for the exchange-correlation energy is

$$E_{XC}^{LDA}[n] = \int n(\boldsymbol{r})\varepsilon_{XC}(n)\,d^3r \tag{3.3.10}$$

where $\varepsilon_{XC}(n)$ is the exchange-correlation energy per electron in a homogeneous electron gas of density n. For a spin-polarized system, the local-spin-density approximation (LSDA) employs two spin-densities, $n_\uparrow$ and $n_\downarrow$ ($n = n_\uparrow + n_\downarrow$), which is given by

$$E_{XC}^{LSDA}[n_\uparrow, n_\downarrow] = \int n(\boldsymbol{r})\varepsilon_{XC}(n_\uparrow, n_\downarrow)\,d^3r \tag{3.3.11}$$

It is well known that the LDA tends to overestimate the bond energy and to underestimate the lattice constants of solids. Generalized gradient approximations (GGA) improve upon the LDA by taking the gradient of the density into account

$$E_{XC}^{GGA}[n_\uparrow, n_\downarrow] = \int n(\boldsymbol{r})\varepsilon_{XC}(n_\uparrow, n_\downarrow, \nabla n_\uparrow, \nabla n_\downarrow)\,d^3r \tag{3.3.12}$$

Two of the most widely used GGA-functionals in calculations involving solids are the Perdew–Wang functional (PW91) [108] and the Perdew–Burke–Ernzerhof functional (PBE) [109]. Usually, very good results for geometries and ground-state energies of solids can be obtained by using the GGA. However, both GGA and LDA fail to completely describe the vdW interactions. The vdW-DF functional [110] makes it possible to distinguish the local and non-local contributions to the total energy. Technically, the correlation part of the GGA

functional $E_{GGA,c}$ is replaced by a sum of an LDA correlation functional $E_{LDA,c}$ and a nonlocal term $E_{NL,c}$ such that the total energy is calculated by

$$E_{vdW-DF} = E_{GGA} - E_{GGA,c} + E_{LDA,c} + E_{NL,c} \qquad (3.3.13)$$

$E_{NL,c}$ can be expressed as a function of the charge density,

$$E_{NL,c} = \frac{1}{2} \int \int dr dr' n(r) \emptyset(r, r') n(r') \qquad (3.3.14)$$

where the kernel function $\emptyset(r, r')$ is discussed in detail in Ref. [110].

3.4 Reactive dynamics simulations using a ReaxFF potential

To date, a series of RFFs have been developed, such as AIREBO [111], ReaxFF [112], COMB [113], and QMDFF [114]. Most of these potentials are based on the bond order concept and have good transferability. Recent advances in the bond order dependent RFFs are summarized and discussed in Ref. [104]. The ReaxFF force field is used in the present work for ALD simulations since it contains well-developed potentials for the Cu system (see Section 5.2). ReaxFF was originally developed by van Duin, Goddard, and co-workers at California Institute of Technology in 2001 [112]. It uses relationships between interatomic distance and bond order as well as between bond order and bond energy to describe bond dissociation. There is no discontinuity in energy or forces even during reactions. Furthermore, the effect of van der Waals and Coulomb interactions are also addressed in this potential. This section is dedicated to the introduction of ReaxFF potential functions as well as their parameterization.

3.4.1 Introduction of the ReaxFF potential functions

The system energy (E_{system}) in ReaxFF is composed of a sum of energy terms [112]:

$$E_{system} = E_{bond} + E_{under} + E_{over} + E_{val} + E_{pen} + E_{tors} + E_{conj} + E_{Coulomb} + E_{vdW}$$
$$(3.4.1)$$

A basic assumption of ReaxFF is that the (uncorrected) bond order BO'_{ij} between a pair of atoms can be obtained directly from the interatomic distance r_{ij} as given in Eq. 3.4.2. In calculating the bond orders, ReaxFF distinguishes between contributions from sigma bonds, pi bonds, and double pi bonds
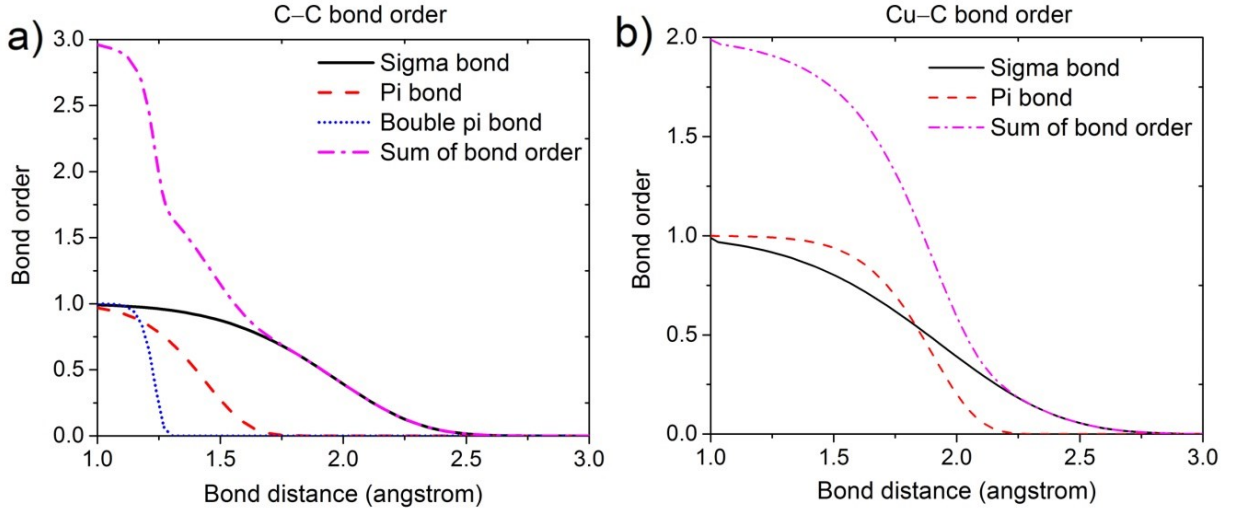
Fig. 3.2 The interatomic distance dependency of the bond order. (a) the C–C bond [112]. (b) the Cu–C bond (this work).

$$BO'_{ij} = BO'^{\sigma}_{ij} + BO'^{\pi}_{ij} + BO'^{\pi\pi}_{ij}$$

$$= \exp\left[p_{bo1} \cdot \left(\frac{r_{ij}}{r_o^{\sigma}}\right)^{P_{bo2}}\right] + \exp\left[p_{bo3} \cdot \left(\frac{r_{ij}}{r_o^{\pi}}\right)^{P_{bo4}}\right] + \exp\left[p_{bo5} \cdot \left(\frac{r_{ij}}{r_o^{\pi\pi}}\right)^{P_{bo6}}\right] \tag{3.4.2}$$

Fig. 3.2a shows the interatomic distance dependency of the C–C bond order. The sigma bond is close to unity within a bond distance of ~1.5 Å but negligible above ~2.5 Å; the pi bond is close to unity below ~1.2 Å but negligible above ~1.7 Å; the double pi bond is close to unity below ~1.2 Å but negligible above ~1.1 Å. By this definition, the maximum bond order of the C–C bond is 3. For the Cu–C bond, only the sigma and pi bonds need to be considered, leading to a maximum bond order of 2 (see Fig. 3.2b).

Based on the uncorrected bond order BO'_{ij}, an uncorrected overcoordination Δ' can be defined for the atoms as the difference between the total order around the atom and the number of its bonding electrons Val. ($Val_i = 4$ for carbon, $Val_i = 1$ for hydrogen)

$$\Delta'_i = -Val_i + \sum_{j=1}^{i} BO'_{ij} \tag{3.4.3a}$$

ReaxFF then uses these uncorrected overcoordination definitions to correct the bond orders BO'_{ij} for overcoordination and for residual 1–3 bond orders in valence angles. A second overcoordination definition Δ'^{boc}_i is used to soften the correction for atoms bearing lone electron pairs.

$$\Delta'^{boc}_i = -Val^{boc}_i + \sum_{j=1}^{i} BO'_{ij} \tag{3.4.3b}$$

The final bond orders in the molecule are obtained by multiplying the bond orders from Eq. 3.4.2 by the correction factors.

$$BO_{ij}^{\sigma} = BO_{ij}^{\prime\sigma} \cdot f_1(\Delta_i', \Delta_j') \cdot f_4(\Delta_i', BO_{ij}') \cdot f_5(\Delta_j', BO_{ij}')$$

$$BO_{ij}^{\pi} = BO_{ij}^{\prime\pi} \cdot f_1(\Delta_i', \Delta_j') \cdot f_1(\Delta_i', \Delta_j') \cdot f_4(\Delta_i', BO_{ij}') \cdot f_5(\Delta_j', BO_{ij}')$$

$$BO_{ij}^{\pi\pi} = BO_{ij}^{\prime\pi\pi} \cdot f_1(\Delta_i', \Delta_j') \cdot f_1(\Delta_i', \Delta_j') \cdot f_4(\Delta_i', BO_{ij}') \cdot f_5(\Delta_j', BO_{ij}')$$

$$BO_{ij} = BO_{ij}^{\sigma} + BO_{ij}^{\pi} + BO_{ij}^{\pi\pi} \tag{3.4.4a}$$

$$f_1(\Delta_i, \Delta_j) = \frac{1}{2}\left[\frac{Val_i + f_2(\Delta_i', \Delta_j')}{Val_i + f_2(\Delta_i', \Delta_j') + f_3(\Delta_i', \Delta_j')} + \frac{Val_j + f_2(\Delta_i', \Delta_j')}{Val_j + f_2(\Delta_i', \Delta_j') + f_3(\Delta_i', \Delta_j')}\right] \tag{3.4.4b}$$

$$f_2(\Delta_i', \Delta_j') = \exp(-p_{boc1} \cdot \Delta_i') + \exp(-p_{boc1} \cdot \Delta_j') \tag{3.4.4c}$$

$$f_3(\Delta_i', \Delta_j') = -\frac{1}{p_{boc2}} \cdot \ln\left\{\frac{1}{2} \cdot \left[\exp(-p_{boc2} \cdot \Delta_i') + \exp(-p_{boc2} \cdot \Delta_j')\right]\right\} \tag{3.4.4d}$$

$$f_4(\Delta_i', BO_{ij}') = \frac{1}{1 + \exp\left[-p_{boc3} \cdot \left(p_{boc4} \cdot BO_{ij}' \cdot BO_{ij}' - \Delta_i'^{boc}\right) + p_{boc5}\right]} \tag{3.4.4e}$$

$$f_5(\Delta_j', BO_{ij}') = \frac{1}{1 + \exp\left[-p_{boc3} \cdot \left(p_{boc4} \cdot BO_{ij}' \cdot BO_{ij}' - \Delta_j'^{boc}\right) + p_{boc5}\right]} \tag{3.4.4f}$$

A corrected overcoordination Δ_i can be derived from the corrected bond orders using Eq. 3.4.5

$$\Delta_i = -Val_i + \sum_{j=1}^{i} BO_{ij} \tag{3.4.5}$$

The values of bond order are updated at each MD step and are used to determine all valence terms listed in Eq. 3.4.1 (see Appendix for detail). For example, the bond energy E_{bond} is calculated as

$$E_{bond} = -D_e^{\sigma} \cdot BO_{ij}^{\sigma} \cdot \exp\{p_{be1}[1 - (BO_{ij}^{\sigma})^{p_{be2}}]\} - D_e^{\pi} \cdot BO_{ij}^{\pi} - D_e^{\pi\pi} \cdot BO_{ij}^{\pi\pi} \tag{3.4.6}$$

In addition to bonded interactions, there are repulsive interactions at short interatomic distances due to the Pauli principle orthogonalization and attraction energies at long distances due to dispersion forces. These nonbonded interactions are comprised of van der Waals and Coulomb force for all atom pairs. To avoid discontinuities when charged species move in and out of the nonbonded cutoff radius, ReaxFF employs a distance-dependent 7th Taper correction for nonbonded energy terms. The van der Waals interactions are described using a distance-corrected Morse-potential. By including a shielded interaction (Eq. 3.4.7)

excessively high repulsions between bonded atoms (1–2 interactions) and atoms sharing a valence angle (1–3 interactions) are avoided.

$$E_{\text{vdW}} = Tap \cdot D_{ij} \cdot \left\{ \exp\left[\alpha_{ij} \cdot \left(1 - \frac{f_{13}(r_{ij})}{r_{\text{vdW}}} \right) \right] - 2 \cdot \exp\left[\frac{1}{2} \cdot \alpha_{ij} \cdot \left(1 - \frac{f_{13}(r_{ij})}{r_{\text{vdW}}} \right) \right] \right\} \tag{3.4.7a}$$

$$f_{13}(r_{ij}) = \left[r_{ij}^{p_{\text{vdW1}}} + \left(\frac{1}{\gamma_{\text{w}}} \right)^{p_{\text{vdW1}}} \right]^{\frac{1}{p_{\text{vdW1}}}} \tag{3.4.7b}$$

Similar to the van der Waals term, a shielded Coulomb potential is used to adjust for orbital overlap between atoms that are close together. (Eq. 3.4.8). Atomic charges are computed using the geometry-dependent charge calculation scheme (EEM scheme) of Janssens et al [115].

$$E_{\text{coulomb}} = Tap \cdot C \cdot \frac{q_i \cdot q_j}{\left[r_{ij}^3 + \left(\frac{1}{r_{ij}} \right)^3 \right]^{1/3}} \tag{3.4.8}$$

3.4.2 Development of the ReaxFF potential

In general, the parameterization of an RFF can be divided into four steps:

1) Preparing a training set by *ab initio* calculations or from experimental data.

2) Reproducing the whole training data using an initial set of ReaxFF parameters, and calculating the error of ReaxFF results relative to the reference data.

3) Adjusting the initial ReaxFF parameters until the error has been minimized.

4) Checking the performance of the optimized ReaxFF parameters within and outside the training set.

Among these steps, the 1st step is the most time-consuming step, since a comprehensive training set is necessary for obtaining a good transferable potential. The training set includes data of geometric structures, bond dissociative curves, adsorption/reaction energies, vdW interactions, charge distributions, angle energy curves, torsion energy curves, and so on. Most of these data must be generated manually, since automatic algorithms such as that based on MD simulations, provide information mainly nearby the equilibrium state. The 3rd step is the most challenging step because there are a large number of general parameters as well as atom-specific parameters. The number of parameters in ReaxFF grows with the third power of the number of elements in a system. Furthermore, most of the parameters interact with each other, making the parameterization a difficult task.

In the majority of ReaxFF parameterizations, a single parameter search (SPS) method has been used [116]. This method employs a parabolic extrapolation procedure to optimize only one parameter at a time. This is simple and straightforward for implementation, but it is also clearly inefficient. Moreover, the approach is prone to become stuck in local minima [117]. The only way SPS can escape local minima is if changes are large enough that neighboring minima can be reached. Recently, Deetz and Faller [118] proposed a parallelized local search algorithm for ReaxFF parameterizations. In this approach, a small list of parameters is assigned to each processor. At the end of each iteration, all parameters are updated simultaneously after being independently evaluated. In comparison to the SPS approach, this method is not only faster but also helps to prevent entrapment in local minima. Another approach for developing ReaxFF parameters is based on evolutionary methods such as genetic algorithms [119]. These methods deliver parameter sets of the same quality with much less effort as compared to SPS, and also offer excellent parallel scaling. More recently, Jaramillo-Botero et al. [120] reported a hybrid multi-objective method (referred as GARFfield) based on genetic algorithms, hill-climbing routines, and conjugate-gradient minimization. The GARFfield program enables efficient and fast parallel optimization of parameters from quantum mechanical data sets for demanding applications like ReaxFF, electron force field, and COMB.

In this work, a new approach based on the Taguchi method is introduced for the parameterization of the ReaxFF potential. The Taguchi method was originally developed for robust design by Taguchi during the 1950s. Robust design is an engineering methodology for optimizing product and process conditions to be minimally sensitive to variations in uncontrollable factors. Thus, high-quality products with low development costs can be manufactured. So far, applications of the Taguchi method have been successfully extended from engineering to biotechnology, advertising, marketing, numerical optimization, and so on. A primer on the Taguchi method can be found in Ref. [121]. Nevertheless, this method is rarely used for force field development.

The Taguchi method is a statistical tool based on the systematic approach, which provides several promising features for the force field development. Firstly, the significance of each parameter can be quantitatively assessed based on statistical analysis of variance (ANOVA). Such information is of great importance regardless of the optimization algorithm used. Secondly, the Taguchi method employs an orthogonal array to design the trial, providing an excellent parameter-screening efficiency. For example, using the Taguchi method it needs only 81 runs to optimize 40 parameters with 3 levels for each, whereas the SPS approach

Table 3.2 L_9 (3^4) orthogonal array.

Experiment	Factors			
	A	B	C	D
1	1	1	1	1
2	1	2	2	2
3	1	3	3	3
4	2	1	2	3
5	2	2	3	1
6	2	3	1	2
7	3	1	3	2
8	3	2	1	3
9	3	3	2	1

requires 120 (40 × 3) calculations. Thirdly, the interactions among different parameters can be (partially) considered by the Taguchi method. This is infeasible for most of the existing approaches. Similar to the parallel version of SPS [118], the Taguchi method can also be performed in parallel.

Two major concepts used in the Taguchi method are the signal-to-noise (S/N) ratio and the orthogonal array (or Taguchi table). The S/N ratio is a logarithmic function of the desired output, which takes both the amount of variation and the mean response into account. There are several categories of S/N ratio available: nominal-is-best, smaller-the-better, and larger-the-better. Parameters that maximize the appropriate S/N ratio are the optimal setting. For the purpose of force field parameterization (i.e., minimization of error), the smaller-the-better characteristic needs to be used and is calculated as follows

$$S/N = -10\log(\frac{1}{n}\sum y^2) \tag{3.4.13}$$

where y is the error between the ReaxFF value ($x_{i,\text{ReaxFF}}$) and the reference value ($x_{i,\text{Ref}}$)

$$y = \frac{x_{i,\text{Ref}} - x_{i,\text{ReaxFF}}}{\sigma} \tag{3.4.14}$$

where σ is a weight specified in the training set. An orthogonal array (OA) is a fractional factorial matrix, which assures a balanced comparison of levels of any factor or interaction of factors. The array is called orthogonal because all columns can be evaluated independently of one another. Table 3.2 shows an example of L_9 (3^4) orthogonal array. The number "9" in L_9 (3^4) represents the run number of an experiment, while "3^4" means that the orthogonal array contains 4 factors with 3 levels for each. In this work, the L_{81} (3^{40}) OA table is used to optimize the sum of about 150 ReaxFF parameters. This OA is able to optimize maximum of 40 factors without considering interactions, or 4 factors with interactions plus 24 factors without interactions. All calculations are performed in parallel on 81 CPU cores. Details of

the L_{81} (3^{40}) OA and the interaction table are shown in the Appendix (Table A12). The use of larger OAs may be more efficient, but at the same time, it will increase the complexity of the program implementation and the analysis of results.

After the entire calculation as listed in the OA table is complete, ANOVA is performed to find out which process parameters are statistically significant. Based on the *S/N* ratio and ANOVA results, the optimal combination of the parameters can be predicted. The mean of *S/N* ratio is calculated as follows

$$M_{Xi} = \frac{1}{n_{Xi}}\sum_{i=1}^{n_{Xi}}(S/N)_{Xi}$$ (3.4.15)

where M_{Xi} is the mean *S/N* ratio of factor *X* in level i, n_{Xi} is the number of occurrences for factor X_i in the OA table [e.g., 27 for L_{81} (3^{40}) OA], $(S/N)_{Xi}$ is the *S/N* ratio of factor X_i. The sum of squares for each factor (SS_X) is calculated by

$$SS_X = \frac{n}{L_X}\sum_{i=1}^{L_X}(M_{Xi} - M_X)^2$$ (3.4.16)

where n is the run number (e.g., 81 for L_{81} OA), L_X is the number of levels for factor *X*, and M_X is the mean *S/N* ratio of the factor. The total sum of squares (SS_{total}) is calculated by

$$SS_{total} = \sum_{i=1}^{n}(S/N)_i^2 - n \times M_X^2$$ (3.4.17)

The mean squares for each factor (MS_X) is calculated by

$$MS_X = \frac{SS_X}{DOF_X}$$ (3.4.18)

where DOF_X is the number of degrees of freedom of factor *X*. The *F* ratio of the factor is estimated by

$$F_X = \frac{MS_X}{MS_{error}}$$ (3.4.19)

where MS_{error} is the mean squares of the error.

The overall computational flow diagram for ReaxFF development using the Taguchi method is depicted in Fig. 3.3 .The first step is the selection of target parameters that need to be optimized in the current calculation. The target parameters include the significant parameters obtained from the last calculation as well as the new parameters which have not been optimized so far. The three-level input values for each target parameter are a_0, $a_0(1 - \beta)$, and $a_0(1 + \beta)$, respectively, where a_0 is the optimal value predicted by last ANOVA, and β is a
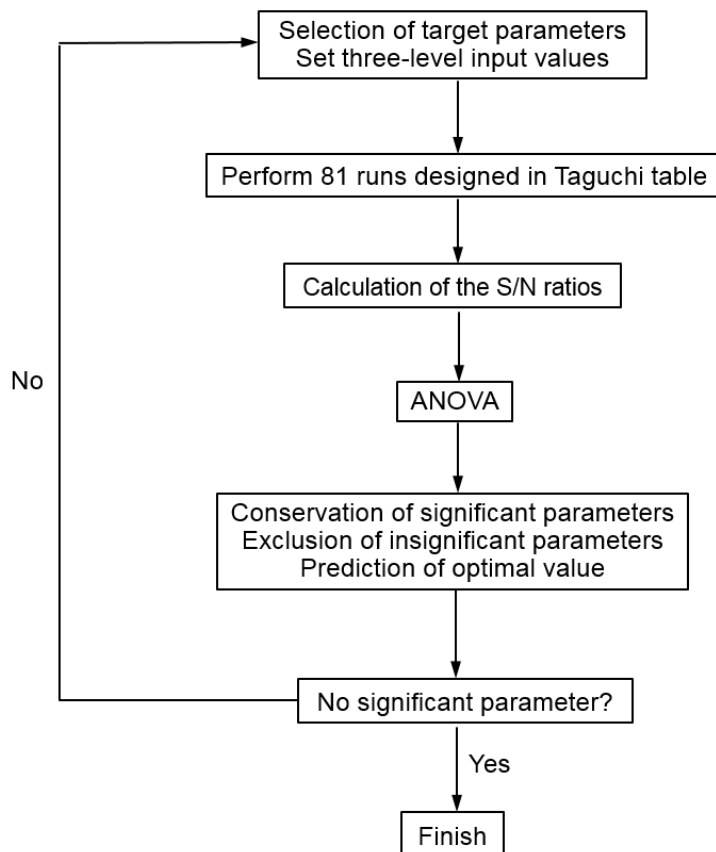
Fig. 3.3 The overall computational flow diagram for ReaxFF development using the Taguchi method.

scaling factor. In the initial training stage β is equal to 0.02, and its value is gradually reduced at the end of calculation. If two ANOVAs predict a same optimal value for one parameter, then the value of β for this parameter is reduced by 50%. Next, 81 runs are performed in parallel as designed in the Taguchi table. The S/N ratio against the training set of each run is calculated according to Eq. 3.4.13. ANOVA is then carried out to find out the significant parameters and to predict the optimal value for each parameter. The significant parameters are conserved in the target parameters, whereas the insignificant parameters will be not considered in the next calculation. The optimization process can be stopped if there is no significant parameter anymore.

3.5 *Ab initio* thermodynamic modeling

Computational thermodynamics approaches have become a valuable tool in the prediction of complex, multicomponent phase equilibria [122]. These methods rely on databases of free energies, obtained from an optimization process involving experimental thermodynamics and phase diagram data [122]. Once armed with the database, a computation can be performed to

minimize the multi-component free energy functional to predict the phase equilibria. Unfortunately, many species of practical interest are not present in the existing thermodynamic databases. This is especially the fact for the field of ALD, which commonly uses newly synthesized metal organic precursors. Furthermore, also the thermodynamic data of adsorbed species on the surface are required since ALD is based on surface reactions.

As shown in Section 3.3, DFT calculations are based on *ab initio* electronic structure theory, which does not rely on semi-empirical or fitted parameters. Using DFT one can obtain detailed insight into atoms, molecules, solids, and solid surfaces/interfaces in the microscopic (electronic) regime. To describe the macroscopic world, which is several time and length scales bigger, an appropriate linkage between the micro- and macroscopic regimes has to be established. Moreover, DFT is often argued to be a zero-temperature, zero-pressure technique. As a consequence, the total energy calculated by DFT has to be transferred with considerable care to typical high-temperature and pressure applications.

To bridge the gap between *ab initio* calculations and macroscopic modeling, *ab initio* thermodynamics was developed. The DFT total energies are incorporated into a calculation of the Gibbs free energy by properly setting a reference state. Based on statistical mechanics, the DFT calculated energy is extended to the finite temperature range. So far, the *ab initio* thermodynamics has been successfully applied to different fields, for example, surface science [123], materials design [124], electrochemistry [125], as well as ALD/CVD [126, 127].

3.5.1 Calculation of thermodynamic properties based on statistical mechanics

It is known that total energies obtained by DFT are only electronic energies, which do not consider contributions from the zero-point energy (*ZPE*), enthalpy (*H*) at non-zero temperatures, and entropy (*S*). Therefore, *ab initio* thermodynamics calculations based on statistical mechanics are performed to calculate the additional contributions to the Gibbs free energies (*G*) (Eq. 3.5.1).

$$G = H - TS \tag{3.5.1}$$

The following theoretical background on statistical mechanics is based on "*Molecular Thermodynamics*" by McQuarrie and Simon [128]. The gaseous species are assumed to be non-interacting particles which can be treated as an ideal gas.

Firstly, the *ZPE* correction is added to the electronic energy in order to account for atomic vibrations in the internal energy. E_{ZPE} is the sum of the individual energies arising from each

vibrational mode, K, where there are 3n–5 vibrational modes in an n-atom linear molecule, 3n–6 in a nonlinear molecule, and 3n–3 in a crystal.

$$E_{\text{ZPE}} = \sum_{K=1}^{N} \frac{1}{2} h v_K \tag{3.5.2}$$

The internal energy (E_{internal}) is then calculated as

$$E_{\text{internal}} = E_{\text{electronic}} + E_{\text{ZPE}} \tag{3.5.3}$$

At a temperature of 0 K, the enthalpy is equal to the internal energy. To account for enthalpy corrections at non-zero temperatures, the heat capacity needs to be integrated from zero to the target temperature

$$H(T) - H(0) = \int_0^T C_p(T')dT' \tag{3.5.4}$$

The partition function (q) of a molecule, which is given by the individual partition functions from the electronic (q_e), vibrational (q_v), rotational (q_r), and translational (q_t) motions (Eq. 3.5.6), can be used to calculate the heat capacity

$$\int_0^T C_p(T')dT' = k_B T^2 \frac{\partial \ln(q)}{\partial T} + k_B T = k_B T \left(\frac{T}{q_e} \frac{\partial \ln q_e}{\partial T} + \frac{T}{q_v} \frac{\partial \ln q_v}{\partial T} + \frac{T}{q_r} \frac{\partial \ln q_r}{\partial T} + \frac{T}{q_t} \frac{\partial \ln q_t}{\partial T} + 1 \right) \tag{3.5.5}$$

$$q = q_e q_v q_r q_t \tag{3.5.6}$$

Similar to the enthalpy, the corrections to the entropy can be expressed as

$$S = k_B N \left\{ 1 + \ln \left[\frac{q(V,T)}{N} \right] + T \left[\frac{\partial \ln(q)}{dT} \right]_V \right\} = k_B \left\{ 1 + \left[\ln(q_e) + T \frac{\partial \ln(q_e)}{\partial T} \right] + \left[\ln(q_t) + T \frac{\partial \ln(q_t)}{\partial T} \right] + \right.$$
$$\left. \left[\ln(q_v) + T \frac{\partial \ln(q_v)}{\partial T} \right] + \left[\ln(q_r) + T \frac{\partial \ln(q_r)}{\partial T} \right] \right\} \tag{3.5.7}$$

The partition function from the electronic motion is

$$q_e = \omega_0 e^{-\frac{\varepsilon_0}{k_B T}} + \omega_1 e^{-\frac{\varepsilon_1}{k_B T}} + \omega_2 e^{-\frac{\varepsilon_2}{k_B T}} + \cdots \tag{3.5.8}$$

where ε_i are the energy levels and ω_i the degeneracies of the levels. Based on the assumption that the first electronic excitation energy is much greater than $k_B T$, the first and higher excited states are inaccessible at any temperature. Moreover, the energy of the ground state is set to zero. Therefore, the electronic partition function can be simplified to

$$q_e = \omega_0 \tag{3.5.9}$$

The electronic contribution to the entropy is therefore

$$S_e = k_B[\ln(q_e) + T\frac{\partial \ln(q_e)}{\partial T}] = k_B \ln(q_e) \qquad (3.5.10)$$

Since there is no temperature dependence of the partition function, the contribution of electronic motion to the heat capacity is zero.

The partition function from the vibrational motion is derived from the harmonic oscillator approximation. The total vibrational contribution is a sum of the contributions from each vibrational mode. Depending on the type of the molecule, each mode has a characteristic vibrational temperature,

$$\Theta_{v,K} = \frac{h\nu_K}{k_B} \qquad (3.5.11)$$

The first vibrational level is chosen as the zero reference, then the partition function for each vibrational level is

$$q_{v,K} = \frac{1}{1 - e^{(-\frac{\Theta_{v,K}}{T})}} \qquad (3.5.12)$$

The overall vibrational partition function is

$$q_v = \prod_K \frac{1}{1 - e^{(-\frac{\Theta_{v,K}}{T})}} \qquad (3.5.13)$$

Therefore, the enthalpy and entropy contributions from the vibrational partition function are

$$H_v(T) - H_v(0) = \frac{k_B T^2}{q_v}\frac{\partial q_v}{\partial T} = k_B \sum_K \Theta_{v,K} \frac{1}{\left[e^{(\frac{\Theta_{v,K}}{T})} - 1\right]} \qquad (3.5.14)$$

$$S_v = k_B\left[\ln(q_v) + T\frac{\partial \ln(q_v)}{\partial T}\right] = k_B\left\{\sum_K \ln\left[\frac{1}{1 - e^{(-\frac{\Theta_{v,K}}{T})}}\right] + \sum_K \frac{\Theta_{v,K}}{T}\frac{1}{\left[e^{(\frac{\Theta_{v,K}}{T})} - 1\right]}\right\} \qquad (3.5.15)$$

For a linear molecule, the rotational partition function is

$$q_r = \frac{1}{\sigma_r}(\frac{T}{\Theta_r}) \qquad (3.5.16)$$

where Θ_r is the characteristic rotational temperature, which can be defined as

$$\Theta_r = \frac{h^2}{8\pi^2 I k_B} \qquad (3.5.17)$$

where I is the moment of inertia. The rotational contributions to the enthalpy and entropy are

$$H_r(T) - H_r(0) = \frac{k_B T^2}{q_r}\frac{\partial q_r}{\partial T} = k_B T \qquad (3.5.18)$$

$$S_r = k_B \left[\ln(q_r) + T \frac{\partial \ln(q_r)}{\partial T} \right] = k_B \left[\ln(\frac{T}{\sigma_r \Theta_r}) + 1 \right] \tag{3.5.19}$$

The rotational partition function for a nonlinear molecule is

$$q_r = \frac{\pi^{0.5}}{\sigma_r} \left[\frac{T^{1.5}}{(\Theta_{r,x} \Theta_{r,y} \Theta_{r,z})^{0.5}} \right] \tag{3.5.20}$$

Now, the rotational contributions to the enthalpy and entropy are

$$H_r(T) - H_r(0) = \frac{k_B T^2}{q_r} \frac{\partial q_r}{\partial T} = 1.5 k_B T \tag{3.5.21}$$

$$S_r = k_B \left[\ln(q_r) + T \frac{\partial \ln(q_r)}{\partial T} \right] = k_B [\ln(q_r) + 1.5] \tag{3.5.22}$$

The partition function from the translational motion is

$$q_t = \left(\frac{2\pi M k_B T}{h^2} \right)^{1.5} V \tag{3.5.23}$$

For an ideal gas, the volume V can be calculated using Eq. 3.5.24

$$V = \frac{k_B T}{P} \tag{3.5.24}$$

By setting a pressure of 1 atm as the standard state, Eq. 3.5.24 can be written as

$$q_t = \left(\frac{2\pi M k_B T}{h^2} \right)^{1.5} \frac{k_B T}{P} \tag{3.5.25}$$

The translational contributions to the enthalpy and entropy are therefore

$$H_t(T) - H_t(0) = \frac{k_B T^2}{q_t} \frac{\partial q_r}{\partial T} = 1.5 k_B T \tag{3.5.26}$$

$$S_t = k_B \left[\ln(q_t) + T \frac{\partial \ln(q_t)}{\partial T} \right] = k_B (\ln q_t + 1.5) \tag{3.5.27}$$

Finally, the total enthalpy and entropy corrections for a gaseous species are the sum of equations (3.5.14), (3.5.21), (3.5.26) and (3.5.15), (3.5.22), (3.5.27), respectively. Once the molecule is adsorbed on the surface, it should be noticed that there are no longer any rotational or translational contributions to the free energy.

In order to evaluate the accuracy of *ab initio* thermodynamics calculations, thermodynamic properties of a few simple molecules have been calculated and compared with the experimental data, as shown in Table 3.3. To make such a comparison accessible, the reference state of experimental enthalpies was changed from the standard condition 298.15 K to 0 K, which is consistent with the *ab initio* thermodynamics. As shown in Table 3.2, there is

Table 3.3 Comparison between the calculated and experimental thermodynamic properties.

Species	Temperature (K)	DFT			Exp. [129]		
		H (eV)	S (meV)	G (eV)	H (eV)	S (meV)	G (eV)
H$_2$O	298.15	0.103	2.018	−0.499	0.103	1.957	−0.481
	350	0.121	2.073	−0.605	0.121	2.013	−0.584
	400	0.139	2.120	−0.710	0.138	2.060	−0.686
	450	0.156	2.162	−0.817	0.156	2.102	−0.790
	500	0.174	2.200	−0.926	0.174	2.141	−0.896
	600	0.211	2.267	−1.149	0.211	2.208	−1.113
	800	0.288	2.378	−1.614	0.289	2.320	−1.567
CO	298.15	0.090	2.049	−0.521	0.090	2.048	−0.521
	350	0.106	2.098	−0.629	0.106	2.097	−0.628
	400	0.121	2.138	−0.734	0.121	2.137	−0.734
	450	0.136	2.174	−0.842	0.136	2.173	−0.842
	500	0.151	2.206	−0.952	0.151	2.206	−0.952
	600	0.183	2.263	−1.175	0.183	2.263	−1.176
	800	0.247	2.356	−1.638	0.247	2.355	−1.637
PH$_3$	298.15	0.105	2.274	−0.573	0.105	2.179	−0.545
	350	0.126	2.338	−0.693	0.126	2.242	−0.659
	400	0.147	2.394	−0.811	0.147	2.299	−0.773
	450	0.169	2.447	−0.932	0.169	2.351	−0.889
	500	0.192	2.496	−1.055	0.192	2.400	−1.008
	600	0.243	2.588	−1.310	0.243	2.492	−1.253
	800	0.356	2.750	−1.844	0.357	2.655	−1.768
O$_2$	298.15	0.090	2.092	−0.534	0.090	2.126	−0.544
	350	0.106	2.141	−0.643	0.106	2.175	−0.655
	400	0.121	2.182	−0.752	0.121	2.217	−0.765
	450	0.137	2.219	−0.862	0.137	2.254	−0.877
	500	0.153	2.253	−0.973	0.153	2.287	−0.991
	600	0.186	2.312	−1.202	0.186	2.347	−1.222
	800	0.254	2.410	−1.674	0.254	2.445	−1.702
H$_2$	298.15	0.090	1.411	−0.331	0.088	1.354	−0.316
	350	0.106	1.460	−0.405	0.103	1.403	−0.388
	400	0.121	1.500	−0.479	0.118	1.443	−0.459
	450	0.136	1.535	−0.555	0.134	1.478	−0.532
	500	0.151	1.567	−0.633	0.149	1.510	−0.606
	600	0.181	1.622	−0.792	0.179	1.566	−0.760
	800	0.241	1.709	−1.126	0.240	1.654	−1.083

a very good agreement between the *ab initio* calculation and experimental values [129]. With only a few exceptions, the deviation of the free energy is smaller than ± 0.05 eV (or ± 5%).

The individual contributions of rotational, vibrational, and translational motions to the total enthalpies and entropies (without *ZPE*) of the Cu precursors are shown in Fig. 3.4. The main contributions of the enthalpy and entropy are from the vibrational motion. Temperature has a significant effect on the vibrational motion, while it has a minor effect on the rotational and translational motions. The thermodynamic data can be used to evaluate the stability of the Cu precursors, which will be discussed in the next chapter.
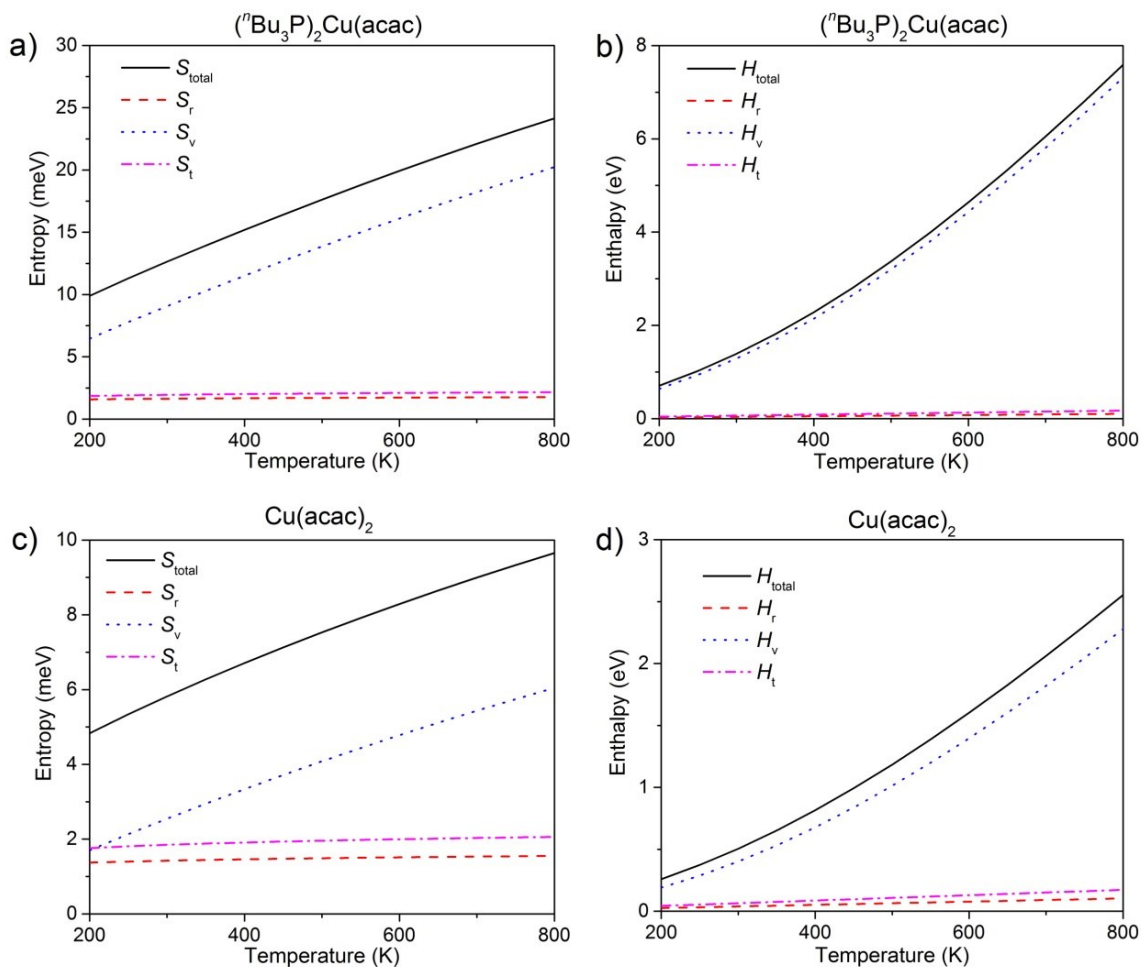
Fig. 3.4 Contributions of vibrational, rotational, and translational motions to the total entropies (a, c) and enthalpies (b, d) of the (^{n}Bu$_3$P)$_2$Cu(acac) and Cu(acac)$_2$ precursors.

3.5.2 Prediction of thermodynamic equilibrium based on Gibbs energy minimization

For a general chemical reaction

$$\alpha A + \beta B \rightleftharpoons \gamma C + \delta D \tag{3.5.28}$$

the chemical equilibrium is a state in which the concentrations of both reactants and products have no further tendency to change with time. Usually, this is the case when the forward and reverse reactions proceed at the same rate, known as a dynamic equilibrium

$$k_+[A]^\alpha[B]^\beta = k_-[C]^\gamma[D]^\delta \tag{3.5.29}$$

where [X] is the activity or fugacity of a species X. The equilibrium constant K_{eq} is the ratio of the forward and reverse rate constants

$$K_{eq} = \frac{k_+}{k_-} = \frac{[C]^\gamma[D]^\delta}{[A]^\alpha[B]^\beta} \tag{3.5.30}$$

At constant temperature and pressure, the K_{eq} can be related to the standard Gibbs free energy change based on the thermodynamic equilibrium

$$\Delta_r G^0 = -RT \ln K_{eq} \tag{3.5.31}$$

For the equilibrium of a multicomponent and multiphase system, the solution strategy can be based on either independent chemical reactions or independent system components. The phase diagram is a widely used tool for the former, which clearly shows boundary conditions of each distinct component or phase. To depict a phase diagram, the phase rule should be first applied to determine the degree of freedom (*DOF*) of system

$$DOF = N_C - N_P + N_E \tag{3.5.32}$$

where N_C is the number of chemically independent components, N_P is the number of phases, and N_E is the number of external factors, which are typically the temperature and partial pressures.

Fig. 3.5 shows the phase diagram of the Cu–O–H system at 400 K. Lines in the phase diagram represent a two-phase equilibrium, which is determined by two external factors (*DOF* = 2). The A and B in Fig. 3.5 are triple points, in which $Cu_2O/CuO/Cu(OH)_2$ or $Cu/Cu_2O/Cu(OH)_2$ can coexist in a stable equilibrium. In contrast to the two-phase equilibrium, the triple point is only determined by one external factor (*DOF* = 1). Although the phase diagram is simple and explicit, this method is rarely used for studying complex reactions because of a large *DOF* in such systems.
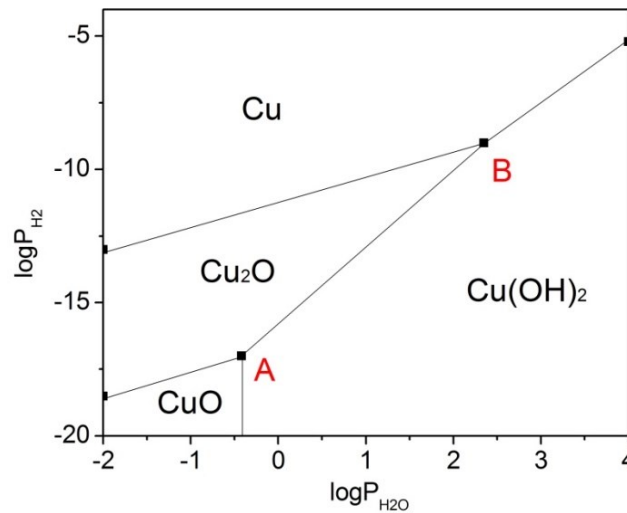

Fig. 3.5 The phase diagram of a Cu–O–H system (400 K) under different partial pressures of H_2 and H_2O. The input thermodynamic data is taken from Ref. [139].

Alternatively, the equilibrium composition of a system can be calculated based on the independent system components using a GEM method [130]. The main advantage of this approach is that it does not require specifying any chemical reactions; it is nevertheless necessary to establish a list of chemical species that are expected to occur in the product mixture. Previously, the GEM method has been successfully applied for the equilibrium prediction of various complex reactive systems, for example, combustion chemistry [131], energy conversion [132, 133], trace element chemistry [134], CVD [105], and so on. However, most of these works were performed using commercial thermochemistry software, such as HSC Chemistry, FactSage or Thermo-Calc. Unfortunately, none of them supports a surface model. Furthermore, thermodynamic data of the Cu beta-diketonate precursors is currently not available in these commercial databases.

In order to predict equilibrium compositions on the Ta(110) and Cu$_2$O(111) substrates, a Langmuir adsorption model was incorporated in the GEM method, allowing the calculation of the chemical potential of surface species. The thermodynamic data of Cu precursors and adsorbed species were calculated by the *ab initio* thermodynamic approach. To simplify the calculation model, the following assumptions have been made:

(1) Each adsorption site can be occupied by only one adsorbate.

(2) The adsorbate prefers to bind to its most stable adsorption site.

(3) The adsorption of large molecules [e.g., Cu(acac)] will lead to the blocking of neighboring adsorption sites due to steric hindrance effects.

(4) The adsorbed species are set as the input for the next half-cycle, whereas the gaseous by-products are completely purged.

(5) The coverage has no influence on the enthalpy and entropy of adsorbed species.

At a given pressure and temperature, the total Gibbs free energy (G_{total}) of the system can be expressed as

$$G_{\text{total}} = \sum_{i=1}^{N} n_i \mu_i \tag{3.5.33}$$

where n_i is the number of moles of the species i, and μ_i the chemical potential. Based on a Langmuir adsorption model, the chemical potential for each gaseous ($\mu_{i,\,\text{gas}}$) and adsorbed species ($\mu_{i,\,\text{ads}}$) can be calculated by following equations

$$\mu_{i,\,\text{gas}} = \mu^0_{i,\,\text{gas}}(T, P^0) + k_\text{B} T \ln(P_i) \tag{3.5.34}$$

$$\mu_{i,\,\text{ads}} = \mu^0_{i,\,\text{ads}}(T, \theta_i) + k_\text{B} T \ln(\theta_i/\theta_\text{free}) \tag{3.5.35}$$

where P_i is the partial pressure of species i, k_B is Boltzmann's constant. The definition of coverage (θ) is the ratio between the number of adsorbates and total adsorption sites ($0 \le \theta \le 1$). The DFT-calculated electronic energies of species in the gas-phase ($E_{i,\,\text{gas}}$) and on the surface ($E_{i,\,\text{ads}}$) at 0 K are set as the reference point

$$\Delta\mu_{i,\,\text{gas}}(T, P^0) = \Delta H_{i,\,\text{gas}}(T, P^0) - TS_{i,\,\text{gas}}(T, P^0) = \mu^0_{i,\,\text{gas}}(T, P^0) - E_{i,\,\text{gas}} \tag{3.5.36}$$

$$\Delta\mu_{i,\,\text{ads}}(T, \theta_i) = \Delta H_{i,\,\text{ads}}(T) - TS_{i,\,\text{ads}}(T) = \mu^0_{i,\,\text{ads}}(T, \theta_i) - E_{i,\,\text{ads}}(\theta_i) \tag{3.5.37}$$

where $\Delta H_{i,\,\text{gas}}$ and $S_{i,\,\text{gas}}$ are the enthalpy and entropy of the gaseous species, respectively. The enthalpy and entropy of the adsorbed species ($\Delta H_{i,\,\text{ads}}$ and $S_{i,\,\text{ads}}$) can be expressed by the following equations

$$\Delta H_{i,\,\text{ads}}(T) = \Delta H_{i+\text{substrate}}(T) - \Delta H_{\text{substrate}}(T) \tag{3.5.38}$$

$$S_{i,\,\text{ads}}(T) = S_{i+\text{substrate}}(T) - S_{\text{substrate}}(T) \tag{3.5.39}$$

where $\Delta H_{\text{substrate}}$ and $\Delta H_{i+\text{substrate}}$ are the enthalpy of the substrate and adsorbate i on it, respectively; $S_{\text{substrate}}$ and $S_{i+\text{substrate}}$ are the entropy of the substrate and adsorbate i on it, respectively. The electronic energy of adsorbed species at given coverage $E_{i,\,\text{ads}}(\theta_i)$ is calculated according to the following equation:

$$E_{i,\,\text{ads}}(\theta_i) = (E_{n \cdot i+\text{substrate}} - E_{\text{substrate}})/n + \sum_{j=1}^{N} E_{i,\,\text{lateral}}(\theta_j) \tag{3.5.40}$$

where $E_{\text{substrate}}$ and $E_{n \cdot i+\text{substrate}}$ are the electronic energies of the substrate and adsorbates n i on it, respectively. An additional term (E_{lateral}) is addressed in order to consider lateral interactions among different co-adsorbed species on the Ta(110) surface

$$E_{i,\,\text{lateral}}(\theta_j) = \left[E_{i,\,\text{ads}}(\theta_j) - E_{i,\,\text{ads}}(\theta_{i,\,\text{low}}) - nE_{j,\,\text{ads}}(\theta_{j,\,\text{low}})\right]/(1 + n) \tag{3.5.41}$$

where $E_{i,\,\text{ads}}(\theta_{i,\,\text{low}})$ is the adsorption energy of species i at a low coverage ($\theta_{i,\,\text{low}} \le 0.1$). $E_{i,\,\text{ads}}(\theta_j)$ can be computed as follows

$$E_{i,\,\text{ads}}(\theta_j) = E_{i+n \cdot j+\text{substrate}} - E_{i,\,\text{gas}} - nE_{j,\,\text{gas}} - E_{\text{substrate}} \tag{3.5.42}$$

where $E_{i+n \cdot j+\text{substrate}}$ is the total electronic energy of adsorbates ($i + nj$) on the substrate. In this model, both the influence of the coverage and the lateral interactions on adsorption energy are

considered. The density of adsorption sites on the $Cu_2O(111)$ surface (6.2 nm^{-2}) is only about half of the value of the Ta(110) surface (12.9 nm^{-2}), which suggests much weaker lateral interactions among co-adsorbed species. Therefore, the $E_{lateral}$ term has been neglected on the $Cu_2O(111)$ surface. By inserting Eq. 3.5.36 and Eq. 3.5.37 into Eq. 3.5.34 and Eq. 3.5.35, respectively, required input data ($\mu_{i,\,gas}$ and $\mu_{i,\,ads}$) for thermodynamic modeling can be obtained

$$\mu_{i,\,gas} = \Delta H_{i,\,gas}(T, P^0) - TS_{i,\,gas}(T, P^0) + E_{i,\,gas} + k_B T \ln(P_i) \tag{3.5.43}$$

$$\mu_{i,\,ads} = \Delta H_{i,\,ads}(T) - TS_{i,\,ads}(T) + E_{i,\,ads}(\theta_i) + k_B T \ln(\theta_i) \tag{3.5.44}$$

The definition of the chemical equilibrium is that G_{total} of the system is minimized. Therefore, the task of equilibrium prediction is to find values of n_i that minimize the objective function given by Eq. 3.5.33, subject to the constraints of elemental mass balance and non-negative definition:

$$\sum_{i=1}^{N} n_i a_{ij} = A_j \tag{3.5.45}$$

$$n_i \geq 0 \tag{3.5.46}$$

where a_{ij} is the number of atoms of jth element present in each species i; A_j is the total number of atoms of jth element in the system. The commonly used method for solving the GEM problem is based on the Lagrange multipliers. By introducing the Lagrange's multipliers (λ_j) to the each restriction, Eq. 3.5.47 can be obtained

$$\sum_{j=1}^{k} \lambda_j \left(\sum_{i=1}^{N} n_i a_{ij} - A_j \right) = 0 \tag{3.5.47}$$

The Lagrange function (L) is composed of the objective function (Eq. 3.5.33) plus restrictions. It can be written as

$$L = \sum_{i=1}^{N} n_i \mu_i + \sum_{j=1}^{k} \lambda_j \left(\sum_{i=1}^{N} n_i a_{ij} - A_j \right) \tag{3.5.48}$$

For L to be an extremum point, the partial derivatives of L with respect to n_i must be zero

$$\frac{\partial L}{\partial n_i} = \mu_i + \sum_{j=1}^{k} \lambda_j a_{ij} = 0 \tag{3.5.49}$$

Eq. 3.5.49 can be formed in terms of a matrix that has i rows, and the problem can be solved using the generalized reduced gradient method.

3.6 Reaction kinetics

One of the most common approaches for modeling the chemical kinetics is transition state theory (TST) [135]. As shown in Fig. 3.6, TST states that the reaction rate is determined by the transition state which lies at the saddle point of a potential energy surface defined as a function of the reaction coordinate. There are two assumptions in TST [135]. First, it supposes that there is a special type of chemical equilibrium (quasi-equilibrium) between the initial and transition states. Secondly, it assumes that continuous transitions from reactant to product are independent, suggesting that each forward transition through the transition-state drives the system from reactant to product. Based on these assumptions, the reactant must overcome an energy barrier on the potential energy surface, preferably at a saddle point where the energy barrier is lowest.

The reaction rate of a reaction can be calculated using the Eyring equation based on statistical mechanics

$$k = \frac{k_B T}{h} \left(\frac{q_{\text{TS}}}{q_{\text{IS}}}\right) e^{-\frac{E_a}{RT}} \tag{3.5.1}$$

The activation energy E_a of the forward reaction is defined as the energy difference (with zero-point energy correction) between the initial and transition state. q_{TS} and q_{IS} are partition functions of the transition and initial states, respectively, which contain vibrational, translational, and rotational contributions (see Section 3.5.1).
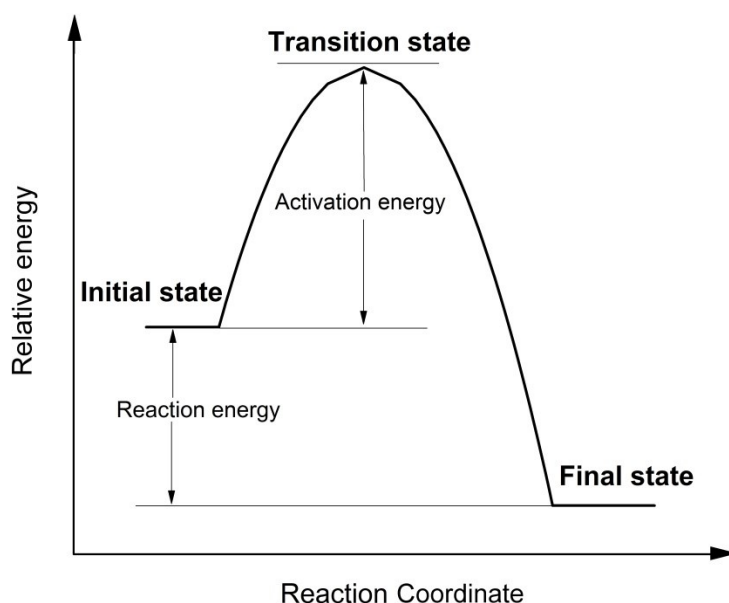

Fig. 3.6 Illustration of the transition state theory.

The central problem for the practical application of TST is the determination of the transition state and the corresponding activation energy. The experimental measurement of the transition state structure is challenging, because of its short lifetime (typically, in order of ps). Therefore, *ab initio* calculations are commonly used as an alternative. The transition state is defined as the state corresponding to the maximum potential energy (saddle point) along the minimum energy path (MEP). After a saddle point has been found, one can follow the gradient of the energy downhill to map out the MEP, connecting the initial and final state as well as the saddle point. Many different methods have been introduced for finding the MEP and the saddle point, based on either the initial state and final state structures, or an initially assumed TS structure. Recent progress in the transition state search based on *ab initio* calculations can be found in Ref. [136].

In this work, the Nudged Elastic Band (NEB) method [137, 138] has been used for investigating the surface dissociation of the Cu precursors. The NEB method is based on building a set of replicas (R) between the initial and final states of a system. As shown in Fig. 3.7, this method works by optimizing a number of intermediate replicas along the reaction path. A spring interaction is applied between neighboring replicas to maintain continuity of the path, thus resembling an elastic band. In the NEB method, the total force $\mathbf{F}_i$ acting on an image is the sum of the spring force $\mathbf{F}_i^{s\parallel}$ along the local tangent and the true force $\mathbf{F}_i^{g\perp}$ perpendicular to the local tangent

$$\mathbf{F}_i = \mathbf{F}_i^{s\parallel} + \mathbf{F}_i^{g\perp} \tag{3.5.3}$$

with

$$\mathbf{F}_i^{s\parallel} = k_s[(\mathbf{R}_{i+1} - \mathbf{R}_i) - (\mathbf{R}_i - \mathbf{R}_{i-1})] \cdot \hat{\boldsymbol{\tau}}_i \hat{\boldsymbol{\tau}}_i \tag{3.5.4}$$

where k_s is the spring constant, $\mathbf{R}_i$ is the coordinates of replica i, and $\hat{\boldsymbol{\tau}}_i$ is the normalized local tangent at replica i. The true force is given by

$$\mathbf{F}_i^{g\perp} = -\nabla V(\mathbf{R}_i) + \nabla V(\mathbf{R}_i) \cdot \hat{\boldsymbol{\tau}}_i \tag{3.5.5}$$

where $\nabla V(\mathbf{R}_i)$ is gradient of the potential at image i. An optimization algorithm is then used to move the replicas according to the force in Eq. 3.5.3. A projected velocity Verlet algorithm is used to make the images converge on the MEP with equal spacing.

While the NEB method can be used for finding the MEP between known reactants and products, the activation energy cannot be directly obtained since the saddle point is not

represented by one specified image. To solve this problem, a modified climbing image NEB (CI-NEB) method can be applied [136]. In this approach, the climbing image (i.e., highest energy image) is driven up to the saddle point, which attempts to maximize its energy along the band, and to minimize it in all other directions. When this image is converged, it will be at the exact saddle point. A comparison of the NEB and CI-NEB calculated reaction pathways is shown in Fig. 3.8.
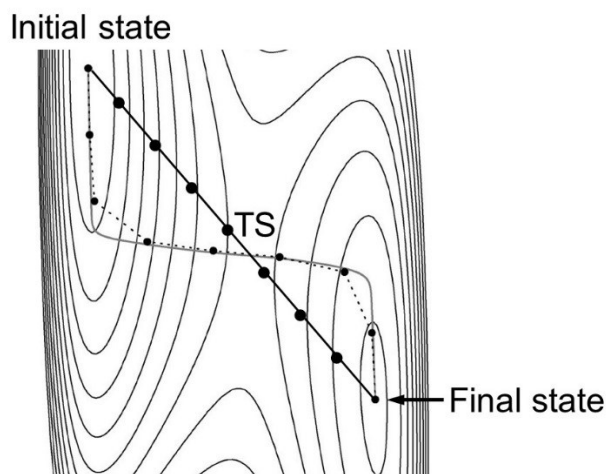

Fig. 3.7 An illustration of the NEB method by using the energy contour of a simple model with two DOF. Reproduced from Ref. [138] with permission from AIP Publishing LLC, copyright 2000. The solid line with larger filled cycles represents an initially guessed MEP that links the initial state and the final state. The dashed curve with small filled cycles denotes the converged MEP pathway obtained by the NEB calculation.
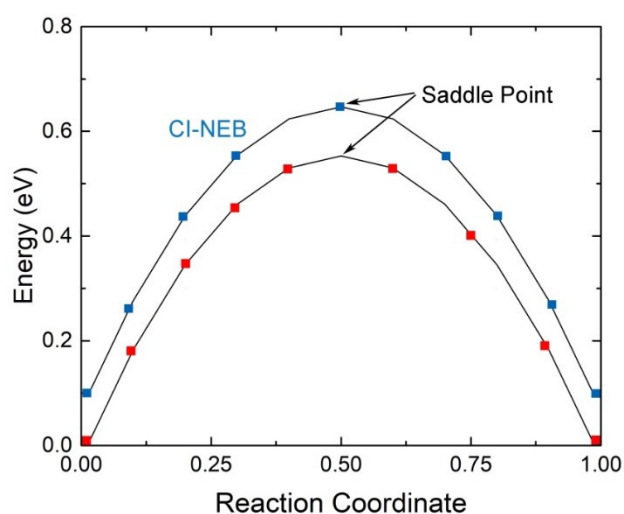

Fig. 3.8 Illustration of the NEB (red) and CI-NEB (blue) calculated reaction pathways. The CI-NEB energies have been shifted by 0.1 eV so that the two curves are distinct.

Table 3.4 Reaction kinetics models used in this study [139].

Reaction models	$f(\alpha)$	$g(\alpha)$
1/2 order	$(1-\alpha)^{0.5}$	$2[1-(1-\alpha)^{0.5}]$
first order	$(1-\alpha)$	$-\ln(1-\alpha)$
3/2 order	$(1-\alpha)^{1.5}$	$2[(1-\alpha)^{-0.5}-1]$
second order	$(1-\alpha)^2$	$(1-\alpha)^{-1}-1$
third order	$(1-\alpha)^3$	$0.5[(1-\alpha)^{-2}-1]$

In experiments, the kinetic parameters (i.e., the kinetic triplet: pre-exponential factor, activation energy, and kinetics model) are commonly derived from the data measured by thermogravimetry [139], differential scanning calorimetry [140], or mass spectroscopy [141]. The reaction rate can be calculated by the following equation

$$\frac{d\alpha}{dt} = k(T)f(\alpha) \tag{3.5.6}$$

where α is the extent of conversion, t is the reaction time, $k(T)$ is the rate constant, and $f(\alpha)$ is the reaction kinetics model. Rearrangement and integration of Eq. 3.5.6 for isothermal conditions give

$$g(\alpha) = k(T)t \tag{3.5.7}$$

where $g(\alpha)$ is the integrated form of the reaction model (see Table 3.4).

The rate constant $k(T)$ at different temperatures is equal to the slope of the straight line obtained by plotting $g(\alpha)$ versus t (Eq. 3.5.7). Finally, the pre-exponential factor (A) and the activation energy E_a are determined using the logarithmic form of the Arrhenius equation by plotting $k(T)$ against $1/T$

$$\ln k(T) = \ln A - \frac{E_a}{RT} \tag{3.5.8}$$

Similar to mass spectroscopy measurements [141], RMD simulations give the quantitative data of the time-dependent species distributions, which can be used for calculating the conversion α. Therefore, the kinetics analysis method used in experiments is also applicable for RMD simulations. In contrast to the CI-NEB approach, the activation energy determined by Eq. 3.5.8 should be viewed as an "apparent" or "global" parameter for the overall process, which consists of a series of elementary reactions.

Chapter 4 Thermodynamic modeling of Cu ALD

Stability and reactivity of the Cu precursors must be well balanced in order to achieve a low-temperature and self-limiting ALD process. In general, the Cu(I) beta-diketonates are more reactive as compared to the Cu(II) beta-diketonates. For example, ALD of copper oxide from Cu(acac)$_2$ requires a strong oxidizing agent (e.g., ozone) and relatively high temperatures (~500 K), whereas with (^{n}Bu$_3$P)$_2$Cu(acac) one can use wet oxygen as a co-reactant at only ~400 K [18, 19]. However, the main limitation of Cu(I) beta-diketonates is that these precursors may easily undergo disproportionation or self-decomposition reactions, defeating the self-limiting nature of ALD processes. So far, the thermostability of the (^{n}Bu$_3$P)$_2$Cu(acac) precursor is rarely systematically investigated. Using XPS characterization, strong disproportionation of (^{n}Bu$_3$P)$_2$Cu(acac) was observed above 200 °C on SiO$_2$ and above 125 °C on Co substrates, respectively [29, 30]. However, the stability of (^{n}Bu$_3$P)$_2$Cu(acac) in the gas-phase and on other substrates is still not clear. In this chapter, the stability of (^{n}Bu$_3$P)$_2$Cu(acac) and Cu(acac)$_2$ is predicted based on *ab initio* thermodynamics calculations. Different substrates with potential applications in interconnect systems are considered. The reaction pathways and the charge transfer states for the surface dissociation of precursors during ALD are also discussed. The GEM method is introduced to calculate the chemical equilibrium between gaseous and adsorbed species of ALD.

4.1 Computational method and model

DFT calculations were performed using the GGA-PBE exchange-correlation potential [109]. The geometric structure and the self-dissociation of Cu precursor molecules were calculated with a cluster model (see Fig. 4.1) using the Dmol3 code [142]. A numerical atomic basis set of double-ζ quality with additional polarization functions was employed. To address relativistic effects, the density functional semicore pseudopotential method [143] was employed for Cu, whereas the P, C, H, and O atoms were treated with an all-electron basis set. The adsorption and the dissociation of precursors on the surface were studied with a periodic model using the Quantum Espresso (QE) package [144]. In the latter case, ultrasoft pseudopotentials [145] with a plane-wave basis set up to a kinetic energy cutoff of 30 Ry (for wave functions) and 240 Ry (for charge density) were used. To investigate the physisorption of Cu precursors on the surface, a nonlocal vdW-DF [110] as implemented in QE was used. Structures were optimized until the total energy changes and all components of all forces are

smaller than 1.26×10^{-4} eV and 2.57×10^{-2} eV/Å, respectively. With the optimized structures, the vibration properties of adsorbed species were calculated using the harmonic approximation based on density-functional perturbation theory. The MEP and the corresponding saddle point were investigated by the CI-NEB method [137, 138]. The charge transfer trends were studied by means of Mulliken population analysis [146] within the plane-wave code CASTEP [147].

AIMD simulations were performed using the QE package in the NVT canonical ensemble (constant number of particles, volume and temperature). A Berendsen thermostat [148] was employed to control the system temperature. The cutoff energies were 25 Ry for wave functions and 200 Ry for charge density, respectively. The time step used in AIMD simulations was 1 fs.

With the target application of seed layers for ULSI damascene metallization in mind, the adsorption of the Cu precursor on Ta(110), Cu(110), Ru(001), Cu_2O(111), hydroxylated SiO_2(001), and N-terminated TaN(111) substrates has been investigated. Only ideal and stoichiometric surfaces were considered in this work in order to simplify calculations. Ta and TaN are liner and diffusion barrier materials used in current interconnect systems, respectively [149]. The Ta-terminated TaN(111) substrate was not considered since its chemical properties are similar to Ta(110). Ru can be used as a candidate for Cu nucleation layers, and it is also a potential component of advanced diffusion barrier systems [150]. SiO_2 is a common substrate used in many experimental ALD studies [19]. Under ambient conditions, the hydroxylated SiO_2 surface is much more stable compared to the dry surface. Cu and Cu_2O are the materials required to be deposited by ALD. Once the initial nucleation has been accomplished, the subsequent layers are needed to be grown on the new Cu or Cu_2O films regardless of the nature of the original substrate.

4.2 Stability of the Cu precursor in the gas-phase

The geometric structures of isolated Cu precursors in the gas-phase are calculated in a first step. The optimized geometry and the structure parameters of $(^nBu_3P)_2Cu(acac)$, $(Me_3P)_2Cu(acac)$, $Cu(acac)_2$, and $^nBu_3P$-ligand are shown in Fig. 4.1 and Table 4.1. A good agreement can be observed between this work and previous theoretical and experimental data [151-153]. The differences are smaller than ± 0.1 Å (or $\pm 3\%$) for bond length and $\pm 2°$ (or $\pm 2\%$) for angles, indicating that the methods are suitable for the simulation of Cu precursors.
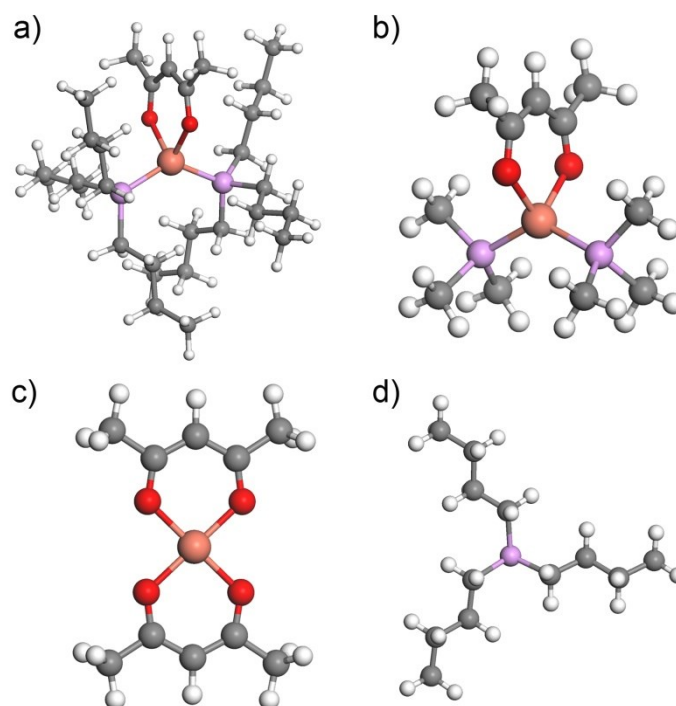
Fig. 4.1 Geometric structures of the precursors (^{n}Bu$_3$P)$_2$Cu(acac) (a), (Me$_3$P)$_2$Cu(acac) (b), Cu(acac)$_2$ (c), and the ^{n}Bu$_3$P-ligand (d). The gray, red, salmon pink, light purple, and white spheres represent C, O, Cu, P, and H atoms, respectively.

Table 4.1 Comparison of structural parameters [bond lengths (Å) and bond angles (°)] of Cu(acac)$_2$, (^{n}Bu$_3$P)$_2$Cu(acac), and ^{n}Bu$_3$P from DFT-calculations and experimental studies.

	Cu(acac)$_2$				(^{n}Bu$_3$P)$_2$Cu(acac)	^{n}Bu$_3$P
	DFT [151]	Exp.[152]	Exp.[153]	This work	This work	This work
Cu–O	1.93	1.91	1.91	1.95	2.09	/
C–O	1.27	1.27	1.27	1.28	1.28	/
C–CH	1.40	1.39	1.40	1.41	1.42	/
C–CH$_3$	1.51	1.48	1.51	1.51	1.52	/
∠Cu–O–C	126.7	125.9	124.8	125.3	123.5	/
∠O–C–CH$_3$	115.8	114.4	115.7	114.8	115.3	/
∠O–C–CH	125.3	124.4	n/a	125.8	126.8	/
∠O–Cu–O	91.9	93.2	92.3	93.4	92.0	/
Cu–P	/	/	/	/	2.23	/
P–C	/	/	/	/	1.86	1.87
CH$_2$–CH$_2$	/	/	/	/	1.53	1.53
∠P–Cu–P	/	/	/	/	139.5	/

n/a: no data is available.

The Mulliken charge and the frontier molecular orbitals of optimized (^{n}Bu$_3$P)$_2$Cu(acac) and Cu(acac)$_2$ are shown in Fig. 4.2. Compared with the Cu(acac)$_2$ precursor, the Mulliken charge of the Cu atom in (^{n}Bu$_3$P)$_2$Cu(acac) is reduced from 1.19 e to 0.79 e, which is in accordance with the shift of its chemical valence. In (^{n}Bu$_3$P)$_2$Cu(acac), the acac-ligand accepts all the charges transferred from the Cu center, whereas the ^{n}Bu$_3$P-ligand is almost electrically neutral. The highest occupied molecular orbital (HOMO) of (^{n}Bu$_3$P)$_2$Cu(acac) is predicted to involve the Cu(acac) part and is particularly localized near the Cu center atom. Thus, as the precursor approaches the surface, a nucleophilic attack through the Cu center onto an electron-deficient adsorption site is possible. However, the HOMO and lowest unoccupied molecular orbital (LUMO) of Cu(acac)$_2$ are spread along the plane of the molecule, implying that both the nucleophilic and electrophilic attacks onto the surface will preferably occur through the acac-ligand of the precursor.
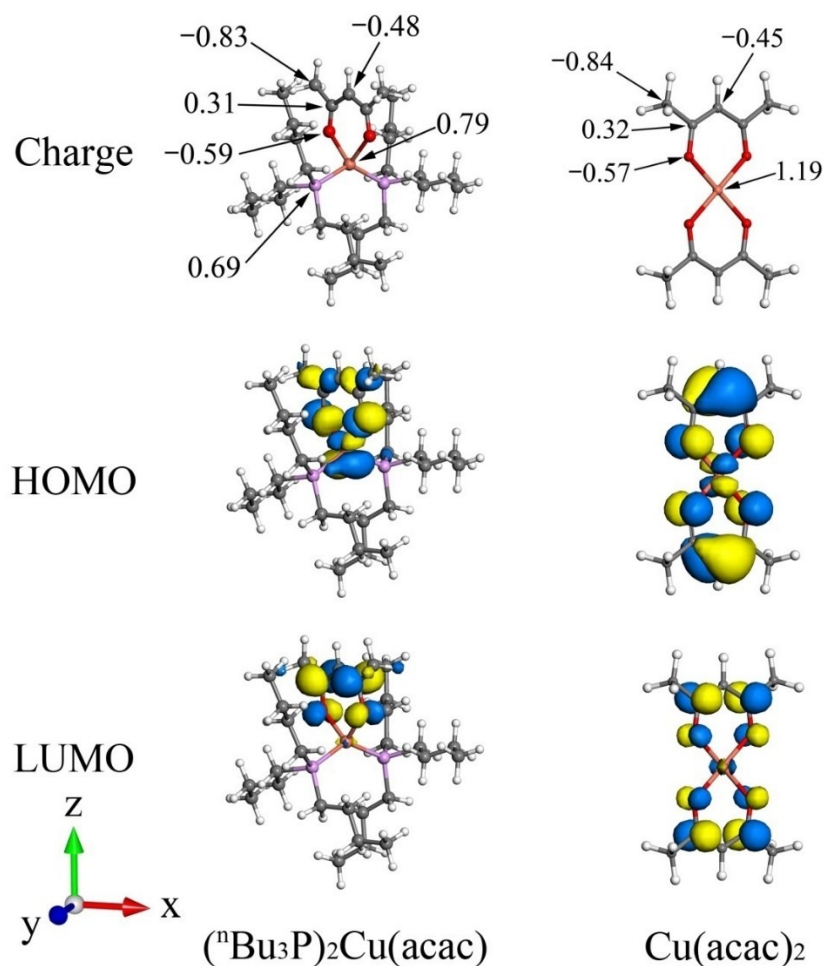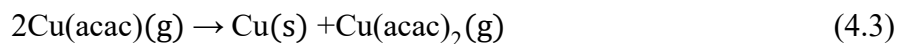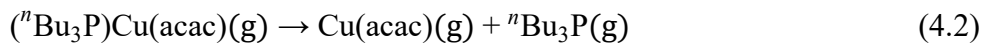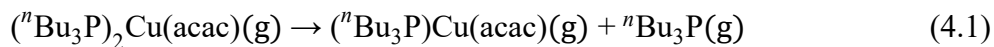

Fig. 4.2 Mulliken charges and frontier molecular orbitals of the (^{n}Bu$_3$P)$_2$Cu(acac) and Cu(acac)$_2$ precursors.

The stability of precursors in the gas-phase is critical for their application, since ALD is a self-limiting process within the ALD window. The $(^nBu_3P)_2Cu(acac)$ precursor may easily undergo the following self-dissociation or disproportionation reactions:

$$(^nBu_3P)_2Cu(acac)(g) \rightarrow (^nBu_3P)Cu(acac)(g) + {^nBu_3P}(g) \tag{4.1}$$

$$(^nBu_3P)Cu(acac)(g) \rightarrow Cu(acac)(g) + {^nBu_3P}(g) \tag{4.2}$$

$$2Cu(acac)(g) \rightarrow Cu(s) + Cu(acac)_2(g) \tag{4.3}$$

For comparison, the self-dissociation of the Cu(II) precursor is also investigated, as shown in reaction (4.4)

$$Cu(acac)_2(g) \rightarrow Cu(acac)(g) + acac(g) \tag{4.4}$$
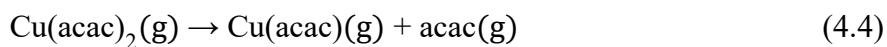
The predicted equilibrium compositions for reactions (4.1)–(4.4) are shown in Fig. 4.3. The total pressure of the system is fixed at 100 Pa, similar to the experimental conditions [19]. As illustrated in Fig. 4.3a, $(^nBu_3P)_2Cu(acac)$ is found to be unstable even at low temperatures, which reveals that the precursor easily releases one of the $^nBu_3P$-ligands in the gas-phase. $(^nBu_3P)_2Cu(acac)$ completely dissociates into $(^nBu_3P)Cu(acac)$ and $^nBu_3P$ above ~375 K. The $(^nBu_3P)Cu(acac)$ precursor exhibits a much higher stability as compared to $(^nBu_3P)_2Cu(acac)$. The decomposition of $(^nBu_3P)Cu(acac)$ starts at temperatures above ~575 K, which is higher than the upper bound of its ALD window (~408 K). The role of the $^nBu_3P$-ligand in Cu(I) beta-diketonate is to prevent the formation of gaseous Cu(acac), avoiding undesired disproportionation reaction. As shown in Fig. 4.3c, once the Cu(acac) complex is dissociated from $(^nBu_3P)Cu(acac)$, it spontaneously disproportionates into metallic Cu and $Cu(acac)_2$, regardless of the system temperature. The $Cu(acac)_2$ precursor is thermally stable within 300–700 K, which meets its application requirements in ALD (Fig. 4.3d).

To reduce computational costs, a simplified Cu(I) beta-diketonate $(Me_3P)_2Cu(acac)$ where the *n*-butyl groups of $(^nBu_3P)_2Cu(acac)$ are replaced by methyl groups, has been used to model the surface reactions. The methyl and *n*-butyl groups have similar chemical properties, and a test study shows that the phosphine-ligand size has a limited effect on the dissociation energies of precursors (see Fig. 4.4). Furthermore, Me_3P is widely used as the Lewis base ligand for the Cu(I) beta-diketonate precursors. The same simplification approach has also been used previously for similar systems [154].
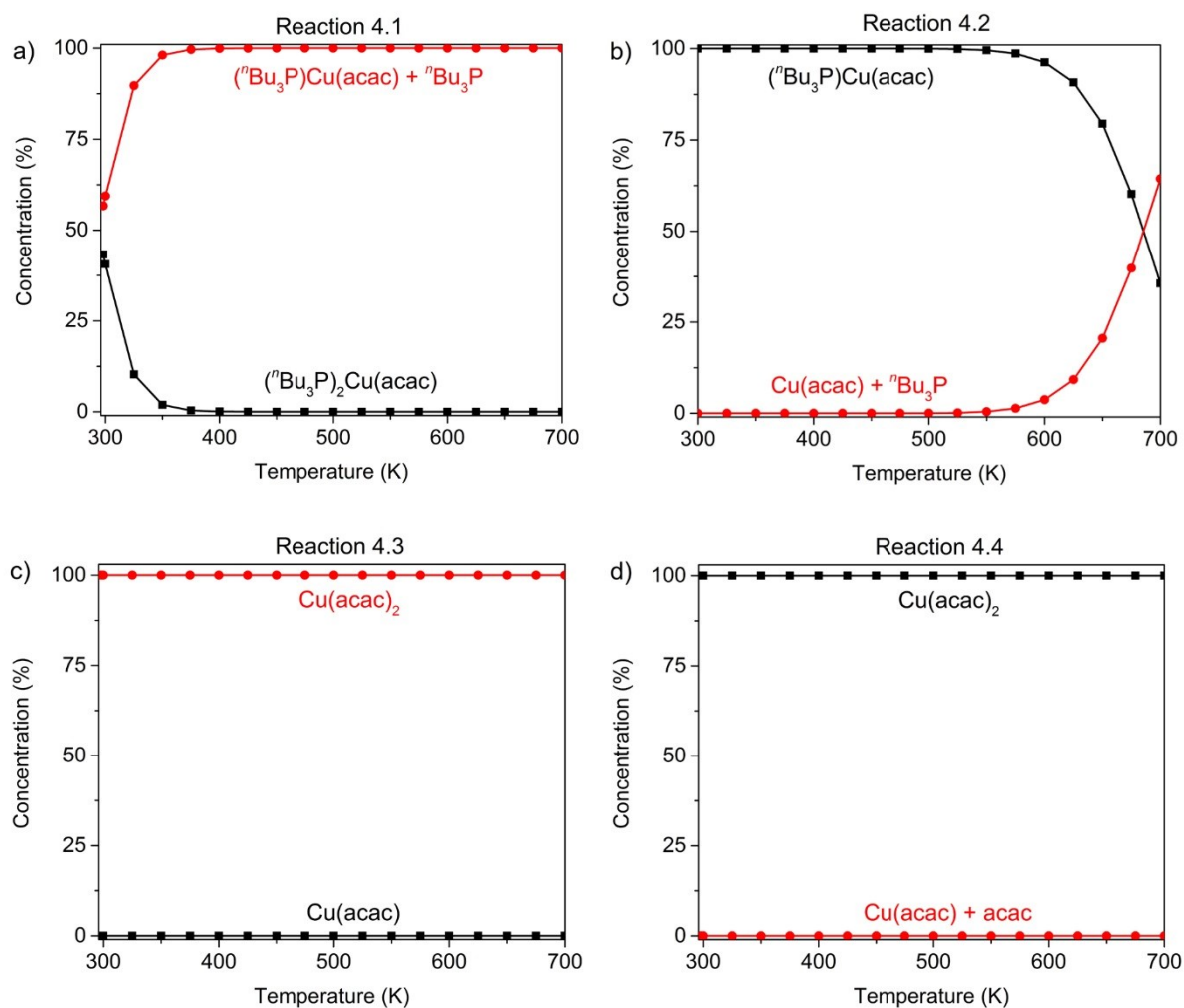
Fig. 4.3 Equilibrium concentrations of reactant (black) and product (red) in the gas-phase at different temperatures. (a)–(d) correspond to reactions (4.1)–(4.4), respectively. ALD windows for the (^{n}Bu$_3$P)$_2$Cu(acac) and Cu(acac)$_2$ precursors are 373–408 K [19] and 423–503 K [18], respectively.
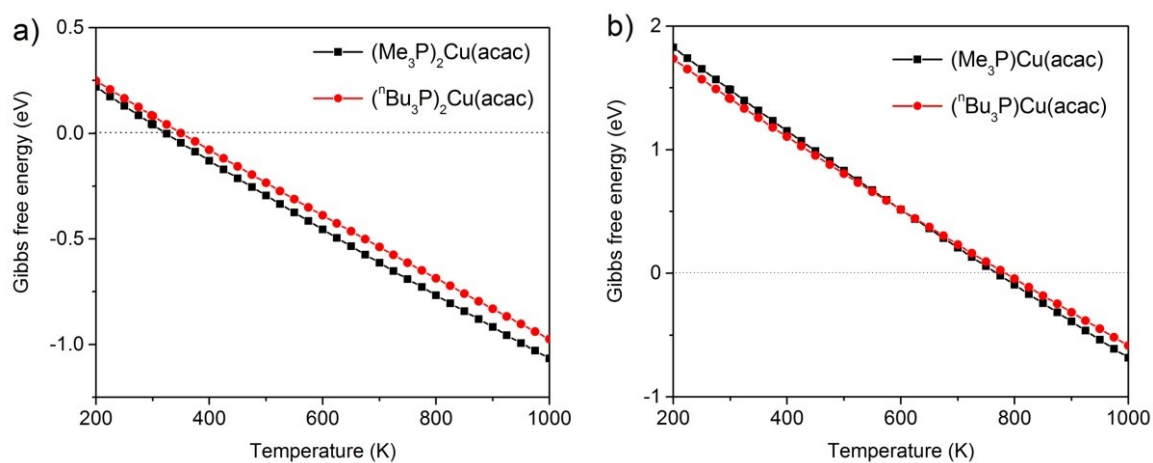
Fig. 4.4 Gibbs free energies for the dissociation of (^{n}Bu$_3$P)$_2$Cu(acac) (a) and (^{n}Bu$_3$P)Cu(acac) (b) at standard pressure. The phosphine-ligand size has a limited effect on the dissociation energies.

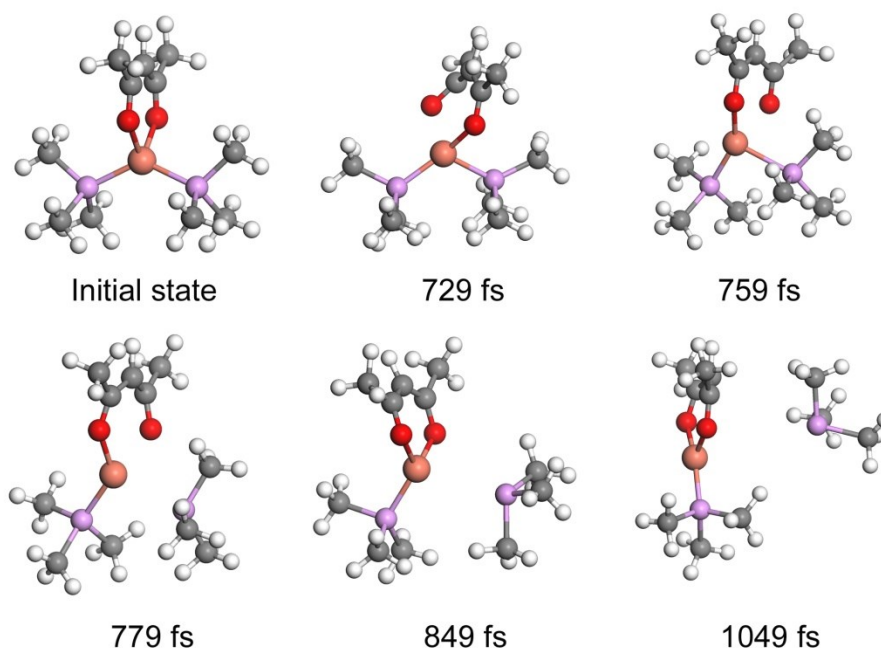**Fig. 4.5** Snapshots of an AIMD simulation for the dissociation of $(Me_3P)_2Cu(acac)$ in the gas-phase at 500 K.

The AIMD simulation provides further details on the stability of the Cu precursor in the gas-phase. The corresponding snapshots of the simulation of $(Me_3P)_2Cu(acac)$ at 500 K are shown in Fig. 4.5. Consistent with the thermodynamic predictions, one of the Me_3P-ligands of $(Me_3P)_2Cu(acac)$ dissociates easily from the Cu precursor (849 fs). However, the remaining $(Me_3P)Cu(acac)$ precursor is found to be stable during the subsequent AIMD simulations. These observations suggest that the strength of the Cu–P bond in $(Me_3P)Cu(acac)$ is much higher than that in $(Me_3P)_2Cu(acac)$.

4.3 Stability of the Cu precursor on different substrates

The chemisorption of a precursor is typically assumed to be the first step of surface reactions within an ALD process. Depending on the substrate properties, the chemisorbed precursor may further undergo decomposition or disproportionation. In this section, the adsorption and dissociation of $(Me_3P)_2Cu(acac)$ and $Cu(acac)_2$ on Ta, Cu, Ru, Cu_2O, SiO_2, and TaN substrates are studied by DFT. Based on the calculated reaction energies and activation energies, the reactivity of different substrates towards precursors can be predicted. The charge transfer between adsorbates and the substrate is studied by Mulliken population analysis. Furthermore, the disproportionation of the $(Me_3P)Cu(acac)$ precursor under different conditions is also discussed.

4.3.1 Adsorption and dissociation of the Cu precursor on Ta(110)

Firstly, the adsorption of (Me$_3$P)$_2$Cu(acac) and Cu(acac)$_2$ as well as their dissociated products on the Ta(110) surface is investigated. The structure of the Ta(110) surface and the corresponding adsorption sites are shown in Fig. 4.6. The selected adsorption structures are depicted in Fig. 4.7. (Me$_3$P)$_2$Cu(acac) favors a perpendicular adsorption geometry to enlarge its projection area on the surface, which leads to enhanced molecule−surface interactions. On the other hand, the Cu(acac)$_2$ and (Me$_3$P)Cu(acac) precursors prefer to adsorb on the Ta surface with a parallel orientation (Figs. 4.7b, c). These adsorption configurations ensure maximum interactions between the planar molecules and a substrate. As listed in Table 4.2, the adsorption energies of (Me$_3$P)$_2$Cu(acac), (Me$_3$P)Cu(acac) (phys.) and Cu(acac)$_2$ calculated by using the PBE functional are only about −0.3 eV. The adsorption site is found to have almost no effect on the adsorption energies. These results, together with the minor role of charge transfer between the adsorbates and the surface (0.10–0.36 e), indicate that the molecule−surface interactions are mostly vdW forces in nature. It is well known that DFT with GGA-functionals like PBE does not capture the vdW forces very well, leading to underestimated adsorption energies [110]. Indeed, larger adsorption energies (about −1.1 eV) are obtained by using the vdW-DF functional (see Table 4.2), suggesting that the vdW forces are the dominant interactions. In order to gain more insight into the role of vdW forces, binding energy curves have been calculated as a function of adsorption distance, as shown in Fig. 4.8. Each point in the graph is obtained by a single-point energy calculation of the optimized structure varying only the distance between the molecule and surface. The minima of the curves in Fig. 4.8 gives the equilibrium adsorption height and energy. It is found that the PBE functional yields a very shallow minimum for the adsorption of (Me$_3$P)Cu(acac) and Cu(acac)$_2$, while the vdW-DF functional produces a much deeper minimum at the adsorption distance of 3.40 Å and 3.72 Å, respectively.
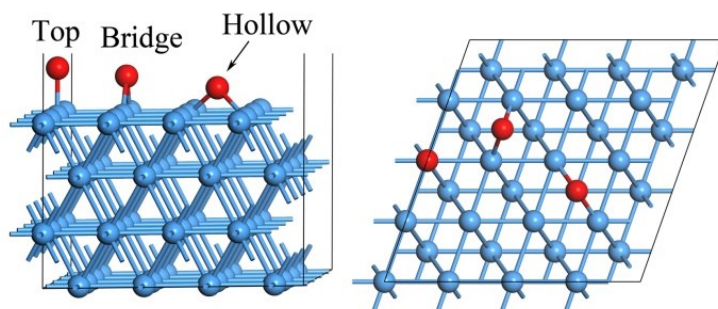

Fig. 4.6 Adsorption sites of species on the Ta(110) surface considered in this work.
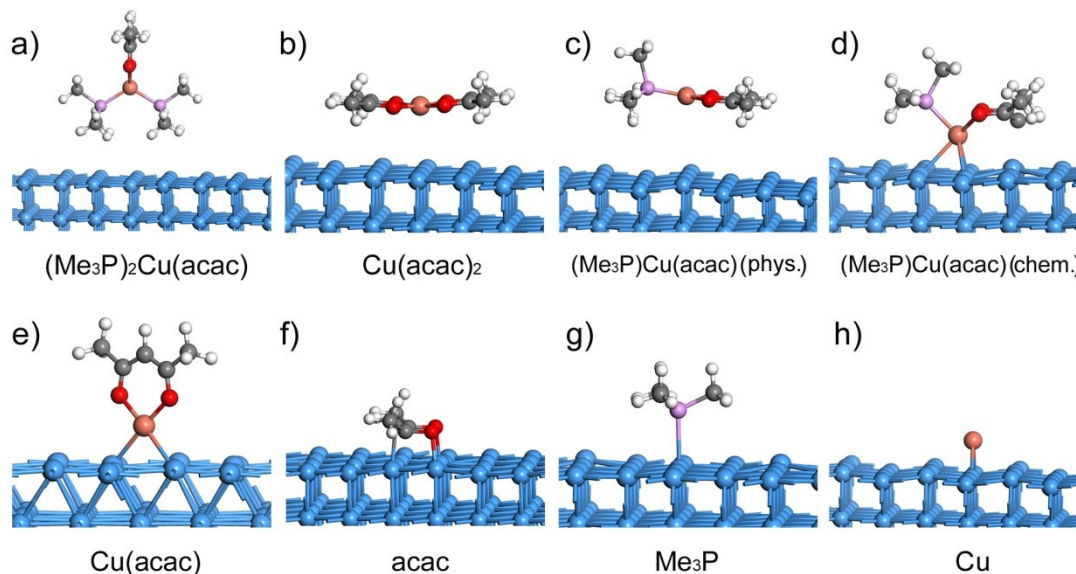
Fig. 4.7 Optimized geometries of different species adsorption on the Ta surface. Phys. and chem. represent the physisorption and chemisorption, respectively.

Table 4.2 Adsorption properties for different species on the Ta(110) surface

Adsorbate	Adsorption mode	Adsorption site	$E_{ads, PBE}$ (eV)	$E_{ads, vdW}$ (eV)	d (Å)	$Q_{ads.}$ (e)
Cu(acac)$_2$	phys.	/	−0.23	−1.21	3.72	−0.36
(Me$_3$P)$_2$Cu(acac)	phys.	/	−0.39	−1.10	3.59	−0.14
(Me$_3$P)Cu(acac)	phys.	/	−0.29	−1.11	3.40	−0.10
	chem.	bridge	−1.61	−2.34	2.53	−0.67
Cu(acac)	chem.	bridge	−2.77	−2.86	2.02	−0.20
Me$_3$P	chem.	top	−1.28	−1.38	2.93	−0.04
acac	chem.	top	−4.24	−4.13	2.17	−1.58
Cu	chem.	bridge	−3.61	−3.13	1.93	0.04

$E_{ads, PBE}$ and $E_{ads, vdW}$ denote the adsorption energies by using the PBE and the vdW-DF functional, respectively. d is the distance between the bottom atom of the adsorbate and the surface calculated by the vdW-DF functional. Q_{ads} is the Mulliken charge of the adsorbate. The adsorption properties of Cu(acac)$_2$ are calculated using a p(5 × 5) Ta surface, while those of other species are calculated using p(4 × 4) Ta surfaces. Only the selected adsorption structures are present here.

Fig. 4.7d shows the structure for the chemisorption of (Me$_3$P)Cu(acac) on the bridge site of Ta(110). The significantly distorted geometry of (Me$_3$P)Cu(acac) deviated from planarity is caused by the interplay between the attractive Cu(acac)–surface interactions and the repulsive Me$_3$P–surface interactions. The PBE and vdW-DF calculated adsorption energy for chemisorbed (Me$_3$P)Cu(acac) are −1.61 eV and −2.34 eV, respectively (see Table 4.2). These values are much larger than the corresponding values for a physisorption mode. The population analysis shows that only a little charge (0.10 e) is transferred from the surface to

physisorbed $(Me_3P)Cu(acac)$. However, once $(Me_3P)Cu(acac)$ is chemisorbed on the Ta surface, more charge (0.67 e) is transferred to the adsorbate. In the case of the $Cu(acac)_2$ precursor, no stable chemisorption structure is obtained on the Ta(110) surface. Once $Cu(acac)_2$ is placed close to the surface ($d_{Cu-Ta} \leq \sim 2.8$ Å), the precursor dissociates spontaneously after ~60 steps of geometric optimization, as shown in Fig. 4.9. $(Me_3P)_2Cu(acac)$ also has no chemisorption configuration, since the Cu center is unable to access the Ta surface.

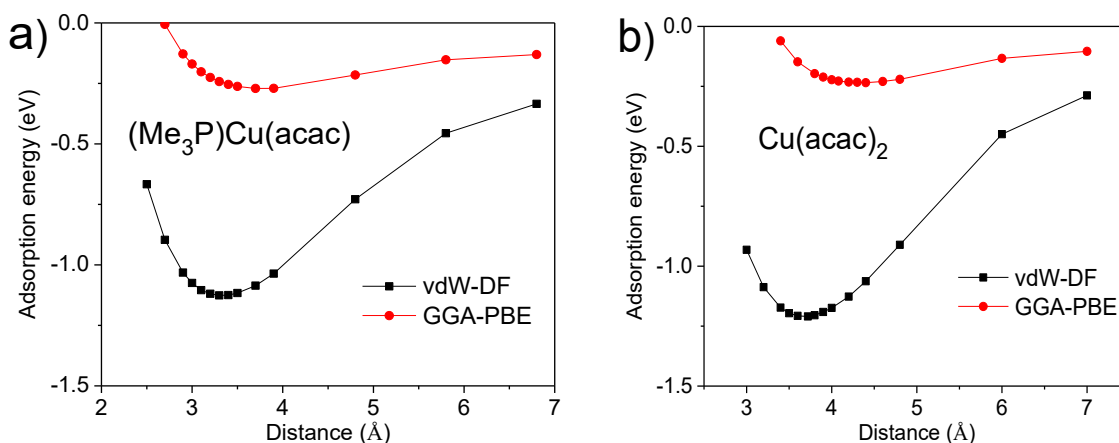**Fig. 4.8** Adsorption energies of $(Me_3P)Cu(acac)$ (a) and $Cu(acac)_2$ (b) on the Ta surface as a function of the adsorption distance. Calculations are performed using the p(4 × 4) Ta surface for $(Me_3P)Cu(acac)$ and p(5 × 5) Ta surface for $Cu(acac)_2$, respectively.

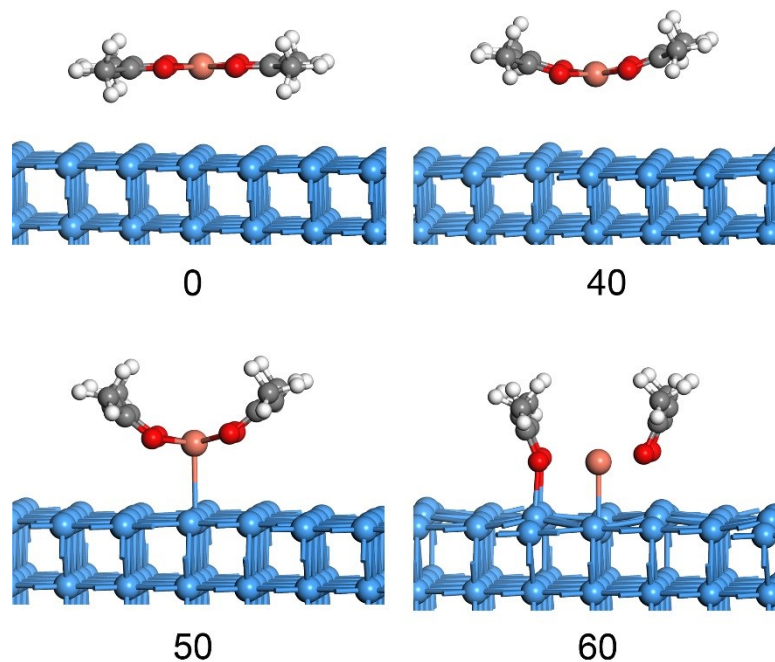**Fig. 4.9** Surface dissociation of $Cu(acac)_2$ during the geometry optimization. Numbers represent the step of the optimization.

As shown in Table 4.2, Cu(acac), Me$_3$P, acac, and Cu species are found to chemisorb on the Ta(110) surface with large binding energies. The most stable adsorption sites are bridge for Cu(acac) ($E_{ads, PBE} = -2.77$ eV) and top for Me$_3$P ($E_{ads, PBE} = -1.28$ eV), respectively. The acac-ligand favors a parallel orientation on Ta(110) with an adsorption energy of -4.24 eV. A significant amount of charge (1.58 e) is transferred from the Ta surface to the acac-ligand because of its unpaired valence electrons.

Reaction pathways and relative energies for the dissociation of (Me$_3$P)$_2$Cu(acac) and Cu(acac)$_2$ on the Ta(110) surface are depicted in Fig. 4.10. The corresponding structures of the transition states TS1–TS3 are shown in Fig. 4.11. The clean Ta(110) surface with a gaseous precursor is selected as the initial state, while Cu(acac) or Cu with the dissociatively co-adsorbed ligands on the surface is set as the final state. In general, the decomposition of Cu beta-diketonates on Ta is a notable exothermic process. The calculated reaction energies for
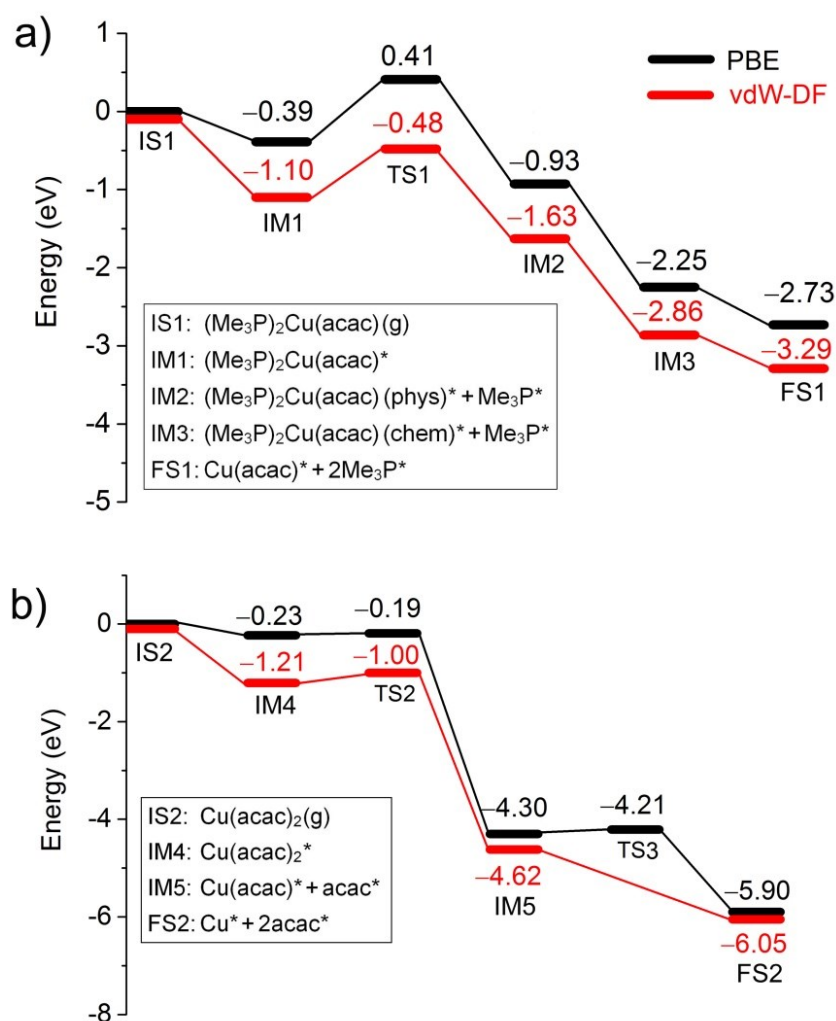

Fig. 4.10 Reaction pathways for the dissociation of (Me$_3$P)$_2$Cu(acac) (a) and Cu(acac)$_2$ (b) on the Ta(110) surface. IS, TS, IM, and FS represent the initial state, transition state, intermediate state, and final state, respectively.
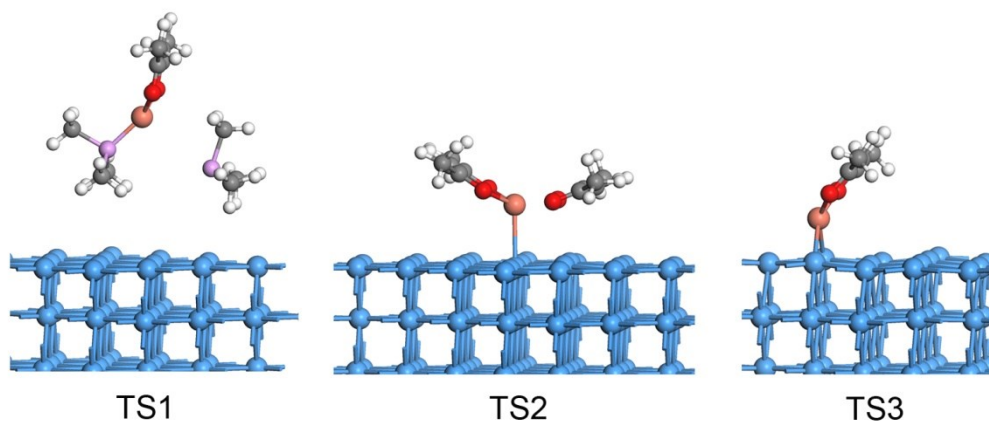
Fig. 4.11 Structures of the transition states denoted in Fig. 4.10 for the decomposition of $(Me_3P)_2Cu(acac)$ and $Cu(acac)_2$ on the Ta(110) surface.

$(Me_3P)_2Cu(acac)$ and $Cu(acac)_2$ using the vdW-DF functional are -3.29 eV and -6.05 eV, respectively. As compared to the PBE results (-2.73 eV and -5.90 eV), the vdW forces affect the reaction energy of $(Me_3P)_2Cu(acac)$, but their influence on that of $Cu(acac)_2$ is minor. The surface dissociation of $(Me_3P)_2Cu(acac)$ into $(Me_3P)Cu(acac) + Me_3P$ requires overcoming a relatively large barrier (0.80 eV for PBE), which is a slow process under low temperatures (~400 K). In contrast, thermodynamic analysis and AIMD simulations (section 4.2) reveal that the gas-phase dissociation of $(Me_3P)_2Cu(acac)$ is favourable under ALD conditions. Therefore, it can be concluded that the first dissociation step of $(Me_3P)_2Cu(acac)$ (Eq. 4.1) is more favorable to occur in the gas-phase rather than on the surface. For $(Me_3P)Cu(acac)$, no significant energy barrier is observed for the transformation of physisorbed to chemisorbed state. The decomposition of $(Me_3P)Cu(acac)$ as well as $Cu(acac)_2$ and $Cu(acac)$ on the Ta surface is a facile process. The calculated activation energies are below ~0.2 eV, which are close to or below the accuracy limit of the DFT-NEB calculations.

The population analysis for the dissociation of $(Me_3P)_2Cu(acac)$ and $Cu(acac)_2$ on Ta(110) is summarized in Fig. 4.12. It is found that a large amount of charge is transferred from the surface to the adsorbates. Both the Cu center and the acac-ligand are reduced upon the dissociative adsorption of precursors. A zero-valence metallic Cu atom is finally formed on the Ta surface. On the other hand, there is a minor change of the charge of the Me_3P-ligand.

In principle, the ligands are used to volatilize the metal atoms. Thus the ligands are expected to remain intact upon adsorption and will be removed by co-reactants (e.g. hydrogen or oxygen) during the subsequent ALD half-cycle [31]. Table 4.3 lists the DFT calculated
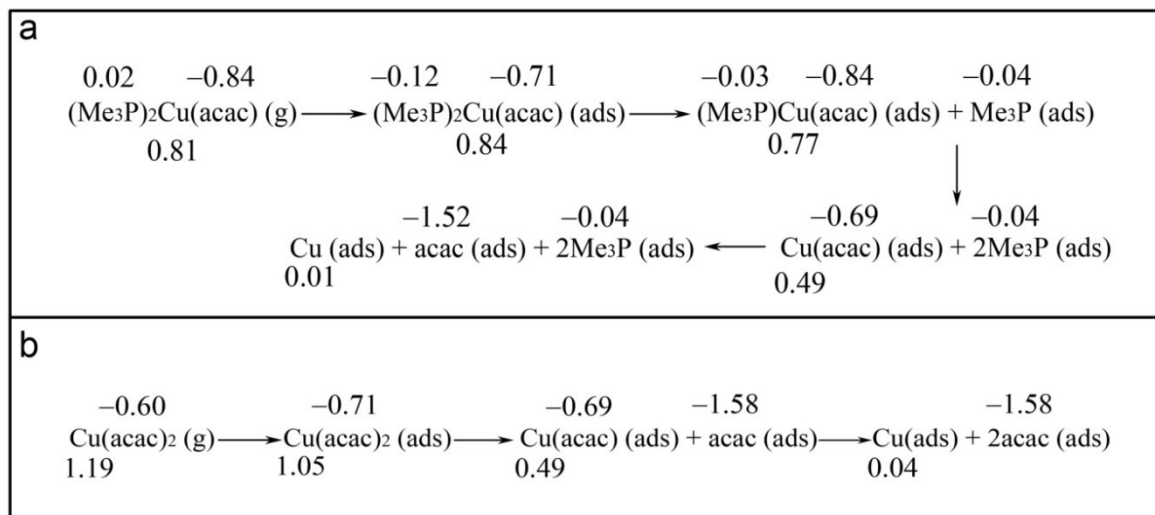
Fig. 4.12 Charges analysis for the adsorption and decomposition of (Me₃P)₂Cu(acac) (a) and Cu(acac)₂ (b) on the Ta(110) surface. The numbers represent the Mulliken charges of Cu atom, acac- and Me₃P-ligands.

Table 4.3 DFT-PBE calculated reaction energies for the dissociation of the acac- and Me₃P-ligands on Ta(110) and Cu(110) surfaces

Reactions		Ta(110)	Cu(110)
$acac^* \rightarrow CH_3CO^* + CH_3COCH^*$	(4.5)	−1.73	1.69
$acac^* \rightarrow CH_3^* + CH_3COCHCO^*$	(4.6)	1.90	2.14
$acac^* \rightarrow 2CH_3CO^* + CH^*$	(4.7)	−2.66	3.03
$acac^* \rightarrow CH_3^* + CO^* + CH_3COCH^*$	(4.8)	−0.99	2.01
$acac^* \rightarrow 2CH_3^* + 2CO^* + CH^*$	(4.9)	−1.19	3.66
$Me_3P^* \rightarrow P^* + 3Me^*$	(4.10)	−2.55	1.67

reaction energies for the surface decomposition of the acac- and Me₃P-ligands (Eqs. 4.5–4.10). Unexpectedly, both the acac- and Me₃P-ligands are prone to decompose on the Ta(110) surface via different pathways. These reactions destroy the self-limitation properties of ALD and provide a channel for carbon contamination.

4.3.2 Adsorption and dissociation of the Cu precursor on Cu(110)

The structure of the Cu(110) surface and the corresponding adsorption sites are shown in Fig. 4.13. The adsorption energies and structures of the Cu precursors and the dissociation products are presented in Table 4.4 and Fig. 4.14. The (Me₃P)₂Cu(acac) precursor is not investigated since under ALD conditions it prefers to decompose into (Me₃P)Cu(acac) and Me₃P in the gas-phase (see Section 4.2). As shown in Table 4.4, the most stable adsorption site for (Me₃P)Cu(acac) and Cu(acac)₂ is a hollow site, with $E_{ads, vdW}$ of −1.85 eV and

−2.16 eV, respectively. As compared to the PBE results (−1.38 eV and −1.51 eV), the vdW forces contribute additional ~0.6 eV to the adsorption energies. Both (Me$_3$P)Cu(acac) and Cu(acac)$_2$ are significantly distorted from planarity due to the repulsive interactions between the H atoms and the Cu surface (see Figs. 4.14b, d). New Cu–O bonds are formed between surface Cu atoms and the O atoms of an acac-ligand, with a bond length of ~2.1 Å. However, the bond length of the original Cu–O bond of Cu precursors is increased by ~0.25 Å upon surface adsorption, which reflects a weakening of its bond strength. The adsorption of (Me$_3$P)Cu(acac) and Cu(acac)$_2$ on a top site is much weaker than that on a hollow site, with $E_{ads, PBE}$ of about −0.5 eV (Table 4.4). As shown in Figs. 4.14a, c, the geometric structures of adsorbed (Me$_3$P)Cu(acac) and Cu(acac)$_2$ are only slightly changed compared to those of gaseous precursors.
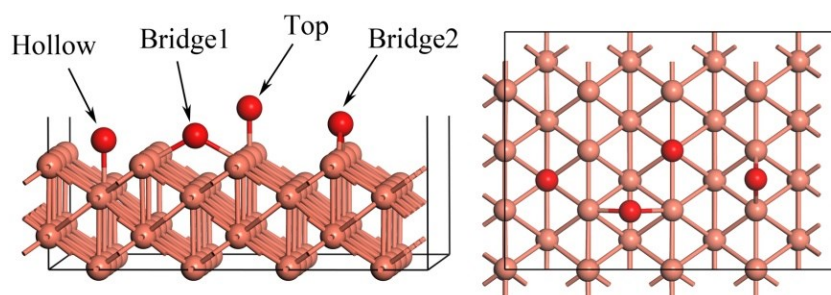

Fig. 4.13 Adsorption sites of species on the Cu(110) surface considered in this work.
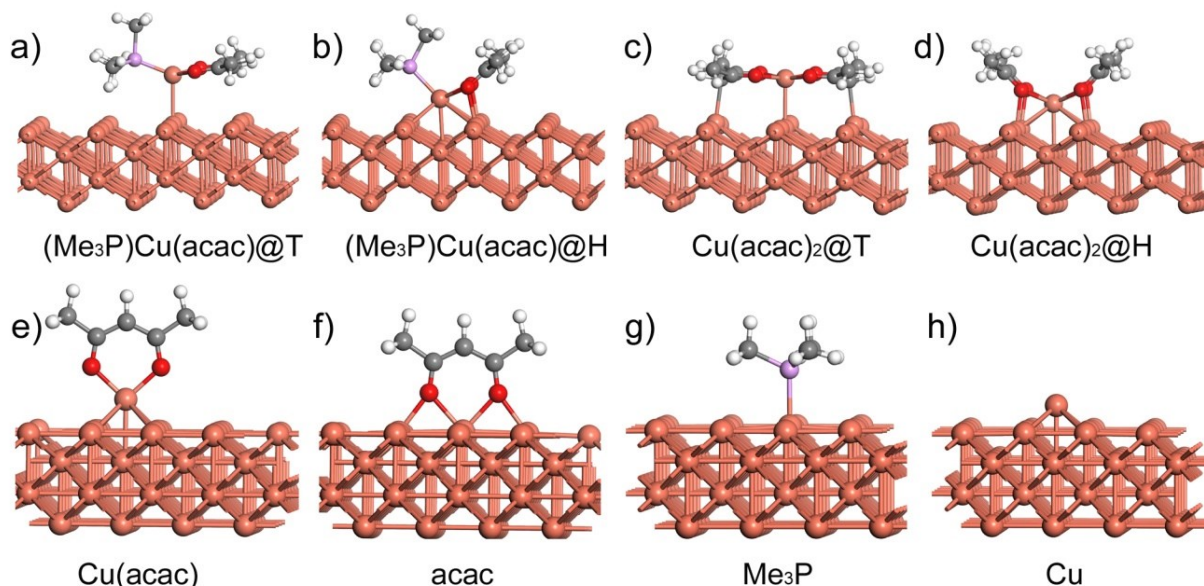

Fig. 4.14 Optimized geometries of different adsorbed species on the Cu(110) surface calculated by the DFT-PBE functional. T and H represent the top and hollow sites, respectively.

Table 4.4 Adsorption properties for different species on Cu(110) surface

	Cu(acac)$_2$		(Me$_3$P)Cu(acac)		Cu(acac)	Me$_3$P	acac	Cu
Adsorption site	top	hollow	top	hollow	hollow	top	top	hollow
$E_{ads, PBE}$ (eV)	−0.48	−1.51	−0.47	−1.38	−2.16	−1.13	−2.68	−3.08
$E_{ads, vdW}$ (eV)	−1.42	−2.16	−1.10	−1.85	−2.08	−1.32	−2.89	−2.81
d(Cu$_p$–Cu$_s$) (Å)	2.65	2.63	2.79	2.59	2.62	/	/	2.53
d(Cu$_p$–O) (Å)	2.04	2.21	2.05	2.22	2.00	/	/	/
d(Cu$_s$–O) (Å)	3.45	2.07	3.33	2.09	3.28	/	2.01	/
d(P–Cu$_s$) (Å)	/	/	4.26	3.38	/	2.29	/	/
Q_{abs} (e)	−0.92	−0.97	−0.70	−0.56	−0.20	−0.14	−0.66	0.08

d(Cu$_p$–Cu$_s$) is the distance between the Cu atom of precursor and nearest surface Cu atom. d(Cu$_p$–O) stands for the distance between the Cu and O atoms of precursor. d(Cu$_s$–O) represents the distance between the O atom of precursor or acac-ligand and nearest surface Cu atom.

Both Cu(acac) and acac prefer to adsorb with the molecular plane being perpendicular to the Cu surface (Figs. 4.14e, f). As shown in Table 4.4, the most stable adsorption sites are a hollow site for Cu(acac) ($E_{ads, PBE}$ = −2.16 eV) and a top site for acac ($E_{ads, PBE}$ = −2.68 eV), respectively. The Cu atom prefers to adsorb on a hollow site, with a binding energy of −3.08 eV for the PBE functional. The vdW forces have no significant influence on the adsorption energies of Cu(acac), acac, and Cu species because the dominant contribution to interactions originates from the chemical bonding.

In order to demonstrate the validity of the calculation results, vibrational frequency calculations have been performed and compared to experimental findings. As shown in Table 4.5, the key vibrational frequencies of Cu(acac)$_2$ calculated by DFT agree well with those obtained in Ref. [156]. Furthermore, the most preferred adsorption geometry of acac reported in this work (Figs. 4.14e), has been confirmed by previous vibrational spectroscopy studies [155]. The vibrational frequencies of adsorbed Cu(acac) and acac are very close to those of a gaseous Cu(acac)$_2$. In contrast, the CO stretch frequency of adsorbed Cu(acac)$_2$ is shifted from 1556 cm^{-1} to 1507 cm^{-1} relative to the gaseous Cu(acac)$_2$. This is consistent with a parallel adsorption geometry causing a distorted molecular structure on the surface.

Once the preferred adsorption geometries have been determined for the different species, the minimum energy pathways for the dissociation of (Me$_3$P)Cu(acac) and Cu(acac)$_2$ on the

Table 4.5 Calculated and measured vibrational frequencies (cm^{-1}) of different species adsorbed on the Cu surface and in the gas-phase.

Cu(acac)$_2$/Cu(110)	Cu(acac)/Cu(110)	acac/Cu(110)	Cu(acac)$_2$	acac/Cu(001)	Cu(acac)$_2$	Assignments
		This work		Ref.[155]	Ref.[156]	
3060	3059	3077	3090	3092	3077	Methyne CH stretch
1507	1556	1543	1556	1563	1554	CO stretch
1442	1450	1439	1434	1430	1415	CH$_3$ deg. def.
1367	1378	1374	1355		1356	CH$_3$ sym. def.
1238	1238	1247	1249		1274	CC + CCH$_3$ stretch
1160	1199	1201	1172		1190	CH bending
1043	1035	1046	1023	1024	1020	CH$_3$ rock

Only the key vibrational frequencies are shown in Table 4.5. The frequencies of acac/Cu(001) are very similar to those of acac/Cu(110), indicating that the orientation of the Cu surface has a minor effect on the normal modes of the acac-ligand.

Cu surface are mapped out using the CI-NEB method, as depicted in Fig. 4.15. The clean Cu(110) surface with a gaseous precursor is selected as the reference state. As shown in Fig. 4.15, the dissociation of both (Me$_3$P)Cu(acac) and Cu(acac)$_2$ is an exothermic process. The calculated reaction energies for dissociation of Cu(acac)$_2$ and (Me$_3$P)Cu(acac) are -1.59 eV and -2.10 eV with PBE, respectively. The vdW-DF functional predicts larger reaction energies of -2.09 eV and -2.61 eV, respectively. (Me$_3$P)Cu(acac) and Cu(acac)$_2$ can easily diffuse from a top site to the nearby lowest energy hollow site, without any significant energy barrier. The dissociation of the Me$_3$P-ligand from (Me$_3$P)Cu(acac) requires overcoming an energy barrier of 0.68 eV (by vdW-DF). On the other hand, the barrier for the dissociation of the acac-ligand from Cu(acac)$_2$ is smaller (0.48 eV by vdW-DF). At the transition state, the acac-ligand is located above a hollow site, with two oxygen atoms bind to the adjacent surface Cu atoms (Fig. 4.16). The activation energy for the decomposition of Cu(acac) is similar to that of Cu(acac)$_2$ (0.50 eV vs. 0.48 eV). Again, the acac-ligand at the transition state is positioned above a hollow site (Fig. 4.16). As compared with the Ta(110) surface, the dissociation of Cu precursors on the Cu(110) surface exhibits much lower reaction energies and much larger activation energies. This result indicates that the Cu(110) surface is less reactive towards Cu precursors than the Ta(110) surface.

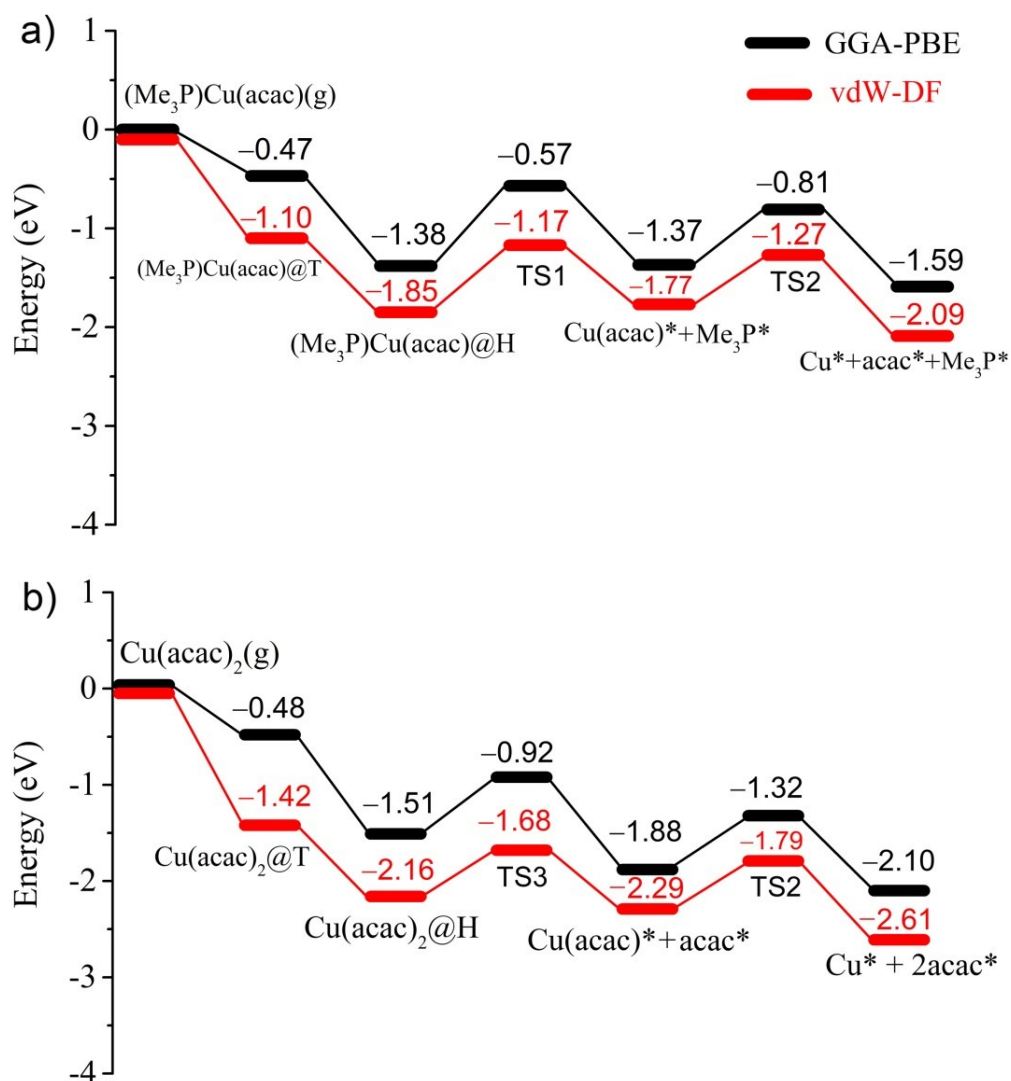**Fig. 4.15** Energy profile of the dissociation processes of (Me₃P)Cu(acac) (a) and Cu(acac)₂ (b) on the Cu(110) surface.
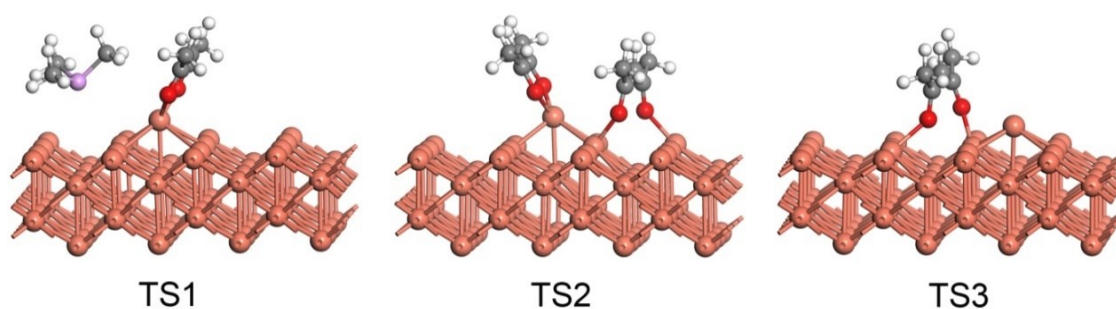
Fig. 4.16 Structures of the transition states denoted in Fig. 4.15 for the decomposition of (Me₃P)Cu(acac) and Cu(acac)₂ on the Cu(110) surface.
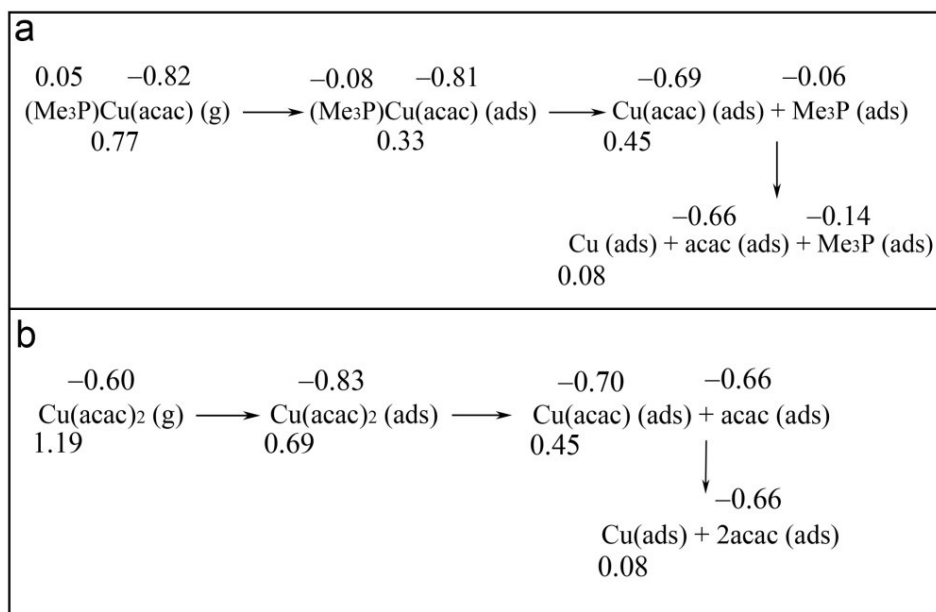
Fig. 4.17 Charges analysis for the adsorption and decomposition of (Me$_3$P)Cu(acac) (a) and Cu(acac)$_2$ (b) on the Cu(110) surface. The numbers represent the Mulliken charges of the Cu atom, the acac- and the Me$_3$P-ligands.

The population analysis shown in Fig. 4.17 suggests that the surface dissociation of (Me$_3$P)Cu(acac) and Cu(acac)$_2$ would lead to a sequential reduction of the Cu center. Eventually, a zero-valence metallic Cu atom is formed on the Cu surface. On the other hand, there are only small changes of the charge of the acac- and Me$_3$P-ligands, suggesting that the metallic substrate is responsible for the reduction of the Cu center. In short, DFT calculations reveal a sequential dissociation and reduction of the Cu precursors on the Cu(110) surface [Cu(acac)$_2$→Cu(acac)→Cu; (Me$_3$P)Cu(acac)→Cu(acac)→Cu].

Table 4.3 shows the reaction energies for the further decomposition of acac- and Me$_3$P-ligands on the Cu(110) surface. In contrast to the Ta surface, large positive energies reveal that the ligand-decomposition on Cu is unfavorable. Thus, the adsorbed acac- and Me$_3$P-ligands may block surface sites and prevent the further adsorption of Cu precursors, and therefore the deposition is self-limiting.

4.3.3 Adsorption of the Cu precursor on Ru(001), Cu$_2$O(111), SiO$_2$(001), TaN(111)

Table 4.6 shows the calculated adsorption energies and bond lengths of different species on the substrates Ru(001), Cu$_2$O(111), hydroxylated SiO$_2$(001), and N-terminated TaN(111). The corresponding adsorption structures and adsorption sites are shown in Figs. 4.18–4.25.

Table 4.6 Adsorption energy and distance of Cu precursor and its dissociation products on different substrates.

Adsorbate	Ru(001)		Cu$_2$O(111)		SiO$_2$(001)		TaN(111)	
	E_{ads} (eV)	d (Å)	E_{ads} (eV)	d (Å)	E_{ads} (eV)	d (Å)	E_{ads} (eV)	d (Å)
(Me$_3$P)Cu(acac)	−1.88	2.56	−1.29	2.14	−0.30	2.98	−0.52	2.89
Cu(acac)	−2.38	2.56	−1.06	1.92	−1.01	1.99	−1.50	1.89
acac	−2.75	2.12	−2.38	2.03	/	/	−0.04	3.59
Cu	−3.20	2.54	−1.14	1.87	−0.66	1.96	−2.40	2.03
Me$_3$P	−1.91	2.35	−2.18	2.17	−0.51	2.26	−0.09	3.33
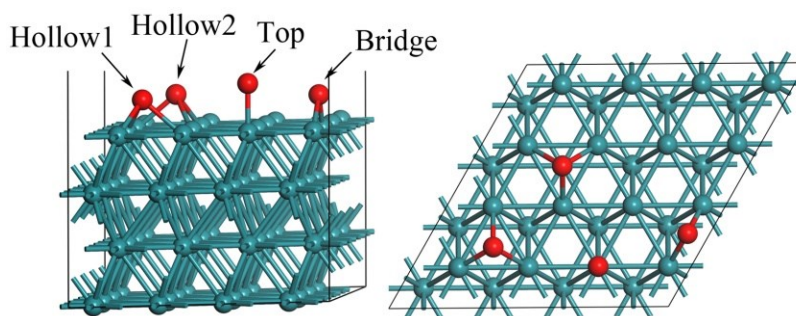
Fig. 4.18 Adsorption sites of species on the Ru(001) surface considered in this work.
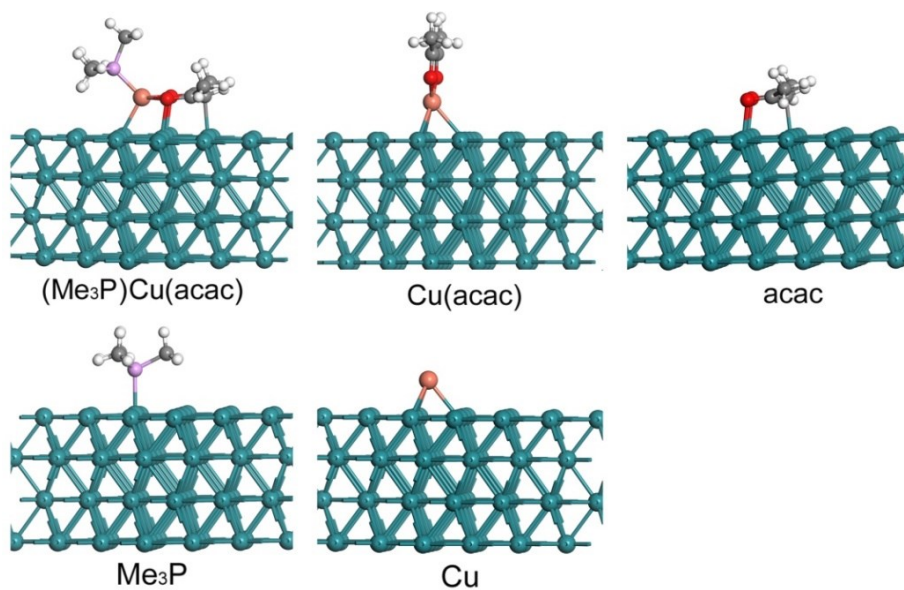
Fig. 4.19 Optimized geometries of different adsorbed species on the Ru(001) surface calculated by the DFT-PBE functional.

As illustrated in Fig. 4.19, (Me$_3$P)Cu(acac) prefers to adsorb on the Ru(001) surface by locating its central Cu atom on a hollow site. The calculated adsorption energy by the PBE functional is −1.88 eV (Table 4.6). Aside from the Cu–Ru bonds, additional C–Ru (2.28 Å) and O–Ru (2.21 Å) bonds are also formed. These bonds may be responsible for a larger

adsorption energy of (Me₃P)Cu(acac) on Ru as compared to that on Ta (−1.61 eV) or Cu (−1.38 eV). The Cu(acac) and Cu species are also in favor of a hollow site, with adsorption energies of −2.38 eV and −3.20 eV, respectively. The acac-ligand prefers to bind to the Ru surface with a parallel geometry, which is similar to acac/Ta(110) but its adsorption energy is much smaller (−2.75 eV vs. −4.24 eV). The Me₃P-ligand favors binding to a top site with an adsorption energy of −1.91 eV and a bond length of 2.35 Å.

As shown in Table 4.6, the adsorption energies of species on the Cu₂O(111) surface are smaller than those on metallic surfaces, with the only exception of the adsorbate Me₃P. Previous *in situ* XPS studies [29] showed that a large amount of P and C impurities (1.8% and 21.4%) are present on the Cu₂O surface after 500 ALD cycles. The authors speculated that the contaminants could be due to either re-adsorption of released ^{n}Bu₃P-ligands on the substrate or a high chemisorption probability of these ligands on Cu₂O. This hypothesis can be supported by the DFT calculation results, which show that the Me₃P-ligand strongly binds to the Cu₂O surface with a large E_{ads} of −2.18 eV.
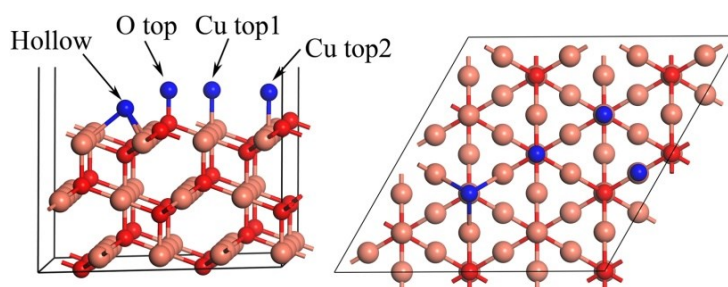
Fig. 4.20 Adsorption sites of species on the Cu₂O(111) surface considered in this work.

Fig. 4.21 Optimized geometries of different adsorbed species on the Cu₂O(111) surface calculated by the DFT-PBE functional.

The most stable adsorbate on the $SiO_2(001)$ surface is Cu(acac), with an adsorption energy of -1.01 eV (see Table 4.6). $(Me_3P)Cu(acac)$ is found to physisorb weakly on SiO_2 ($E_{ads} = -0.30$ eV). Unlike other substrates, the adsorption energy of atomic Cu on SiO_2 is as low as -0.66 eV. This may be caused by the termination of hydrogen on SiO_2, which reduces the reactivity of the surface. It should be noticed that no stable structures are obtained for the adsorption of the acac-ligand. The geometry optimization cannot achieve the required convergence since acac easily reacts with surface H to form H(acac), which is released into the gas-phase. Binding of the Me_3P-ligand on the $SiO_2(001)$ surface is provided through a hydrogen bond. The calculated adsorption energy is only -0.51 eV, indicating a weak interaction between the Me_3P-ligand and the SiO_2 surface. This result is in agreement with the previous *in situ* XPS study [29], which suggested that no $^nBu_3P$-ligand is deposited on the SiO_2 substrate during the $(^nBu_3P)_2Cu(acac)$ precursor pulse.
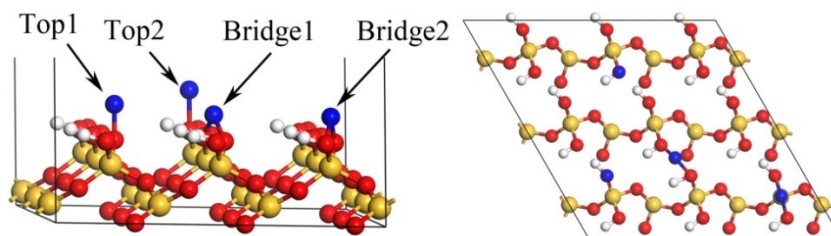
Fig. 4.22 Adsorption sites of species on the hydroxylated $SiO_2(001)$ surface.
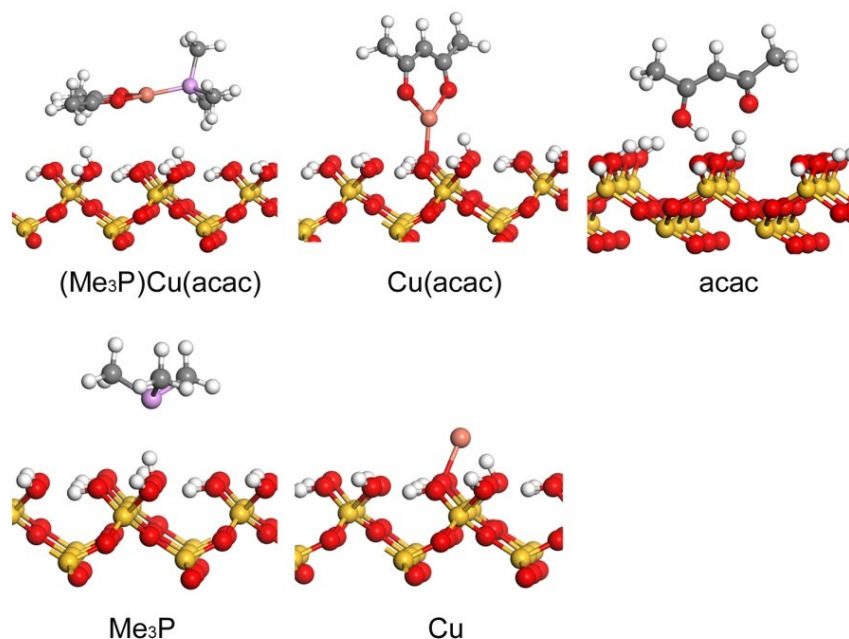
Fig. 4.23 Optimized geometries of different adsorbed species on the hydroxylated $SiO_2(001)$ surface calculated by the DFT-PBE functional.

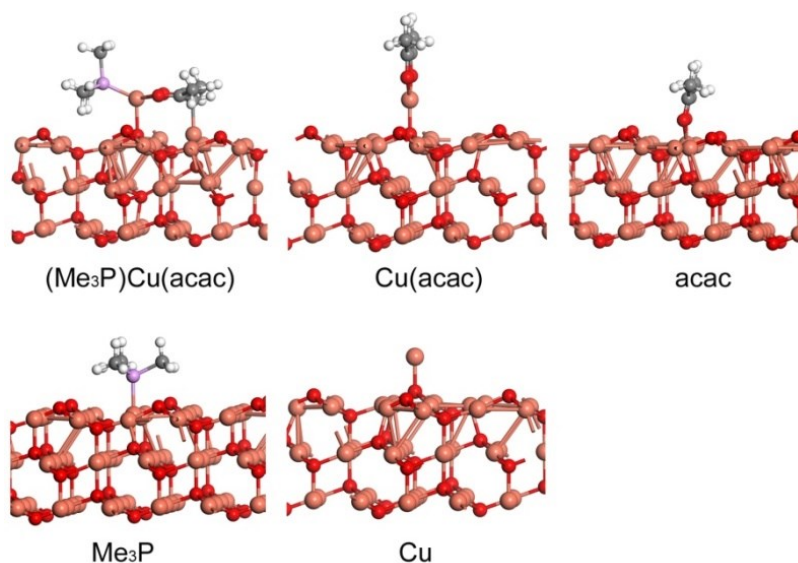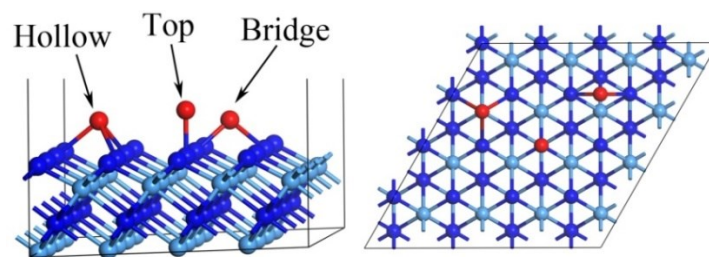**Fig. 4.24** Adsorption sites of species on the N-terminated TaN(111) surface.
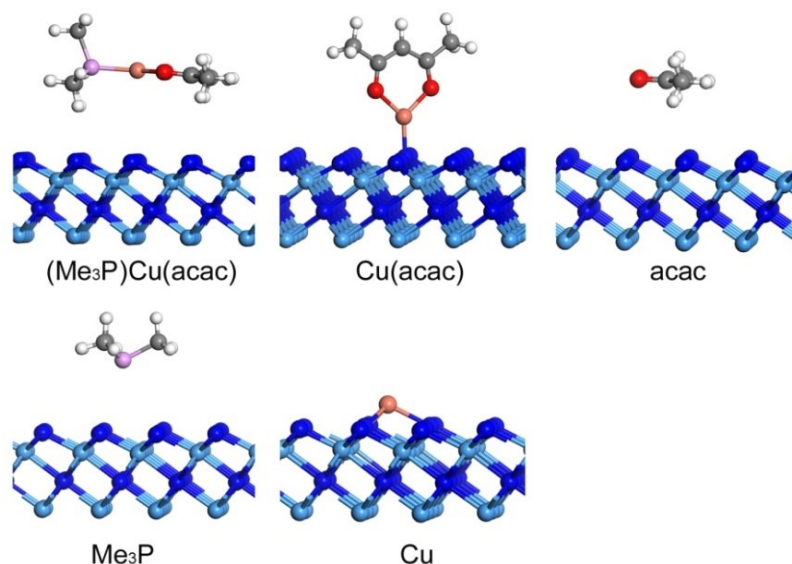
Fig. 4.25 Optimized geometries of different adsorbed species on the N-terminated TaN(111) surface calculated by the DFT-PBE functional.

On the N-terminated TaN(111) surface, only the adsorption of Cu(acac) and Cu is a notable exothermic process, with E_{ads} of −1.50 eV and −2.40 eV, respectively (Table 4.6). (Me₃P)Cu(acac) is weakly adsorbed on TaN with an energy of −0.47 eV. The TaN surface is inert towards Me₃P- and acac-ligands. The calculated adsorption energies of these species are close to zero. This finding agrees well with previous AIMD simulations [88]. It was proposed that the passivation of a Ta surface with N significantly reduces its reactivity towards the Cu(hfac)(tmvs) precursor. This is due to repulsive interactions between the negatively charged hfac- and tvms-ligands and the electron-rich N layer.

4.3.4 Disproportionation of the (Me₃P)Cu(acac) precursor on different substrates

The disproportionation of Cu(I) beta-diketonates is known to be an efficient approach to realize Cu CVD, although such a reaction destroys the self-limiting nature of ALD. CVD using Cu(II) group precursors is undesired since it has a relatively low deposition rate, and typically requires a high substrate temperature. Furthermore, a reducing agent such as hydrogen is needed for the

surface reaction. The disproportionation reaction consists of two steps [157], as shown in Eqs. 4.11 and 4.12.

$$(Me_3P)Cu(acac)(g) \rightarrow Cu(acac)^* + Me_3P(g) \tag{4.11}$$

$$2Cu(acac)^* \rightarrow Cu^* + Cu(acac)_2(g) \tag{4.12}$$
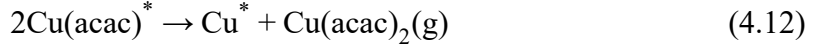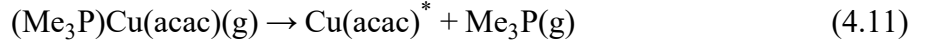
A reactive substrate is necessary for such reactions since the formation of Cu(acac) via the gas-phase decomposition of (Me₃P)Cu(acac) is proven to be infeasible (see Section 4.2). The first step is the chemisorption of the (Me₃P)Cu(acac) precursor on the surface. Two subsequent competing reactions are the desorption of the intact precursor and the dissociation into Me₃P and Cu(acac). In the latter route, Me₃P has high volatility and desorbs quickly, leaving the Cu(acac) species on the surface. Next, two adsorbed Cu(acac) react to form metallic Cu and gaseous Cu(acac)₂ that easily desorbs from the surface (Eq. 4.12).

Table 4.7 shows the calculated reaction energies for the disproportionation and the dissociation of (Me₃P)Cu(acac) on different substrates and under different conditions. The pressure has no effect on reaction (4.11) since the amount of gaseous species in the forward reaction is equal to that in the reverse reaction. It is known that the first step of disproportionation (Eq. 4.11) is determined by the adsorption energy of Cu(acac) on the surface

Table 4.7 Reaction energies (eV) on different substrates.

Reactions	Conditions	Ta(110)	Cu(110)	Ru(001)	TaN(111)	Cu₂O(111)	SiO₂(001)
(4.11)	0 K	−0.91	−0.30	−0.52	0.36	0.81	0.85
	300 K	−1.00	−0.39	−0.61	0.19	0.64	0.68
	400 K	−1.00	−0.39	−0.61	0.16	0.61	0.65
	700 K	−0.91	−0.30	−0.52	0.04	0.49	0.53
(4.12)	0 K, 1 atm.	2.37	1.53	2.00	1.05	1.42	1.81
	300 K, 0.001 atm.	1.66	0.82	1.29	0.54	0.91	1.30
	400 K, 0.001 atm.	1.40	0.56	1.03	0.38	0.75	1.14
	700 K, 0.001 atm.	0.45	−0.39	0.08	−0.12	0.25	0.64
(4.13)	0 K, 1 atm.	0.55	0.93	0.96	1.76	3.03	3.51
	300 K, 0.001 atm.	−0.33	0.04	0.07	0.91	2.18	2.66
	400 K, 0.001 atm.	−0.59	−0.21	−0.18	0.69	1.96	2.44
	700 K, 0.001 atm.	−1.37	−0.99	−0.96	−0.04	1.22	1.70
(4.14)	0 K	−1.60	−0.22	−0.25	2.39	0.68	1.46
(4.15)	0 K	−0.61	−0.05	−0.54	0.79	−0.09	0.65

as well as the bond strength between Cu(acac) and Me$_3$P in the Cu precursor. As shown in Table 4.7, (Me$_3$P)Cu(acac) readily dissociates into Cu(acac) and Me$_3$P on metallic substrates, whereas the nitride or oxide substrates are much less reactive towards the precursor. This result indicates that the disproportionation reaction of the (Me$_3$P)Cu(acac) precursor has a high selectivity towards different substrates.

The second step of the disproportionation reaction (Eq. 4.12) is mainly determined by the difference between the adsorption energies of Cu and Cu(acac). A weak adsorption of Cu(acac) on the surface is preferred for this step since the reaction (4.12) needs to first overcome a barrier of Cu(acac) desorption. As illustrated in Table 4.7, the nitride and oxide substrates are more reactive in this step as compared to the metallic substrates. Furthermore, it is known that species lose the translational and rotational contributions (which are functions of temperature) to the Gibbs energy once they are adsorbed on surfaces. Therefore, the temperature also plays an important role in reactions that have different amounts of gaseous species in the forward and reverse reactions (e.g. Eq. 4.12). As a consequence, the reaction between two adsorbed Cu(acac) (Eq. 4.12) is preferred at high temperatures, whereas the temperature has a minor effect on the dissociative adsorption of (Me$_3$P)Cu(acac) (Eq. 4.11).

Eq. 4.13 shows the overall reaction of the disproportionation of (Me$_3$P)Cu(acac)

$$2(Me_3P)Cu(acac)(g) \rightarrow Cu^* + Cu(acac)_2(g) + 2Me_3P(g) \tag{4.13}$$
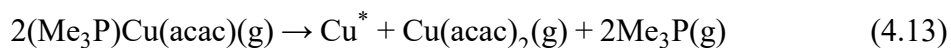
In general, the disproportionation reaction prefers to take place on the metallic substrates. Furthermore, high temperature and low pressure conditions are beneficial for the reaction. By comparison with the overall reaction energy of disproportionation and the desorption energy of Cu(acac) on different substrates, it can be concluded that the most reactive substrate towards the disproportionation of (Me$_3$P)Cu(acac) is Cu(110). Although the disproportionation reaction on Ta(110) has the largest overall reaction energy, it requires overcoming a large barrier to the desorption of Cu(acac). On the other hand, the decomposition of Cu(acac) on the Ta surface is strongly spontaneous and has a very small barrier (see Eqs. 4.14 and 4.15).

$$Cu(acac)^* \rightarrow Cu^* + acac^* \tag{4.14}$$

$$(Me_3P)Cu(acac)^* \rightarrow Cu(acac)^* + Me_3P^* \tag{4.15}$$
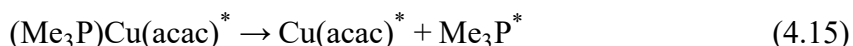
Therefore, it is expected that on Ta(110), the surface decomposition of Cu(acac) is more preferred, rather than the disproportionation reaction.

4.4 Thermodynamic modeling of ALD surface reaction

A thermodynamic analysis is performed to study the surface reactions of Cu oxide ALD, providing the equilibrium compositions between gaseous and surface-adsorbed species. Such information is significant for understanding the reaction mechanisms of ALD and for supporting the experimental investigations. It should be noticed that the results obtained from thermodynamic modeling are based on an assumption that the system is completely in equilibrium which may require a very long time.

To evaluate the performance of the GEM method, test calculations have been performed and compared with reference results, as shown in Fig. 4.26. Using input data from the thermodynamic database [129], the GEM method successfully reproduces the equilibrium compositions of steam reforming that were calculated by the HSC Chemistry software [158]. Furthermore, *ab initio* thermodynamics calculations (Fig. 4.26b) also agree well with the reference results, demonstrating the validity of the computational method and model.
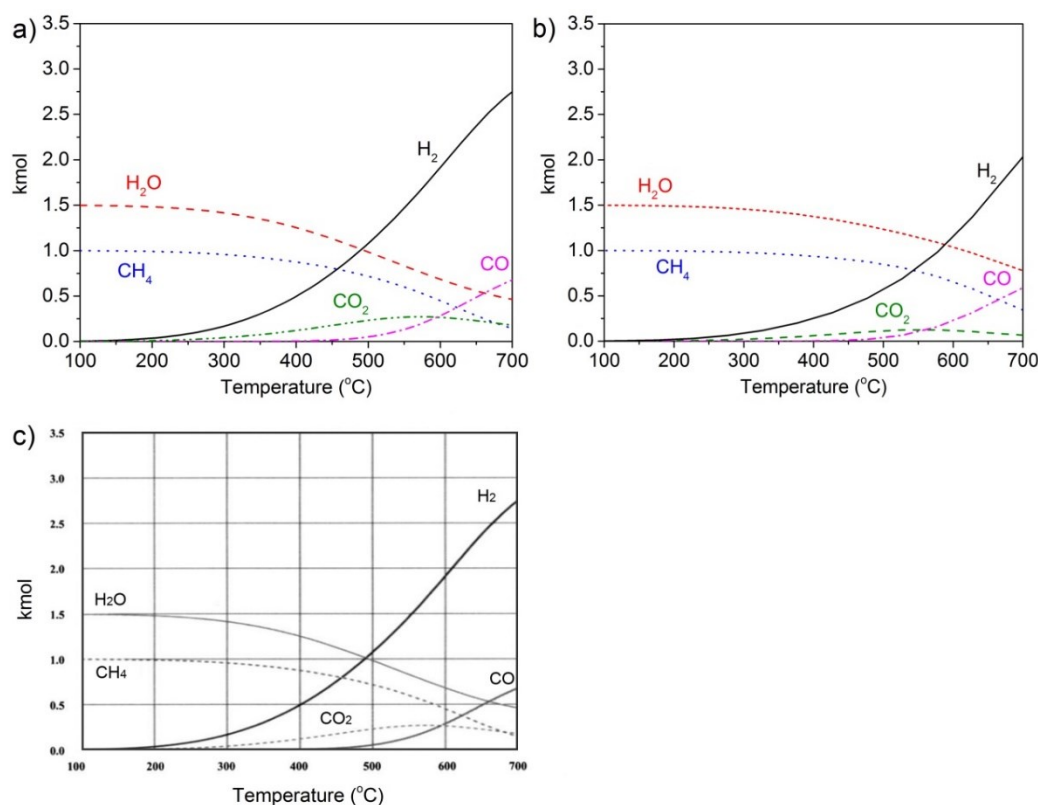
Fig. 4.26 Thermodynamic equilibrium of the steam reforming of methane, using the experimental (a) and *ab initio* calculated (b) input data. For comparison, the results calculated by HSC Chemistry software are also shown (c). Reproduced from Ref. [158] with permission from Electrochemical Society, copyright 2003. Only temperatures between 100 °C and 700 °C are considered in this work, since the higher temperatures are not applicable for ALD.

4.4.1 Equilibrium compositions on Ta(110)

The predicted equilibrium for the ALD of Cu oxides on the Ta(110) surface are shown in Figs. 4.27, 4.28. In the BEOL, tantalum is used as a liner material to enhance the adhesion between copper and diffusion barriers. The Cu precursor is assumed to be pulsed firstly. The system pressure is fixed at 100 Pa. O_3 and wet O_2 are used as the co-reactants for the $Cu(acac)_2$ and $(Me_3P)_2Cu(acac)$ precursors, respectively, which is consistent with experiments [18, 19].

Fig. 4.27 Equilibrium compositions for surface-adsorbed (a, c, e) and gaseous species (b, d, f) during the $(Me_3P)_2Cu(acac)$ pulse (a, b, e, f) and the wet O_2 pulse (c, d). S_A represents the adsorbed species on the surface, where S donates the adsorption site, A donates the adsorbate. For example, Cu_O represents the adsorption of O on the atomic Cu precoated Ta substrate.

Fig. 4.28 Equilibrium compositions for surface-adsorbed (a, c, e) and gaseous species (b, d, f) during the Cu(acac)$_2$ pulse (a, b, e, f) and the O$_3$ pulse (c, d).

In general, the Cu(I) and Cu(II) beta-diketonates have similar reaction mechanisms. Both of them are dissociatively adsorbed on the Ta(110) surface (Figs. 4.27a, 4.28a). The thermodynamic analysis predicts that the most stable Cu-species on Ta is atomic Cu, which increases in amount with raising the deposition temperature. The experimentally observed metal-Cu(acac) complex [32] is found to be unstable in this study since Cu(acac) readily dissociates into Cu and acac on the Ta surface. The main surface contaminants are atomic C and O from the acac-ligands. The thermodynamic modeling results are in accordance with the previous MD simulations for Cu(hfac)(tmvs) on the Ta(001) substrate [88]. It was found [88]

95

that the hfac-ligand of the precursor undergoes rapid decomposition on a Ta surface, forming carbides, oxides, fluorides, and other undesirable species. At temperatures higher than ~500 K, surface O reacts with C to form gaseous CO, which is desorbed from the substrate (Figs. 4.27b, 4.28b). As expected, the disproportionation of $(Me_3P)Cu(acac)$ has not been observed since no $Cu(acac)_2$ is present in the gas-phase.

During the next half-cycle, oxygen reacts with the adsorbed C and CH_3 contaminants, releasing CO_2 and H_2O to the gas-phase (Figs. 4.27d, 4.28d). Besides, the surface Ta and Cu atoms are oxidized into TaO and CuO, respectively (Figs. 4.27c, 4.28c). These observations reveal that a combustion reaction is the likely mechanism during the O_3 or wet O_2 pulse

$$Ta^* + Cu^* + Me^* + C^* + 7.5O(g) \rightarrow TaO^* + CuO^* + 2CO_2(g) + 1.5H_2O(g) \tag{4.16}$$

Combustion reactions were also observed in *in situ* mass spectroscopy studies on IrO_2 ALD from $Ir(acac)_3$ and O_3 [159]. CO_2 and H_2O have been found as the main reaction products in such works [159].

During the subsequent Cu precursor pulse, surface CuO is reduced into Cu, with CO as the by-product (Figs. 4.27e, 4.28e). Moreover, the Cu atoms as well as the CH_3 contaminants are deposited on the TaO surface. These results suggest that the surface O atoms are the reactive surface species during the metal precursor pulse. These findings agree well with previous experimental studies for an $Ir(acac)_3/O_3$ ALD process [159]. As compared with the O_3 or wet O_2 pulse, incomplete combustion reactions during the copper precursor pulse are proposed

$$3.75O^* + (Me_3P)_2Cu(acac)(g) \rightarrow OCu^* + OMeP^* + Me_3P(g) + 3.25CH_4(g) + 3.75CO(g) \tag{4.17}$$

$$4.25O^* + Cu(acac)_2(g) \rightarrow OCu^* + OMe^* + 2.75CH_4(g) + 6.25CO(g) \tag{4.18}$$
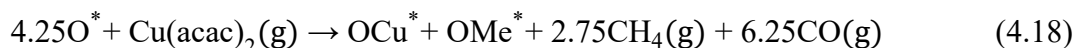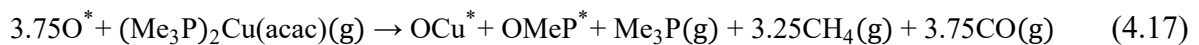
4.4.2 Equilibrium compositions on Cu₂O(111)

For the thermodynamic analysis of the initial surface reaction during ALD on $Cu_2O(111)$ surface, wet O_2 is used as the co-reactant, which is in line with previous experimental studies [19]. After the initial nucleation, surface reactions of Cu_2O ALD only appear on the Cu_2O surface, regardless of the original substrate applied. The predicted equilibrium compositions for the surface reactions during ALD at different temperatures are shown in Fig. 4.29.

As illustrated in Figs. 4.29a, b, the $(Me_3P)_2Cu(acac)$ precursor is found to adsorb dissociatively on the Cu_2O substrate. The entire O and about half of the Cu adsorption sites

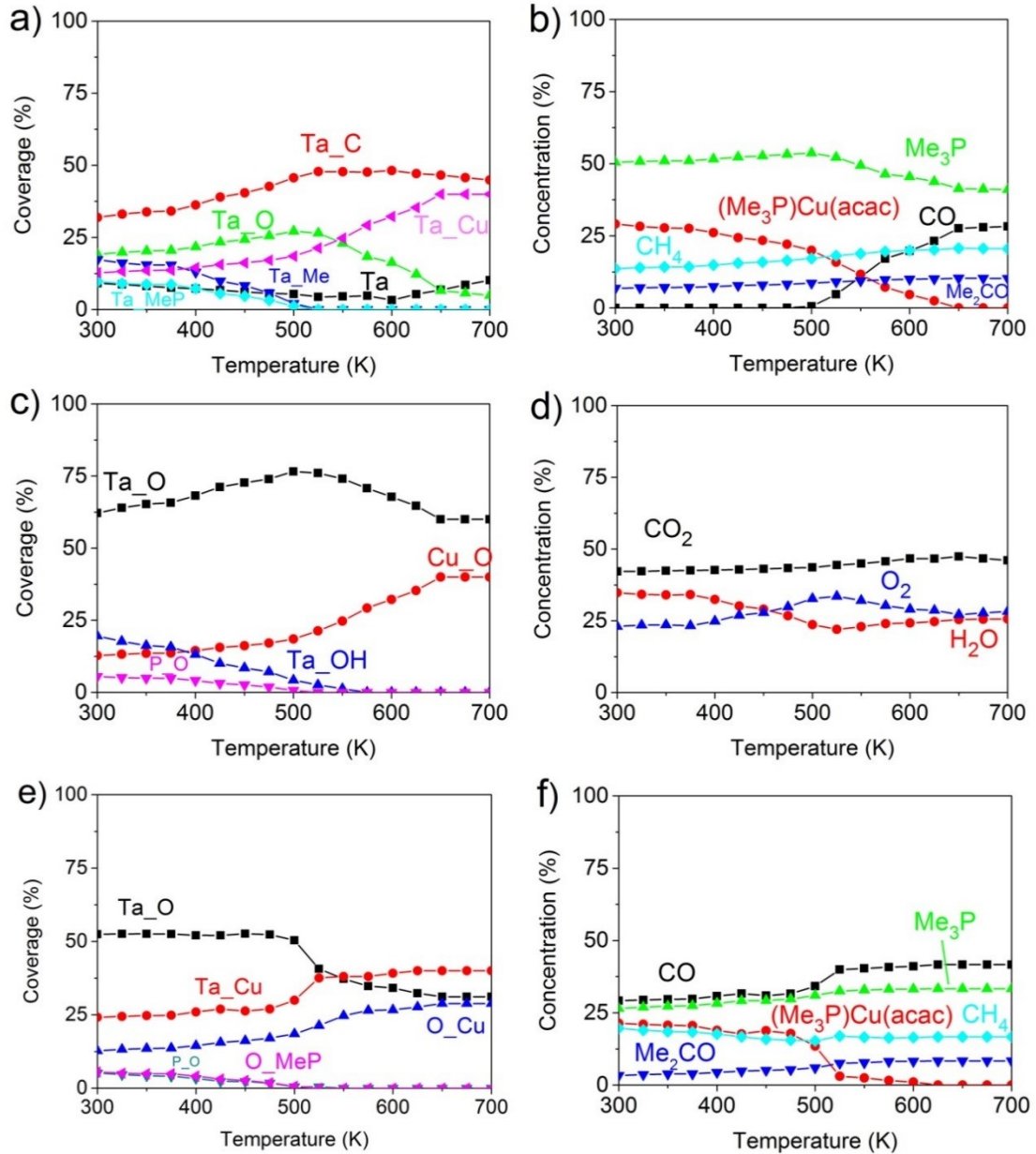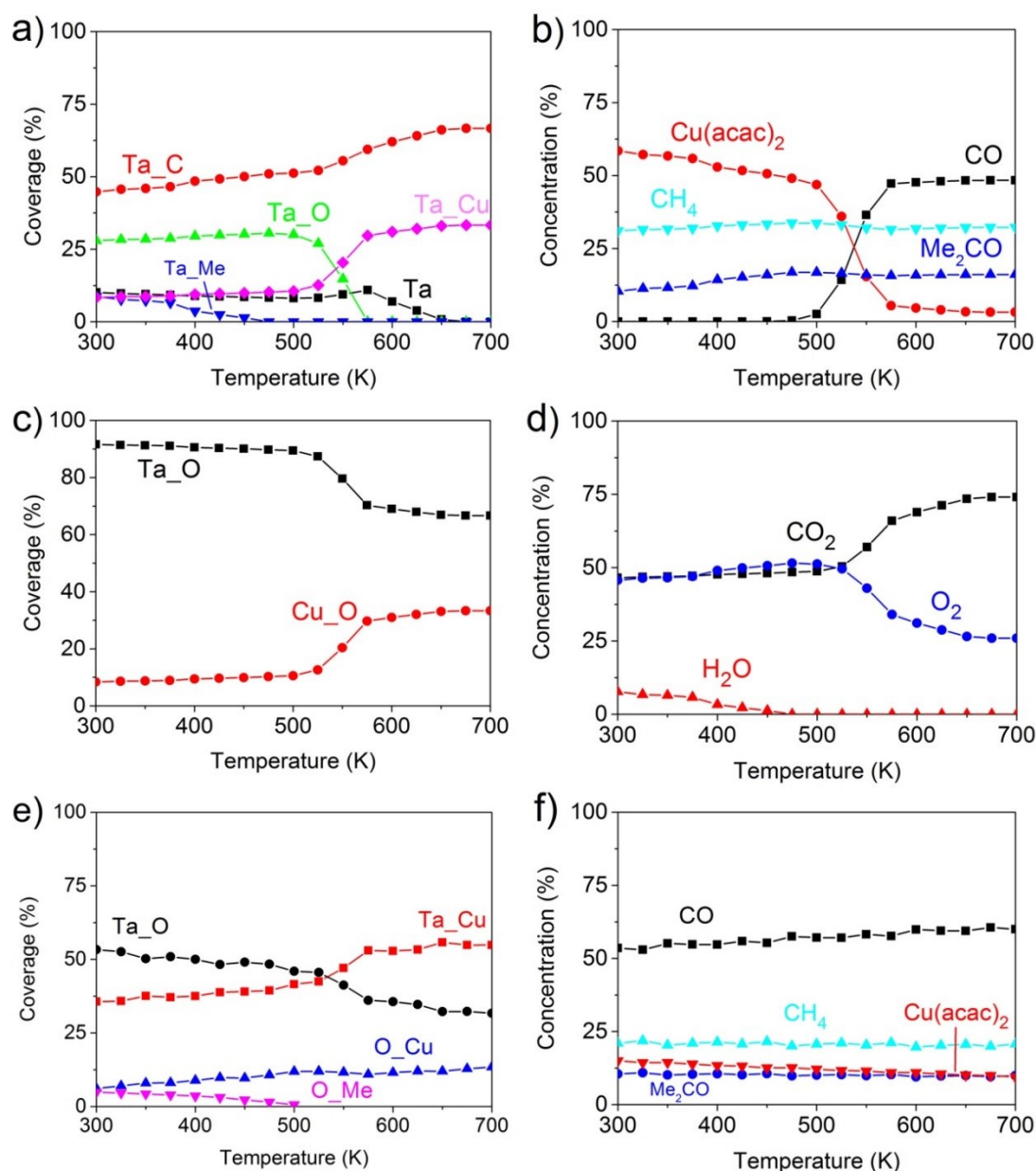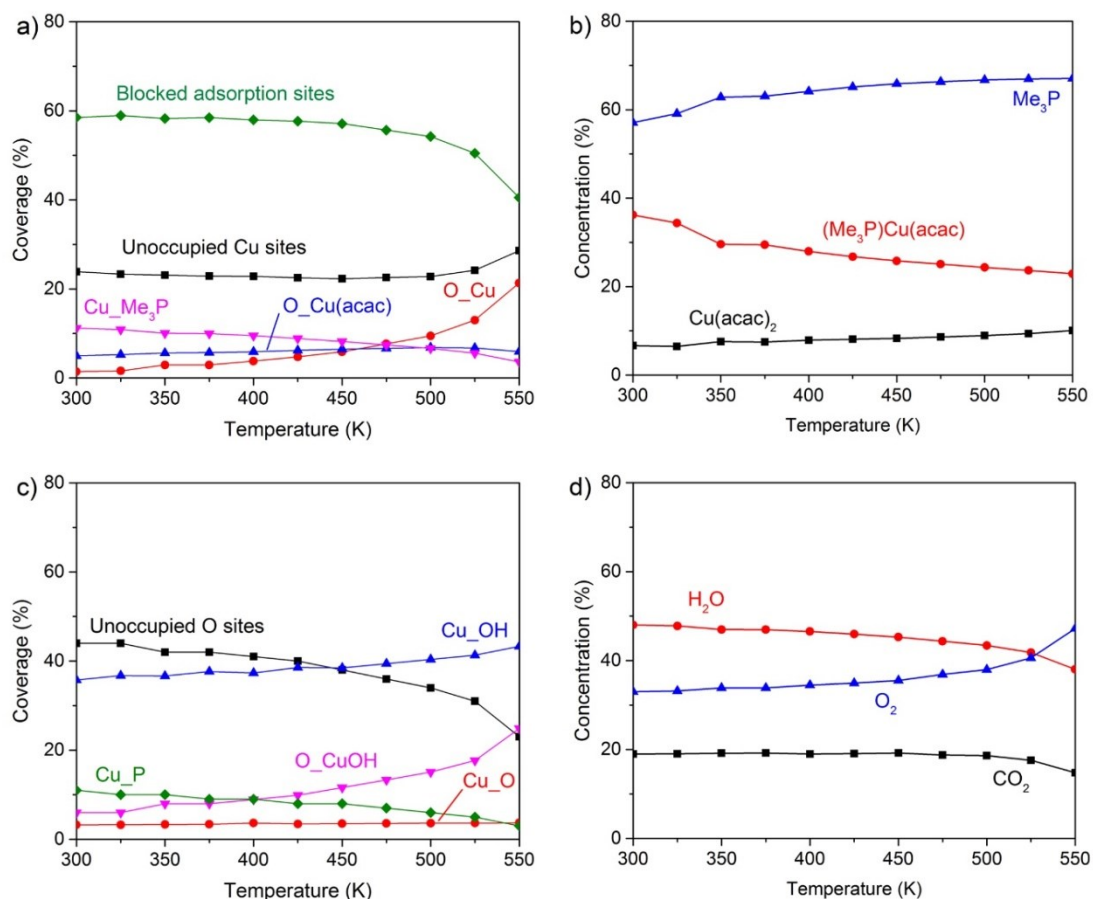**Fig. 4.29** Equilibrium compositions for surface-adsorbed (a, c) and gaseous (b, d) species during the (Me₃P)₂Cu(acac) pulse (a, b) and wet O₂ pulse (c, d).

are either occupied by adsorbates or blocked by the steric hindrance of ligands. Further decomposition of the acac- and Me₃P-ligands has not been observed, perhaps due to the lower reactivity of Cu₂O compared to the metallic substrate Ta. It should be noticed that plenty of the Me₃P-ligands (coverage = 5–11 %) are co-adsorbed on the surface, especially at low temperatures. Therefore, it is possible for the Me₃P-ligand to compete with Cu(acac) for the surface active sites, which may also result in the deposition of C and P contaminants. The presence of metallic Cu on the surface and Cu(acac)₂ in the gas-phase are attributed to a disproportionation reaction, as shown in Eq. 4.12. This reaction is of minor importance below temperatures of 450 K (coverage of Cu ≤ 5%), while it may be significantly enhanced at elevated temperatures. The predictions are consistent with the previous XPS studies [29], where the (ⁿBu₃P)₂Cu(acac) precursor is disproportionated at temperatures higher than ~473 K. Such a disproportionation reaction destroys the self-limiting nature of ALD processes and is known as the main limitation for the use of Cu(I) beta-diketonates. Hence, the upper temperature limit for the ALD of Cu₂O from (ⁿBu₃P)₂Cu(acac) must be below 473 K [29].

During the wet O_2 pulse, O_2 reacts with the adsorbed acac- and Me_3P-ligands, producing gaseous CO_2 and H_2O and leaving abundant O adsorption sites (Figs. 4.29c, d). Besides, most of the surface Cu atoms are oxidized into CuOH (a few Cu atoms into CuO). These O- and OH-groups may act as reactive species for the subsequent Cu precursor pulse. Again, the simulations reveal that a combustion reaction is the likely mechanism during the wet O_2 pulse, as shown in Eq. 4.19.

$$Cu^* + Cu(acac)^* + Me_3P^* + 11.5O_2(g) \rightarrow 2CuOH^* + P^* + 8CO_2(g) + 7H_2O(g) \qquad (4.19)$$

It is well known that the presence of water facilitates Cu oxide CVD and ALD from the Cu beta-diketonate precursors [161,162]. A previous experimental study has shown that ALD using $(^nBu_3P)_2Cu(acac)$ and O_2 deposits only isolated clusters, while continuous films are grown by using wet O_2 as the oxidizing agent [160]. The possible reaction mechanism between Cu(acac) and H_2O is a ligand-exchange reaction:

$$Cu(acac)^* + H_2O(g) \rightarrow CuOH^* + H(acac)(g) \qquad (4.20)$$
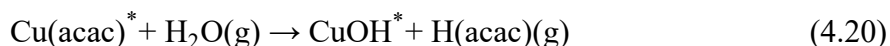
However, such a reaction has not been observed in the thermodynamic analysis, since H(acac) is unstable under oxidation conditions. Indeed, the amount of water in the gas-phase is increased after the wet oxygen pulse. This observation suggests that the produced H(acac) may only exist as an intermediate during ALD. In the next chapter, molecular dynamics simulations will be performed to illuminate the detailed reaction between the Cu(acac) precursor and water.

In summary, the thermodynamic modeling predicts that the Cu precursor decomposes spontaneously on the Ta and Cu_2O substrates. Depending on the substrate reactivity, further decomposition of the adsorbed acac- and Me_3P-ligands are favorable on Ta rather than on Cu_2O. During the co-reactant pulse, a combustion-like reaction (by releasing CO_2 and H_2O) is the most dominant surface reaction. Thermodynamic modeling provides a useful perspective on the surface reaction of Cu oxide ALD.

4.5 Summary

Ab initio calculations are conducted to investigate the stability of Cu precursors in the gas-phase. It is found that $(^nBu_3P)_2Cu(acac)$ readily loses one of the $^nBu_3P$-ligands to form $(^nBu_3P)Cu(acac)$. However, the further dissociation of $(^nBu_3P)Cu(acac)$ requires high temperatures (> 575 K), which exceed the upper bound of the ALD window. Therefore, the $(^nBu_3P)Cu(acac)$ precursor is expected to be stable under ALD conditions. For the Cu(II)

beta-diketonate, $Cu(acac)_2$ is thermally stable within 300–700 K, which satisfies the ALD requirement.

A simplified Cu(I) beta-diketonate $(Me_3P)_2Cu(acac)$ is used in surface calculations since the size of the phosphane-ligand has a limited effect on the precursor dissociation energy. On the basis of the calculated adsorption energies and reaction energies, it can be concluded that metallic substrates (Ta, Cu, Ru) are much more reactive towards the Cu precursor compared to metal oxide (Cu_2O, SiO_2) and metal nitride (TaN) substrates. The $(Me_3P)Cu(acac)$ and $Cu(acac)_2$ precursors easily decompose on the metallic substrates, forming $Cu + acac + Me_3P$ and $Cu + 2acac$, respectively. The further dissociation of the acac- and Me_3P-ligands is thermodynamically favorable on the Ta substrate, which may destroy the self-limiting property of ALD and lead to the deposition of contaminants.

Thermodynamic modeling is performed to predict the equilibrium compositions of the ALD surface reactions. During the O_3 or wet O_2 pulse, adsorbed ligands and contaminants are oxidized into gaseous CO_2 and H_2O, while surface metal atoms (Ta or Cu) are oxidized into metal oxide or metal hydroxide. In general, a combustion-like reaction mechanism has been proposed. However, the role of water in the ALD of Cu_2O is still unclear and needs to be further investigated by RMD simulations.

Chapter 5 Reactive molecular dynamics simulations of Cu ALD

In principle, AIMD is a reliable approach for the dynamic description of chemical reactions. Previously, this method has been demonstrated in literature for the simulation of SiO_2 and HfO_2 ALD [163, 164]. Unfortunately, due to the costs of treating the electronic degrees of freedom, AIMD studies are restricted to model systems consisting of a few hundred atoms and to very short time scales (several ps). In this work, a reactive force field (ReaxFF) is used for the RMD simulations of metallic Cu and Cu oxide ALD. RMD simulations allow the study of large reactive systems with relatively low costs, which are compatible with the power of current computer clusters. Before starting the simulation, the accuracy of ReaxFF force fields has been carefully examined using DFT data as a benchmark. Furthermore, the kinetic analysis for the oxidation of H(acac) is also presented.

5.1 Computational method and model

RMD simulations were performed in the NVT canonical ensemble. A Nose-Hoover thermostat [165, 166] with a damping constant of 100 fs was used for temperature control. The time step used in RMD simulations was 0.1 fs for the reactions between $Cu(acac)_2$ and O_3, and between H(acac) and O_2. For other systems, the timestep was 0.25 fs. Small time steps are required to capture bond breaking and forming involved in chemical reactions so that converged results for the species evolution can be obtained. The simulation temperature was 600 K for surface reactions and above 1750 K for gas-phase reactions. As compared with experiment, higher temperatures were used in order to enhance the reactivity of co-reactants. The initial system was first equilibrated using low-temperature MD at 1 K. After equilibration, the system temperature was raised to a target temperature at a uniform rate of ~3 K/ps. Finally, RMD simulations were performed at the target temperature for a total simulation time of up to 5 ns. All simulations were carried out by using the ReaxFF potential as implemented in LAMMPS [167].

Large surface models consisting of a four-layer slab of $p(22 \times 30)$–Cu(110) $(79.52 \times 76.68 \text{ Å}^2)$, and nine-layer slabs of $p(12 \times 16)$–$Cu_2O(111)$ $(72.46 \times 83.67 \text{ Å}^2)$ and $p(14 \times 12)$–CuO(111) $(80.76 \times 73.70 \text{ Å}^2)$ were used in RMD simulations. To simplify the simulations, only stoichiometric surfaces were considered in this work. During the

simulations, the two bottom layers of Cu(110), and the bottom four layers of Cu_2O(111) and CuO(111) were fixed. To investigate the surface reactions between $Cu(acac)_2$ and different co-reactants, 24 Cu precursors were initially placed on the surface, corresponding to a coverage of ~0.4 molecule/nm^2. Above the adsorbed $Cu(acac)_2$ precursors, 2000 H_2O molecules or H atoms, or 1000 O_3 molecules were distributed randomly, with a density of 0.08 g/cm^3, 0.004 g/cm^3, or 0.1 g/cm^3, respectively. For gas-phase reactions, the model contains 200 H(acac) and 6000 O_2 molecules, with a density of 0.1 g/cm^3. A relatively high density of co-reactants has been used to ensure a sufficient reactivity of the system and hence to obtain results within a reasonable calculation time.

5.2 Assessment of the Cu_vanDuin and CHO_Chenoweth potentials

The ReaxFF potential for the Cu systems was originally developed by van Duin et al. in 2010 [168]. Initially, the Cu/O/H potential parameters were developed for Cu ion/water interactions and Cu metal, metal oxide, and metal hydroxide condensed phases. The parameterization for Cu ion/water interactions was performed using the strategy by Wood et al. [169] described as follows:

(1) Developing an initial set of ReaxFF parameters by training against a DFT data set (ReaxFF^{intital});

(2) Using the obtained ReaxFF^{intital} parameters to perform MD simulation of a Cu^{2+}/water system; calculating the single-point energies for $[Cu(H_2O)_5]^{2+}$ clusters abstracted from this trajectory.

(3) Adding these DFT single-point energies to the training set to refit the ReaxFF^{intital} parameters.

(4) Verifying the refitted ReaxFF parameters (ReaxFF^{refit}) by repeating stage (2) with $[Cu(H_2O)_6]^{2+}$ clusters.

The validation calculations (water binding energy in $[Cu(H_2O)_6]^{2+}$) showed that the average deviation of ReaxFF^{refit} was only slightly larger (6.4 kcal/mol), demonstrating a good transferability of the refitted potentials. For CuO, the training set included the equations of states (EOS) of zinc blende, the NaCl, and the monoclinic C2/c structures, which were calculated by using the spin-polarized B3LYP functional [170]. For Cu_2O and Cu metal, only the EOS of (nonmagnetic) cubic cuprite (space group *Pn3m*) and face centered cubic

structures were investigated, respectively. The optimized potential is able to reproduce the DFT calculated structural and energetic properties of Cu, CuO and Cu_2O condensed-phases.

The ReaxFF potential of C/H/O/N was initially developed for reactive dynamics simulation of glycine ($C_2H_5NO_2$) in the gas-phase and the solution [171]. A training set for the hydrocarbon potential was augmented with several glycine conformers and glycine-water complexes, and the valence and dihedral angle distortions of glycine [171]. The O/H parameters are the same as that used in the Cu potential, which has been validated for water clusters, bulk water, proton transfer reactions and water self-ionization reactions by comparison against experimental data. The optimized C/H/O/N potential could accurately describe the conformational energies of gaseous glycine and the tautomerization between the neutral form and the zwitterionic form of glycine in water [171].

The existing Cu/O/H parameters [168] were then directly integrated into the C/H/O/N potential in 2012 [172]. As mentioned above, these force fields share the same O/H parameters, making such integration relatively straightforward. For the Cu/C and Cu/H parameters, only the non-bonded interactions were addressed in the new potential (referred as Cu_vanDuin). The bonded interactions between Cu and N were taken from unpublished works by the van Duin group. The parameters of the Cu_vanDuin potential are listed in the supplementary material of Ref. [172].

So far, the Cu_vanDuin potential includes the elements Cu, C, H, O, and N, which enables the simulation of different kinds of reactive systems, from a cluster model to a periodic surface model. For example, Huang et al. [172] have applied ReaxFF to investigate the reactive adsorption of NH_3 and H_2O on the Cu(II) benzene 1,3,5-tricarboxylate metal-organic framework. Jeon et al. [173] have studied the oxidation of a metallic Cu surface. Carravetta et al. [174] investigated the adsorption of glycine and glycylglycine on the Cu(110) surface, in combination with the *ab initio* calculations of XPS spectra. In general, the works mentioned above show that ReaxFF succeeds in modeling surface/interface reactions on copper and agrees satisfactorily with the experimental data and other theoretical results.

In this work, the application of ReaxFF is extended to the reactive dynamics simulations of Cu ALD. A series of test calculations have been carried out to evaluate the accuracy of ReaxFF for Cu ALD systems. Table 5.1 shows a comparison of the structural properties of Cu(acac)$_2$, Cu(acac), H(acac), and acac species calculated by ReaxFF and DFT and measured by experiment. Two different ReaxFF potentials, Cu_vanDuin and CHO_Chenoweth, have been tested. The CHO_Chenoweth potential was developed by Chenoweth et al. in 2008 [175].

It is applicable for simulating the oxidation and combustion of different hydrocarbon species. However, this potential does not contain the parameters for copper. In general, a very good agreement is observed between the ReaxFF and DFT results. The largest errors for ReaxFF relative to DFT benchmarks are ~0.15 Å for bond length and ~6° for angle, respectively. The only exception is that ReaxFF fails to predict the Cu–O1–C2 (123.9° vs. 110°) and O1–Cu–O2 (96° vs. 113°) angles of a Cu(acac) molecule. As shown in Figs 5.1 and 5.2, the structure of Cu(acac) obtained by ReaxFF is very close to Cu(acac)₂. This error will disappear as Cu(acac) is adsorbed on the Cu surface, since the structure of adsorbed Cu(acac) is similar to gaseous Cu(acac)₂ (see below).
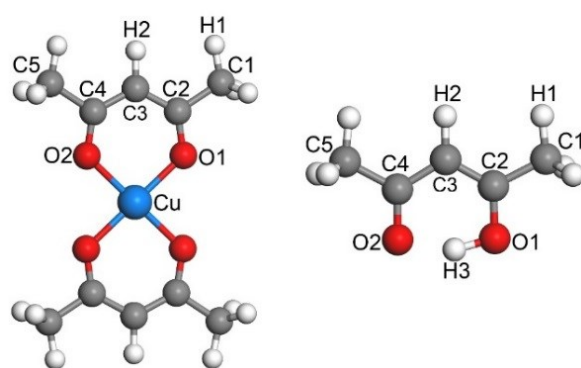
Fig. 5.1 Assignment of atom number for the Cu(acac)₂ and H(acac) species. (See Table 5.1)

Table 5.1 Comparison of the structural properties of Cu(acac)₂, Cu(acac), H(acac), and acac species obtained by theoretical calculation and experimental measurement. The bond lengths and angles are given in units of Å and °, respectively. The assignment of the atom numbers can be found in Fig. 5.1.

	Cu(acac)₂			Cu(acac)		H(acac)		acac	
	Exp.	Dmol3	ReaxFF	Dmol3	ReaxFF	Dmol3	ReaxFF	Dmol3	ReaxFF
Cu–O1	1.91	1.95	1.98	1.89	1.91				
C2–O1	1.27	1.28	1.43	1.30	1.44	1.32	1.48	1.27	1.34
C4–O2	1.27	1.28	1.43	1.30	1.44	1.27	1.35	1.27	1.34
C1–C2	1.48	1.51	1.52	1.51	1.52	1.49	1.52	1.52	1.58
C2–C3	1.39	1.41	1.40	1.42	1.39	1.39	1.37	1.41	1.44
C1–H1		1.10	1.13	1.10	1.13	1.10	1.13	1.10	1.12
C3–H2		1.09	1.12	1.09	1.12	1.09	1.12	1.09	1.11
O1–H3						1.06	1.05		
O2–H3						1.46	1.63		
∠Cu–O1–C2	125.9	126.0	127.9	110.0	123.9				
∠O1–Cu–O2	93.2	92.5	89.7	113.0	96.0				
∠C2–O1–H3						103.5	110.4		
∠O1–C2–C1	114.4	115.3	119.3	113.8	119.5	115.3	117.6	117.3	117.1
∠O1–C2–C3	124.4	125.4	126.8	128.0	126.8	120.8	122.5	121.0	127.9
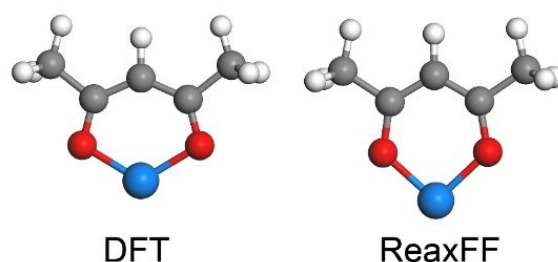
Fig. 5.2 Comparison of the calculated DFT (by Dmol3) and ReaxFF structures of Cu(acac).

Table 5.2 Comparison of the formation enthalpies (in eV) at 0 K of different species by theoretical calculation and experimental measurement.

Molecule	Cu_vanDuin	CHO_Chenoweth	DFT (Dmol3)	Exp.[129]
O_2	−5.60	−5.36	−5.79	−5.12
O_3	−4.71	−5.92	−8.93	−6.17
H_2	−4.72	−4.75	−4.67	−4.48
H_2O	−10.85	−10.30	−10.00	−9.51
CO_2	−17.84	−17.83	−17.15	−16.56
CO	−12.09	−11.90	−10.97	−11.11
CH_4	−18.96	−20.09	−18.17	−17.02
HCOOH	−22.79	−22.72	−21.97	−20.83

Next, the experimental and theoretical formation enthalpies of gaseous species are compared, as shown in Table 5.2. The fully dissociated atoms have been chosen as a reference state for each molecule. As shown in Table 5.2, the largest error of the theoretical values is caused by the O_2 and O_3 molecules. It is well known that DFT poorly describes the high-spin ground state of these molecules. The CHO_Chenoweth potential shows a better result for the formation enthalpy of O_3 as compared to the Cu_vanDuin potential. The underestimated formation enthalpy of O_3 by Cu_vanDuin may lead to an overestimation of the co-reactant reactivity during RMD simulations. For other molecules, both ReaxFF and DFT properly predict the formation enthalpies with an average error of ~8.5% and ~4%, respectively.

Table 5.3 compares the experimental and theoretical reaction enthalpies of Eqs. 5.1–5.15. It should be noticed that the experimental data for Cu precursors are currently not available. Again, the largest error of the Cu_vanDuin potential arises from the O_3 molecule. For the Cu precursor, different reactions that may occur during Cu ALD have been tested, including oxidation or reduction reactions, ligand-exchange reactions with water, and self-dissociation and disproportionation of the Cu precursors. In general, the Cu_vanDuin potential satisfactorily reproduces the trend of the reaction enthalpies calculated by DFT.

$$CO + 0.5O_2 \rightarrow CO_2 \tag{5.1}$$

$$CH_4 + 2O_2 \rightarrow CO_2 + 2H_2O \tag{5.2}$$

$$2H_2 + O_2 \rightarrow 2H_2O \tag{5.3}$$

$$H_2 + O \rightarrow H_2O \tag{5.4}$$

$$H + OH \rightarrow H_2O \tag{5.5}$$

$$H_2 + 1/3O_3 \rightarrow H_2O \tag{5.6}$$

$$H(acac) + 6O_2 \rightarrow 5CO_2 + 4H_2O \tag{5.7}$$

$$H(acac) + 16H \rightarrow 5CH_4 + 2H_2O \tag{5.8}$$

$$2Cu(acac) \rightarrow Cu(acac)_2 + Cu \tag{5.9}$$

$$Cu(acac)_2 + H_2 \rightarrow Cu + 2H(acac) \tag{5.10}$$

$$Cu(acac)_2 + H_2O \rightarrow 2H(acac) + CuO \tag{5.11}$$

$$2Cu(acac) + H_2O \rightarrow 2H(acac) + Cu_2O \tag{5.12}$$

$$Cu(acac)_2 + 12O_2 \rightarrow CuO + 10CO_2 + 7H_2O \tag{5.13}$$

$$Cu(acac)_2 \rightarrow acac + Cu(acac) \tag{5.14}$$

$$Cu(acac) \rightarrow acac + Cu \tag{5.15}$$
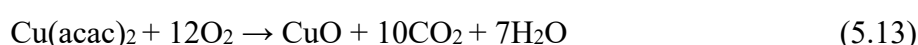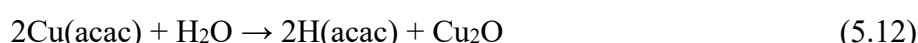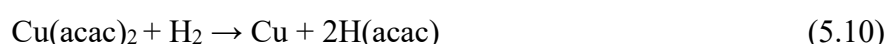
Table 5.3 Comparison of the reaction enthalpies (in eV) at 0 K by theoretical calculation and experimental measurement.

Reactions	Cu_vanDuin	CHO_Chenoweth	Dmol3	Exp.[129]
(5.1)	−2.95	−3.25	−3.30	−2.90
(5.2)	−9.27	−7.62	−7.44	−8.33
(5.3)	−6.56	−5.74	−4.89	−4.95
(5.4)	−6.13	−5.55	−5.33	−5.03
(5.5)	−5.18	−4.90	−5.24	−5.11
(5.6)	−4.56	−3.58	−2.36	−2.98
(5.7)	−27.00	−25.02	−24.03	
(5.8)	−44.61	−47.92	−43.75	
(5.9)	−2.17		−2.90	
(5.10)	−1.97		−1.40	
(5.11)	−0.68		−0.13	
(5.12)	−2.86		−3.17	
(5.13)	−54.68		−48.19	
(5.14)	2.50		2.74	
(5.15)	3.83		3.43	

Finally, the DFT and Cu_vanDuin calculated adsorption properties of different Cu species on the Cu(110) surface are compared, as shown in Table 5.4. Since no benchmark data is currently available for the Cu(acac)$_2$/Cu(110) system, the vdW-DF results are used as a reference to evaluate the accuracy of Cu_vanDuin. Recent DFT calculations for the Cu(dmap)$_2$/Cu(111) system [96] have found that the vdW interactions not only increase the

adsorption energies but also change the nature of adsorption fundamentally. It can be seen from Table 5.4 that most of the Cu_vanDuin results match well with the DFT results. The average energetic and geometric discrepancies between the Cu_vanDuin and vdW-DF results are ±0.22 eV (8.9%) and ±0.18 Å (6.9%), respectively. The only exception is that Cu_vanDuin fails to predict the structure for the adsorption of Cu(acac)$_2$ on a hollow site (see Fig. 5.3). A large distance between the Cu and O atoms (2.88 Å) is associated with the dissociative adsorption of Cu(acac)$_2$ on the surface.

Table 5.4 Adsorption properties for different species on Cu(110) surface

		Cu(acac)$_2$	Cu(acac)$_2$	Cu(acac)$_2$	Cu(acac)	acac	Cu
		top	bridge1	hollow	hollow	top	hollow
E_{ads} (eV)	PBE	−0.48	−0.33	−1.51	−2.16	−2.68	−3.08
	vdW-DF	−1.42	−1.34	−2.16	−2.08	−2.89	−2.81
	Cu_vanDuin	−1.24	−1.33	−2.11	−2.11	−2.44	−3.33
d(Cu$_p$–Cu$_s$) (Å)	PBE	2.65	2.76	2.63	2.62	/	2.53
	vdW-DF	2.70	2.90	2.68	2.63	/	2.59
	Cu_vanDuin	2.47	2.62	2.63	2.61	/	2.61
d(Cu$_p$–O) (Å)	PBE	2.04	2.02	2.21	2.00	/	/
	vdW-DF	2.07	2.04	2.24	2.03	/	/
	Cu_vanDuin	2.01	2.02	2.88	1.97	/	/
d(Cu$_s$–O) (Å)	PBE	3.45	2.99	2.07	3.28	2.01	/
	vdW-DF	3.52	3.13	2.14	3.33	2.08	/
	Cu_vanDuin	3.16	2.72	1.95	3.22	1.99	/

An illustration of the adsorption sites can be found in Fig. 4.13. Only the most stable adsorption structures for the Cu(acac), acac, and Cu species are presented.
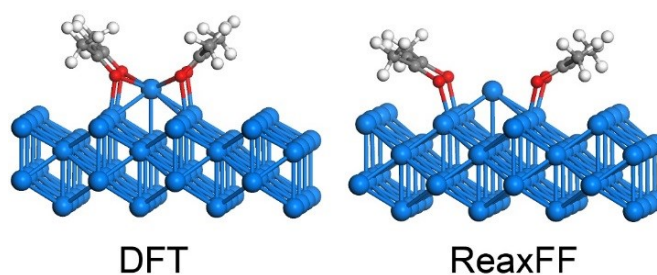

Fig. 5.3 Comparison of the DFT (by Quantum Espresso) and ReaxFF adsorption structures of Cu(acac)$_2$ on the Cu(110) surface.

In summary, the recently developed ReaxFF potential Cu_vanDuin has been assessed for the application of Cu ALD. This potential successfully reproduces the geometric structure and the dissociation energy of Cu(acac)$_2$ as calculated by DFT. Furthermore, there is also a good agreement between the Cu_vanDuin potential and DFT calculated adsorption energies and adsorption distances on the Cu(110) surface. The CHO_Chenoweth potential contains the elements of C, H, and O. It provides a better description for the oxidation of hydrocarbons as compared to the Cu_vanDuin potential. Therefore, the CHO_Chenoweth potential is used in this work for simulating the gas-phase oxidation of H(acac) (see Section 5.5.2).

5.3 Development and assessment of the Cu_Hu potential

It has been mentioned in Section 5.2 that the Cu–H and Cu–C bonding interactions are not considered in the Cu_vanDuin potential. However, such interactions play an important role in surface reactions, especially for the Cu(acac)$_2$/H ALD process (see Section 5.4). Therefore, based on the Cu_vanDuin potential, a new Cu potential (referred as Cu_Hu) that includes the Cu–H and Cu–C bonding interactions has been developed in this work. In addition, the existing Cu–N parameters are re-optimized to accurately describe the adsorption energy of nitrogen species and the bond dissociation of the [Cu(amd)]$_2$ precursor. Other parameters in the Cu_vanDuin potential are unaltered. The parameters of the developed Cu_Hu potential are listed in the Appendix. Details of the parameterization using the Taguchi method have been described in Section 3.4.2. So far, the Cu_Hu potential completely covers the interactions of the Cu/C/H/O/N system. It enables the simulation of a variety of Cu precursors, for example, Cu(acac)$_2$, Cu(dmap)$_2$, [Cu(amd)]$_2$, [Cu(dtip)]$_2$, Cu(Pyrlm)$_2$, and so on. This section is dedicated to the evaluation of the Cu_Hu potential. Furthermore, the significance of the ReaxFF parameters based on the ANOVA is also discussed.

Since the Cu–H and Cu–C bonds exist neither in the Cu(acac)$_2$ precursor nor the surface-adsorbed Cu(acac) and acac, the assessment results of the Cu_vanDuin potential presented in Section 5.2 are also applicable for the Cu_Hu potential. For example, Table 5.5 compares the geometric structures of the Cu(acac)$_2$ and Cu(acac) molecules calculated using the Cu_Hu and Cu_vanDuin potentials. It is evident that there is almost no difference between the Cu_Hu and Cu_vanDuin results.

The training set used for the parameterization of the Cu_Hu potential includes adsorption energies and distances on Cu surfaces; bond dissociation curves; reaction pathways; valence angle energies; and torsion energies. In total, about 150 ReaxFF parameters are fitted by using

Table 5.5 Comparison between the Cu_vanDuin and Cu_Hu results for the structure properties of Cu precursors. The assignment of the atom numbers can be found in Fig. 5.1.

	Cu(acac)$_2$		Cu(acac)	
	Cu_Hu	Cu_vanDuin	Cu_Hu	Cu_vanDuin
Cu–O1	1.983	1.977	1.930	1.914
C2–O1	1.432	1.431	1.442	1.439
C1–C2	1.522	1.519	1.520	1.516
C2–C3	1.397	1.396	1.394	1.391
C1–H1	1.128	1.128	1.129	1.129
C3–H2	1.117	1.117	1.117	1.117
∠Cu–O1–C2	128.4	127.9	125.4	123.9
∠O1–Cu–O2	89.1	89.7	93.9	96.0
∠O1–C2–C1	119.6	119.3	119.9	119.5
∠O1–C2–C3	126.6	126.8	126.6	126.8

more than 500 DFT data sets. Selected results of the evaluation of the Cu_Hu potential are shown below.

A comparison of adsorption energies and distances of different species on the Cu surface calculated by DFT and ReaxFF is listed in Table 5.6. The considered species include single atoms (C, H, N), small molecules (e.g., CH, NH) as well as relatively large molecules [e.g., $C(CH_3)_2$ and $N(CH_3)_3$]. These species are expected to be important for Cu ALD and other reactive systems involving Cu/C/H/N. Only the most stable adsorption site for each species is discussed here. As listed in Table 5.6, with a few exceptions [e.g., N_2H_4 and $C(CH_3)_2$], most of the ReaxFF results agree well with the DFT results. The discrepancies are within ±0.3 eV and ±0.2 Å.

Fig. 5.4 shows the dependence of the adsorption energy on the adsorption distance of different adatoms. The Cu_Hu potential is found to significantly underestimate the adsorption energy of H once the adsorption distance is above ~1.75 Å. The Cu–H bond is predicted to be completely broken with a bond distance above ~2.5 Å, which is close to the cutoff radius of the sigma bond (see Fig. 5.5). Therefore, it is unlikely to solve this problem during the parameterization, unless a correction of the bond order function is made. A similar problem also exists in the Ni–H bond of a Ni/C/H potential developed by Mueller et al [176], as shown in Fig. 5.5. On the other hand, there is a good agreement between the DFT and ReaxFF results for the adsorption of C and N. ReaxFF is also able to accurately describe the dissociation curve of the [Cu(amd)]$_2$ molecule (Fig. 5.4). Furthermore, the parameters of the Cu–C and Cu–N bonds are trained against the formation energies of the CuC and CuN crystals, relative to their corresponding minimum energy structures, as shown in Fig. 5.6.

Table 5.6 Adsorption energy (E_{ads}, in eV) and distance (d, in Å) of different adsorbates on different orientations and sites of the Cu surface.

| Adsorbate	Orientation	Site	DFT		Cu_Hu	
			E_{ads}	d	E_{ads}	d
H	111	hollow	−2.457	1.766	−2.423	1.692
H	111	sub-layer	−1.851	1.846	−2.109	1.665
H	110	hollow	−2.417	1.903	−2.280	1.730
H	100	hollow	−2.427	1.901	−2.271	1.765
C	111	hollow	−4.850	1.873	−4.748	2.009
C	111	sub-layer	−4.953	1.915	−5.147	2.083
CH	111	hollow	−4.977	1.932	−4.676	1.952
CH$_2$	111	bridge	−2.705	1.985	−2.746	1.943
C$_2$H$_2$	111	hollow	−4.561	1.928	−4.641	1.944
CH$_3$	111	top	−1.168	2.024	−1.378	2.057
CCH$_3$	111	hollow	−3.747	1.959	−3.650	1.968
C(CH$_3$)$_2$	111	hollow	−2.018	2.053	−1.423	2.115
C	110	hollow	−5.629	2.046	−5.436	2.202
CH$_2$	110	bridge	−2.948	1.961	−3.104	1.974
CH$_3$	110	top	−1.392	1.989	−1.370	2.034
CCH$_3$	110	hollow	−3.720	2.187	−3.678	2.073
C	100	hollow	−6.124	1.928	−5.332	2.064
CH	100	hollow	−5.675	2.005	−5.091	2.129
C$_2$H$_2$	100	hollow	−5.190	2.746	−4.329	2.478
CH$_3$	100	top	−1.221	2.014	−1.372	2.041
CCH$_3$	100	hollow	−4.253	2.039	−4.006	2.167
N	111	hollow	−3.474	1.840	−3.281	1.946
N	111	sub-layer	−3.224	1.878	−3.668	2.045
NH$_2$	111	bridge	−2.362	1.984	−2.434	1.954
NH$_3$	111	top	−0.533	2.116	−0.850	2.046
N$_2$H$_4$	111	top	−0.517	2.200	−1.380	1.995
NCH$_3$	111	hollow	−2.749	1.925	−2.513	1.944
N(CH$_3$)$_3$	111	top	−0.333	2.344	−0.426	2.051
NH	110	hollow	−3.228	2.137	−3.144	2.092
NH$_3$	110	top	−0.739	2.065	−0.994	2.075
NH	100	hollow	−4.025	2.010	−3.551	2.001
NH$_2$	100	bridge	−2.624	1.963	−2.305	1.945
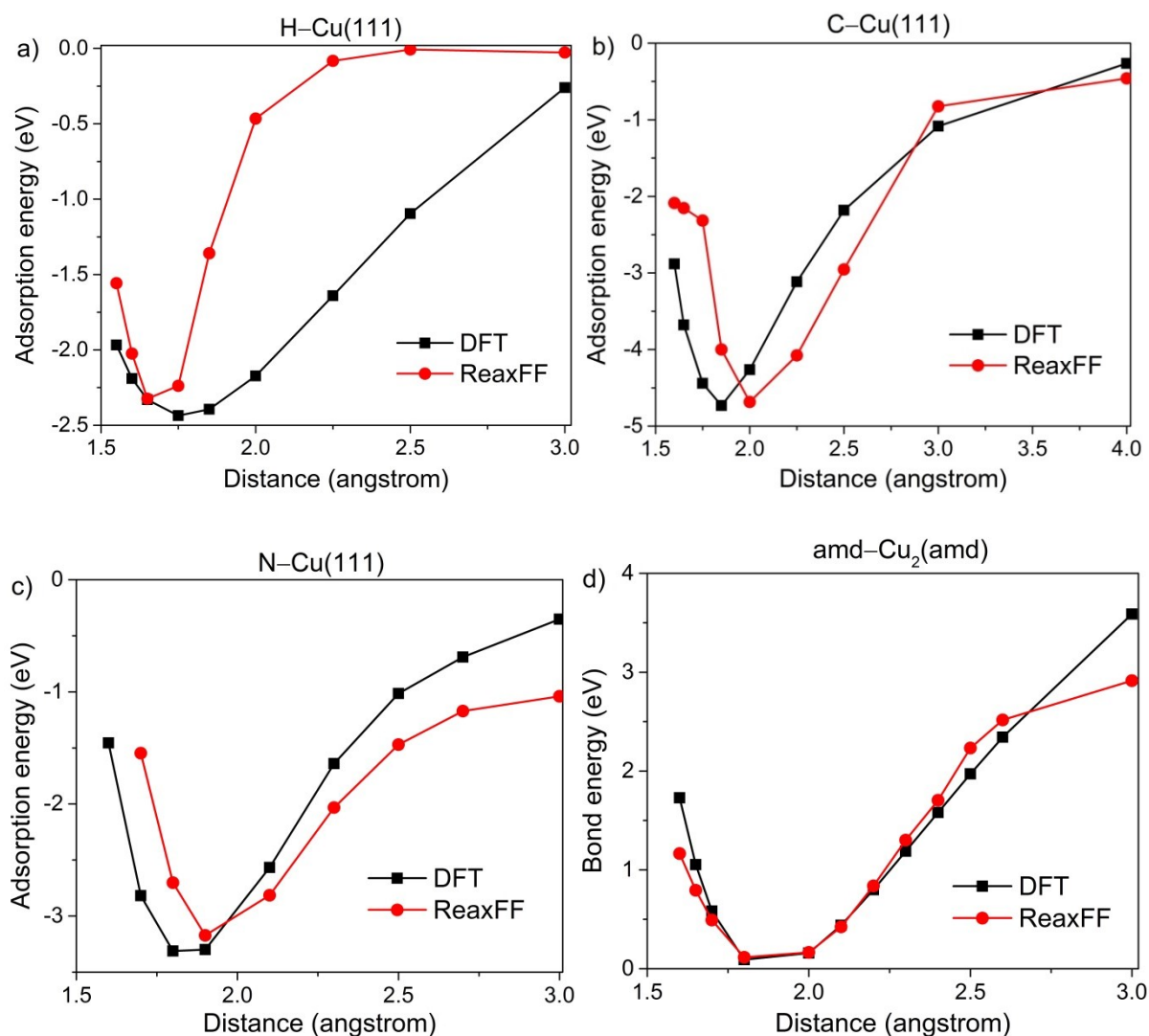
Fig. 5.4 Dependence of the adsorption energies on the adsorption distance for H, C, N atoms (a–c) on the Cu(111) surface and the dissociation energy of the [Cu(amd)]$_2$ molecule (d).
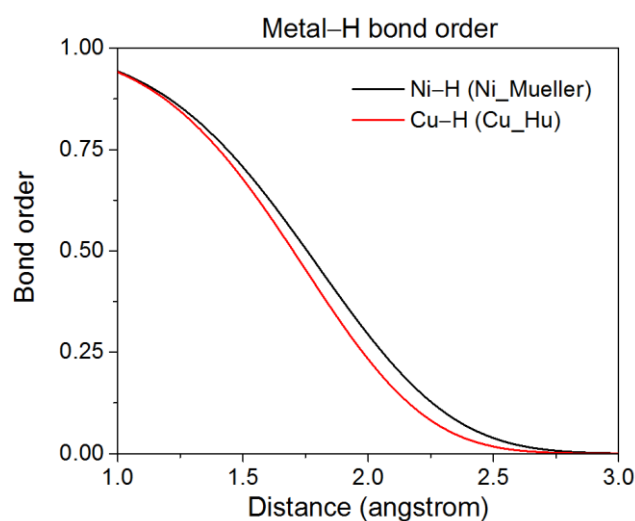

Fig. 5.5 Interatomic distance dependency of the Cu–H and Ni–H bond order (sigma bond).
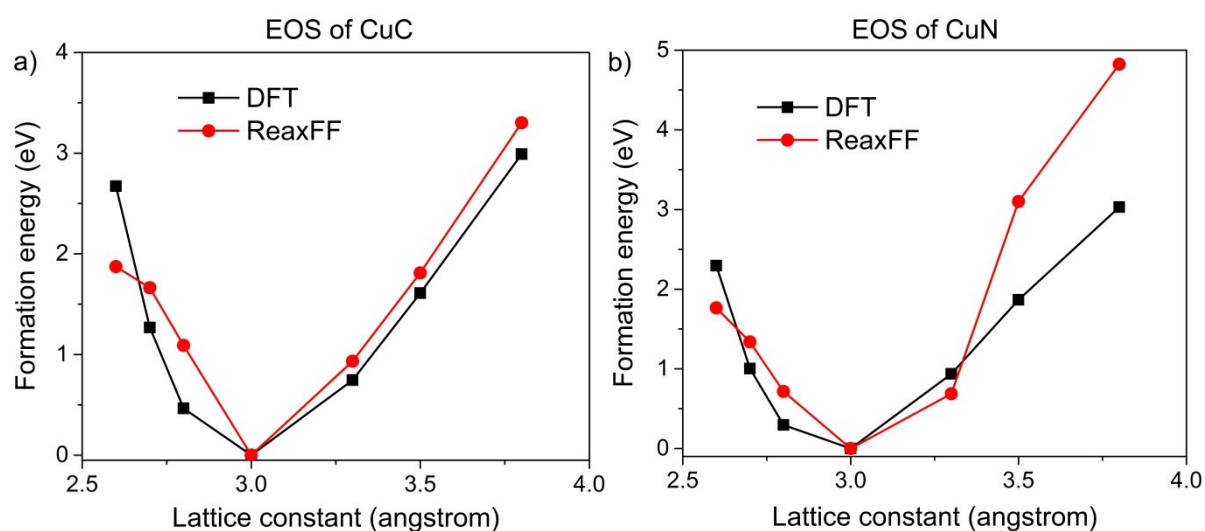
Fig. 5.6 Energy-volume equation of state (EOS) of face-centered cubic CuC (a) and CuN (b) crystals obtained by the DFT and ReaxFF calculations.
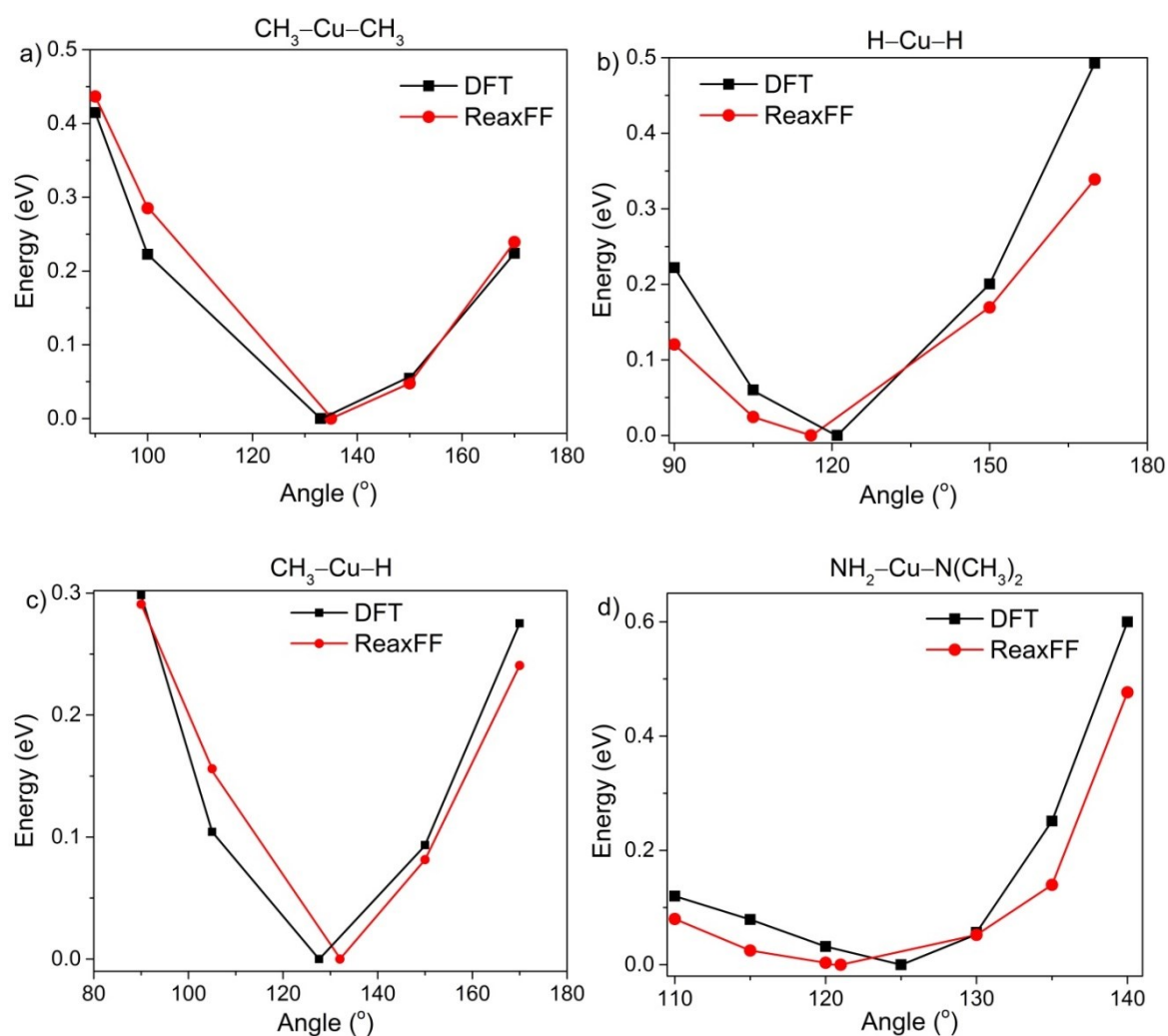

Fig. 5.7 Comparison of distortion energies calculated by ReaxFF and DFT for the bond angles in (a) C–Cu–C, (b) H–Cu–H, (c) C–Cu–H, (d) N–C–N.
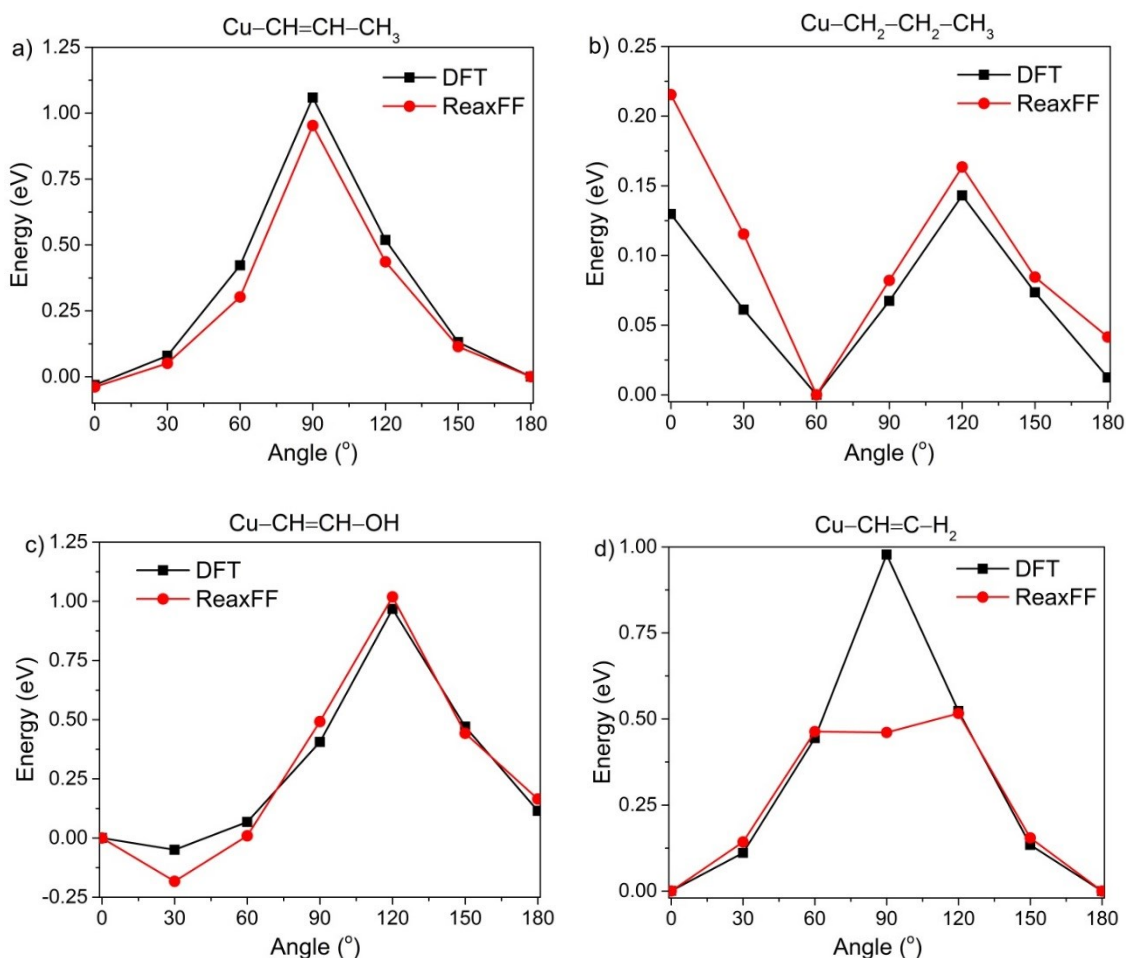
Fig. 5.8 Comparison of distortion energies calculated by ReaxFF and DFT for the dihedral angles in (a) Cu–C=C–C, (b) Cu–C–C–C, (c) Cu–C=C–O, (d) Cu–C=C–H.

To train the bond angle and dihedral angle parameters, DFT calculations are performed on small molecules to obtain the required distortion energies. During the calculations, the bond angle or dihedral angle of interest is restrained, while the rest of the molecule is allowed to relax. The comparison of the DFT and ReaxFF results for the distortion energies relative to completely relaxed molecules are shown in Figs. 5.7 and 5.8.

The training set also contains the intermediate and transition structures of reactions obtained by DFT-NEB calculations. The Cu_Hu potential is found to overestimate some reaction barriers by ~0.5 eV (Fig. 5.9). Finally, DFT calculations are performed to validate the RMD simulation results by the Cu_Hu potential. In such evaluation, single-point energy calculations are carried out using the structures obtained in RMD simulations, which are not part of the training set. The total energy of the initial state is set as the reference point. As shown in Fig. 5.10, with a few exceptions (last 3 points in Fig. 5.10b), there is a good agreement between the DFT and ReaxFF results.
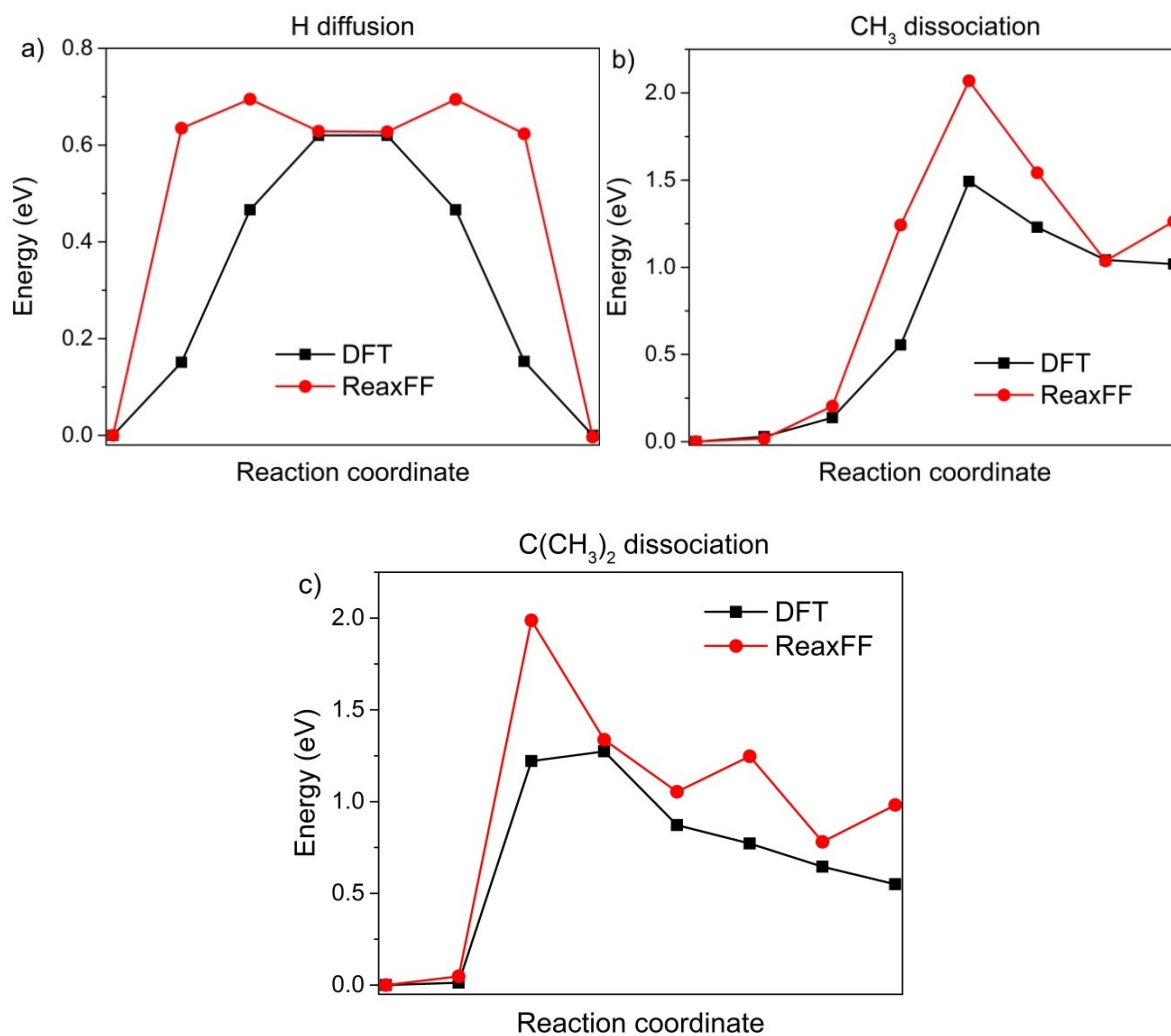
Fig. 5.9 Comparison of minimal energy path calculated by ReaxFF and DFT for the diffusion of H (a) and the dissociation of CH_3 (b) and $C(CH_3)_2$ (c) on the Cu(111) surface.
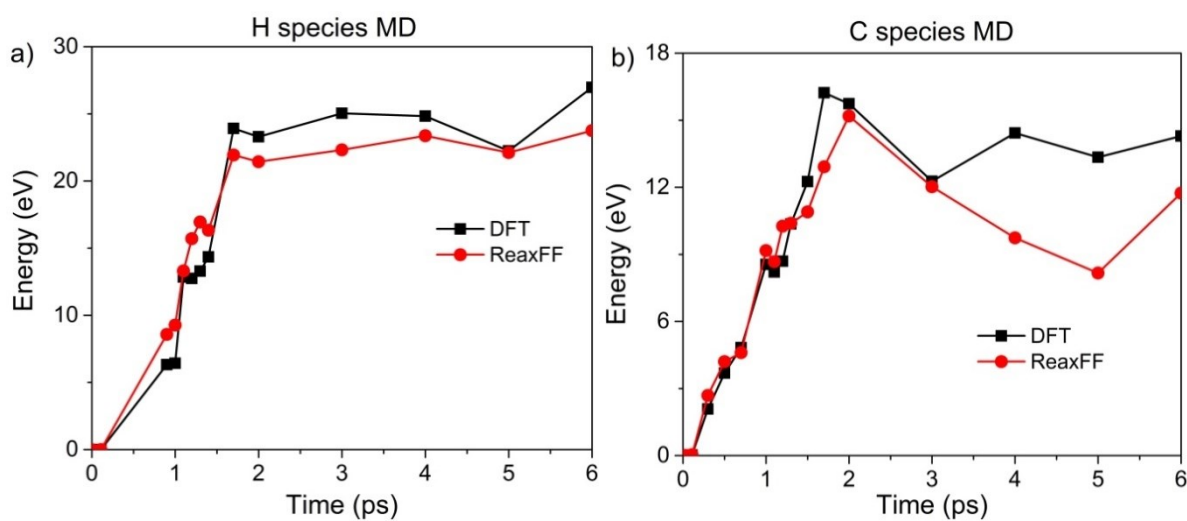

Fig. 5.10 Energy evolution during the MD simulation of H (a) and C (b) species on the Cu(111) surface calculated by ReaxFF and DFT.

Table 5.7 Percentage contribution of each factor to the (signal-to-noise) S/N and the corresponding confidence level (F).

	Factors	Early stage		Middle stage		Late stage	
		Contribution (%)	F	Contribution (%)	F	Contribution (%)	F
Bonding parameters	De(sigma)	11.2	166.9	3.0	13.1	2.9	7.0
	De(pi)	0.1	1.3	0.6	2.7	1.2	2.9
	p(be1)	0.2	2.6	0.0	0.2	1.8	4.2
	p(ovun1)	2.8	41.5	0.0	0.0	0.0	0.1
	p(be2)	0.5	6.9	0.6	2.4	1.2	2.7
	p(bo3)	0.1	1.5	0.3	1.5	6.1	14.5
	p(bo4)	0.2	3.5	0.7	3.2	1.0	2.4
	p(bo1)	0.0	0.7	1.9	8.5	0.8	1.9
	p(bo2)	0.0	0.0	3.5	15.6	0.2	0.6
Off-diagonal parameters	Dij	1.0	14.8	1.1	5.1	0.0	0.1
	RvdW	43.8	653.3	3.8	16.9	2.2	5.3
	alfa	22.9	341.3	2.3	10.1	0.8	2.0
	ro(sigma)	0.6	8.9	58.1	257.1	7.0	16.6
	ro(pi)	0.2	3.3	7.9	34.8	53.6	127.3
C–Cu–C angle parameters	Thetao,0	0.2	2.6	5.9	26.1	1.3	3.1
	p(val1)	0.1	0.8	0.6	2.6	0.8	2.0
	p(val2)	0.1	1.3	0.2	1.0	1.2	2.8
	p(val7)	0.1	0.9	0.5	2.0	0.4	0.9
	p(val4)	0.1	1.8	2.9	12.7	0.0	0.1
Cu–C–C angle parameters	Thetao,0	1.3	19.2	0.1	0.6	0.3	0.7
	p(val1)	4.4	66.1	0.1	0.3	1.0	2.4
	p(val2)	0.2	3.2	0.2	1.0	0.1	0.3
	p(val7)	0.2	2.2	0.1	0.3	0.6	1.5
	p(val4)	1.4	21.4	0.0	0.0	4.0	9.4
Cu–C–Cu angle parameters	Thetao,0	4.8	71.4	0.5	2.4	0.7	1.8
	p(val1)	0.6	9.4	0.3	1.2	0.3	0.7
	p(val2)	0.4	6.5	0.0	0.2	0.2	0.5
	p(val7)	0.1	1.2	0.5	2.2	0.1	0.3
	p(val4)	0.9	13.6	0.4	1.9	0.3	0.6
Cu–C–C–C torsion parameters	V2	0.1	1.9	0.3	1.2	0.1	0.1
	V3	0.5	6.7	0.3	1.4	3.7	8.8
	p(tor1)	0.1	0.7	0.3	1.4	1.4	3.3
Cu–C–C–Cu torsion parameters	V2	0.5	6.8	0.6	2.4	0.8	1.9
	V3	0.1	0.8	0.8	3.7	1.8	4.3
	p(tor1)	0.0	0.6	0.3	1.4	0.2	0.4

Significant at 99% confidence level: $F_{0.01, 2, 8} = 8.7$. The most significant factors ($F \geq 8.7$) are marked with red color.

A statistical analysis has been performed using the ANOVA-scheme. The results during different stages of the parameterization of Cu/C are shown in Table 5.7. It is found that the significance of an individual parameter is always changing during the parameterization. This may depend on the input value, scaling factor, selected parameters, and stage of training. The number of significant factors (above 99% confidence), as well as the corresponding confidence level (F), decreases as the parameterization proceeds. At the late training stage, there are only very few significant factors, suggesting that most of the factors have been well optimized. In general, the most significant parameters are the off-diagonal parameters, which contribute to more than 60% of S/N, regardless of the training stages. This conclusion is also applicable to the optimization of Cu/H and Cu/N parameters. Therefore, a high priority should be given to these parameters in further works of force field development. Furthermore, compared to other parameters, a smaller scaling factor is recommended for the off-diagonal parameters.

In short, a new Cu potential Cu_Hu is developed in this work by using DFT data as a benchmark. The missing Cu/C and Cu/H interactions in the Cu_vanDuin potential have been added, which may be significant for simulating the hydrogen plasma-enhanced ALD process. Furthermore, the existing Cu–N parameters are re-optimized in order to accurately describe the [Cu(amd)]$_2$ precursor. With a few exceptions, the Cu_Hu potential correctly reproduces the adsorption energies and the adsorption distances on the Cu surface as obtained by DFT. The distortion energies of small molecules calculated by the Cu_Hu potential are also in satisfactory agreement with the DFT results. However, the Cu_Hu potential fails to completely predict the Cu–H bond dissociation curve, due to the inherent limitations of the potential functions. Modification of the potential functions is necessary to solve such problem. Statistical analysis based on the ANOVA-scheme shows that the off-diagonal parameters are the most significant parameters in the ReaxFF potential.

5.4 RMD simulations of the reactions between Cu(acac)$_2$ and different co-reactants

Previously, H, H$_2$O and O$_3$ were used as the co-reactants for the Cu(acac)$_2$ precursor with respect to the ALD of metallic Cu or Cu oxides [19, 18, 28]. However, the underlying reaction mechanisms of ALD are still unclear. While H(acac) was proposed as the reaction product for the Cu(acac)$_2$/H and Cu(acac)$_2$/H$_2$O processes, this species has not been directly observed in the experiment. In this section, RMD simulations are performed to investigate the

surface reactions between Cu(acac)$_2$ and different co-reactants. Both the Cu_Hu and Cu_vanDuin potentials have been used to evaluate the effect of Cu/H and Cu/C interactions on surface reactions. RMD simulations show the detailed chemical reactions of ALD as well as the time evolution of species. Based on the reaction rate, the reactivity of different co-reactants towards the Cu(acac)$_2$ precursor can be predicted.

5.4.1 Dissociation of Cu(acac)$_2$ on different substrates

As a first application of the reactive force field, the surface decomposition of Cu(acac)$_2$ is investigated by means of RMD simulation. Snapshots of the decomposition of Cu(acac)$_2$ on the Cu(110) surface at 600 K are shown in Fig. 5.11.

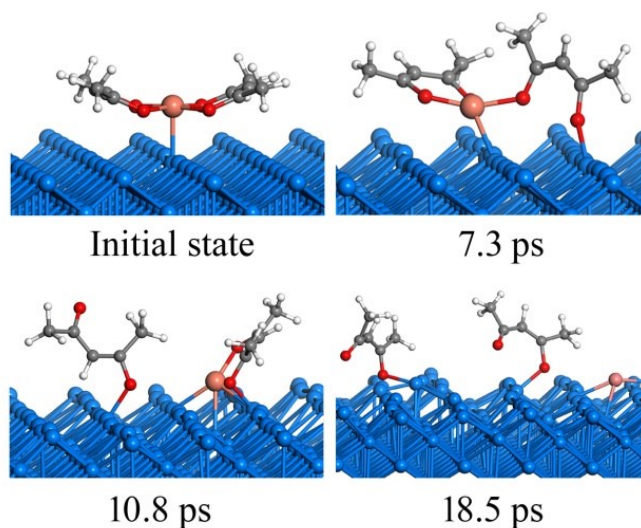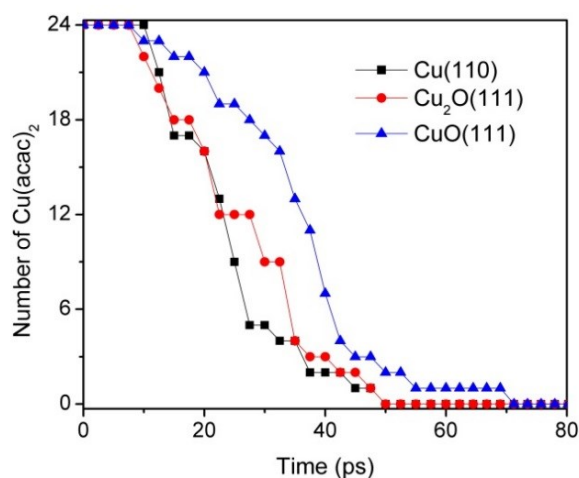**Fig. 5.11** RMD snapshots (by the Cu_vanDuin potential) of the dissociation of Cu(acac)$_2$ on the Cu(110) surface.

Fig. 5.12 Comparison of the dissociation of Cu(acac)$_2$ on Cu(110), Cu$_2$O(111), and CuO(111) surfaces at 600 K (by the Cu_vanDuin potential).

In general, the reaction pathways observed in RMD simulations are consistent with those from the DFT calculations (see Fig. 4.15). As shown in Fig. 5.11, the reaction starts by breaking the Cu–O bond and tilting the acac-ligand (7.3 ps). Next, the acac-ligand dissociates completely from the $Cu(acac)_2$ molecule, forming acac and Cu(acac) species on the surface (10.8 ps). Finally, Cu(acac) dissociates into Cu and acac on the surface after 18.5 ps. Experimentally, the complete decomposition of $Cu(acac)_2$ to metallic Cu is reported to occur at around 300 K [32]. Such a low reaction temperature suggests high reactivity of the Cu surface towards $Cu(acac)_2$, which is consistent with the small activation energy calculated by DFT (Fig. 4.15). In addition, a facile reaction process is also compatible with the time scale of RMD simulations. Fig. 5.12 shows a comparison of the dissociation of $Cu(acac)_2$ on Cu(110), $Cu_2O(111)$, and CuO(111) surfaces. Initially, 24 $Cu(acac)_2$ precursors are placed above the surfaces. As illustrated in Fig. 5.12, the $Cu(acac)_2$ molecules are completely decomposed after ~70 ps at 600 K. The reaction on the copper-rich surfaces [Cu(110) and $Cu_2O(111)$] is faster compared with CuO(111), indicating that surface Cu atoms are the reactive species towards the acac-ligand.

5.4.2 Surface reactions between $Cu(acac)_2$ and atomic H

In order to complement the picture of the surface reactions of $Cu(acac)_2$ on various surfaces, the role of different co-reactants (H_2, H, H_2O, and O_3) is analyzed. These co-reactants are widely used throughout ALD-processes. First, the reaction with molecular hydrogen is studied. The RMD investigations revealed that molecular H_2 hardly reacts with $Cu(acac)_2$ on the surface at 600 K. Instead, the molecules are found to assemble around the precursor, having weak attractive but non-bonding interactions with the structure. Therefore, H_2 molecules are not considered in further studies. Indeed, molecular H_2 is rarely employed as co-reactant for Cu beta-diketonates [28]. Alternatively, a PEALD process [27, 28] or a strong reducing agent [13, 15] is required to directly deposit metallic Cu thin films.

Next, the surface reactions between $Cu(acac)_2$ and gaseous H atoms on Cu(110) are discussed as a model system for the PEALD of Cu. The corresponding RMD snapshots obtained by the Cu_Hu potential are shown in Fig. 5.13. The influences of other plasma-generated components, such as charged particles, electric fields, and heat [42], are not considered in this work. In contrast to the molecular species, atomic hydrogen is found to be very reactive towards the Cu precursor. As illustrated in Fig. 5.13, $Cu(acac)_2$ breaks the Cu–O bonds upon the hydrogen impact, releasing a C_5H_9O molecule into the gas-phase (5.4 ps). The
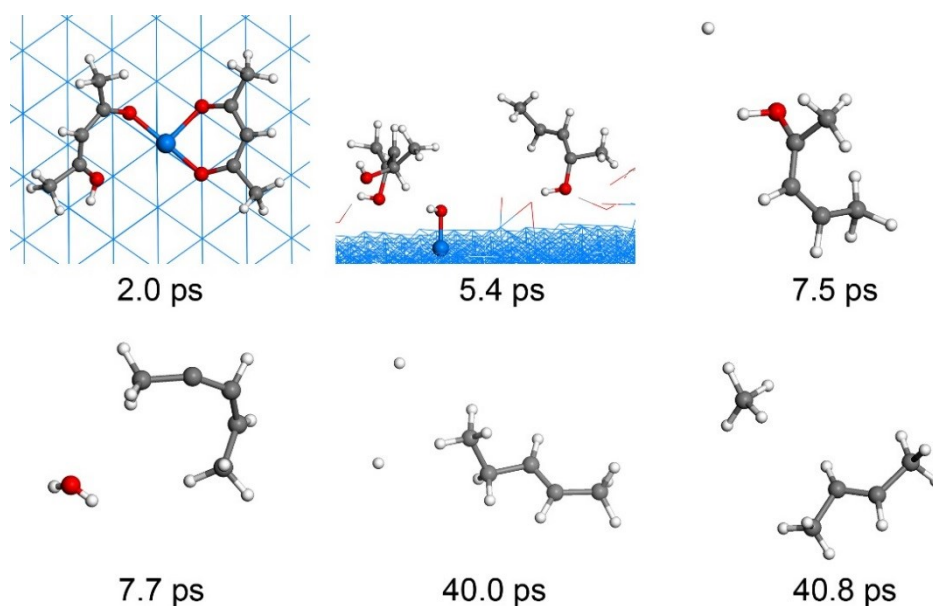
Fig. 5.13 RMD snapshots (by Cu_Hu) of the reactions between Cu(acac)$_2$ and H atoms on the Cu(110) surface.

oxygen atom in C$_5$H$_9$O is then abstracted by the hydrogen, and a water molecule is formed (7.7 ps). Finally, the remaining fragment C$_5$H$_9$ further reacts with the hydrogen to form CH$_4$ and C$_4$H$_6$ molecules (40.8 ps).

A comparison of the Cu_Hu and Cu_vanDuin potentials for the time evolution of species is shown in Fig. 5.14. In the gas-phase, simulation results obtained by both potentials are very similar. The main gaseous by-products observed are C$_x$H$_y$ and H$_x$O. The decomposition of hydrocarbon species on the Cu surface is found to be unfavorable at low temperatures. In the initial state, formation of the H$_x$O species is slightly faster than that of the C$_x$H$_y$ species, indicating that atomic hydrogen reacts first with the oxygen of the Cu precursor. The system reaches equilibrium after about ~150 ps, and reactive H atoms have been completely consumed. On the surface, the Cu_Hu potential results show that most C atoms and about 40% O atoms are removed, whereas the amount of H is increased dramatically due to the adsorption. These H atoms can act as reactive species for the next ALD half-cycle (see below). In contrast, when the Cu_vanDuin potential is used only a few H atoms are present on the surface after simulations since the Cu−H bonding interactions are not considered. As a consequence, the reactivity of H atoms are enhanced, and a larger amount of C$_x$H$_y$ and H$_x$O by-products is released in the gas-phase. In short, the overall surface reaction between Cu(acac)$_2$ and atomic H can be described as follows

$$\text{Cu(acac)}_2^* + 35\text{H(g)} \rightarrow \text{CuH}^* + 10\text{CH}_4\text{(g)} + 4\text{H}_2\text{O(g)} \tag{5.16}$$
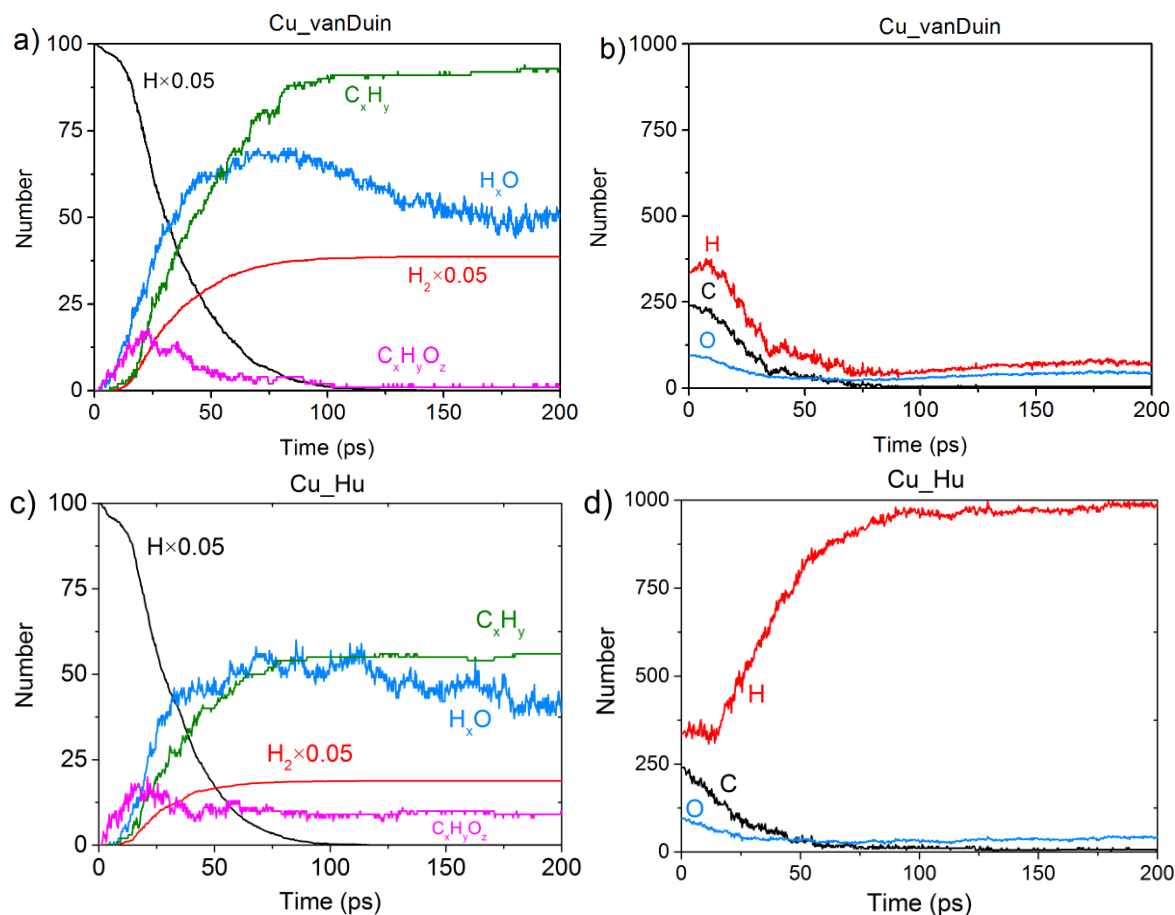
Fig. 5.14 Product evolution in the surface reactions between Cu(acac)$_2$ and atomic H in the gas-phase (a, c) and on the surface (b, d) using the Cu_vanDuin and Cu_Hu potentials.

Previous works [28, 73, 74] have found that the surface-adsorbed H atoms, generated by catalytic substrates or by plasma, exhibit an enhanced reactivity towards Cu precursors as compared to molecular H$_2$. However, the underlying reaction mechanisms have not been investigated in detail. Further RMD simulations are thus performed to support the experimental studies using the Cu_Hu potential and the hydrogen pre-coated Cu surface (0.25 ML coverage). For this situation the Cu_vanDuin potential is not considered, since the chemisorption of hydrogen on the Cu surface cannot be realized.

Some snapshots of the reactions between Cu(acac)$_2$ and adsorbed H are depicted in Fig. 5.15. The Cu(acac)$_2$ precursor first dissociates into Cu(acac) and acac on an H-terminated Cu surface (8.0 ps), which is the same as that taking place on a clean Cu surface. Next, the dissociated Cu(acac) reacts with a nearby H atom, forming the new H−O bond and breaking the existing Cu−O bonds (19.9 ps). An H(acac) molecule is then produced and desorbs from the surface (23.1 ps). The formed H(acac) may also re-adsorb on the surface and react with
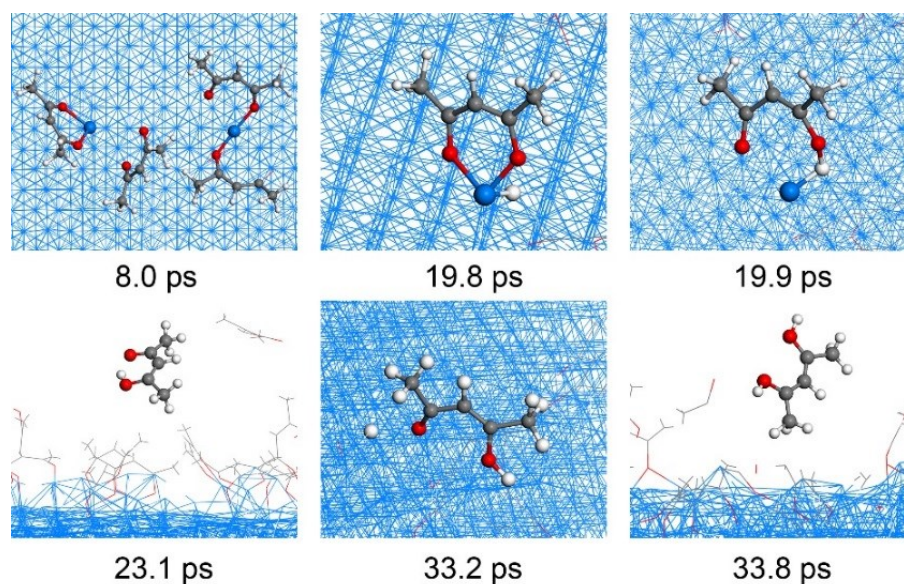
Fig. 5.15 RMD snapshots of the reactions between Cu(acac)$_2$ and adsorbed H on the Cu(110) surface.

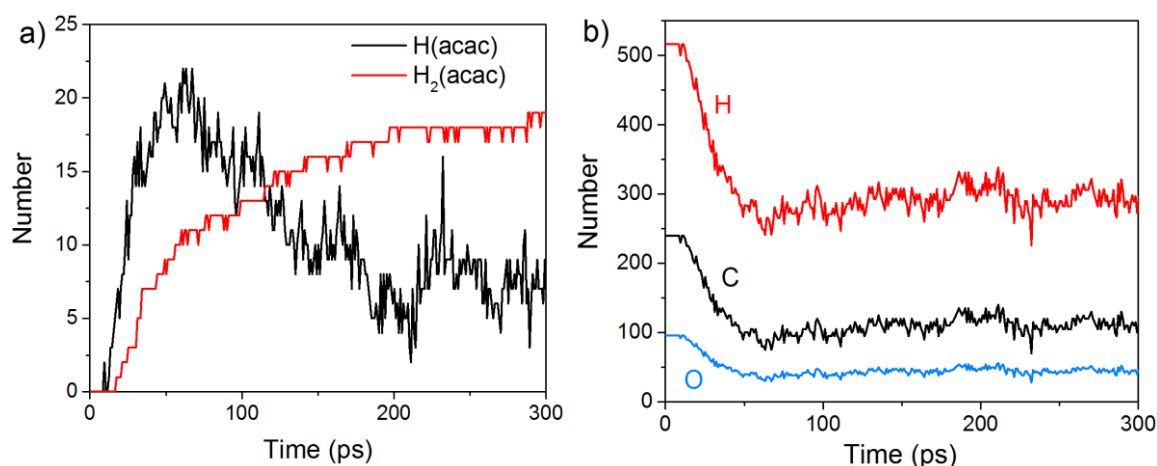**Fig. 5.16** Product evolution in the surface reactions between Cu(acac)$_2$ and adsorbed H in the gas-phase (a) and on the surface (b) using the Cu_Hu potential.

another surface H atom to produce H$_2$(acac) (33.8 ps). Fig. 5.16 shows the time evolution of species during the RMD simulations. It is found that H(acac) and H$_2$(acac) are the only by-products of the surface reactions. At an equilibrium state, about 50% surface acac-ligands are released into the gas-phase. The decomposition of H(acac) and H$_2$(acac) has not been observed, perhaps due to an insufficient amount of reactive H atoms on the surface. The surface reactions proposed are summarized in Eqs. 5.17 and 5.18.

$$Cu(acac)_2^* + H^* \rightarrow Cu(acac)^* + H(acac)(g) \tag{5.17}$$

$$H(acac)(g) + H^* \rightarrow H_2(acac)(g) \tag{5.18}$$
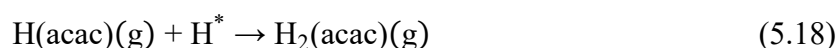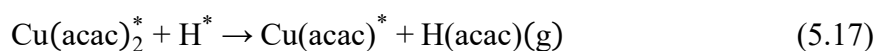
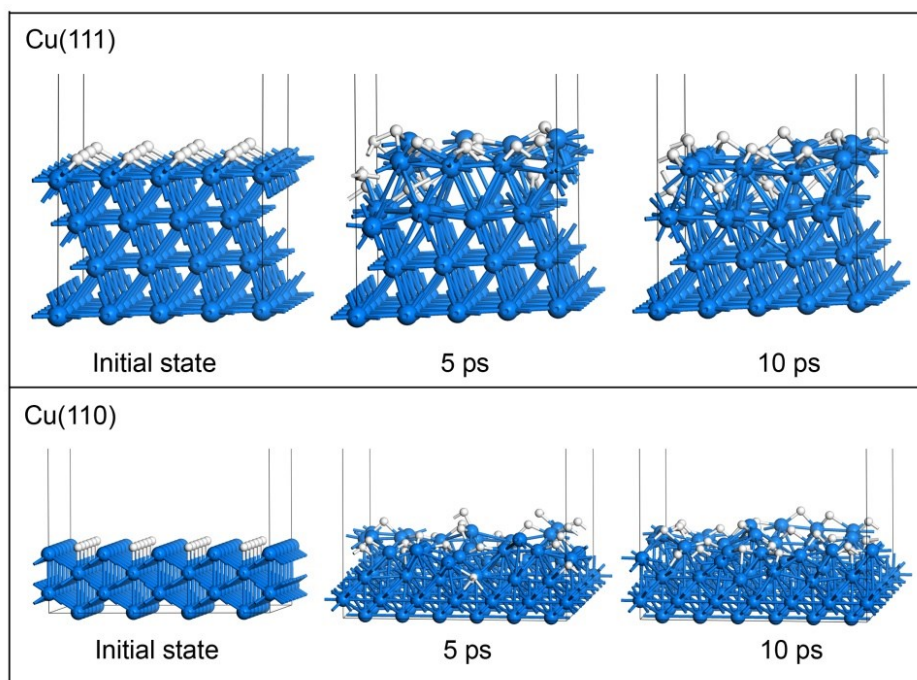**Fig. 5.17** Snapshots of the AIMD simulation of the H precoated Cu(111) and Cu(110) surface.

Guo et al. [81] suggested that the adsorbed H atoms may easily undergo a recombination on the Cu surface, forming molecular H_2 and releasing it into the gas-phase. Therefore, only a few ligands can be removed during the Cu precursor pulse due to the lack of reactive species on the surface. However, the formation and desorption of H_2 molecules is not observed in this study. Instead, about half of the acac-ligands have been removed by the surface H atoms. To verify the RMD simulation results, AIMD is performed to investigate the sticking of atomic H on the Cu(110) and Cu(111) substrates. To enhance the probability of H recombination, the AIMD simulations are performed under a high coverage (1 ML hydrogen) and at an elevated temperature (800 K). As shown in Fig. 5.17, the H atoms may easily migrate on the surface and diffuse into the subsurface (observed in RMD also). However, the recombination of H has not been observed after 10 ps of AIMD simulations, which is consistent with the RMD results.

5.4.3 Surface reactions between Cu(acac)₂ and H₂O

In this section, the surface reactions between Cu(acac)$_2$ and H_2O are analyzed. Cu$_2$O(111) is used as a substrate since Cu beta-diketonates with H_2O primarily deposit cuprous oxide films at low temperatures [19,177,178]. Previous works [161,162] have shown that water facilitates the deposition of Cu$_2$O through the following ligand-exchange reaction:

$$Cu(acac)_2^* + H_2O(g) \rightarrow Cu(acac)OH^* + H(acac)(g) \qquad (5.19)$$

RMD simulations predict the following reaction mechanisms, which are consistent with previous findings. As shown in Fig. 5.18, $Cu(acac)_2$ first dissociates into $Cu(acac)$ and acac on the surface after ~25 ps of simulations. Secondly, a proton is transferred from water to the adsorbed $Cu(acac)$, forming $Cu[H(acac)]$ and OH species on the surface (56.8 ps). Finally, the Cu–O bond of the $Cu[H(acac)]$ intermediate is broken after 118.6 ps, which leads to the desorption of H(acac) from the surface to the gas-phase. A similar ligand-exchange mechanism has been widely observed in water-based metal oxide ALD, for example, in the TMA–H_2O and $Hf(NMe_2)_4$–H_2O processes [12, 164]. During the water pulse, the adsorbed Me- or NMe_2-ligands are replaced by –OH groups, followed by the elimination of gaseous CH_4 or $HNMe_2$ [12,164]. It is noticed that the cleavage of the Cu–O bond of $Cu(acac)_2$ is promoted in the presence of atomic H. In contrast, when water is used as a co-reactant, the proton transition occurs after $Cu(acac)_2$ is completely dissociated on the surface. These observations suggest that water is less reactive towards $Cu(acac)_2$ as compared to atomic H.

Fig. 5.19 shows the time evolution of species in the gas-phase and on the surface. H(acac) is the primary gaseous product during the reactions, while the amount of acac and $H_2(acac)$ is minor. After 800 ps of RMD simulations, about 35%–40% of the surface acac-ligands are released into the gas-phase. The results from the Cu_Hu potential are very similar to those from the Cu_vanDuin potential, but the Cu_Hu potential predicts a higher removal rate of the surface acac-ligands.
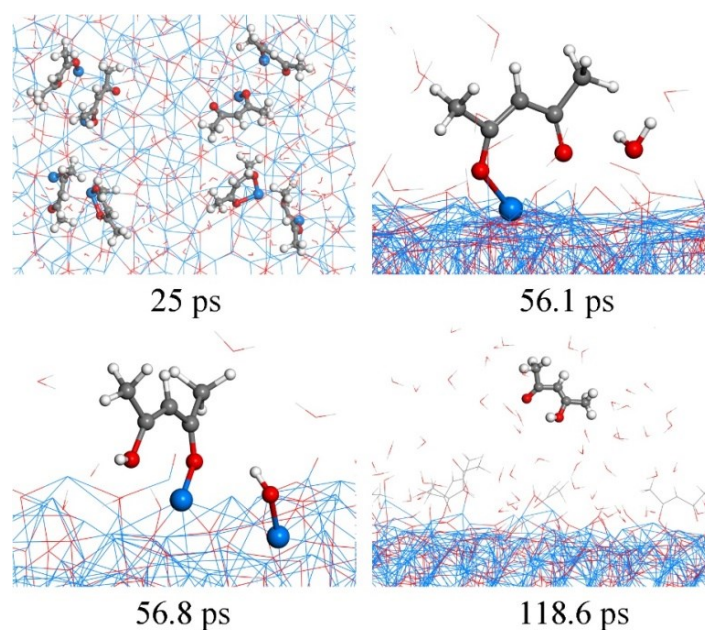

25 ps 56.1 ps

56.8 ps 118.6 ps

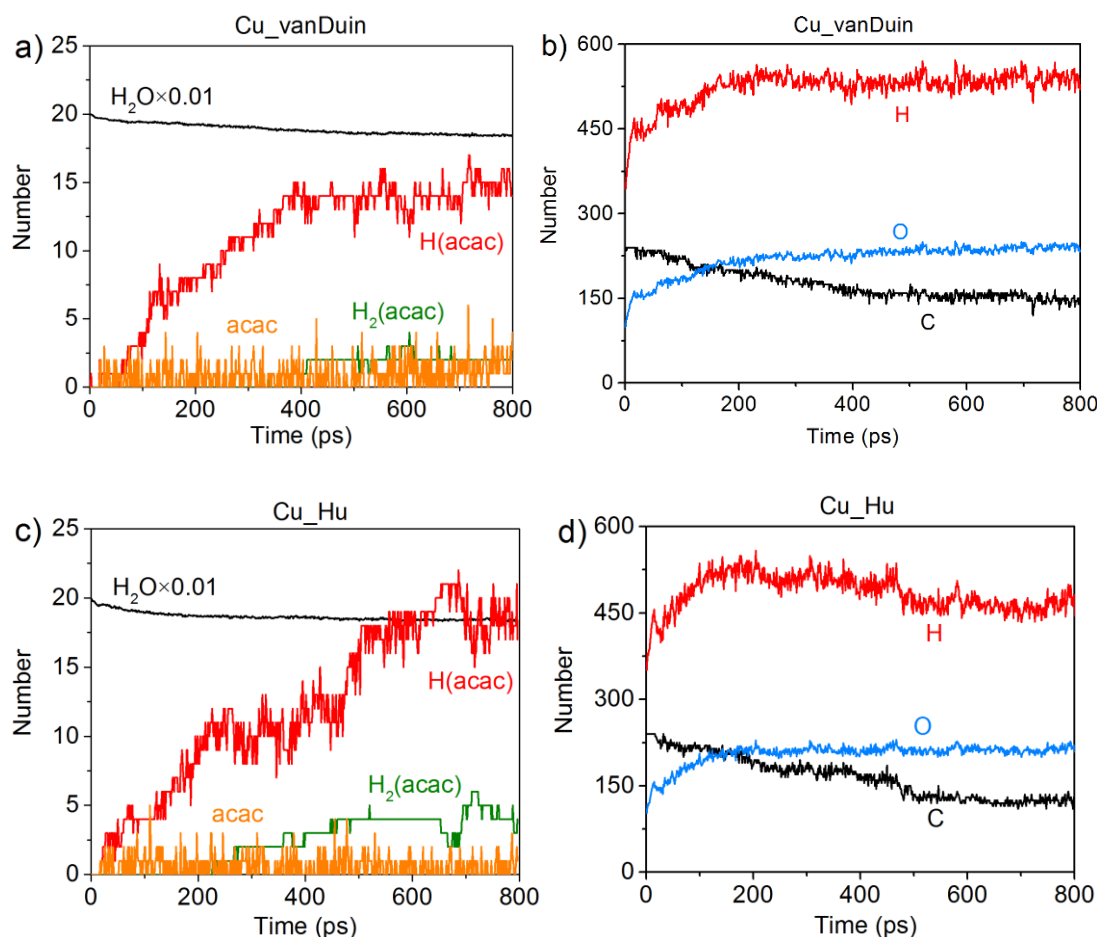**Fig. 5.18** RMD snapshots (by Cu_vanDuin) of the reactions between $Cu(acac)_2$ and H_2O on the Cu(110) surface.

Fig. 5.19 Product evolution in the surface reactions between $Cu(acac)_2$ and H_2O in the gas-phase (a, c) and on the surface (b, d) using the Cu_vanDuin and Cu_Hu potentials.

5.4.4 Surface reactions between $Cu(acac)_2$ and O_3

RMD snapshots (by using Cu_vanDuin) of the surface reactions between $Cu(acac)_2$ and O_3 are shown in Figs. 5.20 and 5.21. The CuO(111) surface is used in these simulations, which is in line with the experimental observation that CuO is deposited by the $Cu(acac)_2–O_3$ ALD process [18]. As depicted in Fig. 5.20, ozone molecules are found to bind readily with the methyl groups, forming hydrogen bonds with an O–H bond length of ~1.9 Å (Fig. 5.20 a). One H atom of the acac-ligand is then abstracted by the ozone, which results in the production of OH and O_2 (16.8 ps). The released OH radical either re-adsorbs on the surface or reacts with the methyl hydrogen to produce H_2O (99.4 ps). Moreover, it is observed that the O atom of O_3 can insert into the C–H bond of a –CH_3 group, leading to the formation of CH_2OH amd O_2 species (94.3 ps). A similar insertion step has been reported to occur in the TMA–O_3 ALD process, proven by infrared spectroscopy and DFT calculations [179–181]. In comparison with the abstraction of hydrogen atoms, the C–C cleavage usually takes place later. As shown

124
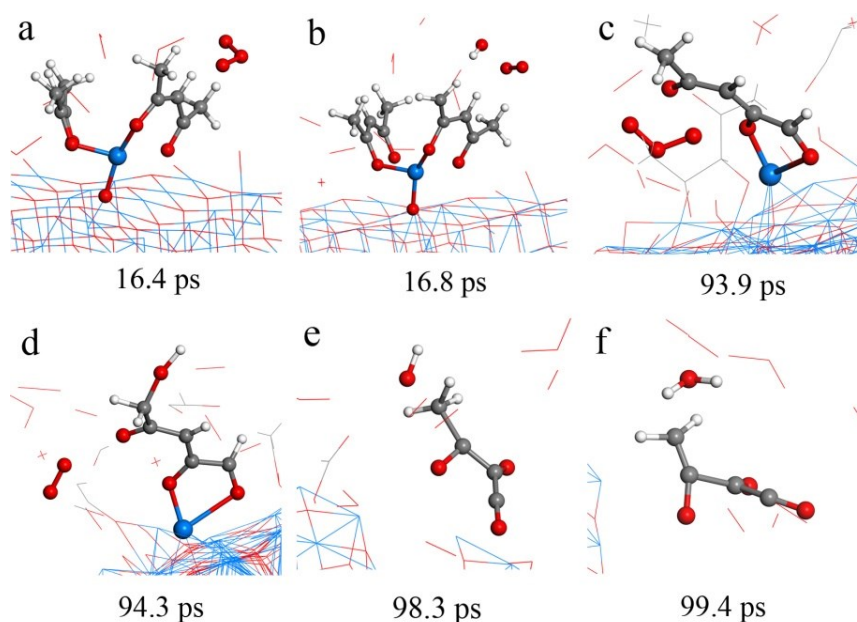
Fig. 5.20 RMD snapshots (by Cu_vanDuin) of H abstraction (a, b), O insertion (c, d), and water formation (e, f), observed during the reactions between Cu(acac)$_2$ and ozone on the CuO(111) surface.
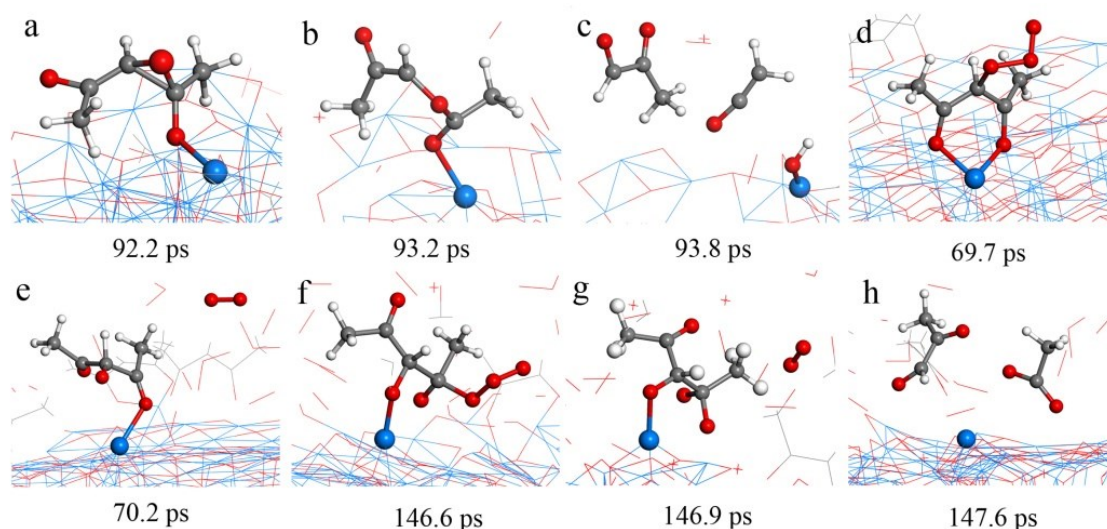
Fig. 5.21 RMD snapshots (by Cu_vanDuin) of the C–C bond breaking observed during the reactions between Cu(acac)$_2$ and ozone on the CuO(111) surface.

in Figs. 5.21 a–c, an oxygen atom first adsorbs on the bridging C–C site to form an epoxide (92.2 ps). The C–C bond is then cleaved by the O atom through an epoxy–ether transformation (93.2 ps). At the same time, the acac-ligand breaks the bond with the surface Cu and is thus released to the gas-phase. Subsequently, the formed complex dissociates into C$_3$H$_4$O$_2$ (methylglyoxal), C$_2$H$_2$O (ethenone), and an adsorbed hydroxyl group (93.8 ps). At last, C$_3$H$_4$O$_2$ and C$_2$H$_2$O species are further oxidized into CO, CO$_2$, and OH after about 80 ps

of simulations. Figs. 5.21 d–h illustrate an alternative reaction pathway for the cleavage of a C–C bond. After the continuous adsorption of two O atoms, the acac-ligand dissociates into gaseous $C_3H_4O_2$ (methylglyoxal) and adsorbed $C_2H_3O_2$ (acetate). The formed $C_2H_3O_2$ readily desorb from the surface and dissociates into CO_2 and CH_3 in the gas-phase.

Fig. 5.22 shows the time evolution of species in the gas-phase and on the surface. There is a very small difference between the Cu_Hu potential and Cu_vanDuin potential results. It is found that most of the O_3 molecule are converted into O_2 after ~180 ps upon either a surface reaction or a self-dissociation in the gas-phase. The H_xO_y and CO_x species are found to be the main reaction products, suggesting a combustion-like reaction mechanism. These findings are consistent with the thermodynamic modeling, in which H_2O and CO_2 are predicted as the reaction products (Section 4.4.1). However, due to an insufficient amount of O_3 in the system, the complete oxidation of the acac-ligands into H_2O and CO_2 is not observed in RMD simulations. The concentration of H_xO_y in the gas-phase first increases and then decreases after 80 ps. At an equilibrium state, about 70% of the surface C impurities are released into the
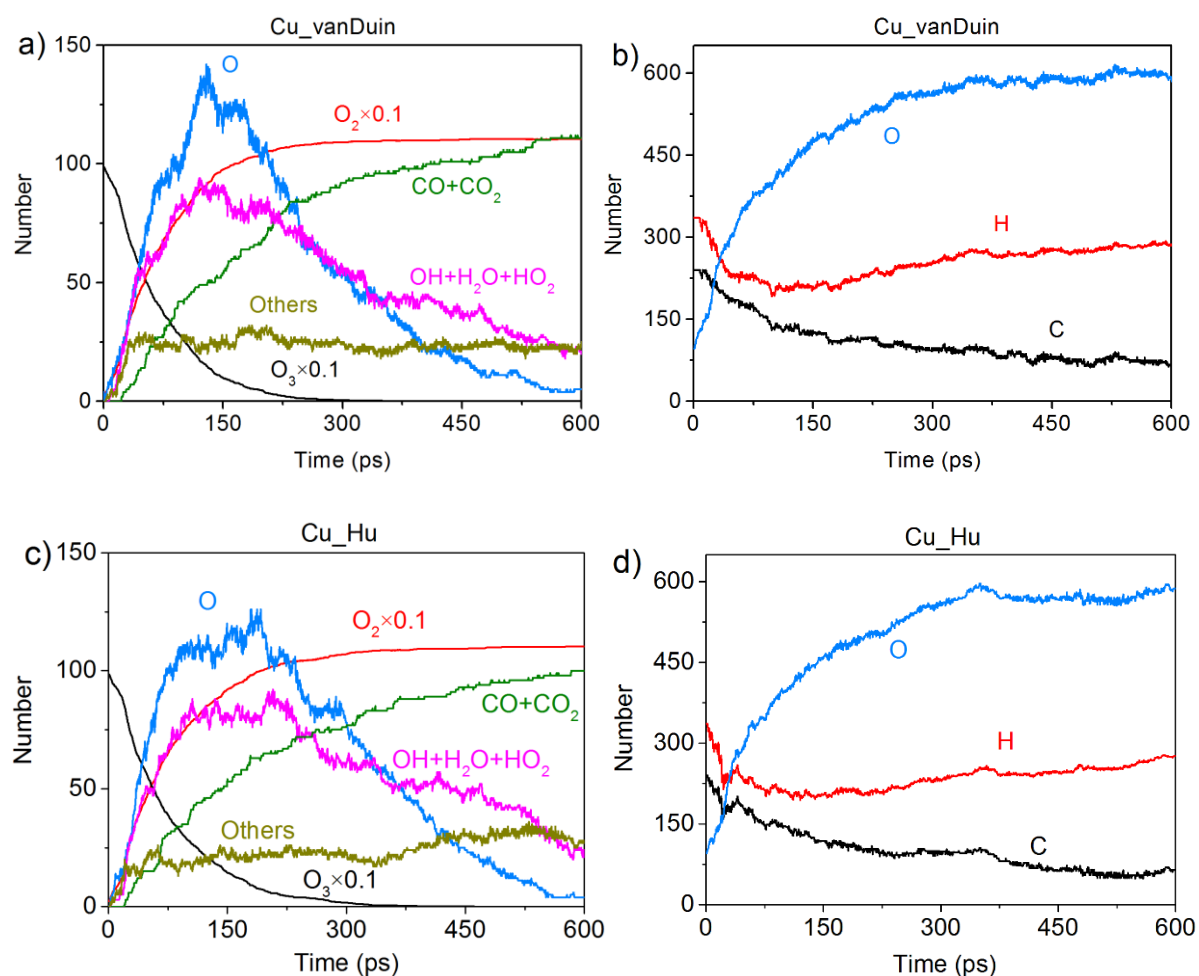

Fig. 5.22 Product evolution in the surface reactions between Cu(acac)$_2$ and O_3 in the gas-phase (a, c) and on the surface (b, d) using the Cu_vanDuin and Cu_Hu potentials.

gas-phase, whereas the amount of surface O increases significantly after the O_3 pulse (Fig. 22b). Most of the gaseous H_xO_y is re-adsorbed on the surface, and thus protons are available for a ligand-exchange reaction during the subsequent $Cu(acac)_2$ pulse, which is similar to the $Cu(acac)_2/H_2O$ ALD process. The overall reaction between $Cu(acac)_2$ and O_3 is summarized in Eq. 5.20

$$Cu(acac)_2^* + 7.83O_3(g) \rightarrow CuOH^* + 10CO_2(g) + 6.5H_2O(g) \tag{5.20}$$

Based on the reaction rate and the carbon removal ratio at different conditions, it can be inferred that the reactivity of co-reactants towards $Cu(acac)_2$ follows the order $H > O_3 > H_2O > H_2$. From experiments, it is well known that the reactivity of co-reactants has a significant effect on the ALD window. The lower bound of the ALD window is mainly determined by the thermal activation of surface reactions as well as by the volatility of precursors [12]. Therefore, the ALD window could be used as an indicator to evaluate the reactivity between the Cu precursor and different co-reactants. A lower deposition temperature is associated with a higher reactivity of the co-reactant towards $Cu(acac)_2$. As reported in the literature, when using H plasma with $Cu(acac)_2$, the ALD window is as low as 85–135 °C [28]. However, much higher temperatures are required when ozone (150–230 °C) [18] or water (210–300 °C) [182] is used as the co-reactant. These findings are consistent with the conclusion that atomic H is more reactive than ozone and water.

By comparison between the Cu_vanDuin and Cu_Hu results (Figs. 5.19 and 5.22), it is observed that the Cu–H and Cu–C interactions play a minor role in oxide surface reactions of the $Cu(acac)_2/H_2O$ and $Cu(acac)_2/O_3$ processes. However, the Cu–H interactions are crucial for the reactions between $Cu(acac)_2$ and H, since the H atoms can easily adsorb on the Cu metal surface (see Fig. 5.14d), and act as reactive species for the next half-cycle (i.e., Cu precursor pulse). On the other hand, after surface reactions most of the adsorbed carbon species are removed into the gas-phase, suggesting a weak interaction between the carbon and the Cu surface. Decomposition of the acac-ligand and other hydrocarbon species on the surface have not been observed under ALD conditions. In short, RMD simulations demonstrate a clean surface chemistry of $Cu(acac)_2$ on the Cu metal surface, which can be supported by DFT calculations (Section 4.3.2) as well as previous experimental studies. As reported in Ref. [28], high purity Cu films (> 95 at. %) with an undetectable amount of C were obtained by PEALD using the $Cu(acac)_2$ precursor.

5.5 RMD simulations of the reactions between Cu(acac) and wet O₂

According to the thermodynamic modeling (Section 4.3), CO_2 and H_2O are predicted as the most favorable gaseous products for the surface reaction between $(Me_3P)_2Cu(acac)$ and wet O_2. In this section, RMD simulations are performed to illuminate the role of water in the ALD of Cu_2O. The mechanism and the kinetics of H(acac) oxidation are also discussed. Cu(acac) is used in this work to model the Cu(I) beta-diketonate precursor. The effect of Me_3P-ligands is not considered since no ReaxFF parameters are currently available for the Cu–P bond.

5.5.1 Surface reactions between Cu(acac) and wet O₂

Typical snapshots of the reactions between adsorbed Cu(acac) and wet O_2 are depicted in Fig. 5.23. First, a water molecule is adsorbed on the Cu_2O surface and diffuses to a nearby Cu(acac). Next, a proton from the water is transferred to Cu(acac), forming Cu[H(acac)] and OH species on the surface. Finally, the Cu–O bond of the Cu[H(acac)] complex is broken, which results in the release of H(acac) into the gas-phase. In general, the reaction between Cu(acac) and wet O_2 is similar to that between $Cu(acac)_2$ and H_2O, as described by following ligand-exchange reaction

$$Cu(acac)^* + H_2O(g) \rightarrow CuOH^* + H(acac)(g) \qquad (G^0_{400K} = 0.55 \text{ eV}) \quad (5.21)$$
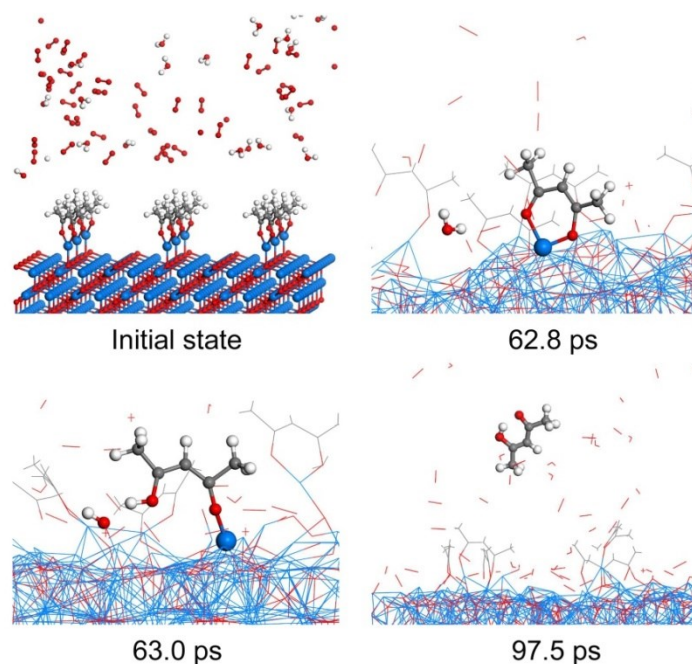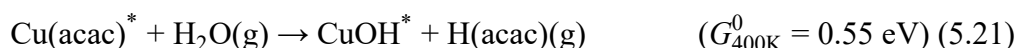

Fig. 5.23 RMD snapshots (by Cu_vanDuin) of the reaction between Cu(acac) and wet oxygen.
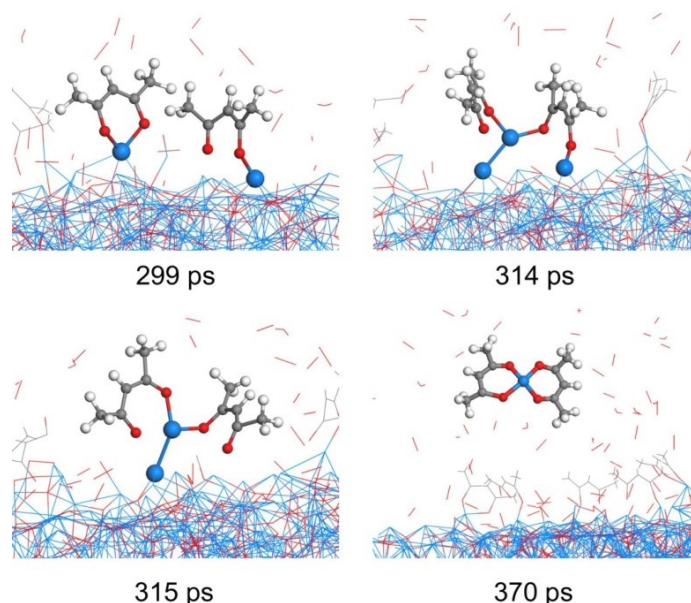
Fig. 5.24 RMD snapshots (by Cu_vanDuin) of the disproportionation of adsorbed Cu(acac).

However, the oxidation by O_2 of the intermediate H(acac) into H_2O and CO_2 (Eq. 5.22), as predicted by thermodynamic modeling, has not been observed in RMD simulations.

$$H(acac)(g) + 6O_2(g) \rightarrow 5CO_2(g) + 4H_2O(g) \qquad (G^0_{400\,K} = -24.25\ eV)\ (5.22)$$
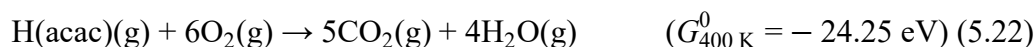
This may be due to a limited simulation time scale, or a low reactivity of O_2 under low temperatures.

Aside from the ligand-exchange reaction, undesired disproportionation of the Cu precursor as well as the direct desorption of the acac-ligand are also observed in RMD simulations, especially at elevated temperatures ($\geq 800\ K$). Fig. 5.24 illustrates snapshots of the disproportionation of adsorbed Cu(acac) at 800 K. An acac-ligand is first dissociated from the Cu precursor and diffuses towards another nearby Cu(acac) (299 ps). One Cu–O bond of Cu(acac) is then broken and its Cu atom bridges between the two acac-ligands (315 ps). Finally, a Cu(acac)$_2$ molecule is formed and is released into the gas-phase (370 ps).

For comparison, the surface reaction between Cu(acac) and dry O_2 is also investigated. It is found that O_2 reacts with the hydrogen of Cu(acac), forming a few OH and OOH species. Nevertheless, their concentrations are too low to drive a ligand-exchange reaction. Most of the acac-ligands remain adsorbed on the Cu$_2$O surface after RMD simulations. The above-mentioned observations indicate that the reaction rate of the ligand-exchange reaction with water is much faster than that of direct oxidation by oxygen. However, it is noticed that the

Fig. 5.25 Product evolution (by Cu_vanDuin) in the surface reactions between Cu(acac) and H_2O.

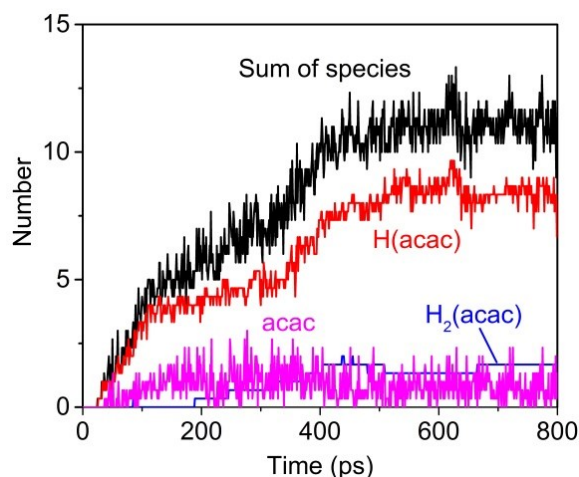ligand-exchange reaction is thermodynamically limited due to a positive reaction energy (see Eq. 5.21). The released H(acac) may re-adsorb on the surface before the next purge step, which leads to a low removal efficiency of the acac-ligands. Fig. 5.25 shows the time evolution of species for the reactions between Cu(acac) and H_2O on the $Cu_2O(111)$ surface. For simplification, O_2 is not addressed in the simulation model. The surface reaction between acac-ligands and H_2O reaches equilibrium after about 500 ps. It is found that only about 1/3 of the acac-ligands are released into the gas-phase. In short, the ligand-exchange reaction (Eq. 5.21) is kinetically feasible but thermodynamically unfavorable, whereas the direct oxidation reaction (Eq. 5.22) is the opposite. Therefore, it can be speculated that there is an interplay between oxygen and water when they are used together. The further oxidation of H(acac) shifts the equilibrium of reaction (5.21), thus facilitating the release of adsorbed acac-ligands. Such a complicated process is very difficult to study within the scope of the present work. Indeed, previous experimental studies [160] have shown that ALD using $(^nBu_3P)_2Cu(acac)$ with either oxygen or water alone deposited only isolated clusters, whereas continuous films were grown by using wet oxygen as the oxidizing agent.

5.5.2 Mechanism and kinetics of H(acac) oxidation

In this section, the oxidation of H(acac) is studied under the dry O_2 and wet O_2 conditions. For RMD simulations, an elevated temperature (2000 K) has been utilized in order to accelerate chemical reactions. The CHO_Chenoweth potential is used, since it gives a better description of the reaction energy of H(acac) oxidation compared to the Cu_vanDuin potential (see Table 5.3).

Fig. 5.26 Species evolution in the reactions between H(acac) and O_2 in the gas-phase.

Fig. 5.27 Pathways for the reactions between H(acac) and O_2 in the gas-phase.

The time evolution of species during the oxidation of H(acac) and the corresponding reaction pathways are shown in Figs. 5.26 and 5.27. In general, there is a trend for the stepwise oxidation of H(acac) into small oxide molecules. The most preferable species are CO, CO_2, H_2O, and CH_2O, accounting for about 90% of the oxidation products. The reaction starts with the abstraction of methyl hydrogen by oxygen, resulting in the formation of hydroperoxyl (HO_2) radical species. Afterwards the remaining acac species loose one of the methyl groups to form acetylketene ($C_4H_4O_2$). The initial dissociation of H(acac) is a fast process, which is completed in the first 1 ns. As shown by the change in potential energy (Fig. 5.28), this process is endothermic, while the overall oxidation of H(acac) is exothermic. Next, an OH radical, from the recombination of HO_2 and CH_3, is bonded with
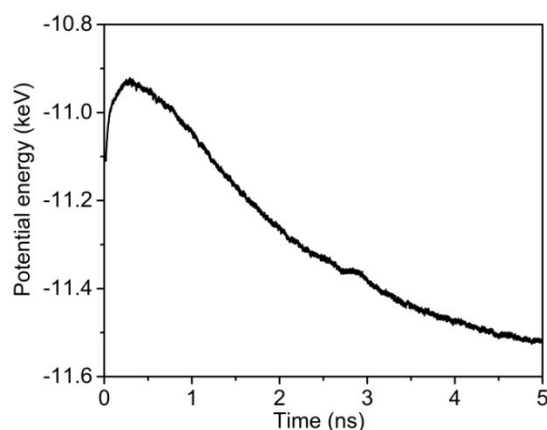
Fig. 28 Evolution of the potential energy in the reactions between H(acac) and O_2 in the gas-phase.
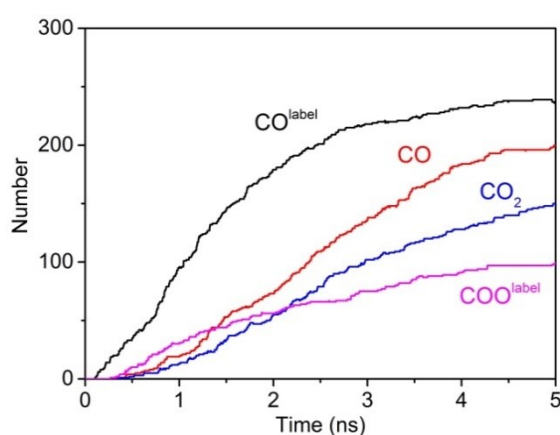
Fig. 5.29 Labeling RMD simulation for the reactions between H(acac) and O_2 in the gas-phase.

$C_4H_4O_2$ to form $C_4H_5O_3$. The formed $C_4H_5O_3$ dissociates fast into CO, C_2H_2O, and CH_3O. Eventually, C_2H_2O and CH_3O will be oxidized into CO_2 and H_2O via the CH_2O intermediate.

The carbon monoxide may be formed either through the dissociation of H(acac), or through the oxidation of carbon-species. To identify the origin of CO, labeling RMD simulations are performed, as shown in Fig. 5.29. A new element O^{label} that has the same parameters as O, is added in the ReaxFF potential and used for H(acac). As confirmed by the labeling RMD simulations (Fig. 5.29), most of the carbon monoxide released in the initial stage is through the dissociation of H(acac), rather than through the oxidation reaction. The formed CO^{label} can be further oxidized into COO^{label}.

Fig. 5.30 shows the effect of water on the oxidation of H(acac). It is found that the presence of water has almost no influence on the initial dissociation of H(acac). However, the reaction rate for the complete oxidation of H(acac) is slower in the presence of water, since existing water may obstruct the production of new water.
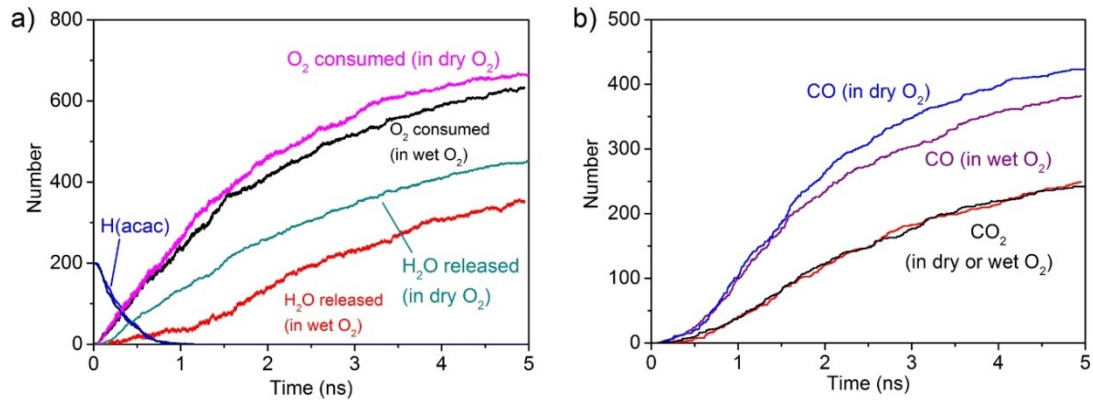
Fig. 5.30 Influence of water on the oxidation of H(acac). (a) Evolution of H(acac), O_2, and H_2O; as well as (b) CO and CO_2.
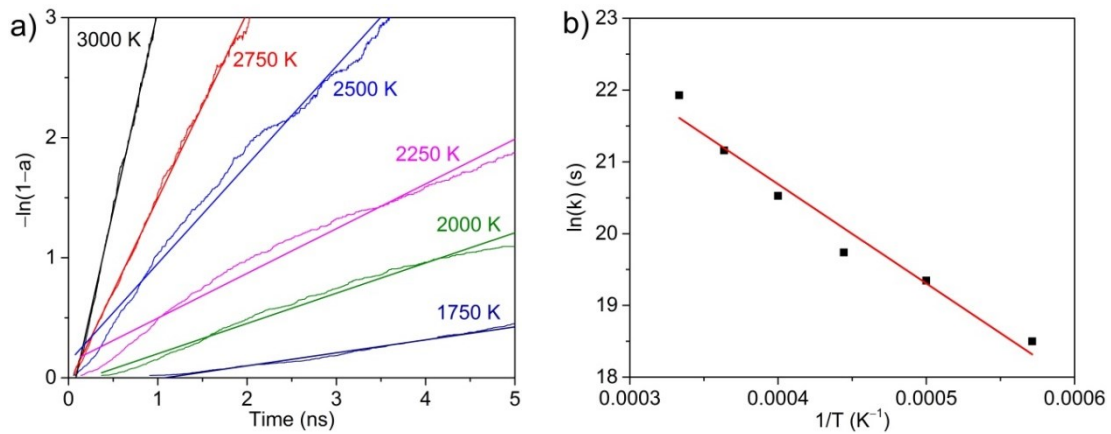

Fig. 5.31 Kinetics analysis for the oxidation of H(acac). (a) Reaction rate at different temperatures; (b) Arrhenius plot.

Based on RMD simulations run at different temperatures, the kinetics of H(acac) oxidation by O_2 is analyzed. In line with experimental approaches (see Section 3.6), the kinetics data are derived by analyzing the extent of conversion α, which is deduced from the amount of reaction products $n(CO + CO_2)$

$$\alpha = n(CO + CO_2)/1000 \tag{5.23}$$

The initial system contains 200 H(acac) molecules (1000 C atoms). The maximum reaction time is 5 ns. In this work, five different reaction kinetics models have been considered, as listed in Table 3.4. As shown in Fig. 5.31a, the first order reaction models $f(a) = (1-\alpha)$ is identified as the best fit for the oxidation of H(acac), with overall variances (R^2) greater than 0.97. The pre-exponential factor and the apparent activation energy are determined using a logarithmic Arrhenius plot, as shown in Fig. 5.31b. The calculated pre-exponential factor and apparent activation energy for H(acac) oxidation are 1.19 eV and 2.447×10^{11} s^{-1}, respectively.

5.6 Summary

The recently developed Cu potentials, Cu_vanDuin and Cu_Hu, have been assessed and applied for the simulation of Cu ALD. The CHO_Chenoweth potential contains the parameters of the C/H/O system and is used to study the oxidation of H(acac) in the gas-phase. The Cu_Hu potential is developed based on the existing Cu_vanDuin potential. It completely covers the interactions of the Cu/C/H/O/N system. With a few exceptions, the Cu_Hu potential successfully reproduces the energetic and geometric data of the Cu precursor as calculated by DFT. The adsorption properties of different Cu-species calculated by using the Cu_Hu potential also satisfy simulation requirements.

RMD simulations have been performed to study the surface reactions of the $Cu(acac)_2$ precursor and to evaluate the reactivity of different co-reactants. Molecular hydrogen is found to be nonreactive towards the $Cu(acac)_2$ precursor; whereas atomic H or water can remove the surface acac-ligands efficiently. The H atoms continuously impact with the Cu precursor, which leads to the breaking of the Cu–O, C–O, and C–C bonds sequentially. In contrast to the mechanism proposed by Wu and Eisenbraun (Eqs. 2.13 and 2.14) [28], the formation of the H(acac) species has not been observed during the atomic H pulse. This may be due to the high reactivity of atomic H towards decomposing the acac-ligands. On the other hand, water reacts with $Cu(acac)_2$ and $Cu(acac)$ on $Cu_2O(111)$ through a ligand-exchange reaction, producing gaseous H(acac) and surface OH species.

A combustion reaction with CO_x and H_xO_y as the main by-products is observed when adsorbed $Cu(acac)_2$ reacts with O_3. Once the equilibrium is reached, all the O_3 co-reactants are consumed by either surface reactions or a conversion into O_2. These findings agree well with the thermodynamic prediction, in which the by-products O_2, CO_2 and H_2O are released into the gas-phase during the O_3 pulse (see Section 4.4.1).

The interplay between the H_2O and O_2 co-reactants for the Cu(acac)/wet O_2 ALD process has been discussed. The presence of O_2 may oxidize the by-product H(acac) into CO, CO_2 and H_2O, hindering the re-adsorption of H(acac) on the surface. The kinetics of the oxidation of H(acac) in the gas-phase is calculated by the Arrhenius equation. The obtained pre-exponential factor and apparent activation energy are 1.19 eV and 2.447×10^{11} s^{-1}, respectively.

Chapter 6 Summary and outlook

ALD is a thin film deposition technique based on sequential surface reactions between precursors and a substrate. The growth of thin films by ALD is self-terminating, which leads to excellent step coverage and conformal deposition even on high aspect ratio structures. In recent years, the ALD of metal oxides (e.g., Al_2O_3 and HfO_2) has been extensively investigated and has been successfully applied in the FEOL as high-k gate oxides. In the BEOL, ALD is one of the most promising approaches for making Cu seed layers for next generation technology nodes (i.e., 10 nm and below), replacing the conventionally used PVD technology. Nevertheless, the ALD of metallic thin films is a great challenge, primarily due to the lack of suitable precursors and the nucleation problem. Besides, more research is required in order to elucidate the fundamental mechanisms of deposition, which involve complex surface chemistry.

This thesis is dedicated to the multiscale simulation of metallic Cu and Cu oxide ALD. Two related Cu beta-diketonates, (^{n}Bu$_3$P)$_2$Cu(acac) and Cu(acac)$_2$, were considered as the Cu precursors. At the atomic-scale, *ab initio* calculations were performed to study the geometric structure and the vibration frequency of the isolated Cu precursors. With the target application of Cu seed layer fabrication, the surface chemistry of the Cu precursors were investigated on Ta(110), Cu(110), Ru(001), Cu$_2$O(111), SiO$_2$(001), and TaN(111) substrates. The data obtained by *ab initio* calculations were then transferred to molecular-scale and macroscale models, which were simulated based on the reactive molecular dynamics and thermodynamic modeling, respectively. As shown in Figs. 6.1 and 6.2, with multiscale simulations it is possible to obtain detailed pictures of the ALD surface reactions. Such information is essential for the development of new precursors and the optimization of ALD processes that can be used in Cu interconnect fabrication.

Stability of the Cu precursor in the gas-phase and on the surface

The stability of precursors plays an important role in ALD since the ALD process is self-limiting within the ALD window. As shown in Fig. 6.1, the (^{n}Bu$_3$P)$_2$Cu(acac) precursor readily loses one of the ^{n}Bu$_3$P-ligands in the gas-phase. However, the further dissociation of (^{n}Bu$_3$P)Cu(acac) requires high temperatures (> 575 K), which is infeasible for ALD. On the surface, a simplified precursor model (Me$_3$P)Cu(acac) has been employed to reduce computational costs. The (Me$_3$P)Cu(acac) precursor prefers to adsorb and decompose into

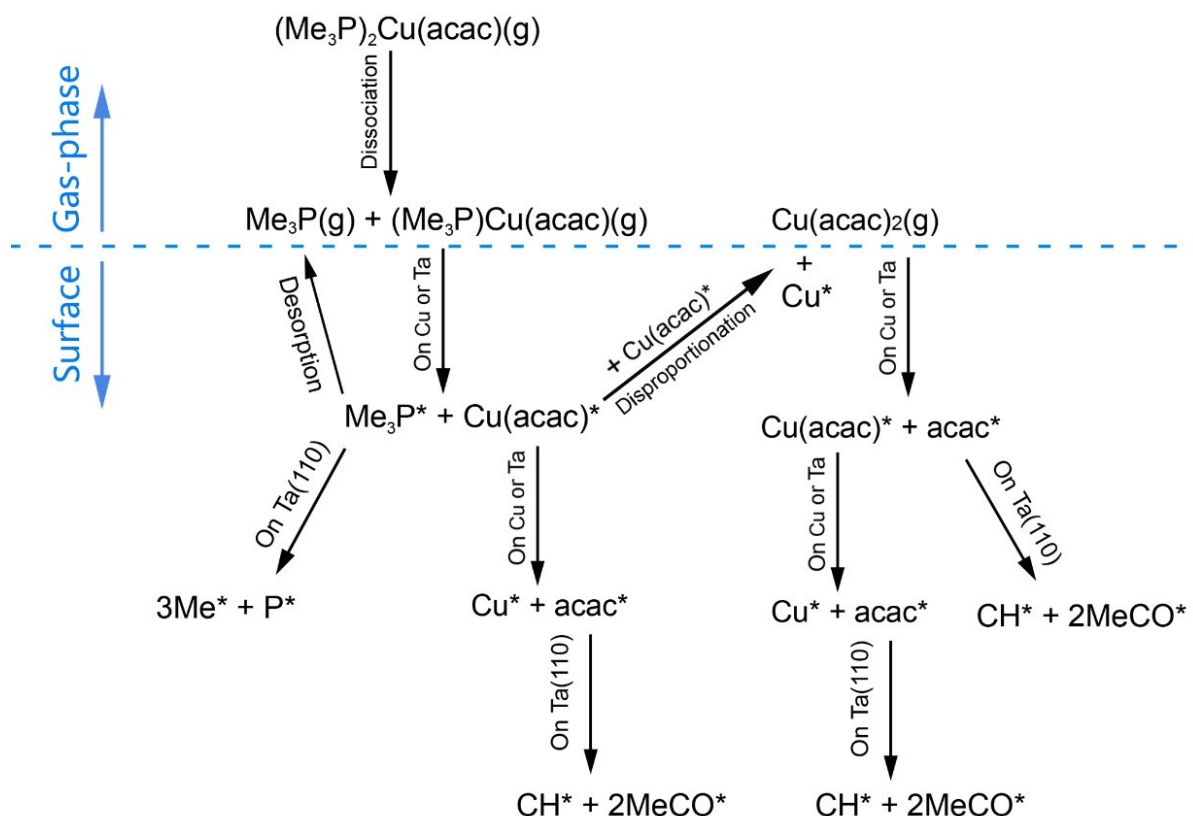**Fig. 6.1** Schematic representation of pathways for the dissociation and reaction of the $(Me_3P)_2Cu(acac)$ and $Cu(acac)_2$ precursors in the gas-phase and on the Ta or Cu surface. The $(^nBu_3P)_2Cu(acac)$ precursor is not shown here, since its behavior in the gas-phase is similar to $(Me_3P)_2Cu(acac)$.

Me_3P and $Cu(acac)$ on the metallic substrates (Ta, Cu, and Ru), rather than on the metal oxide (SiO_2 and Cu_2O) and the metal nitride (TaN) substrates. As reported in previous XPS studies [29], some of the adsorbed Me_3P-ligands are released from the surface into the gas-phase. The adsorbed $Cu(acac)^*$ may react with another nearby $Cu(acac)^*$, producing metallic Cu and gaseous $Cu(acac)_2$ through an undesired disproportionation reaction. In the ALD process, a high substrate temperature should be avoided to prevent such a reaction. Besides, the adsorbed $Cu(acac)$ also undergoes decomposition on the metallic surfaces Ta and Cu, forming Cu^* and $acac^*$ species. The acac- and Me_3P-ligands are stable on the Cu surface, and thus they can block the surface sites and prevent the further adsorption of precursors. However, due to high reactivity, the surface acac- and Me_3P-ligands tend to dissociate into $CH^* + 2MeCO^*$ and $3Me^* + P^*$ on the Ta(110) surface, respectively, leading to an uncontrollable deposition as well as C and P contaminants.

When compared to $(^nBu_3P)_2Cu(acac)$, the $Cu(acac)_2$ precursor is more stable in the gas-phase and its surface chemistry is much more simple and clean (see Fig. 6.1). The *ab initio*

136

calculations reveal a sequential dissociation and reduction of the Cu(acac)$_2$ precursor [Cu(acac)$_2$→Cu(acac)→Cu] on the Cu(110) and Ta(110) surfaces, which is in accordance with XPS investigations [32]. The dissociated acac-ligands must be removed by co-reactants in the next ALD half-cycle.

Surface reactions between Cu precursor and different co-reactants

To understand the surface reactions between the Cu precursors and different co-reactants, RMD simulations were performed employing the ReaxFF potential. RMD simulations provide an accurate approach to describe large reactive systems (thousands of atoms). Thus the gap between AIMD and CMD can be filled. To account for the Cu–H and Cu–C bonding interactions, a new ReaxFF potential (referred as Cu_Hu) has been developed in this work based on the existing Cu potential by van Duin et al [172]. The parameterization procedure has been done through a new parallel algorithm based on the Taguchi method. The accuracy of the Cu_Hu potential was carefully examined using *ab initio* data as a benchmark.

The reaction pathways between the (Me$_3$P)$_2$Cu(acac) precursor and wet O$_2$ on the Cu$_2$O surface are shown in Fig. 6.2. The Me$_3$P-ligands were assumed to be released into the gas-phase, and have a minor effect on the surface reaction. As observed in RMD simulations, the adsorbed Cu(acac) reacts with H$_2$O(g) through a ligand-exchange reaction, producing the gaseous H(acac) and surface CuOH* species. However, the ligand-exchange reaction has a low efficiency, since the formed H(acac)(g) may easily re-adsorb on the surface. Therefore, O$_2$ is required to oxidize H(acac)(g) further, and thus the reactivity of co-reactant can be enhanced.
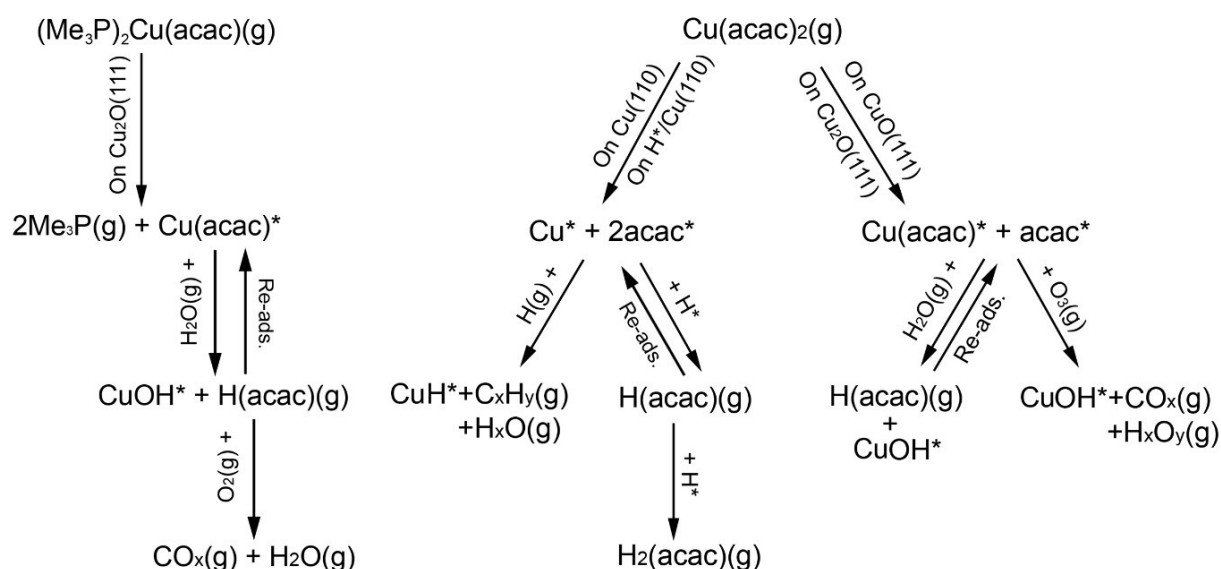

Fig. 6.2 Schematic representation of pathways for the surface reactions between the (Me$_3$P)$_2$Cu(acac) and Cu(acac)$_2$ precursors and different co-reactants.

Such an oxidation reaction, which generates the products $CO_x(g)$ and $H_2O(g)$, is under kinetic control. During the next half-cycle, the surface OH groups are speculated to act as the reactive species, providing protons for the ligand-exchange reaction with the Cu(acac) precursor.

The co-reactants H(g), $H_2O(g)$, and $O_3(g)$ were investigated for the $Cu(acac)_2$ precursor, towards their application in Cu, Cu_2O and CuO ALD, respectively. Molecular $H_2(g)$ is found to be nonreactive towards $Cu(acac)_2$ at low temperatures, due to a large H–H bond energy. On the other hand, atomic H efficiently reacts with the $Cu(acac)_2$ precursor, resulting in the sequential breaking of the Cu–O, C–O, and C–C bonds. The predicted reaction by-products are CuH^*, $C_xH_y(g)$, and $H_xO(g)$. As confirmed by AIMD simulations, the adsorbed H atoms are stable on the Cu surface, acting as the reactive species for the next ALD half-cycle. During the $Cu(acac)_2$ pulse, the surface H atoms can readily transfer to the acac-ligands, forming H(acac)(g) and $H_2(acac)(g)$ species. Perhaps due to a low concentration of H^*, the further dissociation of H(acac)(g) or $H_2(acac)(g)$ has not been observed. The reaction mechanism between $Cu(acac)_2$ and $H_2O(g)$ is similar to that between Cu(acac) and $H_2O(g)$, in which a ligand-exchange reaction has been proposed. For the $Cu(acac)_2/O_3$ process, combustion reactions with the by-products $CO_x(g)$ and $H_xO_y(g)$ are predicted. This observation is consistent with *in situ* mass spectroscopy studies for an $Ir(acac)_3/O_3$ ALD process [159]. The reactivity of different co-reactants towards $Cu(acac)_2$ follows the order $H > O_3 > H_2O > H_2$.

Outlook

In the present work, RMD simulations were performed on metallic Cu and Cu oxides substrates. Because of the limitation of the existing RMD potentials, surface reactions of the Cu precursors on other substrates have not been investigated. As demonstrated in Chapter 4, the Ta surface exhibits a much higher reactivity compared to the Cu and Cu_2O surfaces, which may affect the pathways of ALD surface reactions. Therefore, it is of great interest to develop a ReaxFF potential for Ta, and integrate it into the current Cu_Hu potential that includes the Cu/C/H/O/N interactions. Such a Ta/Cu/C/H/O/N potential would have a significant potential for simulating the surface chemistry of Cu precursors as well as the diffusion barrier properties of Ta/TaN multi-layer structures.

Previously, *ab initio* calculations were conducted for the screening of Cu precursors [89], which helps to reduce experimental costs and to shorten development cycles. However, the formation energy and reaction energy in those works were computed using a simplified cluster model without chemical environment. To obtain accurate data on the stability and the

reactivity of precursors, more reliable multiscale simulation approaches are demanded. Therefore, it would be promising to apply the multiscale simulation in future precursor design and screening studies.

With the exception of a few XPS studies [29, 32], experimental data with respect to the surface chemistry of Cu beta-diketonates remains scarce. Further experimental studies are therefore required to verify and complement the theoretical findings of this work. For example, *in situ* infrared spectroscopy and mass spectrometry technologies can be used to characterize the surface and gas-phase species. Insightful conclusions could be obtained by comparing the measured data with the simulation results.

Appendix

Description of the ReaxFF potential functions

Eqs. A1a–c are used to calculate the valence angle energy contribution. The equilibrium angle Θ_o for a given angle Θ_{ijk} depends on the sum of pi bond orders around the central atom j. Thus, the equilibrium angle changes from around 109.47° for sp3 hybridization (π-bond=0) to 120° for sp2 (pi bond=1) to 180° for sp (pi bond=2) based on the geometry of the central atom j and its neighbors.

$$E_{\mathrm{val}} = f_7(BO_{ij}) \cdot f_7(BO_{jk}) \cdot f_8(\Delta_j) \cdot \left\{ p_{\mathrm{val1}} - p_{\mathrm{val1}} \exp\left[-p_{\mathrm{val2}} (\Theta_o(BO) - \Theta_{ijk})^2 \right] \right\} \quad \text{(A1a)}$$

$$f_7(BO_{ij}) = 1 - \exp(-p_{\mathrm{val3}} \cdot BO_{ij}^{p_{\mathrm{val4}}}) \quad \text{(A1b)}$$

$$f_8(\Delta_j) = p_{\mathrm{val5}} - (p_{\mathrm{val5}} - 1) \cdot \frac{2 + \exp(p_{\mathrm{val6}} \cdot \Delta_j^{\mathrm{angle}})}{1 + \exp(p_{\mathrm{val6}} \cdot \Delta_j^{\mathrm{angle}}) + \exp(-p_{\mathrm{val7}} \cdot \Delta_j^{\mathrm{angle}})} \quad \text{(A1c)}$$

Similar to the angle terms, the torsion energy is calculated as follows

$$E_{\mathrm{tors}} = f_{10}(BO_{ij}, BO_{jk}, BO_{kl}) \cdot \sin\Theta_{ijk} \cdot \sin\Theta_{jkl} \cdot \left\{ \frac{1}{2} V_1 \cdot (1 + \cos\omega_{ijkl}) + \frac{1}{2} V_2 \cdot \exp\left[p_{\mathrm{tor1}} \cdot (BO_{jk}^\pi - 1 + \right. \right.$$
$$\left. \left. f_{11}(\Delta_j, \Delta_k))^2 \right] \cdot (1 - \cos2\omega_{ijkl}) + \frac{1}{2} V_3 \cdot (1 + \cos3\omega_{ijkl}) \right\}$$

$$\text{(A2a)}$$

$$f_{10}(BO_{ij}, BO_{jk}, BO_{kl}) = \left[1 - \exp(-p_{\mathrm{tor2}} \cdot BO_{ij}) \right] \cdot \left[1 - \exp(-p_{\mathrm{tor2}} \cdot BO_{jk}) \right] \cdot \left[1 - \exp(-p_{\mathrm{tor2}} \cdot BO_{kl}) \right]$$

$$\text{(A2b)}$$

$$f_{11}(\Delta_j, \Delta_k) = \frac{2 + \exp\left[-p_{\mathrm{tor3}} \cdot \left(\Delta_j^{\mathrm{angle}} + \Delta_k^{\mathrm{angle}} \right) \right]}{1 + \exp\left[-p_{\mathrm{tor3}} \cdot \left(\Delta_j^{\mathrm{angle}} + \Delta_k^{\mathrm{angle}} \right) \right] + \exp\left[-p_{\mathrm{tor4}} \cdot \left(\Delta_j^{\mathrm{angle}} + \Delta_k^{\mathrm{angle}} \right) \right]} \quad \text{(A2c)}$$

For an overcoordinated atom ($\Delta_i > 0$), Eqs. A3a–b impose an energy penalty on the system. The degree of overcoordination Δ is decreased if the atom contains a broken-up lone electron pair.

$$E_{\mathrm{over}} = \frac{\sum_{j=1}^n p_{\mathrm{ovun1}} \cdot D_e^\sigma \cdot BO_{ij}}{\Delta_i^{\mathrm{lpcorr}} + Val_i} \cdot \Delta_i^{\mathrm{lpcorr}} \cdot \left[\frac{1}{1 + \exp(p_{\mathrm{ovun2}} \cdot \Delta_i^{\mathrm{lpcorr}})} \right] \quad \text{(A3a)}$$

$$\Delta_i^{\mathrm{lpcorr}} = \Delta_i - \frac{\Delta_i^{\mathrm{lp}}}{1 + p_{\mathrm{ovun3}} \cdot \exp\left\{ p_{\mathrm{ovun4}} \cdot \left[\sum_{j=1}^i (\Delta_j - \Delta_j^{\mathrm{lp}}) \cdot (BO_{ij}^\pi + BO_{ij}^{\pi\pi}) \right] \right\}} \quad \text{(A3b)}$$

For an undercoordinated atom ($\Delta_i < 0$), the energy contribution for the resonance of the π-electron between attached under-coordinated atomic centers has to be considered. This is done by Eq. A4, where E_{under} is only important if the bonds between under-coordinated atom i and its under-coordinated neighbors j partly have π-bond character.

$$E_{\text{under}} = -p_{\text{ovun5}} \cdot \frac{1-\exp(p_{\text{ovun6}} \cdot \Delta_i^{\text{lpcorr}})}{1+\exp(-p_{\text{ovun2}} \cdot \Delta_i^{\text{lpcorr}})} \cdot \frac{1}{1+p_{\text{ovun7}} \cdot \exp\left\{p_{\text{ovun8}} \cdot \left[\sum_{j=1}^{i}(\Delta_j - \Delta_j^{\text{lp}}) \cdot (BO_{ij}^\pi + BO_{ij}^{\pi\pi})\right]\right\}}$$

(A4)

Input data for the thermodynamic modeling.

Table A1 Adsorption energies (eV) of different species on the Ta(110) surface.

Cu(acac)$_2$	(Me$_3$P)$_2$Cu(acac)	(Me$_3$P)Cu(acac)	Cu(acac)	acac
$-1.5851+0.7986\theta_S$	$-1.1660 +0.1563\theta_S$	$-1.3398+0.2689\theta_S$	$-2.7878+0.0799\theta_S$	$-4.4877+0.4221\theta_S$
Me$_3$P	P	CO$_2$	CO	
$-1.3544+0.1996\theta_S$	$-5.8405+0.1996\theta_S$	$-1.5008+1.2657\theta_S$	$-1.7842+1.1905\theta$	

Table A2 Adsorption energies and lateral interactions (eV) of different species on the Ta(110) surface.

S_i / S_j	Me	MeP	Cu	O	C
Me	$-2.6104+0.1896\theta_S$	$0.5303\theta_{Sj}$	$0.2690\theta_{Sj}$	$0.5145\theta_{Sj}$	$-0.0027-0.3440\theta_{Sj}$
MeP	$0.0104+0.4624\theta_{Sj}$	$-5.1775+0.7806\theta_S$	$0.7266\theta_{Sj}$	$0.0070+0.5223\theta_{Sj}$	$1.5346\theta_{Sj}$
Cu	$-0.0072+0.1746\theta_{Sj}$	$0.1924\theta_{Sj}$	$-3.6366-0.1416\theta_S$	$0.0010+0.1012\theta_{Sj}$	$0.4116\theta_{Sj}$
O	$-0.0421+0.6075\theta_{Sj}$	$-0.0373+0.9056\theta_{Sj}$	$0.6014\theta_{Sj}$	$-7.9394+0.8691\theta_S$	$-0.0068+0.2857\theta_{Sj}$
C	$-0.0418+1.2656\theta_{Sj}$	$-0.0012+1.4134\theta_{Sj}$	$-0.0276+1.3123\theta_{Sj}$	$-0.0287+1.3380\theta_{Sj}$	$-8.7718+2.0784\theta_S$

Table A3 Adsorption energies and lateral interactions (eV) of different species.

S_i S_j	CuO	OH	O
CuO	$-3.1967+0.8341\theta_S$	$-0.0254+0.8297\theta_{Sj}$	$0.0078+0.8626\theta_{Sj}$
OH	$-0.0947+0.6381\theta_{Sj}$	$-4.8212+0.7370\theta_S$	$-0.0359+0.7555\theta_{Sj}$
O	$-0.0608+0.7531\theta_{Sj}$	$-0.0516+0.7770\theta_{Sj}$	$-7.9394+0.8691\theta_S$

Table A4 Gibbs energies (eV) of simple molecules at a standard pressure.

T (K)	O_2	O_3	CO_2	H_2O	CO	H_2	CH_4
300	−869.4810	−1302.6264	−1028.2843	−469.0868	−590.6067	−32.0165	−220.1573
325	−869.5340	−1302.6901	−1028.3400	−469.1361	−590.6583	−32.0507	−220.2064
350	−869.5880	−1302.7547	−1028.3966	−469.1861	−590.7104	−32.0855	−220.2554
375	−869.6430	−1302.8201	−1028.4540	−469.2367	−590.7631	−32.1208	−220.3060
400	−869.6980	−1302.8862	−1028.5121	−469.2880	−590.8163	−32.1567	−220.3563
425	−869.7540	−1302.9530	−1028.5707	−469.3397	−590.8700	−32.1929	−220.4083
450	−869.8100	−1303.0205	−1028.6301	−469.3920	−590.9241	−32.2297	−220.4599
475	−869.8660	−1303.0886	−1028.6900	−469.4448	−590.9787	−32.2668	−220.5132
500	−869.9230	−1303.1574	−1028.7507	−469.4981	−591.0336	−32.3044	−220.5660
525	−869.9810	−1303.2268	−1028.8118	−469.5519	−591.0889	−32.3422	−220.6206
550	−870.0380	−1303.2967	−1028.8735	−469.6060	−591.1446	−32.3805	−220.6752
575	−870.0970	−1303.3672	−1028.9357	−469.6606	−591.2007	−32.4191	−220.7304
600	−870.1550	−1303.4382	−1028.9986	−469.7157	−591.2575	−32.4583	−220.7852
625	−870.2140	−1303.5098	−1029.0618	−469.7710	−591.3138	−32.4972	−220.8424
650	−870.2730	−1303.5819	−1029.1256	−469.8268	−591.3709	−32.5368	−220.8993
675	−870.3330	−1303.6545	−1029.1898	−469.8830	−591.4282	−32.5766	−220.9567
700	−870.3920	−1303.7276	−1029.2547	−469.9395	−591.4859	−32.6173	−221.0135

Table A5 Gibbs energies (eV) of complex molecules at a standard pressure.

T (K)	MeOH	MeCOOH	Me$_2$CO	MeCHO	MeCOCHO
300	−655.9512	−1247.8553	−998.3595	−810.6740	−1401.2518
325	−656.0135	−1247.9296	−998.4362	−810.7426	−1401.3334
350	−656.0767	−1248.0054	−998.5146	−810.8124	−1401.4167
375	−656.1408	−1248.0827	−998.5946	−810.8834	−1401.5018
400	−656.2058	−1248.1614	−998.6762	−810.9554	−1401.5886
425	−656.2717	−1248.2414	−998.7594	−811.0286	−1401.6769
450	−656.3385	−1248.3228	−998.8442	−811.1029	−1401.7669
475	−656.4061	−1248.4055	−998.9305	−811.1782	−1401.8584
500	−656.4745	−1248.4896	−999.0183	−811.2546	−1401.9514
525	−656.5437	−1248.5748	−999.1077	−811.3320	−1402.0460
550	−656.6138	−1248.6613	−999.1984	−811.4104	−1402.1420
575	−656.6846	−1248.7491	−999.2906	−811.4898	−1402.2394
600	−656.7562	−1248.8380	−999.3842	−811.5702	−1402.3382
625	−656.8285	−1248.9281	−999.4792	−811.6515	−1402.4384
650	−656.9016	−1249.0194	−999.5756	−811.7337	−1402.5400
675	−656.9755	−1249.1118	−999.6734	−811.8169	−1402.6428
700	−657.0500	−1249.2053	−999.7724	−811.9010	−1402.7470

Table A6 Gibbs energies (eV) of P-ligands at a standard pressure.

T (K)	Me$_3$P	Me$_2$P	MeP	P$_2$	P	PH$_3$	PH$_2$	PH
300	−790.5491	−585.9183	−381.3769	−358.4554	−176.7763	−227.9504	−210.7326	−193.6788
325	−790.6366	−585.9954	−381.4407	−358.5123	−176.8188	−228.0053	−210.7879	−193.7300
350	−790.7264	−586.0741	−381.5054	−358.5699	−176.8617	−228.0610	−210.8443	−193.7818
375	−790.8184	−586.1544	−381.5710	−358.6280	−176.9051	−228.1174	−210.9010	−193.8341
400	−790.9127	−586.2363	−381.6375	−358.6868	−176.9488	−228.1746	−210.9587	−193.8870
425	−791.0092	−586.3197	−381.7048	−358.7461	−176.9928	−228.2324	−211.0165	−193.9403
450	−791.1078	−586.4045	−381.7730	−358.8059	−177.0372	−228.2908	−211.0755	−193.9941
475	−791.2085	−586.4908	−381.8419	−358.8662	−177.0818	−228.3499	−211.1342	−194.0483
500	−791.3113	−586.5786	−381.9116	−358.9270	−177.1267	−228.4096	−211.1944	−194.1029
525	−791.4160	−586.6677	−381.9821	−358.9882	−177.1719	−228.4699	−211.2540	−194.1579
550	−791.5228	−586.7582	−382.0534	−359.0499	−177.2174	−228.5308	−211.3147	−194.2133
575	−791.6315	−586.8501	−382.1253	−359.1120	−177.2631	−228.5923	−211.3757	−194.2690
600	−791.7421	−586.9432	−382.1980	−359.1744	−177.3090	−228.6543	−211.4381	−194.3250
625	−791.8545	−587.0377	−382.2714	−359.2373	−177.3552	−228.7169	−211.4992	−194.3814
650	−791.9689	−587.1334	−382.3454	−359.3006	−177.4016	−228.7801	−211.5616	−194.4381
675	−792.0849	−587.2303	−382.4202	−359.3642	−177.4482	−228.8437	−211.6244	−194.4951
700	−792.2028	−587.3285	−382.4956	−359.4279	−177.4949	−228.9079	−211.6888	−194.5524

Table A7 Gibbs energies (eV) of precursors at a standard pressure.

T (K)	(Me$_3$P)$_2$Cu(acac)	Cu(acac)$_2$	(Me$_3$P)Cu(acac)	Cu(acac)	acac	HCu(acac)	H(acac)
300	−4994.1541	−5173.0563	−4203.6337	−3411.7924	−1758.9126	−3429.4712	−1776.8092
325	−4994.3386	−5173.2052	−4203.7768	−3411.8968	−1759.0004	−3429.4747	−1776.8954
350	−4994.5308	−5173.3596	−4203.9253	−3412.0042	−1759.0905	−3429.4784	−1776.9838
375	−4994.7308	−5173.5194	−4204.0791	−3412.1146	−1759.1828	−3429.4820	−1777.0745
400	−4994.9382	−5173.6846	−4204.2381	−3412.2278	−1759.2774	−3429.4858	−1777.1673
425	−4995.1530	−5173.8550	−4204.4021	−3412.3438	−1759.3742	−3429.4896	−1777.2623
450	−4995.3749	−5174.0305	−4204.5711	−3412.4626	−1759.4732	−3429.4935	−1777.3595
475	−4995.6039	−5174.2111	−4204.7449	−3412.5840	−1759.5743	−3429.4975	−1777.4588
500	−4995.8398	−5174.3966	−4204.9235	−3412.7082	−1759.6776	−3429.5015	−1777.5603
525	−4996.0825	−5174.5870	−4205.1068	−3412.8349	−1759.7830	−3429.5056	−1777.6639
550	−4996.3318	−5174.7821	−4205.2947	−3412.9641	−1759.8904	−3429.5098	−1777.7695
575	−4996.5876	−5174.9819	−4205.4871	−3413.0959	−1759.9999	−3429.5140	−1777.8772
600	−4996.8498	−5175.1862	−4205.6838	−3413.2300	−1760.1114	−3429.5183	−1777.9869
625	−4997.1183	−5175.3951	−4205.8849	−3413.3666	−1760.2248	−3429.5227	−1778.0987
650	−4997.3929	−5175.6084	−4206.0903	−3413.5055	−1760.3402	−3429.5271	−1778.2124
675	−4997.6735	−5175.8261	−4206.2997	−3413.6467	−1760.4575	−3429.5315	−1778.3281
700	−4997.9601	−5176.0479	−4206.5133	−3413.7901	−1760.5767	−3429.5360	−1778.4456

Table A8 Adsorption energies (eV) of different species on the Cu$_2$O(111) surface.

Cu	Cu(acac)	Me$_3$P	O
−1.0983−1.4312×0.00132^θ_S	−2.1451+3.4145×θ_S	−3.0010+2.6971×θ_S	−3.2077 −3.0375×0.0002^θ_S
OH	CuO	CO	CuOH
−3.2079−1.5751×0.0075^θ_S	−2.3580+0.9671×θ_S	−1.6823+0.0999×θ_S	−5.2782−1.1384×0.0184^θ_S
C	P		
−2.5166+0.0362×θ_S	−3.2671−0.2607×0.0001^θ_S		

Table A9 Effect of temperature on the adsorption energies on the Cu$_2$O(111) surface

T (K)	Cu	Cu(acac)	Me$_3$P
300	0.0280	2.5487	2.7574
325	0.0230	2.4849	2.7137
350	0.0175	2.4177	2.6674
375	0.0116	2.3473	2.6187
400	0.0053	2.2738	2.5675
425	−0.0014	2.1971	2.5141
450	−0.0084	2.1175	2.4583
475	−0.0158	2.0349	2.4002
500	−0.0235	1.9494	2.3400
525	−0.0316	1.8612	2.2775
550	−0.0399	1.7702	2.2129

Table A10 Effect of temperature on the adsorption energies on the Cu$_2$O(111) surface

T (K)	O	OH	Cu	CuO	CuOH	C	P	CO
300	−0.0496	0.2863	0.0280	0.0288	0.2746	0.0919	0.0273	0.2078
325	−0.0627	0.2752	0.0230	0.0148	0.2555	0.0903	0.0218	0.2011
350	−0.0761	0.2635	0.0175	0.0000	0.2354	0.0883	0.0159	0.1937
375	−0.0900	0.2513	0.0116	−0.0156	0.2142	0.0859	0.0095	0.1857
400	−0.1042	0.2385	0.0053	−0.0320	0.1920	0.0832	0.0028	0.1770
425	−0.1187	0.2251	−0.0014	−0.0490	0.1689	0.0802	−0.0043	0.1677
450	−0.1335	0.2113	−0.0084	−0.0668	0.1450	0.0769	−0.0117	0.1579
475	−0.1487	0.1969	−0.0158	−0.0852	0.1202	0.0733	−0.0195	0.1475
500	−0.1642	0.1821	−0.0235	−0.1042	0.0945	0.0694	−0.0276	0.1365
525	−0.1799	0.1668	−0.0316	−0.1239	0.0681	0.0652	−0.036	0.1251
550	−0.1959	0.151	−0.0399	−0.1441	0.0409	0.0607	−0.0447	0.1132

Table A11 Electronic energies (eV) of different species.

C	Cu	(Me$_3$P)Cu(acac)	CO	CO$_2$	Cu(acac)$_2$
−147.5346	−1649.4148	−4228.5356	−590.0820	−1027.7166	−5202.08482
O	CuO	OH	P	(Me$_3$P)$_2$Cu(acac)	Cu(acac)
−431.4350	−2084.4344	−449.7125	−175.1230	−5027.0530	−3410.8366
Me	MeP	acac	Me$_3$P	Ta	
−201.4487	−380.7296	−1758.0775	−789.7314	−5796.3696	

The Taguchi table used for the parameterization of the Cu_Hu potential.

Table A12 The L_{81} (3^{40}) orthogonal array.

Exp.	21	20	19	18	17	16	15	14	13	12	11	10	9	8	7	6	5	4	3	2	1
1	1	1	1	1	1	1	1	1	1	1	1	1	1	1	1	1	1	1	1	1	1
2	3	3	3	2	2	2	2	2	2	2	2	2	1	1	1	1	1	1	1	1	1
3	3	3	3	2	2	2	2	2	2	2	2	2	1	1	1	1	1	1	1	1	1
4	3	3	3	2	2	2	2	2	2	2	2	2	1	1	1	1	1	1	1	1	1
5	1	1	1	3	3	3	2	2	2	1	1	1	3	3	3	2	2	2	1	1	1
6	1	1	1	3	3	3	2	2	2	1	1	1	3	3	3	2	2	2	1	1	1
7	1	1	1	3	3	3	2	2	2	1	1	1	3	3	3	2	2	2	1	1	1
8	3	3	3	1	1	1	3	3	3	2	2	2	3	3	3	2	2	2	1	1	1
9	3	3	3	1	1	1	3	3	3	2	2	2	3	3	3	2	2	2	1	1	1
10	3	3	3	1	1	1	3	3	3	2	2	2	3	3	3	2	2	2	1	1	1
11	2	2	2	2	2	2	1	1	1	3	3	3	3	3	3	2	2	2	1	1	1
12	2	2	2	2	2	2	1	1	1	3	3	3	3	3	3	2	2	2	1	1	1
13	2	2	2	2	2	2	1	1	1	3	3	3	3	3	3	2	2	2	1	1	1
14	3	2	1	3	2	1	3	2	1	3	2	1	3	2	1	3	2	1	3	2	1
15	3	2	1	3	2	1	3	2	1	3	2	1	3	2	1	3	2	1	3	2	1
16	3	2	1	3	2	1	3	2	1	3	2	1	3	2	1	3	2	1	3	2	1
17	2	1	3	1	3	2	1	3	2	1	3	2	3	2	1	3	2	1	3	2	1
18	2	1	3	1	3	2	1	3	2	1	3	2	3	2	1	3	2	1	3	2	1
19	2	1	3	1	3	2	1	3	2	1	3	2	3	2	1	3	2	1	3	2	1
20	1	3	2	2	1	3	2	1	3	2	1	3	3	2	1	3	2	1	3	2	1
21	1	3	2	2	1	3	2	1	3	2	1	3	3	2	1	3	2	1	3	2	1
22	1	3	2	2	1	3	2	1	3	2	1	3	3	2	1	3	2	1	3	2	1
23	3	2	1	2	1	3	1	3	2	3	2	1	2	1	3	1	3	2	3	2	1
24	3	2	1	2	1	3	1	3	2	3	2	1	2	1	3	1	3	2	3	2	1
25	3	2	1	2	1	3	1	3	2	3	2	1	2	1	3	1	3	2	3	2	1
26	2	1	3	3	2	1	2	1	3	1	3	2	2	1	3	1	3	2	3	2	1
27	2	1	3	3	2	1	2	1	3	1	3	2	2	1	3	1	3	2	3	2	1
28	2	1	3	3	2	1	2	1	3	1	3	2	2	1	3	1	3	2	3	2	1
29	1	3	2	1	3	2	3	2	1	2	1	3	2	1	3	1	3	2	3	2	1
30	1	3	2	1	3	2	3	2	1	2	1	3	2	1	3	1	3	2	3	2	1
31	1	3	2	1	3	2	3	2	1	2	1	3	2	1	3	1	3	2	3	2	1
32	3	2	1	1	3	2	2	1	3	3	2	1	1	3	2	2	1	3	3	2	1
33	3	2	1	1	3	2	2	1	3	3	2	1	1	3	2	2	1	3	3	2	1
34	3	2	1	1	3	2	2	1	3	3	2	1	1	3	2	2	1	3	3	2	1
35	2	1	3	2	1	3	3	2	1	1	3	2	2	1	3	2	1	3	3	2	1
36	2	1	3	2	1	3	3	2	1	1	3	2	2	1	3	2	1	3	3	2	1
37	2	1	3	2	1	3	3	2	1	1	3	2	2	1	3	2	1	3	3	2	1
38	1	3	2	3	2	1	1	3	2	2	1	3	1	3	2	2	1	3	3	2	1
39	1	3	2	3	2	1	1	3	2	2	1	3	1	3	2	2	1	3	3	2	1
40	1	3	2	3	2	1	1	3	2	2	1	3	1	3	2	2	1	3	3	2	1

Factors

Table A12 The L_{81} (3^{40}) orthogonal array (continued).

Exp.	22	23	24	25	26	27	28	29	30	31	32	33	34	35	36	37	38	39	40	41
1	1	1	1	1	1	1	2	2	2	2	2	2	2	2	2	2	2	2	2	2
2	3	3	3	3	3	3	1	1	1	1	1	1	1	1	1	2	2	2	2	2
3	3	3	3	3	3	3	2	2	2	2	2	2	2	2	2	3	3	3	3	3
4	3	3	3	3	3	3	3	3	3	3	3	3	3	3	3	1	1	1	1	1
5	2	2	2	3	3	3	1	1	1	2	2	2	3	3	3	1	1	1	2	2
6	2	2	2	3	3	3	2	2	2	3	3	3	1	1	1	2	2	2	3	3
7	2	2	2	3	3	3	3	3	3	1	1	1	2	2	2	3	3	3	1	1
8	1	1	1	2	2	2	1	1	1	2	2	2	3	3	3	2	2	2	3	3
9	1	1	1	2	2	2	2	2	2	3	3	3	1	1	1	3	3	3	1	1
10	1	1	1	2	2	2	3	3	3	1	1	1	2	2	2	1	1	1	2	2
11	3	3	3	1	1	1	1	1	1	2	2	2	3	3	3	3	3	3	1	1
12	3	3	3	1	1	1	2	2	2	3	3	3	1	1	1	1	1	1	2	2
13	3	3	3	1	1	1	3	3	3	1	1	1	2	2	2	2	2	2	3	3
14	1	2	3	1	2	3	1	2	3	1	2	3	1	2	3	1	2	3	1	2
15	1	2	3	1	2	3	2	3	1	2	3	1	2	3	1	2	3	1	2	3
16	1	2	3	1	2	3	3	1	2	3	1	2	3	1	2	3	1	2	3	1
17	3	1	2	3	1	2	1	2	3	1	2	3	1	2	3	2	3	1	2	3
18	3	1	2	3	1	2	2	3	1	2	3	1	2	3	1	3	1	2	3	1
19	3	1	2	3	1	2	3	1	2	3	1	2	3	1	2	1	2	3	1	2
20	2	3	1	2	3	1	1	2	3	1	2	3	1	2	3	3	1	2	3	1
21	2	3	1	2	3	1	2	3	1	2	3	1	2	3	1	1	2	3	1	2
22	2	3	1	2	3	1	3	1	2	3	1	2	3	1	2	2	3	1	2	3
23	2	3	1	3	1	2	1	2	3	2	3	1	3	1	2	1	2	3	2	3
24	2	3	1	3	1	2	2	3	1	3	1	2	1	2	3	2	3	1	3	1
25	2	3	1	3	1	2	3	1	2	1	2	3	2	3	1	3	1	2	1	2
26	1	2	3	2	3	1	1	2	3	2	3	1	3	1	2	2	3	1	3	1
27	1	2	3	2	3	1	2	3	1	3	1	2	1	2	3	3	1	2	1	2
28	1	2	3	2	3	1	3	1	2	1	2	3	2	3	1	1	2	3	2	3
29	3	1	2	1	2	3	1	2	3	2	3	1	3	1	2	3	1	2	1	2
30	3	1	2	1	2	3	2	3	1	3	1	2	1	2	3	1	2	3	2	3
31	3	1	2	1	2	3	3	1	2	1	2	3	2	3	1	2	3	1	3	1
32	3	1	2	2	3	1	1	2	3	3	1	2	2	3	1	1	2	3	3	1
33	3	1	2	2	3	1	2	3	1	1	2	3	3	1	2	2	3	1	1	2
34	3	1	2	2	3	1	3	1	2	2	3	1	1	2	3	3	1	2	2	3
35	2	3	1	1	2	3	1	2	3	3	1	2	2	3	1	2	3	1	1	2
36	2	3	1	1	2	3	2	3	1	1	2	3	3	1	2	3	1	2	2	3
37	2	3	1	1	2	3	3	1	2	2	3	1	1	2	3	1	2	3	3	1
38	1	2	3	3	1	2	1	2	3	3	1	2	2	3	1	3	1	2	2	3
39	1	2	3	3	1	2	2	3	1	1	2	3	3	1	2	1	2	3	3	1
40	1	2	3	3	1	2	3	1	2	2	3	1	1	2	3	2	3	1	1	2

Table A12 The L_{81} (3^{40}) orthogonal array (continued).

Exp.	42	43	44	45	46	47	48	49	50	51	52	53	54	55	56	57	58	59	60	61
1	2	2	2	2	2	2	2	2	2	2	2	2	2	3	3	3	3	3	3	3
2	2	2	2	2	3	3	3	3	3	3	3	3	3	1	1	1	1	1	1	1
3	3	3	3	3	1	1	1	1	1	1	1	1	1	3	3	3	3	3	3	3
4	1	1	1	1	2	2	2	2	2	2	2	2	2	2	2	2	2	2	2	2
5	2	3	3	3	1	1	1	2	2	2	3	3	3	1	1	1	2	2	2	3
6	3	1	1	1	2	2	2	3	3	3	1	1	1	3	3	3	1	1	1	2
7	1	2	2	2	3	3	3	1	1	1	2	2	2	2	2	2	3	3	3	1
8	3	1	1	1	3	3	3	1	1	1	2	2	2	1	1	1	2	2	2	3
9	1	2	2	2	1	1	1	2	2	2	3	3	3	3	3	3	1	1	1	2
10	2	3	3	3	2	2	2	3	3	3	1	1	1	2	2	2	3	3	3	1
11	1	2	2	2	2	2	2	3	3	3	1	1	1	1	1	1	2	2	2	3
12	2	3	3	3	3	3	3	1	1	1	2	2	2	3	3	3	1	1	1	2
13	3	1	1	1	1	1	1	2	2	2	3	3	3	2	2	2	3	3	3	1
14	3	1	2	3	1	2	3	1	2	3	1	2	3	1	2	3	1	2	3	1
15	1	2	3	1	2	3	1	2	3	1	2	3	1	3	1	2	3	1	2	3
16	2	3	1	2	3	1	2	3	1	2	3	1	2	2	3	1	2	3	1	2
17	1	2	3	1	3	1	2	3	1	2	3	1	2	1	2	3	1	2	3	1
18	2	3	1	2	1	2	3	1	2	3	1	2	3	3	1	2	3	1	2	3
19	3	1	2	3	2	3	1	2	3	1	2	3	1	2	3	1	2	3	1	2
20	2	3	1	2	2	3	1	2	3	1	2	3	1	1	2	3	1	2	3	1
21	3	1	2	3	3	1	2	3	1	2	3	1	2	3	1	2	3	1	2	3
22	1	2	3	1	1	2	3	1	2	3	1	2	3	2	3	1	2	3	1	2
23	1	3	1	2	1	2	3	2	3	1	3	1	2	1	2	3	2	3	1	3
24	2	1	2	3	2	3	1	3	1	2	1	2	3	3	1	2	1	2	3	2
25	3	2	3	1	3	1	2	1	2	3	2	3	1	2	3	1	3	1	2	1
26	2	1	2	3	3	1	2	1	2	3	2	3	1	1	2	3	2	3	1	3
27	3	2	3	1	1	2	3	2	3	1	3	1	2	3	1	2	1	2	3	2
28	1	3	1	2	2	3	1	3	1	2	1	2	3	2	3	1	3	1	2	1
29	3	2	3	1	2	3	1	3	1	2	1	2	3	1	2	3	2	3	1	3
30	1	3	1	2	3	1	2	1	2	3	2	3	1	3	1	2	1	2	3	2
31	2	2	3	1	1	2	3	2	3	1	3	1	2	2	3	1	3	1	2	1
32	2	2	3	1	1	2	3	3	1	2	2	3	1	1	2	3	3	1	2	2
33	3	3	1	2	2	3	1	1	2	3	3	1	2	3	1	2	2	3	1	1
34	1	1	2	3	3	1	2	2	3	1	1	2	3	2	3	1	1	2	3	3
35	3	3	1	2	3	1	2	2	3	1	1	2	3	1	2	3	3	1	2	2
36	1	2	3	1	1	2	3	3	1	2	2	3	1	3	1	2	2	3	1	1
37	2	2	3	1	2	3	1	1	2	3	3	1	2	2	3	1	1	2	3	3
38	1	1	2	3	2	3	1	1	2	3	3	1	2	1	2	3	3	1	2	2
39	2	2	3	1	3	1	2	2	3	1	1	2	3	3	1	2	2	3	1	1
40	3	3	1	2	1	2	3	3	1	2	2	3	1	2	3	1	1	2	3	3

Table A12 The $L_{81}(3^{40})$ orthogonal array (continued).

Exp.	62	63	64	65	66	67	68	69	70	71	72	73	74	75	76	77	78	79	80	81
1	3	3	3	3	3	3	3	3	3	3	3	3	3	3	3	3	3	3	3	3
2	1	1	2	2	2	2	2	2	2	2	2	3	3	3	3	3	3	3	3	3
3	3	3	1	1	1	1	1	1	1	1	1	2	2	2	2	2	2	2	2	2
4	2	2	3	3	3	3	3	3	3	3	3	1	1	1	1	1	1	1	1	1
5	3	3	1	1	1	2	2	2	3	3	3	1	1	1	2	2	2	3	3	3
6	2	2	3	3	3	1	1	1	2	2	2	3	3	3	1	1	1	2	2	2
7	1	1	2	2	2	3	3	3	1	1	1	2	2	2	3	3	3	1	1	1
8	3	3	2	2	2	3	3	3	1	1	1	3	3	3	1	1	1	2	2	2
9	2	2	1	1	1	2	2	2	3	3	3	2	2	2	3	3	3	1	1	1
10	1	1	3	3	3	1	1	1	2	2	2	1	1	1	2	2	2	3	3	3
11	3	3	3	3	3	1	1	1	2	2	2	2	2	2	3	3	3	1	1	1
12	2	2	2	2	2	3	3	3	1	1	1	1	1	1	2	2	2	3	3	3
13	1	1	1	1	1	2	2	2	3	3	3	3	3	3	1	1	1	2	2	2
14	2	3	1	2	3	1	2	3	1	2	3	1	2	3	1	2	3	1	2	3
15	1	2	3	1	2	3	1	2	3	1	2	3	1	2	3	1	2	3	1	2
16	3	1	2	3	1	2	3	1	2	3	1	2	3	1	2	3	1	2	3	1
17	2	3	2	3	1	2	3	1	2	3	1	3	1	2	3	1	2	3	1	2
18	1	2	1	2	3	1	2	3	1	2	3	2	3	1	2	3	1	2	3	1
19	3	1	3	1	2	3	1	2	3	1	2	1	2	3	1	2	3	1	2	3
20	2	3	3	1	2	3	1	2	3	1	2	2	3	1	2	3	1	2	3	1
21	1	2	2	3	1	2	3	1	2	3	1	1	2	3	1	2	3	1	2	3
22	3	1	1	2	3	1	2	3	1	2	3	3	1	2	3	1	2	3	1	2
23	1	2	1	2	3	2	3	1	3	1	2	1	2	3	2	3	1	3	1	2
24	3	1	3	1	2	1	2	3	2	3	1	3	1	2	1	2	3	2	3	1
25	2	3	2	3	1	3	1	2	1	2	3	2	3	1	3	1	2	1	2	3
26	1	2	2	3	1	3	1	2	1	2	3	3	1	2	1	2	3	2	3	1
27	3	1	1	2	3	2	3	1	3	1	2	2	3	1	3	1	2	1	2	3
28	2	3	3	1	2	1	2	3	2	3	1	1	2	3	2	3	1	3	1	2
29	1	2	3	1	2	1	2	3	2	3	1	2	3	1	3	1	2	1	2	3
30	3	1	2	3	1	3	1	2	1	2	3	2	3	1	2	3	1	3	1	2
31	2	3	1	2	3	2	3	1	3	1	2	3	1	2	1	2	3	2	3	1
32	3	1	1	2	3	3	1	2	2	3	1	1	2	3	3	1	2	2	3	1
33	2	3	3	1	2	2	1	1	1	2	3	3	1	2	2	3	1	1	2	3
34	1	2	2	3	1	1	3	3	3	1	2	2	3	1	1	2	3	3	1	2
35	3	1	2	3	1	1	3	3	3	1	2	3	1	2	2	3	1	1	2	3
36	1	2	3	1	2	3	1	2	2	3	1	1	3	2	1	2	3	3	1	2
37	1	2	3	1	2	2	3	1	1	2	3	2	3	3	3	1	2	2	3	1
38	3	1	3	1	2	2	3	1	3	2	3	3	1	1	1	2	3	3	1	2
39	2	3	2	3	1	1	2	3	3	1	2	1	2	3	3	1	2	2	3	1
40	1	2	1	2	3	3	1	2	2	3	1	1	2	2	2	3	1	1	2	3

Table A13 The interaction table of orthogonal array

	1	2	3	4	5	6	7	8	9	10	11	12	13
1		3	2	2	6	5	5	9	8	8	12	11	11
		4	4	3	7	7	6	10	10	9	13	13	12
2			1	1	8	9	10	5	6	7	5	6	7
			4	3	11	12	13	11	12	13	8	9	10
3				1	9	10	8	7	5	6	6	7	5
				2	13	11	12	12	13	11	10	8	9
4					10	8	9	6	7	5	7	5	6
					12	13	11	13	11	12	9	10	8
5						1	1	2	3	4	2	4	3
						7	6	11	13	12	8	10	9
6							1	4	2	3	3	2	4
							5	13	12	11	10	9	8
7								3	4	2	4	3	2
								12	11	13	9	8	10
8									1	1	2	3	4
									10	9	5	7	6
9										1	4	2	3
										8	7	6	5
10											3	4	2
											6	5	7
11												1	1
												13	12
12													1
													11

Table A13 The interaction table of orthogonal array

The Cu_Hu potential (the new parameters have been marked with red color)

```
39      ! Number of general parameters
 50.0000 !Overcoordination parameter
  9.5469 !Overcoordination parameter
  1.6725 !Valency angle conjugation parameter
  1.7224 !Triple bond stabilisation parameter
  6.8702 !Triple bond stabilisation parameter
 60.4850 !C2-correction
  1.0588 !Undercoordination parameter
  4.6000 !Triple bond stabilisation parameter
 12.1176 !Undercoordination parameter
 13.3056 !Undercoordination parameter
-70.5044 !Triple bond stabilization energy
  0.0000 !Lower Taper-radius
 10.0000 !Upper Taper-radius
  2.8793 !Not used
 33.8667 !Valency undercoordination
  6.0891 !Valency angle/lone pair parameter
  1.0563 !Valency angle
  2.0384 !Valency angle parameter
  6.1431 !Not used
  6.9290 !Double bond/angle parameter
  0.3989 !Double bond/angle parameter: overcoord
  3.9954 !Double bond/angle parameter: overcoord
 -2.4837 !Not used
  5.7796 !Torsion/BO parameter
 10.0000 !Torsion overcoordination
  1.9487 !Torsion overcoordination
 -1.2327 !Conjugation 0 (not used)
  2.1645 !Conjugation
  1.5591 !vdWaals shielding
  0.1000 !Cutoff for bond order
  1.7602 !Valency angle conjugation parameter
  0.6991 !Overcoordination parameter
 50.0000 !Overcoordination parameter
  1.8512 !Valency/lone pair parameter
  0.5000 !Not used
 20.0000 !Not used
  5.0000 !Molecular energy (not used)
  0.0000 !Molecular energy (not used)
  0.7903 !Valency angle conjugation parameter
 10    ! Nr of atoms; cov.r; valency;a.m;Rvdw;Evdw;gammaEEM;cov.r2;#
        alfa;gammavdW;valency;Eunder;Eover;chiEEM;etaEEM;n.u.
        cov r3;Elp;Heat inc.;n.u.;n.u.;n.u.;n.u.
```

ov/un;val1;n.u.;val3,vval4

```
C   1.3817  4.0000 12.0000  1.8903  0.1838  0.9000  1.1341  4.0000
    9.7559  2.1346  4.0000 34.9350 79.5548  5.9666  7.0000  0.0000
    1.2114  0.0000 202.2908  8.9539 34.9289 13.5366  0.8563  0.0000
   -2.8983  2.5000  1.0564  4.0000  2.9663  0.0000  0.0000  0.0000
H   0.8930  1.0000  1.0080  1.3550  0.0930  0.8203 -0.1000  1.0000
    8.2230 33.2894  1.0000  0.0000 121.1250  3.7248  9.6093  1.0000
   -0.1000  0.0000 55.1878  3.0408  2.4197  0.0003  1.0698  0.0000
  -19.4571  4.2733  1.0338  1.0000  2.8793  0.0000  0.0000  0.0000
O   1.2450  2.0000 15.9990  2.3890  0.1000  1.0898  1.0548  6.0000
    9.7300 13.8449  4.0000 37.5000 116.0768  8.5000  8.3122  2.0000
    0.9049  0.4056 68.0152  3.5027  0.7640  0.0021  0.9745  0.0000
   -3.5500  2.9000  1.0493  4.0000  2.9225  0.0000  0.0000  0.0000
N   1.2333  3.0000 14.0000  1.9324  0.1376  0.8013  1.1748  5.0000
   10.0667  7.8431  4.0000 32.2482 100.0000  7.5808  7.0000  2.0000
    1.0433 27.7285 119.9837  1.9507  4.3158  3.5229  0.9745  0.0000
   -4.3875  2.6192  1.0183  4.0000  2.8793  0.0000  0.0000  0.0000
S   1.9405  2.0000 32.0600  2.0677  0.2099  1.0336  1.5479  6.0000
    9.9575  4.9055  4.0000 52.9998 112.1416  6.5000  8.2545  2.0000
    1.4601  9.7177 71.1843  5.7487 23.2859 12.7147  0.9745  0.0000
  -11.0000  2.7466  1.0338  6.2998  2.8793  0.0000  0.0000  0.0000
Mg  1.8315  2.0000 24.3050  2.2464  0.1806  0.5020  1.0000  2.0000
   10.9186 27.1205  3.0000 38.0000  0.0000  0.9499  5.6130  0.0000
   -1.3000  0.0000 220.0000 49.9248  0.3370  0.0000  0.0000  0.0000
   -1.0823  2.3663  1.0564  6.0000  2.9663  0.0000  0.0000  0.0000
P   1.5994  3.0000 30.9738  1.7000  0.1743  1.0000  1.3000  5.0000
    9.1909 14.2932  5.0000  0.0000  0.0000  1.8292  7.2520  0.0000
   -1.0000 10.2596  1.5000  0.2205 16.7429 15.9629  0.0000  0.0000
   -2.5000  1.6114  1.0338  5.0000  2.8793  0.0000  0.0000  0.0000
Na  2.0300  1.0000 22.9898  2.3334  0.1481  0.8765 -1.0000  1.0000
   11.0000  9.8000  1.0000  0.0000  0.0000 -3.8501  5.9459  0.0000
   -1.0000  0.0000 67.5458 100.0000 10.0000  0.2500  0.8563  0.0000
   -2.5766  2.5000  1.0338  6.0000  2.5791  0.0000  0.0000  0.0000
Cu  1.9202  2.0000 63.5460  1.9221  0.2826  1.0000  0.1000  1.0000
   10.9889 100.0000  1.0000  0.0000  0.0000  2.7875  6.0000  0.0000
   -1.0000  0.0000 80.7000 34.9555  0.4988  0.0000  0.8563  0.0000
   -5.1872  3.1491  1.0000  4.0000  2.5791  0.0000  0.0000  0.0000
X  -0.0998  2.0000  1.0080  2.0000  0.0000  1.0000 -0.1000  6.0000
   10.0000  2.5000  4.0000  0.0000  0.0000  8.5000  1.5000  0.0000
   -0.1000  0.0000 -2.3700  8.7410 13.3640  0.6690  0.9745  0.0000
  -11.0000  2.7466  1.0338  4.0000  2.8793  0.0000  0.0000  0.0000
40     ! Nr of bonds; Edis1;LPpen;n.u.;pbe1;pbo5;13corr;pbo6
                pbe2;pbo3;pbo4;Etrip;pbo1;pbo2;ovcorr
 1 1 158.2004 99.1897 78.0000 -0.7738 -0.4550  1.0000 37.6117  0.4147
      0.4590 -0.1000  9.1628  1.0000 -0.0777  6.7268  1.0000  0.0000
```

1 2 169.4760 0.0000 0.0000 -0.6083 0.0000 1.0000 6.0000 0.7652
    5.2290 1.0000 0.0000 1.0000 -0.0500 6.9136 0.0000 0.0000

2 2 153.3934 0.0000 0.0000 -0.4600 0.0000 1.0000 6.0000 0.7300
    6.2500 1.0000 0.0000 1.0000 -0.0790 6.0552 0.0000 0.0000

1 3 164.4303 82.6772 60.8077 -0.3739 -0.2351 1.0000 10.5036 1.0000
    0.4475 -0.2288 7.0250 1.0000 -0.1363 4.8734 0.0000 0.0000

3 3 142.2858 145.0000 50.8293 0.2506 -0.1000 1.0000 29.7503 0.6051
    0.3451 -0.1055 9.0000 1.0000 -0.1225 5.5000 1.0000 0.0000

1 4 134.1215 140.2179 79.9745 0.0163 -0.1428 1.0000 27.0617 0.2000
    0.1387 -0.3681 7.1611 1.0000 -0.1000 5.0825 1.0000 0.0000

3 4 130.8596 169.4551 40.0000 0.3837 -0.1639 1.0000 35.0000 0.2000
    1.0000 -0.3579 7.0004 1.0000 -0.1193 6.8773 1.0000 0.0000

4 4 157.9384 82.5526 152.5336 0.4010 -0.1034 1.0000 12.4261 0.5828
    0.1578 -0.1509 11.9186 1.0000 -0.0861 5.4271 1.0000 0.0000

2 3 160.0000 0.0000 0.0000 -0.5725 0.0000 1.0000 6.0000 0.5626
    1.1150 1.0000 0.0000 0.0000 -0.0920 4.2790 0.0000 0.0000

2 4 188.1449 0.0000 0.0000 -0.3819 0.0000 1.0000 6.0000 0.2889
    7.6213 1.0000 0.0000 1.0000 -0.0405 6.0876 0.0000 0.0000

1 5 128.9942 74.5848 55.2528 0.1035 -0.5211 1.0000 18.9617 0.6000
    0.2949 -0.2398 8.1175 1.0000 -0.1029 5.6731 1.0000 0.0000

2 5 151.5159 0.0000 0.0000 -0.4721 0.0000 1.0000 6.0000 0.6000
    9.4366 1.0000 0.0000 1.0000 -0.0290 7.0050 1.0000 0.0000

3 5 0.0000 0.0000 0.0000 0.5563 -0.4038 1.0000 49.5611 0.6000
    0.4259 -0.4577 12.7569 1.0000 -0.1100 7.1145 1.0000 0.0000

4 5 0.0000 0.0000 0.0000 0.4438 -0.2034 1.0000 40.3399 0.6000
    0.3296 -0.3153 9.1227 1.0000 -0.1805 5.6864 1.0000 0.0000

5 5 96.1871 93.7006 68.6860 0.0955 -0.4781 1.0000 17.8574 0.6000
    0.2723 -0.2373 9.7875 1.0000 -0.0950 6.4757 1.0000 0.0000

2 6 58.6896 0.0000 0.0000 -0.0203 -0.1418 1.0000 13.1260 0.0230
    8.2136 -0.1310 0.0000 1.0000 -0.2692 6.4254 0.0000 24.4461

3 6 87.0227 0.0000 43.3991 0.0030 -0.3000 1.0000 36.0000 0.0250
    0.0087 -0.2500 12.0000 1.0000 -0.0439 6.6073 1.0000 24.4461

6 6 32.3808 0.0000 0.0000 -0.0076 -0.2000 0.0000 16.0000 0.2641
    4.8726 -0.2000 10.0000 1.0000 -0.0729 4.6319 0.0000 0.0000

1 7 110.0000 92.0000 0.0000 0.2171 -0.1418 1.0000 13.1260 0.6000
    0.3601 -0.1310 10.7257 1.0000 -0.0869 5.3302 1.0000 0.0000

2 7 0.1466 0.0000 0.0000 0.2250 -0.1418 1.0000 13.1260 0.6000
    0.3912 -0.1310 0.0000 1.0000 -0.1029 9.3302 0.0000 0.0000

3 7 202.5868 164.1808 0.0000 0.5506 -0.5000 1.0000 25.0000 0.4300
    0.0912 -0.1285 16.0342 1.0000 -0.2008 6.2678 1.0000 0.0000

4 7 130.0000 0.0000 0.0000 0.2171 -0.1418 1.0000 13.1260 0.6000
    0.3601 -0.1310 10.7257 1.0000 -0.0869 5.3302 1.0000 0.0000

6 7 0.1000 0.0000 0.0000 0.2500 -0.5000 1.0000 35.0000 0.6000
    0.5000 -0.5000 20.0000 1.0000 -0.2000 10.0000 1.0000 0.0000

7 7 0.0000 0.0000 0.0000 0.2171 -0.5000 1.0000 35.0000 0.6000

```
        0.5000  -0.5000 20.0000  1.0000  -0.2000 10.0000  1.0000  0.0000
 2  8   0.0000   0.0000  0.0000 -1.0000  -0.3000  1.0000 36.0000  0.7000
       10.1151  -0.3500 25.0000  1.0000  -0.1053  8.2003  1.0000  0.0000
 3  8  76.0753   0.0000  0.0000 -0.4452  -0.3000  1.0000 36.0000  0.6433
        5.6834  -0.3500 25.0000  1.0000  -0.0539  8.0273  1.0000  0.0000
 4  8   0.0000   0.0000  0.0000 -1.0000  -0.3000  1.0000 36.0000  0.7000
       10.1151  -0.3500 25.0000  1.0000  -0.1053  8.2003  1.0000  0.0000
 6  8   0.1000   0.0000  0.0000  0.2500  -0.5000  1.0000 35.0000  0.6000
        0.5000  -0.5000 20.0000  1.0000  -0.2000 10.0000  1.0000  0.0000
 7  8   0.1000   0.0000  0.0000  0.2500  -0.5000  1.0000 35.0000  0.6000
        0.5000  -0.5000 20.0000  1.0000  -0.2000 10.0000  1.0000  0.0000
 8  8  27.8052   0.0000  0.0000  0.4022   0.3000  0.0000 25.0000  0.4894
        0.6222  -0.4000 12.0000  1.0000  -0.0500  5.3362  0.0000  0.0000
 4  6   0.0000   0.0000  0.0000 -1.0000  -0.3000  1.0000 36.0000  0.7000
       10.1151  -0.3500 25.0000  1.0000  -0.1053  8.2003  1.0000  0.0000
```

<span style="color:red">

```
 1  9  69.9858   9.7715  0.0000  0.2319  -0.2000  1.0000 16.0000  0.0541
        1.3551  -0.1343 10.8798  1.0000  -0.1517  4.9990  1.0000  0.0000
 2  9 120.4696   0.0000  0.0000 -0.8692   0.0000  1.0000  6.0000  0.1293
        0.1092   1.0000  0.0000  1.0000  -0.1459  4.5892  0.0000  0.0000
```



```
 3  9  81.4346   0.0000  0.0000 -0.1594  -0.3000  1.0000 36.0000  0.0025
        0.2904  -0.2500 12.0000  1.0000  -0.0742  9.3638  0.0000  0.0000
```

<span style="color:red">

```
 4  9  82.5352   0.0000  0.0000  0.9152  -0.3000  1.0000 36.0000  0.5406
        0.7170  -0.2500 12.0000  1.0000  -0.1538  5.1510  0.0000  0.0000
```



```
 9  9  73.6263   0.0000  0.0000  0.0209  -0.2000  0.0000 16.0000  0.3414
        0.4703  -0.2000 15.0000  1.0000  -0.1319  5.9254  0.0000  0.0000
 2 10 192.2699   0.0000  0.0000 -0.4064  -0.2000  0.0000 16.0000  0.3162
        1.0201  -0.2000 15.0000  1.0000  -0.1078  5.2373  0.0000  0.0000
 3 10   0.0000   0.0000  0.0000  0.5000  -0.2000  0.0000 16.0000  0.5000
        1.0001  -0.2000 15.0000  1.0000  -0.1000 10.0000  0.0000  0.0000
 9 10 142.0000   0.0000  0.0000 -0.1000  -0.2000  0.0000 16.0000  0.2561
        1.3569  -0.2000 15.0000  1.0000  -0.1105  5.1362  0.0000  0.0000
10 10 109.2500   0.0000  0.0000  0.1803  -0.2000  0.0000 16.0000  0.3356
        0.9228  -0.2000 15.0000  1.0000  -0.1178  5.6715  0.0000  0.0000
21    ! Nr of off-diagonal terms; Ediss;Ro;gamma;rsigma;rpi;rpi2
 1  2   0.1239   1.4004  9.8467  1.1210  -1.0000 -1.0000
 2  3   0.0283   1.2885 10.9190  0.9215  -1.0000 -1.0000
 2  4   0.0686   1.5116 10.0161  0.9428  -1.0000 -1.0000
 1  3   0.1345   1.8422  9.7725  1.2835   1.1576  1.0637
 1  4   0.1447   1.8766  9.7990  1.3436   1.1885  1.1363
 3  4   0.1048   2.0003 10.1220  1.3173   1.1096  1.0206
 1  5   0.1408   1.8161  9.9393  1.7986   1.3021  1.4031
 2  5   0.0895   1.6239 10.0104  1.4640  -1.0000 -1.0000
 3  5   0.1022   1.9887 10.0605  1.5799   1.4000 -1.0000
 4  5   0.1505   1.9000 10.5104  1.8000   1.4000 -1.0000
 2  6   0.0100   1.6000 13.2979  1.8670  -1.0000 -1.0000
```

3 6   0.0809   1.7000   11.4606   1.5177   -1.0000   -1.0000

3 7   0.0611   1.7624   10.2685   1.7989   1.4523   -1.0000

6 7   0.1801   1.8566   9.8498   0.1000   -1.0000   -1.0000

3 8   0.1592   1.8283   11.7256   1.6655   -1.0000   -1.0000

1 9   0.0818   1.6863   10.7619   1.6526   1.5507   -1.0000

2 9   0.0397   1.7288   11.9258   1.2111   -1.0000   -1.0000

3 9   0.0348   1.7637   12.3562   1.7228   -1.0000   -1.0000

4 9   0.0490   1.7517   12.5446   1.3905   -1.0000   -1.0000

2 10   0.1000   1.7500   10.5000   1.2000   -1.0000   -1.0000

9 10   0.1570   2.1420   10.9943   1.7819   -1.0000   -1.0000

117   ! Nr of angles;at1;at2;at3;Thetao,o;ka;kb;pv1;pv2

1 1 1   59.0573   30.7029   0.7606   0.0000   0.7180   6.2933   1.1244

1 1 2   65.7758   14.5234   6.2481   0.0000   0.5665   0.0000   1.6255

2 1 2   70.2607   25.2202   3.7312   0.0000   0.0050   0.0000   2.7500

1 2 2   0.0000   0.0000   6.0000   0.0000   0.0000   0.0000   1.0400

1 2 1   0.0000   3.4110   7.7350   0.0000   0.0000   0.0000   1.0400

2 2 2   0.0000   27.9213   5.8635   0.0000   0.0000   0.0000   1.0400

1 1 3   53.9517   7.8968   2.6122   0.0000   3.0000   58.6562   1.0338

3 1 3   76.9627   44.2852   2.4177   -25.3063   1.6334   -50.0000   2.7392

1 1 4   79.7483   21.2779   7.5000   0.0000   1.1261   50.0000   1.5236

3 1 4   73.9544   12.4661   7.0000   0.0000   1.1261   0.0000   1.1880

4 1 4   90.0000   20.5594   7.4616   0.0000   1.1261   0.0000   1.5562

2 1 3   65.0000   16.3141   5.2730   0.0000   0.4448   0.0000   1.4077

2 1 4   74.2929   31.0883   2.6184   0.0000   0.1000   0.0000   1.0500

1 2 4   0.0000   0.0019   6.3000   0.0000   0.0000   0.0000   1.0400

1 3 1   72.6199   42.5510   0.7205   0.0000   2.9294   0.0000   1.3096

1 3 3   81.9029   32.2258   1.7397   0.0000   0.9888   68.1072   1.7777

1 3 4   82.4890   31.4554   0.9953   0.0000   3.0000   0.0000   1.0783

3 3 3   80.7324   30.4554   0.9953   0.0000   3.0000   50.0000   1.0783

3 3 4   84.3637   31.4554   0.9953   0.0000   3.0000   0.0000   1.0783

4 3 4   89.7071   31.4554   0.9953   0.0000   3.0000   0.0000   1.1519

1 3 2   70.1101   13.1217   4.4734   0.0000   0.8433   0.0000   3.0000

2 3 3   75.6935   50.0000   2.0000   0.0000   1.0000   0.0000   1.1680

2 3 4   75.6201   18.7919   0.9833   0.0000   0.1000   0.0000   1.0500

2 3 2   85.8000   9.8453   2.2720   0.0000   2.8635   0.0000   1.5800

1 4 1   79.8213   7.0343   1.2383   0.0000   2.9701   0.0000   1.2178

1 4 3   103.3204   33.0381   0.5787   0.0000   2.9701   0.0000   1.2178

1 4 4   50.0000   25.3257   4.7701   0.0000   2.9701   0.0000   1.2199

3 4 3   74.1978   42.1786   1.7845   -18.0069   2.9701   0.0000   1.2178

3 4 4   74.8600   43.7354   1.1572   -0.9193   2.9701   0.0000   1.2178

4 4 4   75.0538   14.8267   5.2794   0.0000   2.9701   0.0000   1.2178

1 4 2   68.0427   29.7566   1.0683   0.0000   0.3531   0.0000   1.4794

2 4 3   81.3686   40.0712   2.2396   0.0000   0.3531   0.0000   1.4794

2 4 4   83.0104   43.4766   1.5328   0.0000   0.3531   0.0000   1.4794

2 4 2   78.8310   17.9747   3.8083   0.0000   0.0222   0.0000   1.9986

1 2 3 0.0000 25.0000 3.0000 0.0000 1.0000 0.0000 1.0400

1 2 4 0.0000 0.0019 6.0000 0.0000 0.0000 0.0000 1.0400

1 2 5 0.0000 0.0019 6.0000 0.0000 0.0000 0.0000 1.0400

3 2 3 0.0000 15.0000 2.8900 0.0000 0.0000 0.0000 2.8774

3 2 4 0.0000 0.0019 6.0000 0.0000 0.0000 0.0000 1.0400

4 2 4 0.0000 0.0019 6.0000 0.0000 0.0000 0.0000 1.0400

2 2 3 0.0000 8.5744 3.0000 0.0000 0.0000 0.0000 1.0421

2 2 4 0.0000 0.0019 6.0000 0.0000 0.0000 0.0000 1.0400

1 1 5 74.4180 33.4273 1.7018 0.1463 0.5000 0.0000 1.6178

1 5 1 79.7037 28.2036 1.7073 0.1463 0.5000 0.0000 1.6453

2 1 5 63.3289 29.4225 2.1326 0.0000 0.5000 0.0000 3.0000

1 5 2 85.9449 38.3109 1.2492 0.0000 0.5000 0.0000 1.1000

1 5 5 85.6645 40.0000 2.9274 0.1463 0.5000 0.0000 1.3830

2 5 2 83.8555 5.1317 0.4377 0.0000 0.5000 0.0000 3.0000

2 5 5 97.0064 32.1121 2.0242 0.0000 0.5000 0.0000 2.8568

2 2 5 0.0000 0.0019 6.0000 0.0000 0.0000 0.0000 1.0400

5 4 5 62.0000 33.4273 1.7018 0.1463 0.5000 0.0000 1.0500

3 5 3 77.0699 39.4349 2.1313 -30.0000 0.9567 0.0000 1.1483

1 5 3 70.0000 35.0000 3.4223 0.0000 1.3550 0.0000 1.2002

1 5 4 70.0000 35.0000 3.4223 0.0000 1.3550 0.0000 1.2002

3 5 4 70.0000 35.0000 3.4223 0.0000 1.3550 0.0000 1.2002

5 1 7 70.0000 35.0000 3.4223 0.0000 1.3550 0.0000 1.2002

1 3 5 73.0990 33.8942 1.2098 0.0000 0.8161 0.0000 1.1776

3 3 5 83.9753 31.0715 3.5590 0.0000 0.8161 0.0000 1.1776

2 3 5 76.9521 20.0000 2.0903 0.0000 1.0000 0.0000 1.0400

2 6 2 0.0000 49.8261 0.2093 0.0000 2.0870 0.0000 2.2895

2 2 6 0.0000 39.7818 3.1505 0.0000 1.1296 0.0000 1.1110

6 2 6 0.0000 0.5047 0.8000 0.0000 0.8933 0.0000 4.6650

2 6 6 0.0000 8.7037 0.0827 0.0000 3.5597 0.0000 1.1198

3 6 3 0.0000 9.2317 0.1000 0.0000 1.0000 0.0000 1.0920

6 3 6 0.0008 25.0000 8.0000 0.0000 1.0000 0.0000 3.0000

2 3 6 66.0423 5.0000 1.0000 0.0000 1.0000 0.0000 1.2500

2 6 3 0.0000 0.5000 0.1000 0.0000 1.0000 0.0000 3.0000

3 3 6 70.0000 20.0000 1.0000 0.0000 1.0000 0.0000 1.2500

3 7 3 88.6293 18.2614 0.8145 0.0000 -0.1780 0.0000 2.3661

2 3 7 75.0000 7.8005 0.9394 0.0000 1.3523 0.0000 1.0400

3 3 7 60.0000 40.0000 4.0000 0.0000 1.0000 0.0000 1.0400

3 2 7 0.0000 10.0000 1.0000 0.0000 1.0000 0.0000 1.0400

6 3 7 41.7798 3.5596 7.5000 0.0000 -0.2621 0.0000 1.0400

7 3 7 50.6740 13.3258 0.1000 0.0000 1.0718 0.0000 1.1254

1 3 7 76.8677 5.4250 3.1105 0.0000 -0.0827 0.0000 2.1396

2 7 3 75.0000 25.0000 2.0000 0.0000 1.0000 0.0000 1.2500

3 7 7 70.0000 25.0000 2.0000 0.0000 1.0000 0.0000 1.2500

3 9 3 96.2265 4.5610 12.0000 0.0000 0.3211 0.0000 1.5204

3 9 3 0.0000 9.1552 7.9919 0.0000 0.1660 0.0000 1.5386

```
 9  3  9 100.0000 10.1065  6.0000  0.0000  1.0000  0.0000  3.6601
 2  3  9  55.0417  3.5032  3.9979  0.0000  1.5171  0.0000  1.0400
 3  3  9  70.0000 30.0000  2.0000  0.0000  1.0000  0.0000  1.2500
 3  9  9  66.7783 14.3146  0.7911  0.0000  1.0000  0.0000  1.2333
 3  9 10  95.2122  5.7090 12.0000  0.0000  0.2248  0.0000  2.8936
 3  9 10   0.0000  9.0054  7.9511  0.0000  0.1482  0.0000  1.6245
 9 10  9   0.0000 15.0054  2.5000  0.0000  1.0000  0.0000  1.5000
 9  9 10  58.0000  5.0000  2.5000  0.0000  1.0000  0.0000  1.2280
10  9 10  38.0000 30.0000  2.0000  0.0000  1.0000  0.0000  1.0500
 3  2 10   0.0000 15.0000  2.8900  0.0000  0.0000  0.0000  2.8774
 3  9  4 100.0000 28.1532 12.0000  0.0000  0.2932  0.0000  1.6489
 3  9  4   0.0000 22.7457  2.9039  0.0000  0.5593  0.0000  1.9764
 4  9  4  87.0081 27.6432  3.9735  0.0000  4.0000  0.0000  1.4578
 4  9  4   0.0000 22.8998  3.1077  0.0000  3.0000  0.0000  1.0696
 3  4  9  70.0000 30.0000  2.0000  0.0000  1.0000  0.0000  1.2500
 4  3  9  70.0000 30.0000  2.0000  0.0000  1.0000  0.0000  1.2500
 4  4  9  70.0000 30.0000  2.0000  0.0000  1.0000  0.0000  1.2500
 4  9  9  66.7783 14.3146  0.7911  0.0000  1.0000  0.0000  1.2333
 4  9 10  95.2122  5.7090 12.0000  0.0000  0.2248  0.0000  2.8936
 4  9 10   0.0000  9.0054  7.9511  0.0000  0.1482  0.0000  1.6245
 4  2 10   0.0000 15.0000  2.8900  0.0000  0.0000  0.0000  2.8774
 1  3  9  55.0000 15.0000  1.0000  0.0000  1.0000  0.0000  1.5000
 1  4  9  55.0000 15.0000  1.0000  0.0000  1.0000  0.0000  1.5000
 1  9  3  54.4500 17.5007  0.7719  0.0000  1.1480  0.0000  1.1828
 9  1  2  58.7214 32.9835  0.5478  0.0000  3.7243  0.0000  0.8839
 9  1  1  36.5763 14.4943  1.5471  0.0000  0.0229  0.0000  1.1316
 2  9  2  65.0000 29.4000  0.9234  0.0000  1.9656  0.0000  2.3147
 1  9  1  46.6784 18.4053  1.1651  0.0000  0.8618  0.0000  1.1235
 9  1  3  34.6430 23.2824  1.9014  0.0000  0.9317  0.0000  1.0923
 9  1  9  95.4080 33.9923  1.7249  0.0000  0.0096  0.0000  1.6262
 1  9  9   5.1683  3.4172  0.6977  0.0000  0.7589  0.0000  2.0758
 2  2  9  10.0992 26.2621  5.0045  0.0000  0.7542  0.0000  1.0058
 9  2  9   0.0000 39.3035  2.1617  0.0000  0.5683  0.0000  2.8494
 2  9  9  29.5402  0.9921  4.7770  0.0000  0.1034  0.0000  3.0305
 1  9  2  49.5000 10.7186  2.4449  0.0000  1.8740  0.0000  1.0404
 1  2  9   7.5750  0.2783  1.1624  0.0000  0.9319  0.0000  3.8123
 2  4  9  63.4375  3.5182  4.0754  0.0000  1.5393  0.0000  0.9933
 9  4  9  98.9705 10.7802  5.7309  0.0000  1.0401  0.0000  3.5676
63    ! Nr of torsions;at1;at2;at3;at4;;V1;V2;V3;V2(BO);vconj;n.u;n
 1  1  1  1  -0.2500 34.7453  0.0288 -6.3507 -1.6000  0.0000  0.0000
 1  1  1  2  -0.2500 29.2131  0.2945 -4.9581 -2.1802  0.0000  0.0000
 2  1  1  2  -0.2500 31.2081  0.4539 -4.8923 -2.2677  0.0000  0.0000
 1  1  1  3   1.2799 20.7787 -0.5249 -2.5000 -1.0000  0.0000  0.0000
 2  1  1  3   1.9159 19.8113  0.7914 -4.6995 -1.0000  0.0000  0.0000
 3  1  1  3  -1.4477 16.6853  0.6461 -4.9622 -1.0000  0.0000  0.0000
```

```
1 1 3 1  0.4816 19.6316 -0.0057 -2.5000 -1.0000  0.0000  0.0000
1 1 3 2  1.2044 80.0000 -0.3139 -6.1481 -1.0000  0.0000  0.0000
2 1 3 1 -2.5000 31.0191  0.6165 -2.7733 -2.9807  0.0000  0.0000
2 1 3 2 -2.4875 70.8145  0.7582 -4.2274 -3.0000  0.0000  0.0000
1 1 3 3 -0.3566 10.0000  0.0816 -2.6110 -1.9631  0.0000  0.0000
2 1 3 3 -1.4383 80.0000  1.0000 -3.6877 -2.8000  0.0000  0.0000
3 1 3 1 -1.1390 78.0747 -0.0964 -4.5172 -3.0000  0.0000  0.0000
3 1 3 2 -2.5000 70.3345 -1.0000 -5.5315 -3.0000  0.0000  0.0000
3 1 3 3 -2.0234 80.0000  0.1684 -3.1568 -2.6174  0.0000  0.0000
1 3 3 1  1.1637 -17.3637  0.5459 -3.6005 -2.6938  0.0000  0.0000
1 3 3 2 -2.1289 12.8382  1.0000 -5.6657 -2.9759  0.0000  0.0000
2 3 3 2  2.5000 -22.9397  0.6991 -3.3961 -1.0000  0.0000  0.0000
1 3 3 3  2.5000 -25.0000  1.0000 -2.5000 -1.0000  0.0000  0.0000
2 3 3 3 -2.5000 -2.5103 -1.0000 -2.5000 -1.0000  0.0000  0.0000
3 3 3 3 -2.5000 -25.0000  1.0000 -2.5000 -1.0000  0.0000  0.0000
0 1 2 0  0.0000  0.0000  0.0000  0.0000  0.0000  0.0000  0.0000
0 2 2 0  0.0000  0.0000  0.0000  0.0000  0.0000  0.0000  0.0000
0 2 3 0  0.0000  0.1000  0.0200 -2.5415  0.0000  0.0000  0.0000
0 1 1 0  0.0000 50.0000  0.3000 -4.0000 -2.0000  0.0000  0.0000
0 3 3 0  0.5511 25.4150  1.1330 -5.1903 -1.0000  0.0000  0.0000
0 1 4 0  0.2176 40.4126  0.3535 -3.9875 -2.0051  0.0000  0.0000
0 2 4 0 -1.5000  0.1032  0.0100 -5.0965  0.0000  0.0000  0.0000
0 3 4 0  1.1397 61.3225  0.5139 -3.8507 -2.7831  0.0000  0.0000
0 4 4 0  0.7265 44.3155  1.0000 -4.4046 -2.0000  0.0000  0.0000
4 1 4 4 -0.0949  8.7582  0.3310 -7.9430 -2.0000  0.0000  0.0000
0 1 5 0  4.0885 78.7058  0.1174 -2.1639  0.0000  0.0000  0.0000
0 5 5 0 -0.0170 -56.0786  0.6132 -2.2092  0.0000  0.0000  0.0000
0 2 5 0  0.0000  0.0000  0.0000  0.0000  0.0000  0.0000  0.0000
0 6 6 0  0.0000  0.0000  0.1200 -2.4426  0.0000  0.0000  0.0000
0 2 6 0  0.0000  0.0000  0.1200 -2.4847  0.0000  0.0000  0.0000
0 3 6 0  0.0000  0.0000  0.1200 -2.4703  0.0000  0.0000  0.0000
1 1 3 3 -0.0002 20.1851  0.1601 -9.0000 -2.0000  0.0000  0.0000
1 3 3 1  0.0002 80.0000 -1.5000 -4.4848 -2.0000  0.0000  0.0000
3 1 3 3 -0.1583 20.0000  1.5000 -9.0000 -2.0000  0.0000  0.0000
1 1 1 7  0.0000 19.3871  0.0103 -25.5765 -1.7255  0.0000  0.0000
7 1 1 7  0.0000 80.5586  0.1104 -8.0928 -1.7255  0.0000  0.0000
0 1 7 0  4.0000 45.8264  0.9000 -4.0000  0.0000  0.0000  0.0000
0 7 7 0  4.0000 45.8264  0.9000 -4.0000  0.0000  0.0000  0.0000
2 1 3 7 -1.5000 13.7486  0.1710 -3.7686  0.0000  0.0000  0.0000
2 3 7 3 -0.3120 -1.7990  0.2371 -3.2710  0.0000  0.0000  0.0000
1 3 7 3 -1.5000 -2.5000  0.6794 -2.5000  0.0000  0.0000  0.0000
7 3 7 3 -1.5000  7.4600 -0.9075 -9.0000  0.0000  0.0000  0.0000
2 3 9 3 -1.5000  6.8333 -0.1978 -1.4683  0.0000  0.0000  0.0000
2 3 9 4 -0.6181  7.1542 -0.0047 -1.6577  0.0000  0.0000  0.0000
2 4 9 3 -1.5000  1.7820 -1.0000 -5.4916  0.0000  0.0000  0.0000
```

2 4 9 4 -0.1959 2.3626 -1.0000 -3.0702 0.0000 0.0000 0.0000

2 1 4 9 0.0000 10.0000 0.3000 -6.0000 -1.0000 0.0000 0.0000

2 1 4 2 0.0000 10.0000 0.3000 -6.0000 -1.0000 0.0000 0.0000

9 1 1 1 0.0000 4.9490 0.3998 -5.7048 0.0000 0.0000 0.0000

9 1 1 2 0.0000 14.8410 0.4204 -3.8397 0.0000 0.0000 0.0000

9 1 1 3 0.0000 15.1500 0.3606 -3.9592 0.0000 0.0000 0.0000

9 1 3 1 0.0000 5.1000 0.3998 -5.7624 0.0000 0.0000 0.0000

9 1 1 9 0.0000 45.1884 0.4162 -3.9984 0.0000 0.0000 0.0000

1 9 3 1 0.0000 5.1676 0.0100 -5.9539 0.0000 0.0000 0.0000

2 1 9 1 0.0000 5.2500 0.0100 -6.0000 0.0000 0.0000 0.0000

1 1 9 1 0.0000 5.1676 0.0100 -5.9539 0.0000 0.0000 0.0000

1 1 9 2 0.0000 5.1676 0.0100 -5.9539 0.0000 0.0000 0.0000

9   ! Nr of hydrogen bonds;at1;at2;at3;Rhb;Dehb;vhb1

3 2 3 2.1200 -3.5800 1.4500 19.5000

3 2 4 1.7207 -4.0250 1.4500 19.5000

4 2 3 1.5182 -3.8664 1.4500 19.5000

4 2 4 1.9326 -5.8272 1.4500 19.5000

3 2 5 1.5000 -2.0000 1.4500 19.5000

4 2 5 1.5000 -2.0000 1.4500 19.5000

5 2 3 1.5000 -2.0000 1.4500 19.5000

5 2 4 1.5000 -2.0000 1.4500 19.5000

5 2 5 1.5000 -2.0000 1.4500 19.5000

Bibliography

[1] Moore, G. E. (1965). Cramming more components onto integrated circuits. *Electronics*, 38(8), 114-117.

[2] International Technology Roadmap for Semiconductors (Interconnects), 2013, available: http://www.itrs.net

[3] Bohr, M. (2014). 14 nm process technology: Opening new horizons. *Intel Developer Forum,* San Diego (USA).

[4] Yeap, G. (2013). Smart mobile SoCs driving the semiconductor industry: Technology trend, challenges and opportunities. *IEEE International Electron Devices Meeting (IEDM),* 16-23.

[5] Fischer, K., Agostinelli, M., Allen, C., Bahr, D., Bost, M., Charvat, P., Chikarmane, V., Fu, Q., Ganpule, C., Haran, M. and Heckscher, M. (2015). Low-k interconnect stack with multi-layer air gap and tri-metal-insulator-metal capacitors for 14nm high volume manufacturing. *Interconnect Technology Conference and 2015 IEEE Materials for Advanced Metallization Conference (IITC/MAM)*, 5-8.

[6] Thompson, S., Anand, N., Armstrong, M., Auth, C., Arcot, B., Alavi, M., Bai, P., Bielefeld, J., Bigwood, R., Brandenburg, J. and Buehler, M. (2002). A 90 nm logic technology featuring 50 nm strained silicon channel transistors, 7 layers of Cu interconnects, low k ILD, and 1 μm2 SRAM cell. *IEEE International Electron Devices Meeting (IEDM)*, 61-64.

[7] Narasimha, S., Onishi, K., Nayfeh, H.M., Waite, A., Weybright, M., Johnson, J., Fonseca, C., Corliss, D., Robinson, C., Crouse, M. and Yang, D. (2006). High performance 45-nm SOI technology with enhanced strain, porous low-k BEOL, and immersion lithography. *IEEE International Electron Devices Meeting (IEDM)*, 1-4.

[8] Lloyd, J. R. and Clement, J. J. (1995). Electromigration in copper conductors. *Thin Solid Films*, 262(1), 135-141.

[9] Andricacos, P. C., Uzoh, C., Dukovic, J. O., Horkans, J. and Deligianni, H. (1998). Damascene copper electroplating for chip interconnections. *IBM Journal of Research and Development*, *42*(5), 567-574.

[10] Sakamoto, Y., Kamada, K., Hamaguchi, J., Sano, A., Numata, Y., Kodaira, S., Toyoda, S. and Suu, K. (2011). Improved step coverage of Cu seed layers by magnetic-field-assisted ionized sputtering. *Japanese Journal of Applied Physics*, 50(5S1), 05EA03.

[11] George, S. M. (2009). Atomic layer deposition: an overview. *Chemical Reviews*, 110(1), 111-131.

[12] Puurunen, R. L. (2005). Surface chemistry of atomic layer deposition: A case study for the trimethylaluminum/water process. *Journal of Applied Physics*, 97(12), 121301.

[13] Knisley, T. J., Ariyasena, T. C., Sajavaara, T., Saly, M. J. and Winter, C. H. (2011). Low Temperature growth of high purity, low resistivity copper films by atomic layer deposition. *Chemistry of Materials*, 23(20), 4417-4419.

[14] Park, K. H. and Marshall, W. J. Remarkably volatile copper (II) complexes of N, N'-unsymmetrically substituted 1, 3-diketimines as precursors for Cu metal deposition via CVD or ALD. *Journal of the American Chemical Society*, 2005, *127*(26), 9330-9331.

[15] Lee, B.H., Hwang, J.K., Nam, J.W., Lee, S.U., Kim, J.T., Koo, S.M., Baunemann, A., Fischer, R.A. and Sung, M.M. (2009). Low-temperature atomic layer deposition of copper metal thin films: Self-limiting surface reaction of copper dimethylamino-2-propoxide with diethylzinc. *Angewandte Chemie International Edition*, 48(25), 4536-4539.

[16] Maårtensson, P. and Carlsson, J. O. (1998). Atomic layer epitaxy of copper growth and selectivity in the Cu (II)-2, 2, 6, 6-tetramethyl-3, 5-heptanedionate/process. *Journal of The Electrochemical Society*, 145(8), 2926-2931.

[17] Utriainen, M., Kröger-Laukkanen, M., Johansson, L. S. and Niinistö, L. (2000). Studies of metallic thin film growth in an atomic layer epitaxy reactor using $M(acac)_2$ (M= Ni, Cu, Pt) precursors. *Applied Surface Science*, 157(3), 151-158.

[18] Alnes, M. E., Monakhov, E., Fjellvåg, H. and Nilsen, O. (2012). Atomic layer deposition of copper oxide using copper (II) acetylacetonate and ozone. *Chemical Vapor Deposition*, 18(4-6), 173-178.

[19] Waechtler, T., Oswald, S., Roth, N., Jakob, A., Lang, H., Ecke, R., Schulz, S.E., Gessner, T., Moskvinova, A., Schulze, S. and Hietschold, M. (2009). Copper oxide films grown by atomic layer deposition from Bis (tri-n-butylphosphane) copper (I) acetylacetonate on Ta, TaN, Ru, and SiO_2. *Journal of The Electrochemical Society*, 156(6), H453-H459.

[20] Waechtler, T., Ding, S.F., Hofmann, L., Mothes, R., Xie, Q., Oswald, S., Detavernier, C., Schulz, S.E., Qu, X.P., Lang, H. and Gessner, T. (2011). ALD-grown seed layers for electrochemical copper deposition integrated with different diffusion barrier systems. *Microelectronic Engineering*, 88(5), 684-689.

[21] Lim, B. S., Rahtu, A. and Gordon, R. G. (2003). Atomic layer deposition of transition metals. *Nature Materials*, 2(11), 749-754.

[22] Li, Z., Barry, S. T. and Gordon, R. G. (2005). Synthesis and characterization of copper (I) amidinates as precursors for atomic layer deposition (ALD) of copper metal. *Inorganic Chemistry*, 44(6), 1728-1735.

[23] Park, J.W., Jang, H.S., Kim, M., Sung, K., Lee, S.S., Chung, T.M., Koo, S., Kim, C.G. and Kim, Y. (2004). Synthesis of Cu(II) aminoalkoxide complexes and their unusual thermolysis to Cu(0). *Inorganic Chemistry Communications*, 7(4), 463-466.

[24] Coyle, J.P., Monillas, W.H., Yap, G.P. and Barry, S.T. (2008). Synthesis and thermal chemistry of copper (I) guanidinates. *Inorganic Chemistry*, 47(2), 683-689.

[25] Willcocks, A.M., Robinson, T.P., Roche, C., Pugh, T., Richards, S.P. (2011). Multinuclear copper (I) guanidinate complexes. *Inorganic Chemistry*, 51(1), 246-257.

[26] Coyle, J.P., Kurek, A., Pallister, P.J., Sirianni, E.R., Yap, G.P. and Barry, S.T. (2012). Preventing thermolysis: precursor design for volatile copper compounds. *Chemical Communications*, 48(84), 10440-10442.

[27] Niskanen, A., Rahtu, A., Sajavaara, T., Arstila, K., Ritala, M., and Leskelä, M. (2005). Radical-enhanced atomic layer deposition of metallic copper thin films. *Journal of The Electrochemical Society*, *152*(1), G25-G28.

[28] Wu, L. and Eisenbraun, E. (2007). Hydrogen plasma-enhanced atomic layer deposition of copper thin films. *Journal of Vacuum Science and Technology B*, 25(6), 2581-2585.

[29] Dhakal, D., Waechtler, T., Schulz, S.E., Gessner, T., Lang, H., Mothes, R. and Tuchscherer, A. (2014). Surface chemistry of a Cu (I) beta-diketonate precursor and the atomic layer deposition of Cu_2O on SiO_2 studied by x-ray photoelectron spectroscopy. *Journal of Vacuum Science and Technology A*, 32(4), 041505.

[30] Dhakal, D., Waechtler, T., Schulz, S.E., Moeckel, S., Lang, H. and Gessner, T. (2014). *In-situ* growth monitoring of ultrathin films of ALD Cu_2O and Cu after successive reduction. *2nd International Conference on ALD Applications and 3rd China ALD Conference*, Shanghai (China).

[31] Zaera, F. The surface chemistry of atomic layer depositions of solid thin films. *The Journal of Physical Chemistry Letters*, 2012, 3(10), 1301-1309.

[32] Ma, Q. and Zaera, F. (2013). Chemistry of Cu (acac)$_2$ on Ni (110) and Cu (110) surfaces: Implications for atomic layer deposition processes. *Journal of Vacuum Science and Technology A*, 31(1), 01A112.

[33] Elliott, S.D., Dey, G., Maimaiti, Y., Ablat, H., Filatova, E.A. and Fomengia, G.N. (2016). Modeling mechanism and growth reactions for new nanofabrication processes by atomic layer deposition. *Advanced Materials*, 28(27), 5367–5380.

[34] Elliott, S. D. (2012). Atomic-scale simulation of ALD chemistry. *Semiconductor Science and Technology*, 27(7), 074008.

[35] Malygin, A. A., Drozd, V. E., Malkov, A. A., and Smirnov, V. M. (2015). From V. B. Aleskovskii's "Framework" Hypothesis to the Method of Molecular Layering/Atomic Layer Deposition. *Chemical Vapor Deposition*, *21*(10-11-12), 216-240.

[36] Puurunen, R. L. (2014). A short history of atomic layer deposition: Tuomo suntola's atomic layer epitaxy. *Chemical Vapor Deposition*, 20(10-11-12), 332-344.

[37] Suntola, T. and Antson, J. (1977). Method for producing compound thin films. U.S. Patent 4,058,430.

[38] Leskelä, M. and Ritala, M. (2003). Atomic layer deposition chemistry: recent developments and future challenges. *Angewandte Chemie International Edition*, 42(45), 5548-5554.

[39] Ferguson, J. D., Weimer, A. W. and George, S. M. (2004). Atomic layer deposition of Al_2O_3 films on polyethylene particles. *Chemistry of Materials*, 16(26), 5602-5609.

[40] Widjaja, Y. and Musgrave, C. B. (2002). Quantum chemical study of the mechanism of aluminum oxide atomic layer deposition. *Applied Physics Letters*, 80(18), 3304-3306.

[41] Puurunen, R. L. (2003). Growth per cycle in atomic layer deposition: a theoretical model. *Chemical Vapor Deposition*, 9(5), 249-257.

[42] Profijt, H. B., Potts, S. E., Van de Sanden, M. C. M. and Kessels, W. M. M. (2011). Plasma-assisted atomic layer deposition: Basics, opportunities, and challenges. *Journal of Vacuum Science and Technology A*, 29(5), 050801.

[43] Heil, S. B. S., Van Hemmen, J. L., Hodson, C. J., Singh, N., Klootwijk, J. H., Roozeboom, F, van de Sanden, M. C. M. and Kessels, W. M. M. (2007). Deposition of TiN and HfO_2 in a commercial 200mm remote plasma atomic layer deposition reactor. *Journal of Vacuum Science and Technology A*, 25(5), 1357-1366.

[44] Heil, S. B. S., Kudlacek, P., Langereis, E., Engeln, R., Van De Sanden, M. C. M. and Kessels, W. M. M. (2006). In situ reaction mechanism studies of plasma-assisted atomic layer deposition of Al_2O_3. *Applied Physics Letters*, 89(13), 131505.

[45] Marichy, C., Bechelany, M. and Pinna, N. (2012). Atomic layer deposition of nanostructured materials for energy and environmental applications. *Advanced Materials*, 24(8), 1017-1032.

[46] Paracchino, A., Laporte, V., Sivula, K., Grätzel, M. and Thimsen, E. (2011). Highly active oxide photocathode for photoelectrochemical water reduction. *Nature Materials*, 10(6), 456-461.

[47] Shim, J. H., Chao, C. C., Huang, H. and Prinz, F. B. (2007). Atomic layer deposition of yttria-stabilized zirconia for solid oxide fuel cells. *Chemistry of Materials*, 19(15), 3850-3854.

[48] Wilson, C. A., Grubbs, R. K. and George, S. M. (2005). Nucleation and growth during Al_2O_3 atomic layer deposition on polymers. *Chemistry of Materials*, 17(23), 5625-5634.

[49] Lu, J., Fu, B., Kung, M. C., Xiao, G., Elam, J. W., Kung, H. H. and Stair, P. C. (2012). Coking- and sintering-resistant palladium catalysts achieved through atomic layer deposition. *Science*, 335(6073), 1205-1208.

[50] Kim, H., Lee, H. and Maeng, W. J. (2009). Applications of atomic layer deposition to nanofabrication and emerging nanodevices. *Thin Solid Films*, 517(8), 2563-2580.

[51] Niinistö, J., Kukli, K., Heikkilä, M., Ritala, M. and Leskelä, M. (2009). Atomic layer deposition of high-k oxides of the group 4 metals for memory applications. *Advanced Engineering Materials*, 11(4), 223-234.

[52] Hwang, C. S., Kim, S. K., and Lee, S. W. (2014). Mass-Production Memories (DRAM and Flash). In *Atomic Layer Deposition for Semiconductors* (Eds: Hwang, C. S.), 73-122, Springer US.

[53] Kim, S.K., Choi, G.J., Lee, S.Y., Seo, M., Lee, S.W., Han, J.H., Ahn, H.S., Han, S. and Hwang, C.S. (2008). Al-doped TiO_2 films with ultralow leakage currents for next generation DRAM capacitors. *Advanced Materials*, 20(8), 1429-1435.

[54] Mistry, K., Allen, C., Auth, C., Beattie, B., Bergstrom, D., Bost, M., Brazier, M., Buehler, M., Cappellani, A., Chau, R. and Choi, C.H. (2007). A 45nm logic technology with high-k+ metal gate transistors, strained silicon, 9 Cu interconnect layers, 193nm dry patterning, and 100% Pb-free packaging. *IEEE International Electron Devices Meeting (IEDM)*, 247-250.

[55] Auth, C., Allen, C., Blattner, A., Bergstrom, D., Brazier, M., Bost, M., Buehler, M., Chikarmane, V., Ghani, T., Glassman, T. and Grover, R. (2012). A 22nm high performance and low-power CMOS technology featuring fully-depleted tri-gate transistors, self-ligned contacts and high density MIM capacitors. *VLSI Technology (VLSIT),* 131-132.

[56] Bohr, M. (2011). The evolution of scaling from the homogeneous era to the heterogeneous era. *IEEE International Electron Devices Meeting (IEDM)*, 1-1.

[57] Kittl, J. A., Opsomer, K., Popovici, M., Menou, N., Kaczer, B., Wang, X. P., ... and Govoreanu, B. (2009). High-k dielectrics for future generation memory devices. *Microelectronic Engineering*, *86*(7), 1789-1795.

[58] Park, H. B., Cho, M., Park, J., Lee, S. W., Hwang, C. S., Kim, J. P., ... and Oh, S. J. (2003). Comparison of HfO_2 films grown by atomic layer deposition using $HfCl_4$ and H_2O or O_3 as the oxidant. *Journal of Applied Physics*, *94*(5), 3641-3647.

[59] Kukli, K., Ritala, M., Sajavaara, T., Keinonen, J., and Leskelä, M. (2002). Atomic layer deposition of hafnium dioxide films from hafnium tetrakis (ethylmethylamide) and water. *Chemical Vapor Deposition*, *8*(5), 199-204.

[60] Cho, M., Park, H. B., Park, J., Lee, S. W., Hwang, C. S., Jang, G. H. and Jeong, J. (2003). High-k properties of atomic-layer-deposited HfO_2 films using a nitrogen-containing $Hf[N(CH_3)_2]_4$ precursor and H_2O oxidant. *Applied Physics Letters*, 83(26), 5503-5505.

[61] Han, J. H., Cho, M., Delabie, A., Park, T. J., and Hwang, C. S. (2014). Front End of the Line Process. In *Atomic Layer Deposition for Semiconductors* (Eds: Hwang, C. S.), 175-208, Springer US.

[62] Kim, H., Kim, S. H and Lee, L. (2014). Back End of the Line. In *Atomic Layer Deposition for Semiconductors* (Eds: Hwang, C. S.), 209-238, Springer US.

[63] Knisley, T. J., Kalutarage, L. C. and Winter, C. H. (2013). Precursors and chemistry for the atomic layer deposition of metallic first row transition metal films. *Coordination Chemistry Reviews*, 257(23), 3222-3231.

[64] Kim, H. (2003). Atomic layer deposition of metal and nitride thin films: Current research efforts and applications for semiconductor device processing. *Journal of Vacuum Science and Technology B*, 21(6), 2231-2261.

[65] Kaloyeros, A. E. and Eisenbraun, E. (2000). Ultrathin diffusion barriers/liners for gigascale copper metallization. *Annual Review of Materials Science*, 30(1), 363-385.

[66] Gambino, J. P. (2011). Copper interconnect technology for the 22 nm node. *VLSI Technology, Systems and Applications (VLSI-TSA),* 1-2.

[67] Haynes, W. M. (Ed.). (2014). *CRC handbook of chemistry and physics*. CRC press.

[68] Martensson, P. and Carlsson, J. O. (1997). Atomic layer epitaxy of copper on tantalum. *Chemical Vapor Deposition*, 3(1), 45-50.

[69] Solanki, R. and Pathangey, B. (2000). Atomic layer deposition of copper seed layers. *Electrochemical and Solid-State Letters*, 3(10), 479-480.

[70] Li, Z., Rahtu, A. and Gordon, R. G. (2006). Atomic layer deposition of ultrathin copper metal films from a liquid copper (I) amidinate precursor. *Journal of The Electrochemical Society*, *153*(11), C787-C794.

[71] Vidjayacoumar, B., Emslie, D. J., Clendenning, S. B., Blackwell, J. M., Britten, J. F. and Rheingold, A. Investigation of AlMe$_3$, BEt$_3$, and ZnEt$_2$ as co-reagents for low-temperature copper metal ALD/pulsed-CVD. *Chemistry of Materials*, 2010, *22*(17), 4844-4853.

[72] Kang, S. W., Yun, J. Y. and Chang, Y. H. Growth of Cu Metal Films at Room Temperature Using Catalyzed Reactions. *Chemistry of Materials*, 2010, *22*(5), 1607-1609.

[73] Hagen, D.J., Povey, I.M., Rushworth, S., Wrench, J.S., Keeney, L., Schmidt, M., Petkov, N., Barry, S.T., Coyle, J.P. and Pemble, M.E. Atomic layer deposition of Cu with a carbene-stabilized Cu (I) silylamide. *Journal of Materials Chemistry C*, 2014, *2*(43), 9205-9214.

[74] Georgi, G., Melzer, M., Dhakal, D., Assim, K., Lang, H., Ecke, R., Schulz, S. E. and Gessner, T. (2016). Thermal ALD of metallic copper on cobalt for advanced interconnects. 14th International Conference on Atomic Layer Deposition, Dublin (Ireland).

[75] Li, Z. and Gordon, R. G. (2006). Thin, continuous, and conformal copper films by reduction of atomic layer deposited copper nitride. *Chemical Vapor Deposition*, *12*(7), 435-441.

[76] Park, J. M., Jin, K., Han, B., Kim, M. J., Jung, J., Kim, J. J. and Lee, W. J. (2014). Atomic layer deposition of copper nitride film and its application to copper seed layer for electrodeposition. *Thin Solid Films*, *556*, 434-439.

[77] Kalutarage, L. C., Clendenning, S. B. and Winter, C. H. (2014). Low-temperature atomic layer deposition of copper films using borane dimethylamine as the reducing co-reagent. *Chemistry of Materials*, *26*(12), 3731-3738.

[78] Jezewski, C., Lanford, W. A., Wiegand, C. J., Singh, J. P., Wang, P. I., Senkevich, J. J. and Lu, T. M. (2005). Inductively coupled hydrogen plasma-assisted Cu ALD on metallic and dielectric surfaces. *Journal of The Electrochemical Society*, *152*(2), C60-C64.

[79] Moon, D. Y., Han, D. S., Shin, S. Y., Park, J. W., Kim, B. M. and Kim, J. H. (2011). Effects of the substrate temperature on the Cu seed layer formed using atomic layer deposition. *Thin Solid Films*, *519*(11), 3636-3640.

[80] Coyle, J.P., Dey, G., Sirianni, E.R., Kemell, M.L., Yap, G.P., Ritala, M., Leskelä, M., Elliott, S.D. and Barry, S.T. (2013). Deposition of copper by plasma-enhanced atomic layer deposition using a novel N-heterocyclic carbene precursor. *Chemistry of Materials*, *25*(7), 1132-1138.

[81] Guo, Z., Li, H., Chen, Q., Sang, L., Yang, L., Liu, Z. and Wang, X. (2015). Low-temperature atomic layer deposition of high purity, smooth, low resistivity copper films by using amidinate precursor and hydrogen plasma. *Chemistry of Materials*, *27*(17), 5988-5996.

[82] Shen, Y. Z., Leschke, M., Schulz, S. E., Ecke, R., Gessner, T. and Lang, H. (2004). Synthesis of tri-n-butylphosphine copper (I) beta-diketonates and their use in chemical vapour deposition of copper. *Chinese Journal of Inorganic Chemistry*, *20*(11), 1257-1264.

[83] Rahtu, A., Alaranta, T., and Ritala, M. (2001). *In situ* quartz crystal microbalance and quadrupole mass spectrometry studies of atomic layer deposition of aluminum oxide from trimethylaluminum and water. *Langmuir*,*17*(21), 6506-6509.

[84] Langereis, E., Heil, S. B. S., Knoops, H. C. M., Keuning, W., Van De Sanden, M. C. M., and Kessels, W. M. M. (2009). In situ spectroscopic ellipsometry as a versatile tool for studying atomic layer deposition. *Journal of Physics D: Applied Physics*, *42*(7), 073001.

[85] Mårtensson, P., Larsson, K., and Carlsson, J. O. (1998). Atomic layer epitaxy of copper: an ab initio investigation of the CuCl/H_2 process: I. Adsorption of CuCl on Cu (111). *Applied Surface Science*, *136*(1), 137-146.

[86] Mårtensson, P., Larsson, K., and Carlsson, J. O. (1999). Atomic layer epitaxy of copper: an ab initio investigation of the CuCl/H_2 process: II. Reaction energies. *Applied surface science*, *148*(1), 9-16.

[87] Mårtensson, P., Larsson, K., and Carlsson, J. O. (2000). Atomic layer epitaxy of copper: an ab initio investigation of the CuCl/H_2 process: III. Reaction barriers. *Applied Surface Science*, *157*(1), 92-100.

[88] Machado, E., Kaczmarski, M., Ordejón, P., Garg, D., Norman, J., and Cheng, H. (2005). First-principles analyses and predictions on the reactivity of barrier layers of Ta and TaN towards organometallic precursors for deposition of copper films. *Langmuir*, *21*(16), 7608-7614.

[89] Orimoto, Y., Toyota, A., Furuya, T., Nakamura, H., Uehara, M., Yamashita, K., and Maeda, H. (2009). Computational method for efficient screening of metal precursors for nanomaterial syntheses. *Industrial and Engineering Chemistry Research*, *48*(7), 3389-3397.

[90] Coyle, J. P., Johnson, P. A., DiLabio, G. A., Barry, S. T., and Müller, J. (2010). Gas-phase thermolysis of a guanidinate precursor of copper studied by matrix isolation, time-of-flight mass spectrometry, and computational chemistry. *Inorganic Chemistry*, *49*(6), 2844-2850.

[91] Dai, M., Kwon, J., Halls, M. D., Gordon, R. G., and Chabal, Y. J. (2010). Surface and interface processes during atomic layer deposition of copper on silicon oxide. *Langmuir*, *26*(6), 3911-3917.

[92] Lin, J. M., Teplyakov, A. V., and Rodríguez-Reyes, J. C. F. (2013). Competing reactions during metalorganic deposition: Ligand-exchange versus direct reaction with the substrate surface. *Journal of Vacuum Science and Technology A*, *31*(2), 021401.

[93] Dey, G., and Elliott, S. D. (2012). Mechanism for the atomic layer deposition of copper using diethylzinc as the reducing agent: a density functional theory study using gas-phase molecules as a model. *The Journal of Physical Chemistry A*, *116*(35), 8893-8901.

[94] Dey, G., and Elliott, S. D. (2014). Copper reduction and atomic layer deposition by oxidative decomposition of formate by hydrazine. *RSC Advances*, *4*(65), 34448-34453.

[95] Dey, G., and Elliott, S. D. (2015). Quantum chemical study of the effect of precursor stereochemistry on dissociative chemisorption and surface redox reactions during the atomic layer deposition of the transition metal copper. *The Journal of Physical Chemistry C*, *119*(11), 5914-5927.

[96] Maimaiti, Y., and Elliott, S. D. (2015). Precursor adsorption on copper surfaces as the first step during the deposition of copper: a density functional study with van der Waals correction. *The Journal of Physical Chemistry C*, *119*(17), 9375-9385.

[97] Holmqvist, A., Törndahl, T., and Stenström, S. (2012). A model-based methodology for the analysis and design of atomic layer deposition processes—Part I: Mechanistic modelling of continuous flow reactors. *Chemical Engineering Science*, *81*, 260-272.

[98] Reese, J. S., Raimondeau, S., and Vlachos, D. G. (2001). Monte Carlo algorithms for complex surface reaction mechanisms: efficiency and accuracy. *Journal of Computational Physics*, *173*(1), 302-321.

[99] Dkhissi, A., Estève, A., Mastail, C., Olivier, S., Mazaleyrat, G., Jeloaica, L., and Djafari Rouhani, M. (2008). Multiscale modeling of the atomic layer deposition of HfO2 thin film grown on silicon: How to deal with a kinetic Monte Carlo procedure. *Journal of Chemical Theory and Computation*, *4*(11), 1915-1927.

[100] Dkhissi, A., Mazaleyrat, G., Estève, A., and Rouhani, M. D. (2009). Nucleation and growth of atomic layer deposition of HfO_2 gate dielectric layers on silicon oxide: a multiscale modelling investigation. *Physical Chemistry Chemical Physics*, *11*(19), 3701-3709.

[101] Shirazi, M., and Elliott, S. D. (2014). Atomistic kinetic Monte Carlo study of atomic layer deposition derived from density functional theory. *Journal of Computational Chemistry*, *35*(3), 244-259.

[102] Graves, D. B., and Brault, P. (2009). Molecular dynamics for low temperature plasma–surface interaction studies. *Journal of Physics D: Applied Physics*, *42*(19), 194011.

[103] Hu, Z., Shi, J., and Turner, H. (2009). Molecular dynamics simulation of the Al2O3 film structure during atomic layer deposition. *Molecular Simulation*, *35*(4), 270-279.

[104] Liang, T., Shin, Y. K., Cheng, Y. T., Yilmaz, D. E., Vishnu, K. G., Verners, O., ... and van Duin, A. C. (2013). Reactive potentials for advanced atomistic simulations. *Annual Review of Materials Research*, *43*, 109-129.

[105] Xue, J., Yin, X., Ye, F., Zhang, L., and Cheng, L. (2013). Thermodynamic analysis on the codeposition of SiC–Si3N4 composite ceramics by chemical vapor deposition using $SiCl_4$–NH_3–CH_4–H_2–Ar mixture gases. *Journal of the American Ceramic Society*, *96*(3), 979-986.

[106] Hohenberg, P., and Kohn, W. (1964). Inhomogeneous electron gas. *Physical Review*, 136(3B), B864.

[107] Kohn, W., and Sham, L. J. (1965). Self-consistent equations including exchange and correlation effects. *Physical Review*, 140(4A), A1133.

[108] Perdew, J. P., and Wang, Y. (1992). Accurate and simple analytic representation of the electron-gas correlation energy. *Physical Review B*, *45*(23), 13244.

[109] Perdew, J. P., Burke, K., and Ernzerhof, M. (1996). Generalized gradient approximation made simple. *Physical Review Letters*, *77*(18), 3865.

[110] Dion, M., Rydberg, H., Schröder, E., Langreth, D. C., and Lundqvist, B. I. (2004). Van der Waals density functional for general geometries. *Physical Review Letters*, *92*(24), 246401.

[111] Stuart, S. J., Tutein, A. B., and Harrison, J. A. (2000). A reactive potential for hydrocarbons with intermolecular interactions. *The Journal of Chemical Physics*, *112*(14), 6472-6486.

[112] van Duin, A. C., Dasgupta, S., Lorant, F., and Goddard, W. A. (2001). ReaxFF: a reactive force field for hydrocarbons. *The Journal of Physical Chemistry A*,*105*(41), 9396-9409.

[113] Liang, T., Shan, T. R., Cheng, Y. T., Devine, B. D., Noordhoek, M., Li, Y., ... and Sinnott, S. B. (2013). Classical atomistic simulations of surfaces and heterogeneous interfaces with the charge-optimized many body (COMB) potentials. *Materials Science and Engineering: R: Reports*, *74*(9), 255-279.

[114] Grimme, S. (2014). A general quantum mechanically derived force field (QMDFF) for molecules and condensed phase simulations. *Journal of Chemical Theory and Computation*, *10*(10), 4497-4514.

[115] Janssens, G. O., Baekelandt, B. G., Toufar, H., Mortier, W. J., and Schoonheydt, R. A. (1995). Comparison of cluster and infinite crystal calculations on zeolites with the electronegativity equalization method (EEM).*The Journal of Physical Chemistry*, *99*(10), 3251-3258.

[116] van Duin, A. C., Baas, J. M., and van de Graaf, B. (1994). Delft molecular mechanics: a new approach to hydrocarbon force fields. Inclusion of a geometry-dependent charge calculation. *Journal of the Chemical Society, Faraday Transactions*, *90*(19), 2881-2895.

[117] Senftle, T. P., Hong, S., Islam, M. M., Kylasa, S. B., Zheng, Y., Shin, Y. K., ... and van Duin, A. C. (2016). The ReaxFF reactive force-field: development, applications and future directions. *NPJ Computational Materials*, *2*, 15011.

[118] Deetz, J. D., and Faller, R. (2014). Parallel optimization of a reactive force field for polycondensation of alkoxysilanes. *The Journal of Physical Chemistry B*, *118*(37), 10966-10978.

[119] Larsson, H. R., Duin, A. C., and Hartke, B. (2013). Global optimization of parameters in the reactive force field ReaxFF for SiOH. *Journal of Computational Chemistry*, *34*(25), 2178-2189.

[120] Jaramillo-Botero, A., Naserifar, S., and Goddard III, W. A. (2014). General multiobjective force field optimization framework, with application to reactive force fields for silicon carbide. *Journal of Chemical Theory and Computation*, *10*(4), 1426-1439.

[121] Roy, R. K. (2010). *A primer on the Taguchi method*. Society of Manufacturing Engineers.

[122] Lukas, H. L., Fries, S. G., and Sundman, B. (2007). *Computational thermodynamics: the Calphad method*. Cambridge: Cambridge University Press.

[123] Reuter, K., and Scheffler, M. (2001). Composition, structure, and stability of RuO_2 (110) as a function of oxygen pressure. *Physical Review B*, *65*(3), 035406.

[124] Liu, Z. K., Chen, L. Q., Raghavan, P., Du, Q., Sofo, J. O., Langer, S. A., and Wolverton, C. (2004). An integrated framework for multi-scale materials simulation and design. *Journal of Computer-aided Materials Design*, *11*(2-3), 183-199.

[125] Nørskov, J. K., Rossmeisl, J., Logadottir, A., Lindqvist, L. R. K. J., Kitchin, J. R., Bligaard, T., and Jonsson, H. (2004). Origin of the overpotential for oxygen reduction at a fuel-cell cathode. *The Journal of Physical Chemistry B*, *108*(46), 17886-17892.

[126] Terranova, U., and Bowler, D. R. (2011). Effect of hydration of the TiO_2 anatase (101) substrate on the atomic layer deposition of alumina films. *Journal of Materials Chemistry*, *21*(12), 4197-4203.

[127] Zhang, W., Wu, P., Li, Z., and Yang, J. (2011). First-principles thermodynamics of graphene growth on Cu surfaces. *The Journal of Physical Chemistry C*, *115*(36), 17782-17787.

[128] McQuarrie, D. A., and Simon, J. D. (1999). *Molecular thermodynamics*. University Science Books: Sausalito.

[129] NIST Standard Reference Database Number 69, June 2005 Release, http://kinetics.nist.gov/janaf/

[130] S. Gordon, B.J. McBride, Computer Program for Calculation of Complex Chemical Equilibrium Compositions and Applications, Report No. NASA RP-1311, NASA Lewis Research Center, Cleveland, OH 44135–3191, USA, October 1994.

[131] Zheng, L., and Furimsky, E. (2003). Assessment of coal combustion in $O_2 + CO_2$ by equilibrium calculations. *Fuel Processing Technology*, *81*(1), 23-34.

[132] Liu, S., Zhang, K., Fang, L., and Li, Y. (2008). Thermodynamic analysis of hydrogen production from oxidative steam reforming of ethanol. *Energy and Fuels*, *22*(2), 1365-1370.

[133] Shabbar, S., and Janajreh, I. (2013). Thermodynamic equilibrium analysis of coal gasification using Gibbs energy minimization method. *Energy Conversion and Management*, 65, 755-763.

[134] Miller, B. B., Kandiyoti, R., and Dugwell, D. R. (2004). Trace element behavior during co-combustion of sewage sludge with polish coal. *Energy and Fuels*, 18(4), 1093-1103.

[135] Pechukas, P. (1981). Transition state theory. *Annual Review of Physical Chemistry*, *32*(1), 159-177.

[136] Henkelman, G., Jóhannesson, G., and Jónsson, H. (2002). Methods for finding saddle points and minimum energy paths. In *Theoretical Methods in Condensed Phase Chemistry* (pp. 269-302). Springer Netherlands.

[137] Henkelman, G., Uberuaga, B. P., and Jónsson, H. (2000). A climbing image nudged elastic band method for finding saddle points and minimum energy paths. *The Journal of Chemical Physics*, *113*(22), 9901-9904.

[138] Henkelman, G., and Jónsson, H. (2000). Improved tangent estimate in the nudged elastic band method for finding minimum energy paths and saddle points. *The Journal of Chemical Physics*, *113*(22), 9978-9985.

[139] Monazam, E. R., Breault, R. W., and Siriwardane, R. (2014). Kinetics of Hematite to Wustite by Hydrogen for Chemical Looping Combustion. *Energy and Fuels*, *28*(8), 5406-5414.

[140] Jubsilp, C., Damrongsakkul, S., Takeichi, T., and Rimdusit, S. (2006). Curing kinetics of arylamine-based polyfunctional benzoxazine resins by dynamic differential scanning calorimetry. *Thermochimica Acta*, *447*(2), 131-140.

[141] Yu, J., Yue, J., Liu, Z., Dong, L., Xu, G., Zhu, J., ... and Sun, L. (2010). Kinetics and mechanism of solid reactions in a micro fluidized bed reactor. *AICHE Journal*, *56*(11), 2905-2912.

[142] Delley, B. (1990). An all-electron numerical method for solving the local density functional for polyatomic molecules. *The Journal of Chemical Physics*, *92*(1), 508-517.

[143] Delley, B. (2002). Hardness conserving semilocal pseudopotentials. *Physical Review B*, *66*(15), 155125.

[144] Giannozzi, P., Baroni, S., Bonini, N., Calandra, M., Car, R., Cavazzoni, C., ... and Dal Corso, A. (2009). QUANTUM ESPRESSO: a modular and open-source software project for quantum simulations of materials. *Journal of Physics: Condensed Matter*, *21*(39), 395502.

[145] Vanderbilt, D. (1990). Soft self-consistent pseudopotentials in a generalized eigenvalue formalism. *Physical Review B*, *41*(11), 7892.

[146] Segall, M. D., Shah, R., Pickard, C. J., and Payne, M. C. (1996). Population analysis of plane-wave electronic structure calculations of bulk materials. *Physical Review B*, *54*(23), 16317.

[147] Segall, M. D., Lindan, P. J., Probert, M. A., Pickard, C. J., Hasnip, P. J., Clark, S. J., and Payne, M. C. (2002). First-principles simulation: ideas, illustrations and the CASTEP code. *Journal of Physics: Condensed Matter*, *14*(11), 2717.

[148] Berendsen, H. J., Postma, J. V., van Gunsteren, W. F., DiNola, A. R. H. J., and Haak, J. R. (1984). Molecular dynamics with coupling to an external bath. *The Journal of Chemical Physics*, *81*(8), 3684-3690.

[149] Wang, M. T., Lin, Y. C., and Chen, M. C. (1998). Barrier properties of very thin Ta and TaN layers against copper diffusion. *Journal of The Electrochemical Society*, *145*(7), 2538-2545.

[150] Qu, X. P., Tan, J. J., Zhou, M., Chen, T., Xie, Q., Ru, G. P., and Li, B. Z. (2006). Improved barrier properties of ultrathin Ru film with TaN interlayer for copper metallization. *Applied Physics Letters*, *88*(15), 1912.

[151] de Almeida, K. J., Cesar, A., Rinkevicius, Z., Vahtras, O., and Ågren, H. (2010). Modelling the visible absorption spectra of copper (II) acetylacetonate by Density Functional Theory. *Chemical Physics Letters*, *492*(1), 14-18.

[152] Lebrun, P. C., Lyon, W. D., and Kuska, H. A. (1986). Crystal structure of bis (2, 4-pentanedionato) copper (II). *Journal of Crystallographic and Spectroscopic Research*, *16*(6), 889-893.

[153] Shibata, S., Sasase, T., and Ohta, M. (1983). The molecular structure of bis (acetylacetonato) copper (II) in the gas phase as determined from electron diffraction data. *Journal of Molecular Structure*, *96*(3-4), 347-352.

[154] Somani, S., Mukhopadhyay, A., and Musgrave, C. (2011). Atomic layer deposition of tantalum nitride using a novel precursor. *The Journal of Physical Chemistry C*, *115*(23), 11507-11513.

[155] Girolami, G. S., Jeffries, P. M., and Dubois, L. H. (1993). Mechanistic studies of copper thin-film growth from CuI and CuII. beta.-diketonates. *Journal of the American Chemical Society*, *115*(3), 1015-1024.

[156] Nakamoto, K., and Martell, A. E. (1960). Infrared Spectra of Metal-Chelate Compounds. I. A Normal Coordinate Treatment on Bis-(Acetylacetonato)-Cu (II). *The Journal of Chemical Physics*, *32*(2), 588-597.

[157] Ekerdt, J. G., Sun, Y. M., Szabo, A., Szulczewski, G. J., and White, J. M. (1996). Role of surface chemistry in semiconductor thin film processing. *Chemical Reviews*, *96*(4), 1499-1518.

[158] Sasaki, K., and Teraoka, Y. (2003). Equilibria in fuel cell gases I. Equilibrium compositions and reforming conditions. *Journal of The Electrochemical Society*, *150*(7), A878-A884.

[159] Knapas, K., and Ritala, M. (2011). *In situ* reaction mechanism studies on atomic layer deposition of Ir and IrO_2 from $Ir(acac)_3$. *Chemistry of Materials*, *23*(11), 2766-2771.

[160] Waechtler, T. (2009). Thin films of copper oxide and copper grown by atomic layer deposition for applications in metallization systems of microelectronic devices [Ph.D. thesis]. Chemnitz University of Technology <http://www.nbnresolving.de/urn:nbn:de:bsz:ch1-201000725>.

[161] Pinkas, J., Huffman, J. C., Baxter, D. V., Chisholm, M. H., and Caulton, K. G. (1995). Mechanistic role of H_2O and the ligand in the chemical vapor deposition of Cu, Cu_2O, CuO, and Cu_3N from Bis (1, 1, 1, 5, 5, 5-hexafluoropentane-2, 4-dionato) copper (II). *Chemistry of Materials*, *7*(8), 1589-1596.

[162] Huo, J., Solanki, R., and McAndrew, J. (2002). Characteristics of copper films produced via atomic layer deposition. *Journal of Materials Research*, *17*(09), 2394-2398.

[163] Fang, G., Chen, S., Li, A., and Ma, J. (2012). Surface Pseudorotation in Lewis-Base-Catalyzed Atomic Layer Deposition of SiO2: Static Transition State Search and Born–Oppenheimer Molecular Dynamics Simulation. *The Journal of Physical Chemistry C*, *116*(50), 26436-26448.

[164] Shirazi, M., and Elliott, S. D. (2013). Multiple proton diffusion and film densification in atomic layer deposition modeled by density functional theory. *Chemistry of Materials*, *25*(6), 878-889.

[165] Nosé, S. (1984). A unified formulation of the constant temperature molecular dynamics methods. *The Journal of Chemical Physics*, *81*(1), 511-519.

[166] Hoover, W. G. (1985). Canonical dynamics: equilibrium phase-space distributions. *Physical Review A*, *31*(3), 1695.

[167] Plimpton, S. (1995). Fast parallel algorithms for short-range molecular dynamics. *Journal of Computational Physics*, *117*(1), 1-19.

[168] van Duin, A. C., Bryantsev, V. S., Diallo, M. S., Goddard, W. A., Rahaman, O., Doren, D. J., ... and Hermansson, K. (2010). Development and validation of a ReaxFF reactive force field for Cu cation/water interactions and copper metal/metal oxide/metal hydroxide condensed phases. *The Journal of Physical Chemistry A*, *114*(35), 9507-9514.

[169] Wood, R. H., Yezdimer, E. M., Sakane, S., Barriocanal, J. A., and Doren, D. J. (1999). Free energies of solvation with quantum mechanical interaction energies from classical mechanical simulations. *The Journal of Chemical Physics*, *110*(3), 1329-1337.

[170] Becke, A. D. (1993). Density-functional thermochemistry. III. The role of exact exchange. *The Journal of Chemical Physics*, *98*(7), 5648-5652.

[171] Rahaman, O., van Duin, A. C., Goddard III, W. A., and Doren, D. J. (2010). Development of a ReaxFF reactive force field for glycine and application to solvent effect and tautomerization. *The Journal of Physical Chemistry B*, *115*(2), 249-261.

[172] Huang, L., Joshi, K. L., van Duin, A. C., Bandosz, T. J., and Gubbins, K. E. (2012). ReaxFF molecular dynamics simulation of thermal stability of a $Cu_3(BTC)_2$ metal–organic framework. *Physical Chemistry Chemical Physics*, *14*(32), 11327-11332.

[173] Jeon, B., Sankaranarayanan, S. K., van Duin, A. C., and Ramanathan, S. (2011). Influence of surface orientation and defects on early-stage oxidation and ultrathin oxide growth on pure copper. *Philosophical Magazine*, *91*(32), 4073-4088.

[174] Carravetta, V., Monti, S., Li, C., and Ågren, H. (2013). Theoretical simulations of structure and X-ray photoelectron spectra of glycine and diglycine adsorbed on Cu (110). *Langmuir*, *29*(32), 10194-10204.

[175] Chenoweth, K., Van Duin, A. C., and Goddard, W. A. (2008). ReaxFF reactive force field for molecular dynamics simulations of hydrocarbon oxidation. *The Journal of Physical Chemistry A*, *112*(5), 1040-1053.

[176] Mueller, J. E., van Duin, A. C., and Goddard III, W. A. (2010). Development and validation of ReaxFF reactive force field for hydrocarbon chemistry catalyzed by nickel. *The Journal of Physical Chemistry C*, *114*(11), 4939-4949.

[177] Lee, C., and Lee, H. H. (2005). A potential novel two-step MOCVD of copper seed layers. *Electrochemical and Solid-state Letters*, *8*(1), G5-G7.

[178] Vestal, C., and Devore, T. (2001). Reaction between bis-(2, 4-pentanedionato) copper and water vapor. *International Symposion on High Temperature Corrosion and Materials Chemistry III, Washington DC: Electrochemical Society*, 285-292.

[179] Elliott, S. D., Scarel, G., Wiemer, C., Fanciulli, M., and Pavia, G. (2006). Ozone-based atomic layer deposition of alumina from TMA: Growth, morphology, and reaction mechanism. *Chemistry of Materials*, *18*(16), 3764-3773.

[180] Kwon, J., Dai, M., Halls, M. D., and Chabal, Y. J. (2008). Detection of a formate surface intermediate in the atomic layer deposition of high-κ dielectrics using ozone. *Chemistry of Materials*, *20*(10), 3248-3250.

[181] Goldstein, D. N., McCormick, J. A., and George, S. M. (2008). Al_2O_3 atomic layer deposition with trimethylaluminum and ozone studied by in situ transmission FTIR spectroscopy and quadrupole mass spectrometry. *The Journal of Physical Chemistry C*, *112*(49), 19530-19539.

[182] Törndahl, T., Ottosson, M., and Carlsson, J. O. (2006). Growth of copper (I) nitride by ALD using copper (II) hexafluoroacetylacetonate, water, and ammonia as precursors. *Journal of The Electrochemical Society*, *153*(3), C146-C151.

List of Figures

List of Tables

Versicherung

Hiermit versichere ich, dass ich die vorliegende Arbeit ohne unzulässige Hilfe Dritter und ohne Benutzung anderer als der angegebenen Hilfsmittel angefertigt habe; die aus fremden Quellen direkte oder indirekt übernommene Gedanken sind als solche kenntlich gemacht.

Bei der Auswahl und Auswertung des Materials sowie bei der Herstellung des Manuskripts habe ich Unterstützungsleistungen von folgenden Personen erhalten:

– keine –

Weitere Personen waren an der Abfassung der vorliegenden Arbeit nicht beteiligt. Die Hilfe eines Promotionsberaters habe ich nicht in Anspruch genommen. Weitere Personen haben von mir keine geldwerten Leistungen für Arbeiten erhalten, die im Zusammenhang mit dem Inhalt der vorgelegten Dissertation stehen.

Die Arbeit wurde bisher weder im Inland noch im Ausland in gleicher oder ähnlicher Form einer anderen Prüfungsbehörde vorgelegt.

Chemnitz, 21.11.2016

Xiao Hu

Theses

of the dissertation

"Multiscale Simulation of Metallic Copper and Copper Oxide Atomic Layer Deposition from Cu Beta-diketonates"

for attainment of the title 'Dr.-Ing.' At Technische Universität Chemnitz, Faculty for Electrical Engineering and Information Technology,

presented by M. Sc. Xiao Hu

Chemnitz, 2016

1. To keep pace with Moore's law, the feature size of metal-oxide field effect transistors is continuously scaled down, resulting in the improvement in device performance and the reduction in manufacturing cost. However, shrinking of the cross-sectional dimension of interconnect lines may degrade the signal propagation speed, which compromises the benefits offered by transistor scaling.

2. Cu interconnects are widely used to replace aluminum because of low resistivity and superior resistance to electromigration. The fabrication of Cu interconnects requires thin conductive seed layers before the subsequent Cu filling by electrochemical deposition.

3. Atomic layer deposition (ALD) is one of the most promising approaches for making Cu seed layers for next generation technology nodes, due to its excellent conformality and precise thickness control.

4. For the deposition of Cu films by ALD, three different approaches have been reported, including thermal ALD of Cu, indirect ALD of Cu, and PEALD of Cu. In the case of an indirect Cu ALD route, ALD is first applied for the deposition of Cu oxide or nitride films, which are subsequently reduced into the metallic Cu films.

5. An understanding of the surface chemistry of Cu precursor is crucial for development and optimization of ALD processes that could be used in Cu interconnect fabrication.

6. *Ab initio* calculations performed at an atomic scale can be used to obtain input data for the

molecular-scale and macroscale simulations, which can be realized through the reactive molecular dynamics and thermodynamic modeling, respectively.

7. A simplified Cu(I) precursor model [i.e., $(Me_3P)_2Cu(acac)$] reduces the computational costs of the surface calculations while preserving the required accuracy.

8. In the gas-phase, the $(^nBu_3P)_2Cu(acac)$ precursor is predicted to readily lose one of the $^nBu_3P$-ligands, whereas the $Cu(acac)_2$ precursor is stable over wide temperature ranges.

9. The $(Me_3P)_2Cu(acac)$ and $Cu(acac)_2$ precursors prefer to dissociate on the metallic substrates (Ta, Cu, Ru) rather than on the metal oxide (Cu_2O, SiO_2) and metal nitride (TaN) substrates. Electrons are continuously transferred from the metal surface to the adsorbed Cu precursor, leading to a sequential reduction of the Cu center atom.

10. The adsorbed Me_3P- and acac-ligands on the Cu surface block surface reactive sites and prevent further adsorption of precursors.

11. The equilibrium composition of ALD surface reaction is predicted through the Gibbs energy minimization method. The co-reactant O_3 or wet O_2 reacts with the surface Me_3P- and acac-ligands to form the gaseous products of CO_2 and H_2O.

12. The newly developed Cu_Hu potential satisfactorily reproduces most of the energetic and geometric data of the Cu precursor systems as calculated by DFT.

13. Molecular hydrogen is nonreactive towards the $Cu(acac)_2$ precursor; whereas atomic H can remove the surface acac-ligands efficiently.

14. The reactivity of the co-reactants towards $Cu(acac)_2$ follows the order $H > O_3 > H_2O > H_2$.

15. Water reacts with Cu(acac) on the $Cu_2O(111)$ surface through a ligand-exchange reaction, producing gaseous H(acac) and surface OH species. The presence of O_2 may further oxidize the by-product H(acac) into CO, CO_2, and H_2O, hindering its re-adsorption on the surface.

16. Multiscale simulation is an efficient and reliable route to gain valuable insights into the surface chemistry of ALD.

17. In future, multiscale simulation can be applied to the design and screening of precursors.

Curriculum vitae

Name: Xiao Hu

Date of birth: Oct 19th, 1985

Nationality: P. R. China

Marital status: Married, one child

Education

- 2008−2011, Master of Engineering
- Major: Ferrous Metallurgy
- College of Metallurgy and Energy, Hebei United University.
- Supervisors: Prof. Qing Lu and Prof. Shuhui Zhang
- 2004−2008, Bachelor of Engineering
- Major: Metallurgical Engineering
- College of Metallurgy and Energy, Hebei Polytechnic University.

Professional experience

- 06.2012−current, Zentrum für Mikrotechnologien, Technische Universität Chemnitz
  Simulation of the surface chemistry of atomic layer deposition.

  Topic of the thesis: "Multiscale simulation of copper metal and copper oxide atomic layer deposition from Cu beta-diketonates"

- 09.2008−03.2011, College of Metallurgy and Energy, Hebei United University
  Experimental and theoretical study of arsenic removal during the sintering.

  Topic of the thesis: "Fundamental investigation of arsenic removal from arsenic–bearing iron ores in sintering" (Outstanding master's thesis of Hebei province)

Own publications

Peer reviewed journal publications

[1] <u>Xiao Hu</u>, Jörg Schuster, Stefan E. Schulz, Thomas Gessner. Simulation of ALD chemistry of (^{n}Bu$_3$P)$_2$Cu(acac) and Cu(acac)$_2$ precursors on Ta(110) surface. *Microelectronic Engineering*, 2015, 137(2), 23-31.

[2] <u>Xiao Hu</u>, Jörg Schuster, Stefan E. Schulz, Thomas Gessner. Surface chemistry of copper metal and copper oxide atomic layer deposition from copper(II)acetylacetonate: a combined first-principles and reactive molecular dynamics study. *Physical Chemistry Chemical Physics*, 2015, 17(40), 26892-26902.

[3] <u>Xiao Hu</u>, Jörg Schuster, Stefan E. Schulz. Multiparameter and parallel optimization of ReaxFF reactive force field for modeling the atomic layer deposition of copper. *The Journal of Physical Chemistry C*, 2017, 121(50), 28077-28089.

Contributions to conferences

[1] <u>Xiao Hu</u>, Jörg Schuster, Stefan E. Schulz, Thomas Gessner. Thermodynamics and kinetics of Cu$_2$O ALD from Cu(I) acetylacetonate. *2nd International Conference on ALD Applications & 3rd China ALD conference*, Shanghai (China), 2014. (Oral presentation)

[2] <u>Xiao Hu</u>, Jörg Schuster, Stefan E. Schulz, Thomas Gessner. Surface chemistry of Cu(II) acetylacetonate on Cu(110) surface from reactive molecular dynamics and first-principles. *2nd International Conference on ALD Applications & 3rd China ALD conference*, Shanghai (China), 2014. (Poster presentation)

[3] <u>Xiao Hu</u>, Jörg Schuster, Stefan E. Schulz, Thomas Gessner. Mechanism for the atomic layer deposition (ALD) of copper oxide from (^{n}Bu$_3$P)$_2$Cu(acac) and wet O$_2$: a theoretical study. *14th International Conference on Atomic Layer Deposition,* Kyoto (Japan), 2014. (Poster presentation, best poster award)

[4] <u>Xiao Hu</u>, Jörg Schuster, Stefan E. Schulz, Thomas Gessner. Simulation of ALD chemistry of copper metalorganic precursors on Ta(110) Surface. *Materials for Advanced Metallization (MAM 2014)*, Chemnitz (Germany), 2014. (Poster presentation, best poster award)

[5] <u>Xiao Hu</u>, Jörg Schuster, Stefan E. Schulz, Thomas Gessner. Reactive molecular dynamics study of copper metal and copper oxide atomic layer deposition from Copper(II) acetylacetonate. *15th International Conference on Atomic Layer Deposition,* Portland (USA), 2015. (Presented by Dr. Zienert)

[6] <u>Xiao Hu</u>, Jörg Schuster, Stefan E. Schulz, Thomas Gessner. Large-scale reactive dynamics simulations of Cu ALD using a newly developed ReaxFF potential. *16th International Conference on Atomic Layer Deposition,* Dublin (Ireland), 2016. (Oral presentation)

[7] Dileep Dhakal, <u>Xiao Hu</u>, Colin Georgi, Jörg Schuster, Stefan E. Schulz. Growth of ultrathin Cu films deposited by atomic layer deposition for BEOL application. *Materials for Advanced Metallization (MAM 2016)*, Brussels (Belgium), 2016.

[8] <u>Xiao Hu</u>, Jörg Schuster, Stefan E. Schulz. Reactive dynamics simulation of metallic Cu and Cu oxide ALD from the $(^nBu_3P)_2Cu(acac)$ precursor. *Materials for Advanced Metallization (MAM 2017)*, Dresden (Germany), 2017. (Poster presentation)

[9] <u>Xiao Hu</u>, Jörg Schuster, Stefan E. Schulz. Reactive molecular dynamics simulations of metallic Cu and Cu oxides ALD. *Joint EuroCVD-21 BalticALD-15*, Linköping (Sweden), 2017. (Oral presentation)

Acknowledgement